UNIVERSIDAD POLITÉCNICA DE MADRID
Escuela Técnica Superior de Ingenieros de Telecomunicación

Development of Technologies for Solar Fuel Production: Optimization of Photovoltaic Conversion Processes, Carbon Dioxide Capture, and Electrolyzer Design

TESIS DOCTORAL

Presentada para optar al título de Doctor por:

Alfonso González del Valle Mezo
Doble Grado en Química e Ingeniería de Materiales y Máster en Materiales Avanzados, Nanotecnología y Fotónica

Madrid, 2025

UNIVERSIDAD POLITÉCNICA DE MADRID
Escuela Técnica Superior de Ingenieros de
Telecomunicación

Doctorado en Energía Solar Fotovoltaica

Development of Technologies for Solar Fuel Production: Optimization of Photovoltaic Conversion Processes, Carbon Dioxide Capture, and Electrolyzer Design

TESIS DOCTORAL

Presentada para optar al título de Doctor por:

Alfonso González del Valle Mezo

Doble Grado en Química e Ingeniería de Materiales y Máster en
Materiales Avanzados, Nanotecnología y Fotónica

Bajo la dirección de:

Dr. Antonio Martí Vega

Dr. Pablo García-Linares Fontes

Madrid, 2025

Título: Development of Technologies for Solar Fuel Production: Optimization of Photovoltaic Conversion Processes, Carbon Dioxide Capture, and Electrolyzer Design

Autor: Alfonso González del Valle Mezo

Programa de Doctorado: Energía Solar Fotovoltaica

Dirección de tesis:

Dr. Antonio Martí Vega, Catedrático, Universidad Politécnica de Madrid (Director)

Dr. Pablo García-Linares Fontes, Profesor Contratado Doctor, Universidad Politécnica de Madrid (Director)

Revisores externos:

Tribunal de tesis:

Fecha de defensa:

Esta Tesis ha sido financiada por los proyectos CEOTRES-CM (Y2020/EMT-6419), financiado por la Comunidad de Madrid y DEFYCO2 (TED2021-129694B-C22), financiado por la Unión Europea a través de los fondos NextGeneration EU

”Driving out into the sun
Let the ultraviolet cover me up
Went looking for a creation myth
Ended up with a pair of cracked lips”
-Phoebe Bridgers

Agradecimientos

A mis padres, Agurtzane y Javier.

A mis hermanos, Íñigo y Javier.

A mi tía, Alicia.

Abstract

This Thesis is driven by the need to explore complementary solutions alongside renewable energy to help mitigate the impacts of global warming resulting from increasing CO_2 emissions. It develops along two objectives. The first objective aims to contribute to reducing CO_2 emissions in sectors where implementing photovoltaics (PV) is difficult. To address this, the Thesis explores the optimization of green H_2 production systems powered by renewable energy sources through electrolysis. The second targets the reduction of atmospheric CO_2 that has already been emitted. Here, the Thesis evaluates experimentally a direct air capture (DAC) system capable of extracting CO_2 from the atmosphere. This objective is extended to include the conversion of the captured CO_2 into formic acid, a value-added fuel, reinforcing the rationale for atmospheric CO_2 capture.

The work related to the green H_2 production technology is focused on the study of the interconnection between the PV generation and electrolyzer stages. For that purpose, three coupling strategies between PV systems and the electrolyzer are analysed: direct, indirect, and indirect with battery storage. In the direct coupling, the electrical terminals of the PV system are connected directly to the input terminals of the electrolyzer, while the indirect coupling incorporates a power stage between PV and electrolyzer. The indirect configuration outperforms the direct one, showing greater reliance to atmospheric variability and suboptimal PV generator performance. The inclusion of a battery further enhances the techno-economic performance, delivering the highest annual H_2 output, the best overall efficiency, the highest share of energy allocated to H_2 production, and the greatest overall profitability throughout the lifespan of the electrolyzer.

Regarding the reduction of atmospheric CO_2, an experimental DAC method using diamine is assessed. Diamine reacts with CO_2 to form an insoluble carbamic acid (CA1), thus capturing it. Heating this CA1 compound releases the CO_2, which can then be concentrated. This method achieves experimental capture efficiencies of up to 95%. A thermodynamic analysis based on this DAC method is also conducted to compare the theoretical minimum energy consumption, also determined in this Thesis, with the actual energy demand of the process.

To utilize the captured CO_2, a three-chamber electrolyzer is implemented for formic acid production, based on a commercial prototype. The choice of formic acid is supported by market research, which considers the production of several carbon-based potential compounds. This analysis considers factors such as production profitability, energy requirements, market size, and ease of handling of the different candidate products. The Thesis also includes the design and fabrication of most electrolyzer components, except for the cathode

and both anodic and cathodic membranes. The electrolyzer is assembled to ensure operational readiness, followed by its electrical characterization and an analysis of the compounds generated during operation.

Resumen

Esta Tesis surge de la necesidad de explorar soluciones complementarias al uso de energías renovables para mitigar los efectos del calentamiento global derivados del aumento de las emisiones de CO_2. El trabajo se articula en torno a dos objetivos. El primero busca contribuir a la reducción de emisiones de CO_2 en sectores donde la implementación de sistemas fotovoltaicos (PV) resulta complicada. Para ello, la Tesis estudia la optimización de sistemas de producción de H_2 verde alimentados por fuentes de energía renovable mediante electrólisis. El segundo objetivo se centra en la reducción del CO_2 atmosférico que ya ha sido emitido. En este caso, la Tesis evalúa experimentalmente un sistema de captura directa del aire (DAC) capaz de extraer CO_2 de la atmósfera. Este objetivo se amplía con la conversión del CO_2 capturado en ácido fórmico, un combustible de valor añadido, lo que refuerza la justificación de su captura.

El trabajo relacionado con la tecnología de producción de H_2 verde se enfoca en el estudio de la interconexión entre la generación fotovoltaica y la etapa del electrolizador. Para ello, se analizan tres estrategias de acoplamiento entre los sistemas PV y el electrolizador: directa, indirecta e indirecta con almacenamiento en baterías. En el acoplamiento directo, los terminales eléctricos del sistema PV se conectan directamente a las bornas de entrada del electrolizador, mientras que el acoplamiento indirecto incorpora una etapa de potencia entre ambos. La configuración indirecta supera a la directa, mostrando una mayor resiliencia frente a la variabilidad atmosférica y al rendimiento subóptimo del generador fotovoltaico. La inclusión de una batería mejora aún más el desempeño tecno económico, proporcionando la mayor producción anual de H_2, la mejor eficiencia global, la mayor proporción de energía destinada a la producción de H_2 y la máxima rentabilidad a lo largo de la vida útil del electrolizador.

Con respecto a la reducción del CO_2 atmosférico, se evalúa un método experimental de DAC que emplea diamina. Esta reacciona con el CO_2 formando un ácido carbámico (CA1) insoluble, lo que permite su captura. Al calentar este compuesto CA1, el CO_2 es liberado y puede concentrarse. Este método experimental alcanza eficiencias de captura de hasta un 95%. También se realiza un análisis termodinámico basado en este método DAC para comparar el consumo mínimo teórico de energía, también determinado en esta Tesis, con la demanda energética real del proceso.

Para dar uso al CO_2 capturado, se implementa un electrolizador de tres cámaras para la producción de ácido fórmico basado en un prototipo comercial. La elección del ácido fórmico está respaldada por un estudio de mercado que considera la producción de varios compuestos potenciales basados en carbono. Este análisis toma en cuenta factores como la rentabilidad de producción, los requerimientos energéticos, el tamaño del mercado y la facilidad de manejo de los diferentes productos candidatos. La Tesis también incluye el diseño y la fabricación de la mayoría de los componentes del electrolizador, con excepción del cátodo y de las membranas anódica y catódica. El electrolizador se ensambla para garantizar su operatividad, seguido de su caracterización eléctrica y del análisis de los compuestos generados durante su funcionamiento.

List of contents

List of acronyms

ABS	Acrylonitrile butadiene styrene
AM1.5G	Air mass 1.5 global spectrum
B3LYP	Becke- Lee-Yang-Parr functionals
BPP	Bipolar plates
CA1	Carbamic acid
CAPEX	Capital expenditure
CCS	Carbon capture and storage
CCU	Carbon capture and usage
CCUS	Carbon capture, usage, and storage
CNC	Computer numerical control
CO2RR	Carbon reduction reaction
CSIC	Consejo Superior de Investigaciones Científicas
DAC	Direct air capture
DFT	Density functional theory
DMSO	Dimethyl sulfoxide
EBOS	Energy balance of system
FF	Fill factor
GC	Gas chromatography
GDE	Gas diffusion electrode
GDL	Gas diffusion layer
GHGs	Greenhouse gases
GWEC	Global Wind Energy Council
HCOOH	Formic acid
HFCs	Hydrofluorocarbons
HPLC	High-performance liquid chromatography
ICP	Instituto de Catálisis y Petroleoquímica
IEA	International Energy Agency
IES-UPM	Instituto de Energía Solar – Universidad Politécnica de Madrid

IPA	iso-2-propanol
IPCC	Intergovernmental Panel on Climate Change
IPDA	Isophorone diamine
LCOE	Levelized cost of electricity
M06	Minnesota 06 functionals
MEA	Membrane electrode assembly
MPP	Maximum power point
MPPT	Maximum power point tracker
OER	Oxygen evolution reaction
OPEX	Operational expenditure
PBE0	Perdew-Burke-Ernzerhof functionals
PEM	Proton exchange membrane
PFCs	Perfluorocarbons
PLA	Polylactic acid
PP	Polypropylene
PS	Power stage
PV	Photovoltaic
RES	Renewable energy sources
SBOS	Structure balance of system
SDM	Single diode model
S-H	Solar-Hydrogen
SHE	Standard hydrogen electrode
SMR	Steam methane reforming
SOC	State of charge
SOE	Solid oxide electrolysis
SOECs	Solid oxide electrolyzer cells
STC	Standard test conditions
TMY	Typical meteorological year

List of symbols

G_t	Incident irradiance ($\mathrm{W \cdot m^{-2}}$)
T	Temperature (K)
J	Current density ($\mathrm{A \cdot cm^{-2}}$)
I	Current (A)
I_c	Current of PV cell (A)
V	Voltage (V)
J_c	Current density of PV cell ($\mathrm{A \cdot cm^{-2}}$)
$J_{\mathrm{ph},c}$	Photogenerated current density of PV cell ($\mathrm{A \cdot cm^{-2}}$)
$J_{0,c}$	Reverse saturation current density of PV cell ($\mathrm{A \cdot cm^{-2}}$)
q	Electron charge (C)
V_c	Output voltage of PV cell (V)
V_{oc}	Open-circuit Voltage of PV cell (V)
$r_{s,c}$	Series resistance of PV cell ($\Omega \cdot \mathrm{cm}^{-2}$)
$r_{\mathrm{sh},c}$	Shunt resistance of PV cell ($\Omega \cdot \mathrm{cm}^{-2}$)
n	Diode ideality factor (adim.)
k_B	Boltzmann constant ($\mathrm{eV \cdot K^{-1}}$)
G_n	Irradiance at STC ($\mathrm{W \cdot m^{-2}}$)
T_0	Temperature at STC (K)
$J_{0\mathrm{n}}$	Saturation current density at STC ($\mathrm{A \cdot cm^{-2}}$)
E_g	Bandgap (eV)
α	Temperature coefficient ($\mathrm{A \cdot K^{-1}}$)
A_c	Area of PV cell ($\mathrm{cm^2}$)
I_{PV}	Output current of PV module (A)
V_{PV}	Output voltage of PV module (V)
A	Area of PV module ($\mathrm{cm^2}$)
N_s	Number of series-connected PV cells
N_P	Number of parallel-connected PV cells
I_{SC}	Short-circuit current of PV module (A)
I_{MPP}	Current at maximum power point (A)

V_{MPP}	Voltage at maximum power point (V)
FF	Fill factor (adim.)
η_m	Efficiency of PV module (%)
P_{MPP}	Maximum power point (W)
$\Delta G_{R,0}$	Gibbs free energy of reaction at standard conditions ($\mathrm{kJ \cdot mol^{-1}}$)
V_{rev}	Reversible voltage of reaction (V)
Z	Number of electrons transferred in reaction (adim.)
F	Faraday's constant ($\mathrm{C \cdot mol^{-1}}$)
$V_{\mathrm{th},c}$	Threshold voltage of electrolytic cell (V)
k	Threshold voltage non-ideality factor
$V_{\mathrm{EL},c}$	Voltage of electrolytic cell (V)
V_{act}	Activation overpotential (V)
V_{con}	Concentration overpotential (V)
V_{ohm}	Ohmic overpotential (V)
$V_{\mathrm{act},a}$	Anodic activation overpotential (V)
$V_{\mathrm{act},c}$	Cathodic activation overpotential (V)
R	Universal gas constant ($\mathrm{J \cdot K^{-1} \cdot mol^{-1}}$)
I_{EL}	Current through electrolyzer (A)
A_{EL}	Area of electrolyzer ($\mathrm{cm^2}$)
α_a	Anodic charge transfer coefficient (adim.)
α_c	Cathodic charge transfer coefficient (adim.)
$j_{0,a}$	Anodic exchange current density ($\mathrm{A \cdot cm^{-2}}$)
$j_{0,c}$	Cathodic exchange current density ($\mathrm{A \cdot cm^{-2}}$)
E_{exc}	Activation energy of water electrolysis reaction ($\mathrm{J \cdot mol^{-1}}$)
j_L	Maximum current density of electrolyzer ($\mathrm{A \cdot cm^{-2}}$)
r_{ohm}	Electric resistance of PEM membrane ($\Omega \cdot \mathrm{cm^{-2}}$)
t_m	PEM membrane thickness (cm)
σ	PEM conductivity ($\mathrm{S \cdot cm^{-1}}$)
σ_{ref}	PEM conductivity at T_{ref} ($\mathrm{S \cdot cm^{-1}}$)
T_{ref}	Reference temperature (K)

E_{pro}	PEM activation energy for H^+ transport ($\mathrm{J \cdot mol^{-1}}$)
S_{cell}	Number of series-connected electrolytic cells
k	Threshold voltage non-ideality factor
V_{EL}	Voltage of electrolyzer (V)
μ_F	Faradaic efficiency (%)
$\dot{m}\mathrm{H}_2$	Production rate of hydrogen ($\mathrm{kg \cdot h^{-1}}$)
$\dot{m}\mathrm{O}_2$	Production rate of oxygen ($\mathrm{kg \cdot h^{-1}}$)
$M\mathrm{H}_2$	Cumulative hydrogen production (kg)
C_{bat}	Energy stored in battery at a given time ($\mathrm{W \cdot h}$)
C_{max}	Maximum energy storage capacity of battery ($\mathrm{W \cdot h}$)
SOC	State of charge (%)
η_{global}	Global efficiency of hydrogen production (%)
E_{H2}	Energy content of produced hydrogen ($\mathrm{kWh \cdot y^{-1}}$)
E_{in}	Total incident energy on the PV module in a year ($\mathrm{kWh \cdot m^{-2} \cdot y^{-1}}$)
C	Cost (€)
$CAPEX$	Capital expenditure (€)
$OPEX$	Operational expenditure (€)
ny	Number of years
B_g	Gross benefits (€)
P_{H2}	Price of hydrogen ($€ \cdot \mathrm{kg^{-1}}$)
Ex	Energy fed into the grid (kWh)
P_{Ex}	Price of surplus energy ($€ \cdot \mathrm{MWh^{-1}}$)
B_n	Net benefits (€)
η_{DC}	Efficiency of DC-DC converter (%)
P	Pressure (Pa)
V_i	Volume (L)
N_i	Amount of species (mol)
x	Concentration of carbon dioxide in air
U	Internal energy change (J)
S	Entropy ($\mathrm{J \cdot K^{-1}}$)

μ	Chemical potential ($\mathrm{J \cdot mol^{-1}}$)
ΔU_S	Energy change of system (J)
ΔU_{RV}	Energy change of reservoir (J)
W	Work (J)
ΔS_S	Entropy change of system ($\mathrm{J \cdot K^{-1}}$)
ΔS_{RV}	Entropy change of reservoir ($\mathrm{J \cdot K^{-1}}$)
ΔV_S	Volume change of system (L)
ΔV_{RV}	Volume change of reservoir (L)
G	Gibbs free energy (J)
ΔG_S	Change in Gibbs free energy of system (J)
T_{RV}	Temperature of reservoir (K)
P_{RV}	Pressure of reservoir (Pa)
S_i^0	Standard entropy ($\mathrm{J \cdot K^{-1}}$)
$c_{v,i}$	Specific heat of a gas at constant volume ($\mathrm{J \cdot K^{-1} \cdot kg}$)
$\Delta S_{\mathrm{mixing}}$	Entropy of mixing ($\mathrm{J \cdot K^{-1}}$)
F	Force (N)
P_i	Partial pressure (Pa)
η_{cap}	Capture efficiency (%)
N_{cap}	Quantity of CO_2 captured ($\mathrm{mol \cdot h^{-1}}$)
N_D	Quantity of CO_2 bubbled ($\mathrm{mol \cdot h^{-1}}$)
m_i	Mass (g)
Δm	Mass change (g)
M	Molecular weight ($\mathrm{g{\cdot}mol^{-1}}$)
$\emptyset$	Volumetric flow rate ($\mathrm{mL \cdot min^{-1}}$)
V_{air}	Volume of air bubbled (L)
$C_{p,i}$	Specific heat of a gas at constant pressure ($\mathrm{J \cdot K^{-1} \cdot kg}$)
Q	Heat (J)
T_{CO2}	Temperature of CO_2 desorption (K)
G_{air}	Gibbs free energy of air (J)
G_{air0}	Gibbs free energy of air without CO_2 (J)

$\hat{H}$	Hamiltonian (J)
Ψ	Wave function ($\mathrm{m}^{-3/2}$)
$\hat{T}$	Kinetic energy (J)
$\hat{V}$	Potential energy (J)
$\hat{U}$	Electron-electron interaction energy (J)
$n(r)$	Electron density (m^{-3})
E_x^{HF}	Hartree-Fock energy functional (J)
E_x^{B}	Becke functional (J)
E_c^{LYP}	Lee-Yang-Parr functional (J)
E_x^{PBE}	Perdew-Burke-Ernzerhof functional (J)
E_c^{PBE}	Perdew-Burke-Ernzerhof functional (J)
E_x^{DFT}	Local DFT exchange energy (J)
E_{xc}^{D3}	Empirical dispersion correction of Grimme's D3 method (J)
w_D	Weight of empirical dispersion correction
H	Enthalpy ($\mathrm{kJ \cdot mol^{-1}}$)
ΔH_f^0	Standard enthalpy of formation ($\mathrm{kJ \cdot mol^{-1}}$)
ΔS_f^0	Standard entropy of formation ($\mathrm{J \cdot mol^{-1} \cdot K^{-1}}$)
ΔG_f^0	Standard Gibbs free energy of formation ($\mathrm{kJ \cdot mol^{-1}}$)
ΔG_r^0	Standard Gibbs free energy of reaction ($\mathrm{kJ \cdot mol^{-1}}$)
μ_i^0	Standard chemical potential ($\mathrm{J \cdot mol^{-1}}$)
E_{cell}^0	Standard cell voltage (V)
E_{CO2RR}^0	Standard voltage for carbon reduction reaction (V)
E_{OER}^0	Standard voltage for oxidation evolution reaction (V)
R_E	Total series resistance of three chambers electrolyzer (kΩ)

List of Figures

List of Tables

Chapter 1. Motivation and framework of reference for this Thesis

This Thesis has been developed at the Institute of Solar Energy of the Universidad Politécnica de Madrid (IES-UPM), whose initial research works began in the late 1970s. Since then, this Institute has been a pioneering center entirely dedicated to the development of the science and technology of photovoltaic (PV) energy conversion. IES-UPM is now a globally recognized center, having made contributions to the international community, for example in silicon solar cell technology, III-V multijunction cells, more efficient new concepts for solar cells, including associated quantum calculations and intermediate band solar cells. Additionally, their members have dedicated themselves to the analysis of PV plants, regardless of their size, while considering also the social aspects of their use.

Only in recent times has IES-UPM expanded its research field to novel applications of solar PV energy, such as the development of energy storage technology based on the latent heat of molten silicon and its recovery through the thermophotovoltaic effect, as well as systems to produce solar fuels, which store energy in the form of chemical energy, whether hydrogen (H_2) or fuels derived from H_2O and carbon dioxide (CO_2) captured from the atmosphere. In this respect, this is the first Thesis developed at IES-UPM focused on the production of solar fuels.

This Thesis is motivated by the need to identify and investigate complementary solutions to the development and implementation of renewable energy, in order to combat or mitigate the effects of global warming caused by the increasing emissions of greenhouse gases (GHGs), especially CO_2. The Thesis specifically considers two solutions to this issue, which serve as the main pillars of the study.

The first of these aims is to contribute to research focused on reducing CO_2 emissions as a GHG. More specifically, it seeks to reduce CO_2 emissions in sectors where the implementation of mature, industrial-scale renewable energies, such as PV, is challenging. Accordingly, Chapter 2 of this Thesis addresses green H_2 production systems, those based on electrolysis powered by renewable energy sources. Since green H_2 is projected to become the main energy carrier in the energy transition, the optimization of its production systems has attracted growing interest, highlighting the need for further in-depth study.

The second pillar of this Thesis addresses a solution that not only aims to mitigate the effects of the greenhouse effect by reducing CO_2 emissions but also seeks to reduce the amount of CO_2 already released into the atmosphere. Thus, Chapter 3 of this Thesis presents a thermodynamic study aimed at determining the minimum energy cost required to remove one ton of CO_2 from the atmosphere. This is a fundamental question, as if this minimum cost were excessively high, it would make little sense to even explore technologies based on atmospheric CO_2 capture. Once it is concluded that the thermodynamic cost is not prohibitive, Chapter 4 focuses on the study of a specific direct air CO_2 capture system based on the use of diamines, initially studied by a research team at the University of Tokyo, which achieves a capture efficiency greater than 99%. The high efficiency of this capture system motivates also a thermodynamic analysis, with the aim of determining the actual energy cost of capturing one ton of CO_2 from the air with this practical system. After determining the energy cost involved, the next step is to consider potential uses or final destinations for the CO_2 captured from the atmosphere. Currently, two main pathways are being explored: storage or utilization. CO_2 is a compound from which numerous value-added products can be derived, so considering the energy and economic costs involved in its capture,

CO_2 utilization appears to be a justified option, at least economically. Accordingly, Chapter 5 includes an analysis aimed at identifying which CO_2-derived products are most favorable for production. Upon selecting one such value-added product, the chapter also delves into aspects related to the design, fabrication, and characterization of a technology capable of converting the captured CO_2 into the target product.

Finally, this first chapter briefly reviews several key topics related to the development of the contents of this Thesis in order to place it within its broader context. These include the review of the impact of CO_2 emissions, electrolysis techniques for green H_2 production, various technologies for atmospheric CO_2 capture, and the main electrochemical methods for CO_2 conversion.

1.1 The impact of CO_2 emissions

The Industrial Revolution represented a pivotal moment in human history, bringing profound changes not only to society but also to the composition of Earth's atmosphere. The steady increase in anthropogenic GHGs such as CO_2, methane (CH_4), nitrous oxide (N_2O), hydrofluorocarbons (HFCs), perfluorocarbons (PFCs), and sulfur hexafluoride (SF_6) has led to observable changes in Earth’s climate systems [1]. Among these gases, CO_2 has emerged as the most consequential due to its overwhelming contribution—approximately 76% of total emissions—and its persistence in the atmosphere [2,3]. Its long atmospheric lifetime and the sheer volume released by activities such as fossil fuel combustion, deforestation, and industrial expansion suggest that CO_2 will remain at the center of global climate change discussions [4].

While the greenhouse effect is a natural process necessary for maintaining habitable temperatures, the excessive accumulation of CO_2 disrupts the delicate radiative balance of the Earth. As CO_2 concentrations have risen sharply since the pre-industrial era, they have intensified the greenhouse effect, leading to global warming, as depicted in Figure 1.1. Multiple studies attribute observable phenomena – such as rising sea levels, melting glaciers, and an increased frequency of extreme weather events – directly to temperature raise caused by CO_2 and other GHGs [5,6]. The Intergovernmental Panel on Climate Change (IPCC) has warned that if current emission trajectories persist, the global mean temperature could exceed a 1.5°C increase above pre-industrial levels as early as 2030 [7], with severe repercussions for both natural ecosystems and human societies [8]. The role of CO_2 as an energy-related emission underscores the direct relationship between economic activity, energy consumption, and environmental impact. The significance of focusing on CO_2 is paramount not only from a scientific perspective but also from a policy standpoint because any meaningful reduction in global warming potential is contingent upon curbing CO_2 emissions.

In response to the escalating crisis, a number of political and legislative strategies have been proposed and implemented with varying degrees of success. Two of the most prominent frameworks are the Paris Agreement of 2015 and the Agenda 2030 for Sustainable Development.

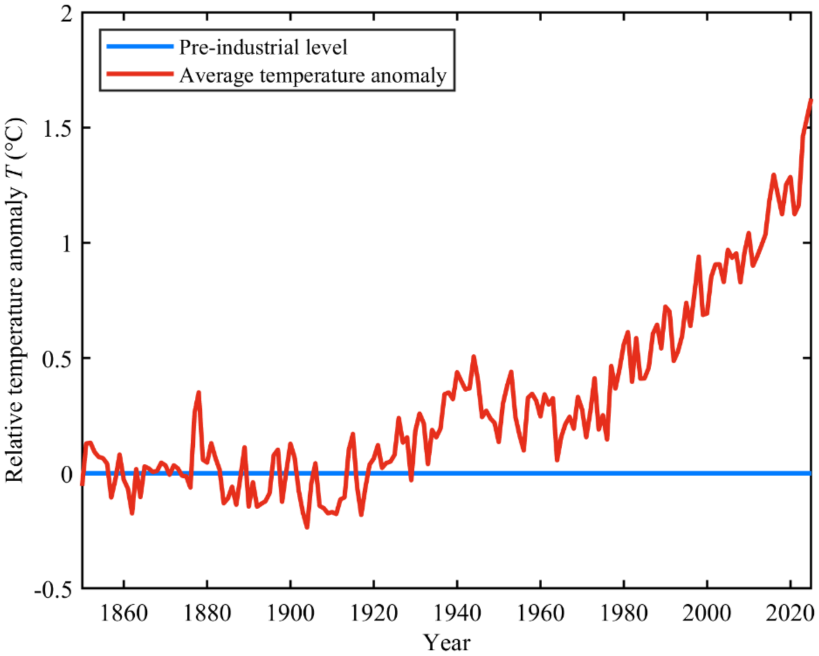

Figure 1.1 Worldwide annual temperature anomalies relative to the pre-industrial period. The period 1861-1890 is used as the baseline to measure temperature changes relative to pre-industrial times. Data was obtained from Met Office Hadley Centre - HadCRUT5 (2025) with major processing by Our World in Data.

The Paris Agreement represents a landmark in international climate policy, as it formalized a global commitment to limit the rise in mean global temperatures to well below 2°C and to pursue efforts to limit the increase to 1.5°C above pre-industrial levels before 2100 [9]. This international accord requires that all participating countries submit and periodically update their national plans (Nationally Determined Contributions) for reducing emissions. The emphasis on temperature thresholds reflects an understanding of the nonlinear and potentially catastrophic impacts of climate change, whereby even small increases in temperature could lead to disproportionately high adverse effects on weather patterns, biodiversity, and human livelihoods.

Complementing the Paris Agreement is the Agenda 2030 for Sustainable Development, adopted by the United Nations in 2015. Agenda 2030 outlines 17 Sustainable Development Goals (SDGs), one of which directly addresses climate action (SDG 13). This strategy offers a holistic approach by integrating climate change mitigation and adaptation within a broader framework of environmental, economic, and social sustainability [10]. By promoting renewable energy resources (RES), sustainable urban development, and innovative technologies that reduce reliance on carbon-intensive fuels, Agenda 2030 forms the backbone of many national and international policy approaches aimed at curbing CO_2 emissions.

These frameworks are complemented by various regional and national measures, including carbon pricing, energy efficiency mandates, and investment in renewable energy infrastructure. The integration of legislative initiatives with economic incentives demonstrates that scientific insights into the effects of CO_2 emissions can be translated into concrete political action. Consequently, the global community is increasingly recognizing that long-term resilience and sustainable development require immediate and sustained reductions in GHGs emissions, especially CO_2.

The intensity of CO_2 emissions is critically associated with various sectors of economic activity, with certain industries and transportation emerging as the largest contributors, as depicted in

Figure 1.2. Notably, energy production and transportation stand out as the two sectors responsible for the highest levels of CO_2 emissions globally [11].

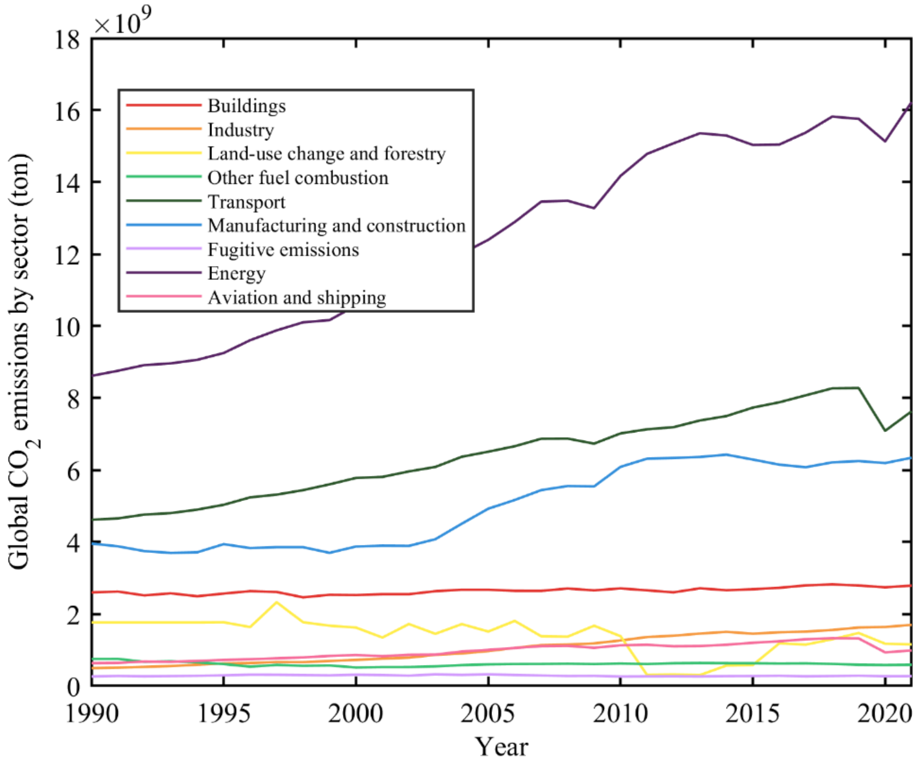

Figure 1.2 Worldwide CO_2 emissions by different sectors in the period from 1990 to 2021. Data was obtained from Met Office Hadley Centre - HadCRUT5 (2025) with major processing by Our World in Data.

The energy sector is recognized as the primary source of CO_2 emissions, stemming largely from the combustion of fossil fuels such as coal, oil, and natural gas to generate electricity. Recent estimates indicate that the energy sector accounted for approximately 63% of total global CO_2 emissions [12]. This sector is a major factor driving climate change. The International Energy Agency (IEA) has projected that energy-related CO_2 emissions may increase as global demand for energy rises, particularly in developing countries [12]. The reliance on carbon-intensive fossil fuel sources for electricity generation and heat production accentuates the urgency for transitioning toward RES, which can substantially reduce emissions. Fossil fuel combustion is projected to contribute significantly to total global CO_2 emissions, underscoring the need for effective management and replacement strategies within the energy domain [13,14].

In addition to energy production, the transportation sector emerges as another leading contributor to global CO_2 emissions, accounting for about 24% of total emissions as of 2021 [12]. This sector encompasses various modes, including personal vehicles, public transit, aviation, and maritime transport. A report by the International Energy Agency indicated that in 2019, the transportation sector was responsible for approximately 27% of the world's total energy consumption and corresponding emissions [12]. This growing footprint is partly attributable to urbanization and increasing mobility needs, which have driven demand for transportation infrastructure.

As energy production remains one of the primary sectors contributing to CO_2 emissions, a significant focus of global efforts to mitigate climate change revolves around promoting and developing RES that are associated with lower emissions. Among these renewable sources, wind and PV solar energy have gained traction.

Wind energy has gained recognition as a clean, renewable source of power that can effectively displace fossil fuel usage. Technological advancements in wind turbine designs and efficiency have significantly increased the viability of wind energy, allowing for large-scale wind farms both onshore and offshore. According to the Global Wind Energy Council (GWEC), wind power capacity grew significantly in recent years, providing an essential contribution to meeting energy needs while reducing carbon footprints [15].

Solar PV technology, however, has experienced unprecedented growth in recent years, emerging as one of the leading sources of renewable energy globally. Since 2010, the cost of PV technology has plummeted, by 82%, making it increasingly accessible and appealing for both residential and commercial applications [16]. This sharp decline in costs is attributed to advancements in manufacturing processes, economies of scale, and increased competition among PV manufacturers, which has fueled a surge in installations worldwide.

Moreover, the versatility of solar PV technology allows for various applications, including utility-scale solar farms, rooftop installations, and even small-scale distributed generation in residential areas. The International Renewable Energy Agency (IRENA) noted that as of 2023, solar power capacity exceeded 1,000 gigawatts, accounting for a significant portion of new energy capacity installations [17]. This trend has been mirrored in countries like China, the United States, India, Japan, and Germany, where favorable policies and incentives have facilitated large-scale investments in solar infrastructure.

In addition to cost reductions and increased installations, several innovative technologies within the solar PV sector are emerging. These include bifacial solar panels, which can harvest sunlight from both sides, increasing energy output; thin-film solar cells, which are lightweight and more flexible than traditional silicon-based panels; and solar tracking systems, which adjust the position of panels throughout the day to maximize energy capture [18]. Furthermore, energy storage systems are increasingly integrated with solar installations, enhancing grid resilience and enabling greater utilization of solar energy even during non-daylight hours [19].

The transition to RES, while crucial for reducing associated CO_2 emissions, faces two significant challenges that limit their broader application. First, the intermittency of RES presents a critical issue; energy production can exceed demand at times, leading to waste, while at other times, demand surpasses production capacity, resulting in shortfalls. This fluctuation necessitates reliable energy storage solutions or backup systems to ensure a steady supply.

Secondly, certain sectors—including heavy transportation, industrial processes, and specific agricultural practices—contribute substantially to CO_2 emissions but are difficult to electrify [20]. These sectors resist the straightforward integration of RES due to their specific operational demands and the lack of viable alternatives, making comprehensive emissions reductions a complex challenge [21].

RES do not emit CO_2 during their operation, although some emissions occur during their manufacturing. Anyways, RES significantly reduce the rate of CO_2 emissions by displacing fossil fuel use, but they do not address the underlying issue of existing atmospheric CO_2 levels. This is not an inherent problem with renewable energy itself but rather a limitation in its scope—renewables mitigate ongoing emissions but do not directly remove the excess CO_2 already accumulated in the atmosphere. The cumulative GHGs already emitted pose a substantial and ongoing challenge to global climate stability. Despite the transition towards renewables, the historical emissions—amounting to over 1.5 trillion metric tons of CO_2 since the Industrial Revolution—continue to exert a tangible effect on Earth's climate, contributing to global warming, increased extreme weather events, and systemic ecological disruptions (IPCC, 2021).

Therefore, while the expansion of renewable energy technologies is essential to preventing further increases in emissions, it must be complemented by additional strategies. Carbon removal and sequestration efforts are necessary to actively address the significant legacy of past emissions and effectively combat climate change and its associated impacts.

Energy vectors, which serve as carriers of energy capable of transporting, storing, or delivering energy in various forms, present a promising solution to these challenges [22]. H_2 is increasingly recognized as the most promising energy vector in contemporary discussions surrounding energy transition and decarbonization.

1.2 Hydrogen as an energy vector

H_2 is used to generate electricity [23,24], to power industries [25–27], or fuel transportation [28,29], making it a key enabler of a more flexible and resilient energy infrastructure. Specifically, H_2 can be transported and distributed to various sectors that require a stable and reliable energy supply, such as heavy industry [30,31], transportation [25,28,29], and residential heating [32] as depicted Figure 1.3. In addition, H_2 serves as a crucial component in the production of fertilizers, which is essential for ammonia (NH_3) synthesis [31,33] as shown in Figure 1.3. It also plays a key role in the chemical industry as a reactant, enabling more sustainable industrial processes, and in the steel industry [25], where it can replace carbon-intensive methods, significantly reducing emissions (Figure 1.3). There are basically three types of H_2: grey, blue, and green.

Grey H_2 is produced from natural gas through steam methane reforming (SMR), a process that releases large amounts of CO_2 into the atmosphere [34]. Conversely, blue H_2 follows the same production process as grey H_2 but incorporates carbon capture and storage (CCS) technologies to reduce emissions [34]. However, CCS is not always 100% effective, meaning some carbon emissions still occur [35]. Green H_2, on the other hand, is generated through electrolysis, a process that splits water (H_2O) into H_2 and oxygen (O_2) using electricity [36]. When this electricity comes from renewable sources such as solar, wind, or hydroelectric power, the process is free of greenhouse gas emissions, making it a sustainable energy carrier.

The use of renewable energy in H_2 production is interesting for two main reasons. First, it ensures that H_2 does not contribute to carbon emissions during its operation, distinguishing it from grey and blue H_2 [28]. Second, it allows for better integration of intermittent renewable energy sources into the energy system. As a larger portion of the electricity demand is covered by renewable sources, the PV and wind technologies become overweight in terms of installed capacity in the electric system. This translates into greater losses due to excess production in peak periods (if no storage method is considered), thus converting green H_2 production into one of the most promising and effective solutions for the urgent energy storage needs that will be required in the coming decades [37].

By serving as a bridge between renewable energy surplus and end-use applications, Green H_2 ensures more efficient use of renewable resources while reducing dependency on fossil fuels. By integrating green H_2 into critical sectors, its potential as a cornerstone of the energy transition becomes even more evident, offering a viable path toward deep decarbonization across multiple industries. Although there are still technological challenges to be solved, they do not seem likely to hinder the advancement of this energy vector in the future. However, the challenge of reducing the costs of H_2 production, storage, and end-use technology is not solvable in the short or medium term, making it a key issue on which efforts should be focused.

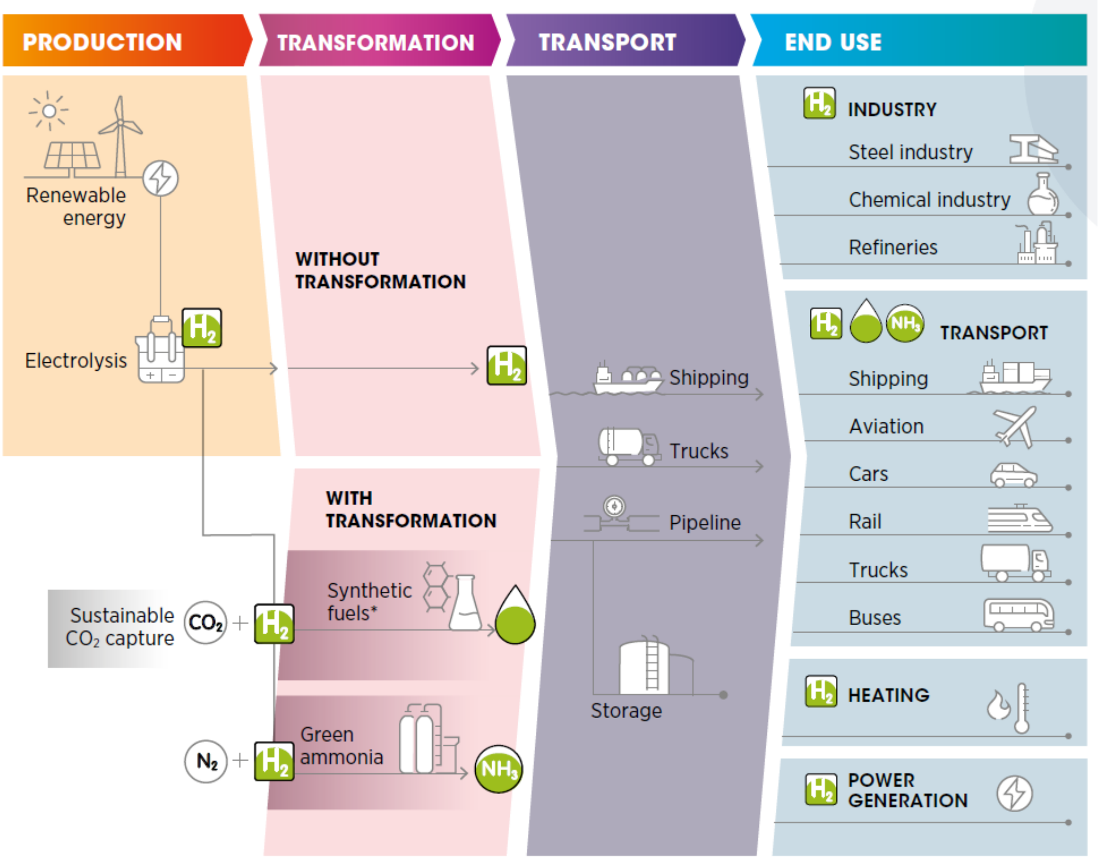

Figure 1.3 Worldwide overview of the green H_2 value chain, illustrating production through renewable energy, potential transformations into synthetic fuels and green ammonia, various transport methods (shipping, truck and pipeline), storage, and diverse end-use applications in industry, transport, heating, and power generation. Imagen taken from Green Hydrogen – A Guide to Policy Making. IRENA (International Renewable Energy Agency). 2020 [17].

Systems using PV technology as an energy source for H_2 production are mostly known as solar-hydrogen (S-H) systems. The main components of S-H systems are the PV generator, which converts sunlight into electric energy [21], and the electrolyzer, which uses this electricity to split water into H_2 and O_2 through electrolysis. There are currently three commercially available water electrolysis technologies: (1) alkaline electrolysis, (2) proton exchange membrane (PEM) electrolysis, and (3) solid oxide electrolysis (SOE) [38,39]. Each of these technologies presents distinct characteristics that make them more suitable for different applications and scales of production [36,40–42].

Alkaline electrolysis is the most mature and widely utilized technology for H_2 production, characterized by its use of a liquid alkaline electrolyte, typically potassium hydroxide (KOH) or sodium hydroxide (NaOH). One of the key advantages of alkaline electrolysis is its relatively low capital costs, making it an attractive option for many existing H_2 production facilities. This technology also benefits from long operational lifetimes, which can exceed several decades with proper maintenance. However, its efficiency is somewhat limited in terms of current density, a measure of how much H_2 can be produced per unit area of the electrode, and its response time to fluctuating renewable energy inputs is slower. As a result, alkaline electrolysis is often deemed more suitable for continuous operation, where electricity supply is stable and there are minimal fluctuations in demand. In contrast, its integration with intermittent renewable energy sources such as solar and wind power, which can produce variable output, is less effective, as the electrolysis systems require time to adjust to changes in energy supply. This limitation calls for advancements in system design and operational strategies to enhance the adaptability of alkaline electrolysis for use with renewable energy sources [43,44].

PEM electrolysis, on the other hand, is emerging as one of the most promising technologies for green H_2 production, largely due to its numerous advantages over alkaline systems. PEM electrolysis operates using a solid polymer electrolyte, enabling a compact and modular system design. One of the standout features of PEM electrolyzers is their ability to achieve high current densities, which translates to higher H_2 production rates in a smaller footprint. Moreover, PEM systems exhibit rapid response times, allowing them to quickly adapt to fluctuations in renewable energy supply [45]. This characteristic is particularly beneficial in the context of variable RES such as PV, where rapid adaptation to changes in electricity generation is often essential to maintain system efficiency and reliability. Additionally, PEM electrolysis produces high-purity H_2, which is increasingly important in various industrial applications. Despite its many advantages, PEM technology does have some drawbacks, primarily involving its higher initial costs and the reliance on expensive materials like platinum and iridium as catalysts. However, ongoing advancements in materials science and system optimization show promise in driving down these costs while enhancing efficiency and performance [46].

SOE technology represents a third approach to H_2 production that operates at elevated temperatures, typically between 700-1,000 °C, utilizing a ceramic electrolyte. The high-temperature operation of SOE allows for greater overall efficiency, as it can capitalize on waste heat generated from industrial processes or other energy-intensive applications. This feature not only improves the energy efficiency of the H_2 production process but also helps to reduce emissions associated with the production of H_2, making it an attractive option for integrated applications within industries. However, SOE technology is still in the early stages of commercialization compared to alkaline and PEM electrolysis technologies. It faces challenges related to material degradation under high operating temperatures, which can significantly impact system durability and long-term reliability. As research continues to address these material challenges and develop more resilient components, solid oxide electrolysis may become a more viable option for large-scale H_2 production in the future [47].

While each technology has its advantages and challenges, PEM electrolysis is poised to become the dominant technology for water electrolysis due to its adaptability, efficiency, and ability to operate effectively with intrinsically intermittent renewable energy sources [45]. As the demand for green H_2 continues to rise, improvements in electrolyzer design, cost reduction strategies, and advancements in energy efficiency will further solidify PEM's role as a key enabler of the H_2 economy.

Given that the PV system limits the overall efficiency of the process, the way it is coupled with the electrolyzer plays a significant role in overall system performance. A poor design can cause efficiency losses and lead to wasted energy within the S-H system. These losses not only reduce the system's effectiveness but also increase the cost of green H_2 production. Therefore, efforts should be directed toward optimizing S-H systems to minimize energy waste. In this context, until the production costs of green H_2 are reduced, its prices will remain uncompetitive compared to grey or blue H_2. In studies analyzing integrated systems of wind turbines and electrolysis, the reported costs of green H_2 production are around 10.15–10.8 $\$ \cdot \mathrm{kg}^{-1}$ H_2 [48]. In contrast, technologies based on methane reforming with carbon capture and storage (blue H_2) can reach costs of around 2.20 $\$ \cdot \mathrm{kg}^{-1}$ H_2 [48]. This price gap highlights the need to focus on cost reduction through technological improvements and economies of scale, although such progress is expected to be gradual and, in some cases, may not lead to competitiveness until the medium term.

1.3 Carbon capture, usage and storage (CCUS)

As stated above, RES help mitigate ongoing emissions but do not remove the excess CO_2 already in the atmosphere. The cumulative greenhouse gases present a significant challenge to climate stability. While expanding renewable technologies is crucial, it must be combined with carbon removal and sequestration efforts to address past emissions and effectively combat climate change.

The significance of CCUS becomes particularly evident when considering varying greenhouse gas emission scenarios. The Shared Socioeconomic Pathways (SSPs) outline contrasting future trajectories for emissions, illustrating potential outcomes based on different policies and technological advances. For example, SSP5-8.5 represents a high-emission scenario characterized by rapid economic growth and reliance on fossil fuel consumption without substantial mitigation efforts as depicted with the red line in Figure 1.4 [49]. This trajectory is likely to result in severe climate impacts and challenges in stabilizing global temperatures. Conversely, the SSP2-4.5 scenario suggests a middle ground, where emissions are reduced through RES, balancing economic expansion with emissions control [49]. This scenario, depicted with the yellow line in Figure 1.4, underscores the importance of implementing CCUS as part of a broader strategy to manage emissions from industrial processes effectively [49].

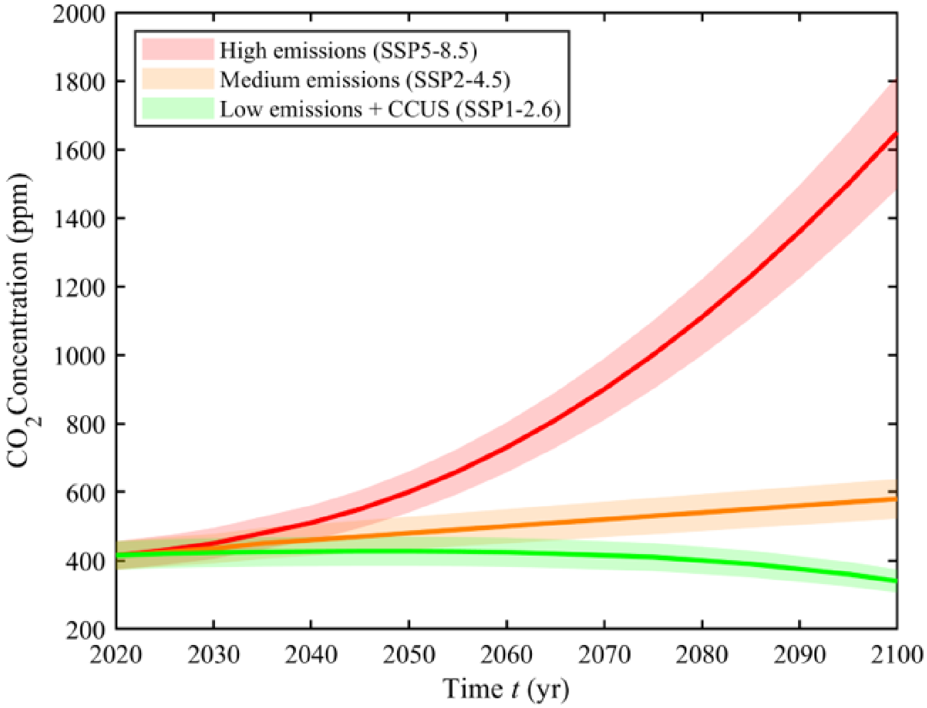

Figure 1.4 Projected atmospheric CO_2 concentration under different shared socioeconomic pathways (SSPs) from 2020 to 2100. The red curve corresponds to a high emissions scenario (SSP5-8.5), the orange to a medium emissions scenario (SSP2-4.5), and the green to a low emissions scenario including carbon capture, utilization, and storage (CCUS) measures (SSP1-2.6). Shaded areas represent the uncertainty ranges associated with each pathway [49].

At the most optimistic end of the spectrum, the SSP1-2.6 scenario emphasizes low emissions transition combined with aggressive implementation of CCUS technologies, enabling a pathway towards meeting the ambitious climate goals set by international agreements [50]. This is represented by the green line in Figure 1.4. This scenario envisions a sustainable future with net-negative emissions, where not only are future emissions significantly curtailed, but a substantial portion of the existing atmospheric CO_2 is removed through advanced carbon management practices.

1.3.1 Carbon capture

The justification for carbon capture strategies revolves around their ability to mitigate climate change by addressing two primary routes for CO_2 removal: capturing CO_2 from concentrated industrial emissions and implementing direct air capture (DAC) technology, which extracts CO_2 directly from ambient air. The former is more limited, carbon capture systems are typically installed at the source of high CO_2 emissions, such as power plants or industrial facilities. By doing so, these systems can prevent significant amounts of CO_2 from entering the atmosphere, ensuring that emissions do not increase further [51]. However, it is important to understand that this approach does not reduce the existing concentration of CO_2 in the atmosphere; it merely curtails future emissions and helps maintain current levels, which is not sufficient for achieving the long-term climate goals outlined in SSP1-2.6 [51].

DAC is increasingly recognized as a pivotal technology to transition toward more ambitious scenarios like SSP1-2.6, which aims to limit global warming to 1.5 °C above pre-industrial levels. DAC has the unique capacity to remove CO_2 from the atmosphere regardless of emission sources or their geographical locations, thus holding promise in reversing past emissions that have contributed to current climate challenges [52]. As such, it is seen as an essential mechanism for managing atmospheric CO_2 levels and moving toward net-zero emissions.

The main challenge of DAC methods lies in the fact that the concentration of CO_2 in the atmosphere is so low that large amounts of energy are required to separate CO_2 from the other components of the air. This energy-intensive process stems from the fact that atmospheric CO_2 concentration is approximately 0.04% (or 400 ppm), making the effective separation of CO_2 particularly energy demanding [53]. As a result, the high energy demand translates into elevated separation costs, which can pose significant barriers to the large-scale implementation of CO_2 capture systems.

There are several primary methods of DAC, each with its own advantages and disadvantages. The most discussed include:

Physical adsorption, or physisorption, utilizes solid materials known as sorbents to capture CO_2 by leveraging van der Waals forces. Commonly employed materials in this method include zeolites and metal-organic frameworks. The air is drawn through beds of these sorbents, allowing CO_2 to adhere to their surfaces. Once the sorbent reaches saturation, it typically undergoes heating or reduced pressure to release the captured CO_2 [54]. The versatility of solid sorbents is a significant advantage, as they can be engineered to optimize CO_2 capture under varying humidity levels, making this method adaptable to different environmental conditions. However, while physical adsorption presents opportunities for effective CO_2 capture, it often requires lower temperatures to function optimally and may not perform as efficiently in humid environments when compared to chemical sorbents [54].

Membrane technology represents another promising method for CO_2 capture, employing membranes that separate CO_2 from other gases based on differences in size or molecular affinity. This approach has potential for relatively low energy requirements, allowing for selective capture of CO_2 while reducing overall operational costs. Membrane systems can be integrated into existing infrastructures, enhancing the efficiency of CO_2 removal processes and contributing to overall emission reduction strategies [55]. By facilitating the separation of gases with minimal energy input, membrane technology not only improves the productivity of DAC systems but also promotes the feasibility of large-scale implementation to combat climate change.

Chemical absorption is a widely established DAC method, primarily employing liquid solvents such as amines. In this process, air is passed over the solvent, allowing CO_2 to bind to the amine molecules. The captured CO_2 is subsequently released by applying heat to the solvent, facilitating the regeneration of the capturing material [56]. One of the significant advantages of chemical absorption is its effectiveness in producing high-purity CO_2, which can be further utilized or sequestered. However, while this method is currently one of the most mature forms of DAC technology, it does come with challenges. The process is energy-intensive, necessitating substantial operational resources, which can lead to elevated costs that offset its immediate benefits [56]. Moreover, the reliance on amines, while effective, also raises concerns over their regeneration efficiency and lifecycle impacts [56].

Given the wide variety of available amines, the possibility of selecting different options represents an advantage when implementing DAC methods based on chemical absorption. However, both the heating temperature and the CO_2 capture efficiency depend on the specific amine used. Among the most employed amines, ethanolamine stands out. For this reason, there is an ongoing interest in identifying amines that operate at lower heating temperatures and allow for repeated use, in order to improve the overall performance and practicality of the process.

A research group from the University of Tokyo has proposed a DAC method based on a diamine. They report a lower heating temperature compared to other DAC methods, the ability to reuse the diamine for at least five heating–cooling cycles, and a capture efficiency of 99%—features that, in principle, make this approach a promising option for industrial implementation [57]. As mentioned, it will be this particular approach the one that will be reviewed in detail in this Thesis in Chapter 4.

1.3.2 Carbon usage via carbon reduction reaction

An increasing awareness of the impacts of anthropogenic CO_2 emissions has motivated the development of CO_2 utilization technologies. The CO_2 captured, whether through DAC or from more concentrated gas streams, can be transformed into value-added products via carbon reduction reaction (CO2RR), as depicted in Figure 1.5. By converting this captured CO_2 into chemicals, fuels, or advanced carbon materials, the process aligns with the principles of carbon capture and utilization (CCU), providing the dual benefits of mitigating greenhouse gas emissions while producing economically attractive outputs. In this context, further development of CO2RR technologies also helps to justify the implementation of DAC systems, since the possibility of obtaining marketable products with commercial value can offset, at least partially, the high energy and economic costs associated with CO_2 separation from the atmosphere.

Electrocatalytic CO2RR is an emerging utilization strategy that can provide a low-carbon route to carbon-based products, typically carried out in electrolyzers. Electrolyzer system designs have proliferated, and the greatest challenges before the field of CO_2 electrocatalysis, achieving energy and carbon efficiency, motivate much more on these complex systems [58]. One of the primary limitations of CO2RR is the inherently low selectivity of many catalysts. This low selectivity means that, rather than exclusively producing a single desired product, most catalysts tend to generate multiple products simultaneously, as depicted in Figure 1.5, complicating product separation and diminishing overall process efficiency.

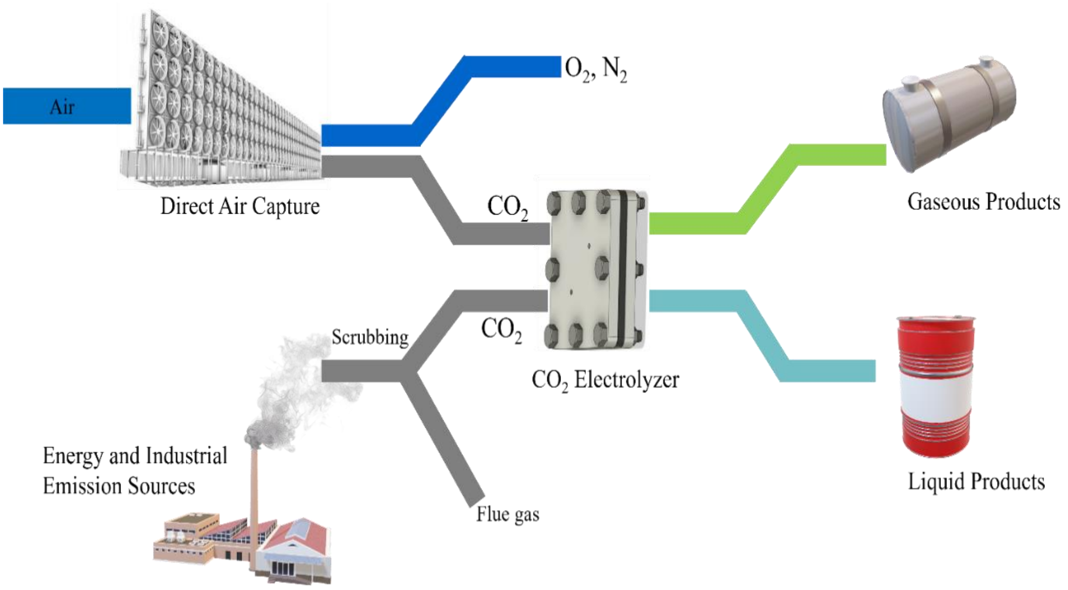

Figure 1.5 Schematic representation of the electrochemical CO_2 reduction process, including upstream (DAC or capture from industrial sources) and downstream steps involved in converting CO_2 into chemicals and fuels. Image of direct air capture system was borrowed from Carbon Engineering™ [59].

Several figures of merit are commonly used to evaluate the performance of CO_2 electrolyzers, providing a framework to assess and compare different technologies for potential large-scale implementation.

One of the central metrics is faradaic efficiency, which indicates the percentage of electrical current that is effectively used to produce the desired product. For instance, a faradaic efficiency of 90% for carbon monoxide means that 90% of the electrons are used exclusively for converting carbon dioxide into carbon monoxide. This measure reflects the system's selectivity toward a given product [58].

Current density is another important parameter. It expresses the amount of electrical current per unit area of the electrode, typically in milliamperes or amperes per square centimeter. A higher current density generally corresponds to a greater rate of product formation, which is particularly relevant for practical and industrial applications, where productivity is a determining factor [58].

The voltage reflects the total electrical energy required to drive the reaction, including both the minimum thermodynamic potential and additional losses such as overpotentials, resistive losses, and mass transport limitations. Efficient systems operate at high current densities while keeping the cell voltage as low as possible, which improves energy conversion and reduces operational costs [58].

Energy efficiency relates the chemical energy stored in the generated product to the total electrical energy consumed. A high energy efficiency indicates favorable conversion conditions and becomes especially relevant when integrating electrolyzers with renewable energy sources, where maximizing energy utilization is important from both environmental and economic perspectives [58].

Operational stability is also a critical aspect. A CO_2 electrolyzer must be capable of maintaining its performance over extended periods, ideally, over thousands of hours. Factors such as catalyst degradation, membrane fouling, and changes in electrode morphology can negatively affect system stability and need to be addressed to ensure long-term functionality [58].

The concentration of the target product and its crossover through the membrane are critical factors that influence the system's overall efficiency. When the desired product is generated at low concentrations, additional separation and purification steps become necessary, which in turn increases energy requirements as well as operational costs. This additional energy input is unavoidable because the diluted product stream must be concentrated to achieve the purity levels required for downstream applications. Furthermore, product crossover—the migration of generated products across the membrane to the opposite electrode—can have particularly detrimental effects. Such crossover not only reduces the overall yield and adversely affects the process selectivity but it also has the potential to damage sensitive components such as electrodes and membranes. This degradation may lead to a shorter lifespan for these components and a subsequent need for more frequent replacements, further impacting the economic viability of the system. Ongoing research efforts are focused on optimizing membrane properties and catalyst selectivity to mitigate these issues, thereby enhancing the energy efficiency and cost-effectiveness of CO_2 reduction systems [58].

There are several architectures commonly used in CO_2 electrolysis, each with its own set of characteristics and design nuances. One of the most widely employed configurations in laboratory research is the H-cell. In this configuration, both the working and counter electrodes are immersed in a liquid electrolyte that contains dissolved CO_2. A membrane—often a proton exchange membrane or a bipolar membrane—is typically used to separate the cathode and anode compartments, preventing product crossover and maintaining distinct reaction environments. Although the H-cell is simple to assemble, making it well suited for catalyst testing and fundamental studies, it suffers from inherent mass transport limitations due to the low solubility of CO_2 in water. These limitations constrain the achievable current density and pose challenges when scaling the process up for industrial applications [58].

To address the mass transport issues observed in H-cells, flow cells were developed as an alternative design. In flow cell configurations, a gas diffusion electrode (GDE) is employed, which enables gaseous CO_2 to be delivered directly to the electrochemical interface. This direct introduction of CO_2 significantly improves mass transport and bypasses some of the limitations of dissolved CO_2 in the liquid phase. Additionally, flow cells incorporate membranes—typically cation or anion exchange membranes—to separate the anodic and cathodic compartments. The presence of these membranes not only helps to maintain ion balance and prevent product crossover but also plays a crucial role in enhancing the system's current density. Despite these improvements, flow cells require careful management of water and ion transport. Issues such as flooding or inconsistent hydration of the GDE can compromise performance, necessitating ongoing research into optimizing these systems for long-term stability [58].

More advanced architectures, such as membrane electrode assemblies (MEA), integrate the catalyst layers directly with an ion-exchange membrane, eliminating the need for a bulk liquid electrolyte. In an MEA configuration, the membrane performs a dual role: it facilitates ion transport between the electrodes while also acting as a physical barrier that limits the mixing of reactants and products. This close integration results in a thinner reaction zone, supports high current density operation, and generally aligns more closely with industrial requirements. However, MEAs also present challenges. Water management becomes critical to keep the membrane adequately hydrated without causing flooding, and the risk of salt precipitation within the membrane channels can lead to performance degradation over time. Additionally, component degradation, particularly at the electrode-membrane interface, remains a significant hurdle that researchers are striving to overcome through improved materials and design optimization [58].

Another approach involves solid oxide electrolyzer cells (SOECs), which operate at elevated temperatures, typically between 600 and 850 degrees Celsius. At these temperatures, a portion of the energy required for CO_2 reduction is supplied as heat, allowing the electrochemical process to proceed with less electrical input. This high-temperature operation results in greater energy efficiency and makes SOECs particularly suitable for integration into industrial processes that already generate or require heat. These systems use ceramic electrolytes, such as yttria-stabilized zirconia, which conduct oxide ions. While SOECs can achieve high performance and product output, they are still limited by issues related to thermal cycling, material degradation, and complex heat management requirements. Despite these challenges, they remain a promising option, especially where waste heat can be effectively utilized [58].

The configuration of the electrolyzer has a significant influence on the product obtained from CO2RR. Depending on the desired product, different electrolyzer setups are selected. If these electrolyzers are powered by solar energy, the chemicals produced through CO2RR can be considered solar fuels. This approach combines renewable energy with carbon conversion, offering a more sustainable route to chemical production.

The aim of this Thesis is, therefore, to develop and optimize alternative and/or complementary technologies to the use of PV solar energy, in order to address the effects of climate change associated with the increase in greenhouse gas emissions.

Chapter 2. Optimization of green hydrogen production

Given that green H_2 is expected to play a key role in energy transition, optimizing S-H systems is essential to enable their large-scale implementation and to ensure that green H_2 generation becomes economically competitive with grey and blue H_2. Let us remember from Chapter 1 that S-H systems are composed of both PV and electrolyzers, which transform H_2O into H_2 and O_2. PV and electrolyzer can be connected in various ways, each representing a different configuration.

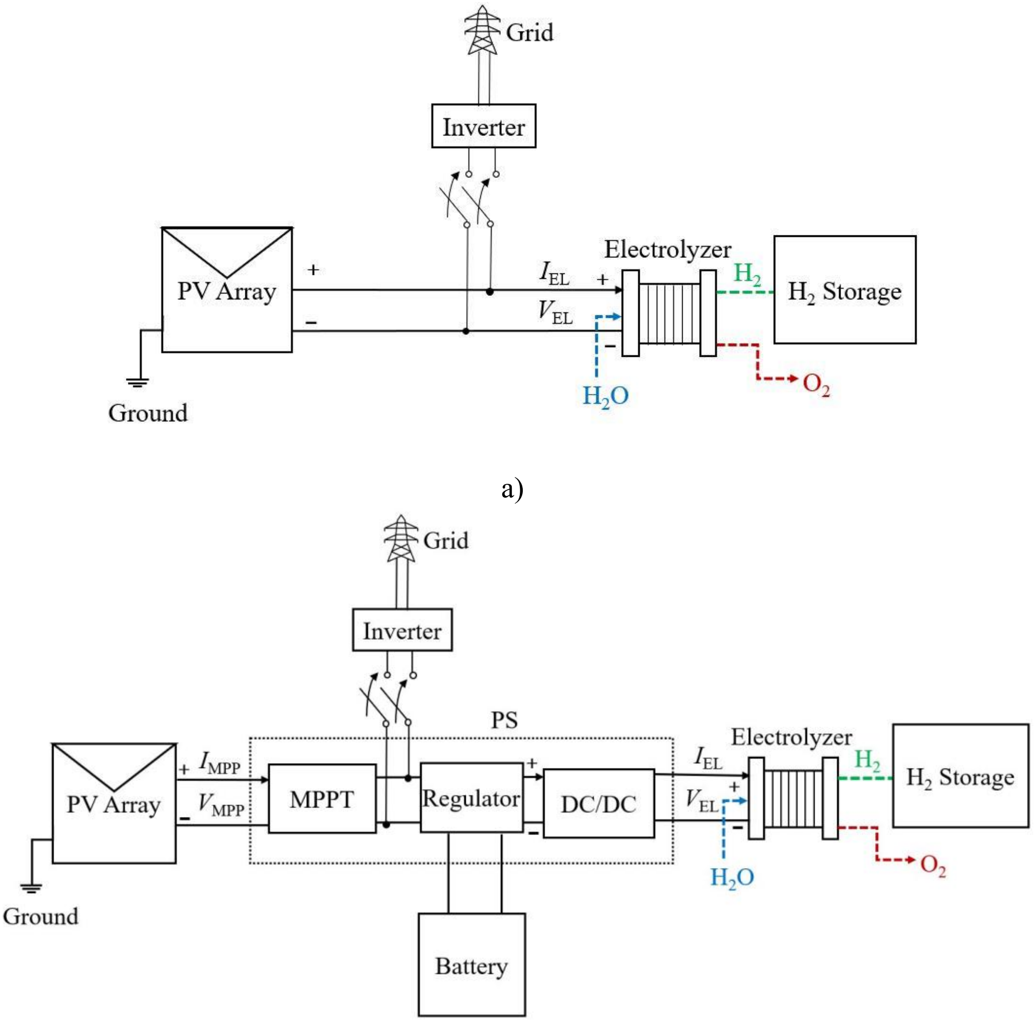

a)

b)

Figure 2.1 a) Schematic of a solar-hydrogen (S-H) system with a direct configuration, consisting of a PV array, an electrolyzer, H_2 storage, and the grid connection. b) Schematic of S-H systems with different indirect configurations, both include the elements of the indirect configuration and the power stage (PS). One configuration features a regulator and a battery, while the other does not.

The S-H systems in which the electrolyzer input is directly connected to the electrical output of the PV generator, without an intermediate power stage (PS), are oftentimes referred to as being in a direct coupling configuration, as shown in Figure 2.1a [60–62]. In this setup, the PV generator supplies power to the electrolyzer without any additional electronics to regulate voltage (V) or current (I). On the other hand, indirect coupling configurations (Figure 2.1b) incorporate power electronics to regulate and optimize energy transfer from the PV generator to the electrolyzer [61,63–65]. This is achieved by using a maximum power point tracker (MPPT), which ensures that the PV generator operates at its maximum power point (MPP) despite changes in meteorological conditions. The DC-DC converter then adjusts the voltage and current levels to match the power requirements of the electrolyzer. The MPPT continuously tracks the point where the PV generator produces the maximum possible power, which is determined by the product of I_{MPP} and V_{MPP}, which are the current and voltage at MPP. The DC-DC converter then adjusts this power to meet the input requirements of the electrolyzer, which operates at I_{EL} and V_{EL} (current and voltage values specific to the electrolyzer) [66].

In practice, the MPPT and DC-DC converter are often integrated into a single PS that ideally transfers power from the PV generator to the electrolyzer with minimal losses.

Given the intermittent availability of RES, H_2 production in S-H systems can fluctuate. The peak power output (W_p) of a PV generator under standard test conditions (STC), i.e., 25 °C and 1,000 $\mathrm{W \cdot m^{-2}}$ under air mass 1.5 global spectrum (AM1.5G), hardly ever takes place throughout the day or even the year, in a given place. Therefore, as the output power of the photovoltaic generator is highly variable, due to the different temperatures and inclination of the sun throughout the day, to ensure that the PV generator can reliably power the electrolyzer, it is necessary to oversize its power relative to the electrolyzer requirements. Proceeding in this way, it is also likely that the PV array will produce for some periods more power than the electrolyzer can take, generating an energy surplus not used instantaneously. Storing this surplus energy from the PV generator in batteries helps stabilize H_2 production [63,64,67]. Indirect systems are particularly adaptable for this purpose by only adding a battery and a regulator (as shown in Figure 2.1b), enhancing their versatility. The regulator, as well as the MPPT and DC/DC converter, are common elements used in conventional PV systems where the energy from the PV generator needs to be coupled to other loads different from electrolyzers. In this regard, lithium-ion batteries offer significant advantages over other battery technologies. Firstly, they have a high energy density, allowing them to store a large amount of energy relative to their size and weight [64,67]. Secondly, lithium-ion batteries typically have a longer lifespan and can endure more charge-discharge cycles compared to alternative battery technologies, making them cost-effective [68,69].

The advantages and disadvantages of each configuration continue to be a topic of debate. In favor of direct coupling, one could argue that, with the proper design of the PV array and electrolyzer, this configuration can operate the electrolyzer near its MPP effectively. In ideal conditions, direct coupling systems can achieve coupling factors of up to 90% [41,42,45,46,60], meaning that a significant portion of the power generated by the PV array is efficiently utilized by the electrolyzer. This high level of efficiency, when properly managed, can make direct coupling economically advantageous. By eliminating the need for additional power conversion stages, such as the MPPT and DC-DC converter required in indirect coupling systems, the overall system cost is significantly reduced. These electronic components can be expensive, adding to the capital costs of the system, and their removal of direct coupling systems results in a lower overall investment. Specifically, the cost associated with these electronic coupling systems is estimated at approximately $0.045\ \text{€} \cdot \mathrm{W}^{-1}$ [42,65,70]. Moreover, direct coupling can be simpler to maintain, as it involves fewer components and fewer potential points of failure. Simplicity and cost-effectiveness make it an attractive option for applications where budget constraints are an important consideration, or where a relatively stable solar resource is available to minimize fluctuations in PV output [71–74]. However, the main drawback is that the electrolyzer operates under the fluctuating power output of the PV generator, which varies depending on solar irradiance (G_t), temperature (T), and other environmental factors. These variations can lead to suboptimal H_2 production efficiency and increased stress on the electrolyzer components.

The advantage of the indirect coupling configuration is that it maximizes H_2 production by ensuring that the PV generator always operates at its peak efficiency [75]. This system can optimize the performance of both the PV generator and the electrolyzer independently, ensuring that the energy generated by the PV array is efficiently converted into H_2. This optimization is particularly important in systems where the resource is intermittent, as it helps to maintain a stable and reliable hydrogen production rate. However, the inclusion of power electronics comes with some trade-offs. While they improve the overall efficiency of the system, they also introduce additional costs related to the purchase and maintenance of these components [76,77]. Moreover, there are conversion inefficiencies, meaning that some energy is lost during the conversion process between the PV system and the electrolyzer [65,78].

What will be presented below has already been covered in detail in my previous works, titled *"Optimizing Hydrogen Production: A Comparative Study of Direct and Indirect Coupling Between Photovoltaics and Electrolyzer"* [79] and *"Comparative Analysis of Hydrogen Production and Economic Feasibility: Direct Versus Indirect Coupling of Photovoltaic Systems with Electrolyzers"* [76], previously published.

This chapter will assess, both energetically and economically, the annual performance of three different PV-to-electrolyzer coupling configurations: direct, indirect, and indirect with battery storage. Subsection 2.1 details the models of the PV array, electrolyzer, and batteries. Subsection 2.2 details the optimization of some of the main elements of the S-H system, such as the PV module and the battery capacity, under the assumption that we fix the size and characteristics of the electrolyzer. The comparison will provide a comprehensive overview of energy production, energy utilization, and H_2 output in subsections 2.3.1 and 2.3.2. Additionally, an economic feasibility analysis of the three configurations will be conducted to evaluate which one offers the highest net benefits in subsection 2.3.32.3. Furthermore, in subsections 2.3.4 and 2.3.5 we will study how sensitive the direct and indirect configurations are to incident G_t and how the DC-DC converter efficiency impacts the H_2 production on the indirect coupling configuration.

2.1 System models

The calculation of annual H_2 production from the PV generator output involves several steps. First, annual data of G_t and T at the location of the PV generator are obtained. This data is essential for accurately modeling the PV system performance throughout the year. Next, the output power of the PV generator is modeled based on G_t and T conditions, estimating the amount of energy the PV system can generate at any given time. The third step involves modeling the electrolyzer, which converts the electrical energy from the PV generator and water into H_2 and O_2. In the case of the indirect configuration, the PS and the battery (if included) are also simulated.

2.1.1 Irradiance and temperature operating conditions

The initial stage of the simulation involves obtaining G_t and T data for every hour from a typical meteorological year (January 1st to December 31st), totaling 8,760 hours, at a specific location. For this study, we have chosen Madrid, Spain, located at coordinates (40.453N, -3.727E), corresponding to the IES-UPM, where this research is being conducted. Figure 2.2 represents the hourly variation of G_t (blue line) and T (red line) throughout the year at the location corresponding to IES-UPM. The data were sourced from the PVGIS-SARAH2 [80] database on a fixed plane with optimal tilt and azimuth angles of 36° and 0°, respectively. In this location, the total incident solar energy on the plane of the PV generator throughout the year is $2.79\ \mathrm{MWh \cdot m^{-2}}$.

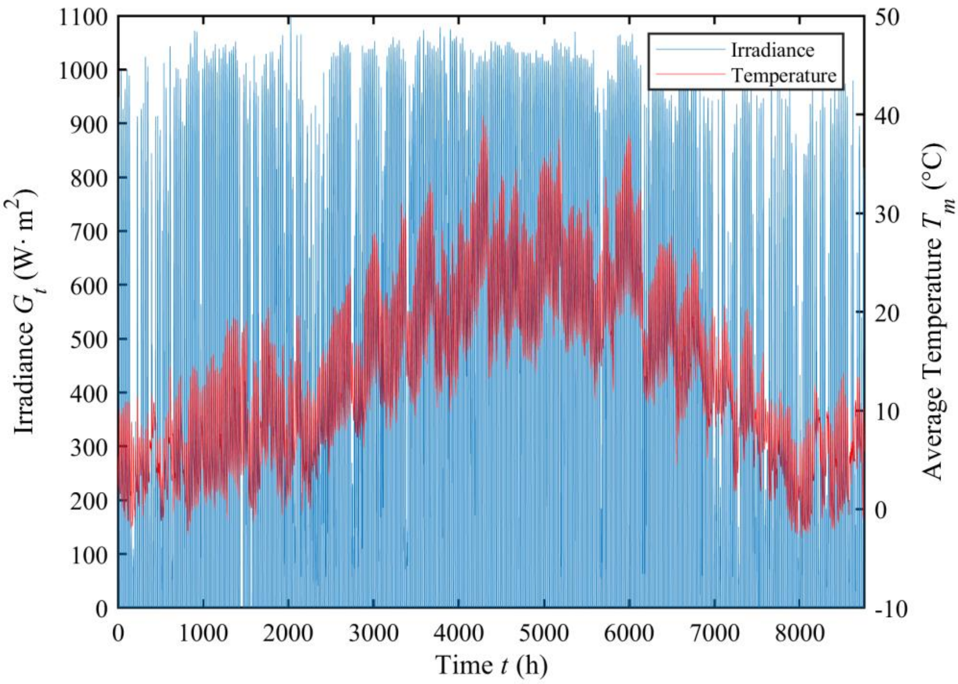

Figure 2.2 Annual (Jan. 1st to Dec. 31st) average temperature (T_m) and irradiance (G_t) on a fixed PV module with an elevation of 36° and south oriented, at coordinates 40.453N, -3.727E.

2.1.2 PV generator model

The fundamental unit of the PV generator is the solar cell, which is responsible for converting sunlight into electrical energy. The performance of a solar cell is primarily defined by its current density-voltage ($J - V$) characteristic, which describes the relationship between the current generated and the voltage across the cell under different operating conditions. In this study, the $J - V$ characteristic of the solar cell will be modeled using a single diode model (SDM), a widely accepted approach that provides a good balance between accuracy and computational efficiency [81,82]. This model captures the essential electrical behavior of the solar cell, allowing for a reliable estimation of the PV generator's overall performance under varying irradiance and temperature conditions.

$$J_c = J_{\mathrm{ph},c} - J_{0,c}\left(\exp\frac{qV_c + qr_{s,c}J_c}{nk_BT} - 1\right) - \frac{V_c + r_{s,c}J_c}{r_{\mathrm{sh},c}} \tag{2.1}$$

where: q is the charge of the electron in absolute value; J_c is the electron current density through the solar cell; V_c is the output voltage of the solar cell; $r_{s,c}$ is the series resistance of the solar cell per unit area, which accounts for resistive losses in the contacts and semiconductor material; $r_{sh,c}$ is the shunt resistance of the solar cell per unit area, representing leakage pathways that affect performance; $J_{0,c}$ is the reverse saturation current density of the solar cell, which determines the recombination losses and influences the open-circuit voltage (V_{oc}); k_B is Boltzmann constant ($eV \cdot K^{-1}$); n is the diode ideality factor, which accounts for the type of recombination that takes place in the diode; and $J_{ph,c}$ is the photogenerated current density, which corresponds to the current generated by the absorption of photons. These parameters define the electrical behavior of the solar cell and are used to model its $I - V$ (current-voltage) characteristics under different operating conditions. The total current through the cell (I_c) is calculated multiplying J_c by the area of the cell, A_c [83].

$$I_c = J_c A_c = I_{\mathrm{ph},c} - I_{0,c}\left(\exp\frac{qV_c + qR_{s,c}I_c}{nk_BT} - 1\right) - \frac{V_c + R_{s,c}I_c}{R_{\mathrm{sh},c}} \tag{2.2}$$

This model (SDM) is represented in circuit form in Figure 2.3, where the diode D1 counts for the exponential term. It is worth noting that $I_{\mathrm{ph},c}$ and $I_{0,c}$ represent currents obtained by multiplying $J_{\mathrm{ph},c}$ and $J_{0,c}$ by A_c respectively. Similarly, $R_{s,c}$ and $R_{\mathrm{sh},c}$ are derived by dividing $r_{\mathrm{s},c}$ and $r_{\mathrm{sh},c}$ by A_c.

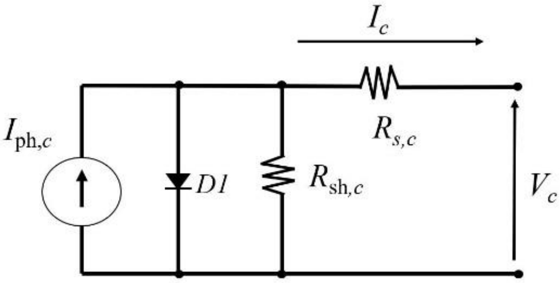

Figure 2.3 Schematic of the equivalent circuit representing the SDM used to model the PV generator.

These clarifications on how A_c influences the model and its ability to adjust the total current of the solar cell from a given solar cell current density will be relevant later when discussing the potential for designing an optimized PV generator for the direct coupling case. The photogenerated current density $J_{\mathrm{ph},c}$ depends on G_t and T, as [81,84]

$$J_{\mathrm{ph},c} = \frac{G_t}{G_n}(J_{\mathrm{sc}} + \alpha\,(T - T_0)) \tag{2.3}$$

where G_n and T_0 are the solar irradiance and operation temperature at STC ($G_n = 1{,}000\ \mathrm{W\cdot m^{-2}}$ and room temperature, $T_0 = 298.15$ K), J_{sc} is the short-circuit current density of the solar cell in standard conditions and α is the temperature coefficient of J_{sc}, which quantifies the variation in short-circuit current density as a function of temperature changes, reflecting the thermal sensitivity of this solar cell feature.

The reverse saturation current density of the solar cell also varies with temperature, as it is influenced by the intrinsic carrier concentration and recombination processes within the semiconductor material. This dependence can be expressed mathematically as [85]

$$J_{0,c} = J_{0\mathrm{n}}\left(\frac{T_0}{T}\right)^3 \exp\left(\frac{qE_g}{nk_B}\left(\frac{1}{T_0} - \frac{1}{T}\right)\right) \tag{2.4}$$

$J_{0\mathrm{n}}$ being the reverse saturation current density of the solar cell at T_0 and E_g the bandgap of the semiconductor the solar cell is made off. In reality, E_g slightly decreases as temperature increases, which would further influence both the operating voltage and current, and the overall solar cell performance. However, in this analysis, E_g is considered constant for the sake of simplicity while still capturing the primary trend: as T rises, $J_{0,c}$ increases, leading to a reduction in V_{oc} and overall efficiency of the solar cell.

In a PV module, multiple solar cells are typically connected in series to increase the output voltage while maintaining the same current. When N_s identical solar cells are connected in series, the overall voltage of the module is the sum of the voltages of each individual cell, while the current remains equal to that of a single cell. As a result, the current-voltage characteristic of the module is expressed as [86]

$$I_{\mathrm{PV}} = I_{\mathrm{ph},c} - I_{0,c}\left(\exp\frac{qV_{\mathrm{PV}}/N_s + qR_{s,c}I_{\mathrm{PV}}}{nk_BT} - 1\right) - \frac{V_{\mathrm{PV}} + N_sR_{s,c}I_{\mathrm{PV}}}{N_sR_{\mathrm{sh},c}} \tag{2.5}$$

Where I_{PV} represents the current flowing through the PV module and the module voltage is given by $V_{\mathrm{PV}} = V_cN_S$. Notice that the parameters $I_{\mathrm{ph},c}$, $I_{0,c}$, $R_{s,c}$, and $R_{\mathrm{sh},c}$correspond to the cell-level characteristics previously defined in Eq. (2.2). These parameters influence the overall behavior of the PV module, as the series connection affects the voltage output while maintaining the same current as a single cell.

To further increase the current output of the PV module, multiple strings of N_s series-connected solar cells can be connected in parallel. If N_p identical strings are arranged in parallel, the total module current increases while the voltage remains the same as that of a single string. In this case, the current-voltage characteristic of the PV module is expressed as [86]

$$I_{\mathrm{PV}} = N_p\left[I_{\mathrm{ph},c} - I_{0,c}\left(\exp\frac{qV_{\mathrm{PV}}/N_s + qR_{s,c}I_{\mathrm{PV}}/N_p}{nk_BT} - 1\right) - \frac{V_{\mathrm{PV}} + N_sR_{s,c}I_{\mathrm{PV}}/N_p}{N_sR_{\mathrm{sh,c}}}\right] \tag{2.6}$$

The modules can be further connected in series to other PV modules to increase the output voltage of the generator or in parallel, to increase further the output current. However, despite this potential, we will restrict ourselves to the case in which the PV generator consists of a single module with all its solar cells connected in series ($N_p = 1, N_s \geq 1$). The reason is that, allowing for the series connection of the solar cells, together with the possibility of tuning the solar cell area, will provide, in our case, with sufficient room to optimize, in terms of output current and voltage, the design of the PV module for the direct connection case (which is the restrictive one in this regard), while preserving the simplicity of the model and without altering the conclusions of the results.

The parameters of the solar cell that form the fundamental building block of the PV module ($J_{0,c}$, $J_{\mathrm{ph,c}}$, $r_{s,c}$, $r_{\mathrm{sh,c}}$ and n) were selected to ensure that the module achieves a nominal power output of 200 $\mathrm{W_p}$ under STC. Additionally, these parameters were adjusted so that the module electrical performance and conversion efficiency (η_m) closely match that of commercially available silicon-based PV modules. A conservative, round η_m value of 20% is chosen for this technology to account for inevitable efficiency losses of real devices. Since the efficiency η_m at STC is defined as the ratio between the nominal power output and the incident power G_t of 1,000 $\mathrm{W \cdot m^{-2}}$, this results in a module area of $A = 1\ \mathrm{m^2}$. The nominal power was selected to be 200 $\mathrm{W_p}$ because it is easily scalable and will be sufficient for demonstrating the key concepts of the study without sacrificing general applicability. Additionally, the values for the cell area A_c and the number of cells in series N_s were determined through an optimization process. This optimization ensures that the annual H_2 production for the direct coupling configuration, considering the solar irradiance conditions detailed in Subsection 2.1.1, is maximized. This approach balances practical considerations with the need for an efficient and scalable design, making it well-suited for the objectives of the study. The optimization of the PV model is discussed in subsection 2.2.1. Besides, the characteristics of the electrolyzer are discussed in subsection 2.1.3.

Table 2.1 summarizes the parameters of both the PV cell and the PV module, including the corresponding values of the variables obtained for the PV module under STC. These include the short-circuit current (I_{SC}), V_{OC}, fill factor (FF), maximum power point current (I_{MPP}), and maximum power point voltage (V_{MPP}) for the PV module. These parameters are essential for evaluating the performance and efficiency of the module under standard conditions, providing valuable insights into the expected behavior of the system in practical applications.

Table 2.1 PV cell and module parameters (at STC) used in the simulations.

Cell		Module	
Cell area, A_c (cm ^{2})	417	Module area, A (m^2)	1
Reverse saturation current density, $J_{0,c}$ ($\mathrm{A \cdot cm^{-2}}$) [87]	$8.14 \cdot 10^{-12}$	Short circuit current, I_{SC} (A)	14.24
Photogenerated current density, $J_{\mathrm{ph},c}$ ($\mathrm{mA \cdot cm^{-2}}$) [88]	34.1	Open circuit voltage, V_{OC} (V)	17.38
Cell series resistance, $r_{s,c}$ ($\Omega \cdot \mathrm{cm^{-2}}$) [89]	19.9	Current at the maximum power point, I_{MPP} (A)	13.52
Cell shunt resistance, $r_{\mathrm{sh},c}$ ($\mathrm{k}\Omega \cdot \mathrm{cm^{-2}}$) [89]	147	Voltage at the maximum power point, V_{MPP}(V)	14.83
Cell diode ideality factor, n [90]	1.18	Fill factor, FF	0.810
Temperature coefficient, α [91]	$3.20 \cdot 10^{-3}$	Efficiency, η_m (%)	20.0
Band gap, E_g (eV) [92]	1.10	Number of cells in series, N_s	24

Figure 2.4 illustrates a family of current-voltage ($I_{\mathrm{PV}} - V_{\mathrm{PV}}$) characteristics for a 200 W$_p$, 24-cell PV module, showing how these characteristics vary with different levels of solar irradiance G_t ranging from 100 $\mathrm{W \cdot m^{-2}}$ to 1,000 $\mathrm{W \cdot m^{-2}}$. The Figure 2.4 highlights the direct relationship between G_t and the photogenerated current, which increases proportionally with the irradiance. For each irradiance level, the maximum power point (P_{MPP}) of the PV module is calculated and marked on the $I_{\mathrm{PV}} - V_{\mathrm{PV}}$ curve with round markers. As the irradiance increases, the V_{OC} and MPP move to higher values.

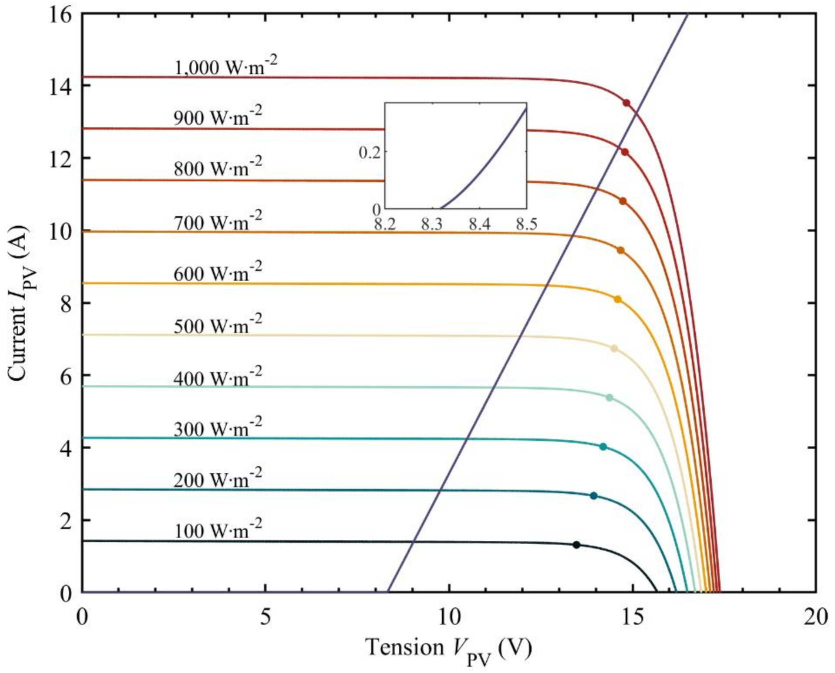

Figure 2.4 Current-voltage curves of 200 W$_p$, 24-cell PV module for G_t 100-1,000 $\mathrm{W \cdot m^{-2}}$ with corresponding MPP and the electrolyzer. The inset shows the electrolyzer curve at voltage values very close to the electrolyzer threshold voltage ($V_{\mathrm{th,EL}}$).

2.1.3 Electrolyzer model

The electrolyzer, as shown in Figure 2.5, converts a portion of the supplied electrical energy into chemical energy by dissociating H_2O into H_2 and O_2 through an electrolysis process. In this chapter, the PEM electrolyzer has been chosen, as this technology is widely used in industry due to its efficiency and versatility. In a PEM electrolyzer, the anode (oxidation electrode) and cathode (reduction electrode) are separated by a solid polymeric membrane, which serves as both an electrolyte and a proton (H^+) conductor. This membrane allows for the efficient transport of protons from the anode to the cathode while preventing the mixing of H_2 and O_2 gases produced at each electrode.

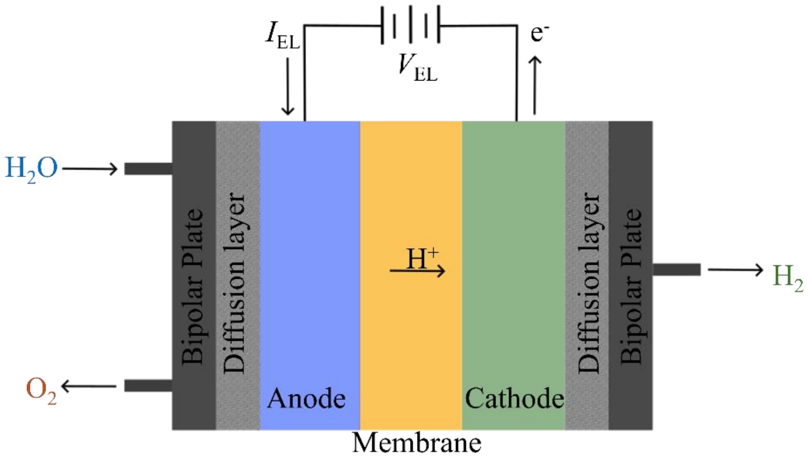

Figure 2.5 Schematic of an ideal PEM cell, including bipolar plates, anode, cathode, polymeric membrane, gas diffusion layers, and electrical contacts.

The combination of the electrodes and the polymeric membrane forms what is known as the electrolytic cell, which serves as the fundamental unit of the electrolyzer. To achieve higher hydrogen production rates and improve overall efficiency, multiple electrolytic cells can be electrically connected in series, creating a stack. Within each cell, the gas diffusion layers are positioned between the electrodes and the bipolar plates, playing a crucial role in the transport of the generated gases. These porous layers facilitate the movement of hydrogen and oxygen (produced at the cathode and anode, respectively) from the electrode surfaces to the bipolar plates [93]. The bipolar plates, in turn, collect and channel the gases towards an external gas circuit for further processing or storage. Additionally, the bipolar plates serve other essential functions: they provide mechanical support to protect both the stacking structure and the diffusion layers, while also ensuring efficient electrical conduction between adjacent cells, enabling a stable and uniform operation of the electrolyzer [93]. In this work, the PEM electrolyzer has been modelled following the model by Falcão et al [94].

In an acidic environment, such as that found in PEM electrolyzers, electrochemical reactions occur at the anode and cathode, leading to the dissociation of water into its constituent elements. At the anode, water molecules undergo oxidation, generating gaseous O_2, releasing electrons that travel through the external circuit, and producing protons H^+ that migrate through the polymeric membrane toward the cathode (R.1). Once at the cathode, these protons combine with the incoming electrons to form H_2 on the electrode surface (R.2). The overall electrochemical process can be represented by summing the anodic and cathodic half-reactions, resulting in the global reaction equation (R.3). For simplicity, and to facilitate energy balance considerations, we assume that all reactions take place under standard conditions, with a pressure of 1 atm and a temperature of 298 K.

$$H_2O \rightarrow 2H^+ + \frac{1}{2}O_2 + 2e^- \tag{R.1}$$

$$2H^+ + 2e^- \rightarrow H_2 \tag{R.2}$$

$$H_2O \rightarrow H_2 + \frac{1}{2}O_2 \tag{R.3}$$

At these conditions, the overall reaction remains a non-spontaneous process, as indicated by its positive Gibbs free energy ($\Delta G_{R,0} = 237.23\ \mathrm{kJ \cdot mol^{-1}}$) [95]. From a thermodynamic perspective, assuming the process is reversible, $\Delta G_{R,0}$ also represents the minimum electrical work required to drive the reaction at constant pressure and temperature. This means that for the reaction (R.3) to proceed, an external energy input is necessary. Specifically, each electron circulating through the external circuit must carry an energy amount equal to qV_{rev}, where q is the elementary charge and V_{rev} is the voltage needed to drive the process. This voltage corresponds to the theoretical minimum potential that must be applied to initiate and sustain water electrolysis under standard conditions and can be expressed as Eq. (2.7)

$$qV_{\mathrm{rev}} = q\frac{\Delta G_{R,0}}{ZF} = 1.23\ \mathrm{eV} \tag{2.7}$$

with Z representing the number of mol electrons transferred per mol of water in the reaction ($Z = 2$), and F being the Faraday constant ($96{,}500\ \mathrm{C \cdot mol^{-1}}$). This energy per electron manifests in the electrolyzer as $V_{\mathrm{rev}} = 1.23\ \mathrm{V}$. This means that, under standard conditions, a potential difference of at least 1.23 V must be applied across the cell for an electric current to flow and drive the water-splitting reaction. Any voltage below this threshold would be insufficient to overcome the thermodynamic energy barrier needed to dissociate water into hydrogen and oxygen. In real operating conditions, the actual voltage required to drive electrolysis exceeds the reversible voltage V_{rev} due to the absence of an external heat source, so additional electrical energy must be supplied to maintain the temperature of the system. As a result, the threshold voltage ($V_{\mathrm{th},c}$) necessary to sustain the reaction is greater than the reversible voltage V_{rev}, ensuring that sufficient energy is provided to overcome these inefficiencies and sustain continuous H_2 production. There are several expressions in literature to determine $V_{\mathrm{th},c}$ empirically, for instance Eq. (2.8) [96]

$$V_{\mathrm{th},c} = -(1-k)\frac{\Delta G_{R,0}}{ZF} \tag{2.8}$$

where k counts for the presence of these non-idealities. In our experience working with electrolyzers, $k = 2.12$ seems a reasonable choice what leads to $V_{\mathrm{th},c} = 1.38$ V. As the current circulates through the cell, the actual voltage for the reaction surpasses $V_{\mathrm{th},c}$, due to additional losses within the cell. These losses are considered by the overpotentials, so that the voltage of the electrolytic cell ($V_{\mathrm{EL},c}$) is given by

$$V_{\mathrm{EL},c} = V_{\mathrm{th},c} + V_{\mathrm{act}} + V_{\mathrm{con}} + V_{\mathrm{ohm}} \tag{2.9}$$

where V_{act} is the activation overpotential, V_{con} is the concentration overpotential, and V_{ohm} is the ohmic overpotential. The activation overpotential arises from the intrinsic energy barriers that must be overcome for the electrochemical reactions to proceed at the electrode surfaces. This overpotential has two distinct contributions: $V_{\mathrm{act},a}$ and $V_{\mathrm{act},c}$, associated with the anode and the cathode, respectively. The total activation overpotential is the sum of these two components as expressed in Eq. (2.10)

$$V_{\mathrm{act}} = V_{\mathrm{act},a} + \left|V_{\mathrm{act},c}\right| \tag{2.10}$$

These activation overpotentials depend on the electrode material, the reaction kinetics, and the applied current density. The Butler-Volmer equation is frequently used for calculating activation overpotentials [94,97]

$$V_{\mathrm{act},a} = \frac{RT}{\alpha_a ZF} \operatorname{arcsinh}\left(\frac{I_{\mathrm{EL}}}{2A_{\mathrm{EL}} j_{0,a}}\right) \tag{2.11}$$

$$V_{\mathrm{act},c} = -\frac{RT}{\alpha_c ZF} \operatorname{arcsinh}\left(\frac{I_{\mathrm{EL}}}{2A_{\mathrm{EL}} j_{0,c}}\right) \tag{2.12}$$

In these equations, R represents the universal gas constant ($8.314\ \mathrm{J} \cdot \mathrm{K}^{-1} \cdot \mathrm{mol}^{-1}$), while α_a and α_c are the charge transfer coefficients corresponding to the anode and cathode, respectively. The terms $j_{0,a}$ and $j_{0,c}$ denote the exchange current densities for the anode and cathode, measuring how much current flows at each electrode when the oxidation and reduction reactions occur in equilibrium, reflecting how easily the material allows electron exchange with the medium. Additionally, A_{EL} is the effective area of the electrolyzer for current transport. To simplify the analysis in this study, we assume $\alpha_a = \alpha_c = 0.5$, as commonly adopted in electrochemical modeling [94]. Some authors propose a further simplified expression [98,99], which remains valid under the condition that I_{EL} is significantly larger than $A_{\mathrm{EL}} j_{0,\mathrm{ref}}$. Given that our case satisfies this condition, this approximation will be applied in the subsequent calculations

$$V_{\mathrm{act},a} = \frac{RT}{\alpha_a ZF} \ln\left(\frac{I_{\mathrm{EL}}}{A_{\mathrm{EL}} j_{0,a}}\right) \tag{2.13}$$

$$V_{\mathrm{act},c} = -\frac{RT}{\alpha_c ZF} \ln\left(\frac{I_{\mathrm{EL}}}{A_{\mathrm{EL}} j_{0,c}}\right) \tag{2.14}$$

In respect to $j_{0,a}$ and $j_{0,c}$, the values found in literature vary significantly. Consequently, certain authors opt to select values that best align with their models [94,98]. Since these values exhibit temperature dependency, an expression connecting them with temperature proves highly valuable. Such an expression is commonly found in the literature, typically formulated employing an Arrhenius equation as follows

$$j_0 = j_{0,\mathrm{ref}} \exp\left[-\frac{E_{\mathrm{exc}}}{R}\left(\frac{1}{T} - \frac{1}{T_{\mathrm{ref}}}\right)\right] \tag{2.15}$$

where $j_{0,\mathrm{ref}}$ is a reference value obtained from literature or experimentally [100], T_{ref} is the temperature at which $j_{0,\mathrm{ref}}$ is measured, and E_{exc} is the activation energy of the reaction. Eq. (2.15) is valid for both the exchange current densities of the anode and cathode, with the difference lying in the value of $j_{0,\mathrm{ref}}$ for each electrode. Table 2.2 collects the parameters of the PEM electrolyzer simulated in this work.

The concentration overpotential arises due to the limited ability of the system to maintain the proper concentration of reactants (H_2O and H^+) at the electrode surface during electrolysis. As the current increases, the reaction rate at the electrodes increases, depleting the reactants near the surface and causing a concentration gradient. This results in a higher resistance for the reaction, increasing the overpotential. It becomes more significant at higher current densities ($\approx 4\ \mathrm{A} \cdot \mathrm{cm}^{-2}$), contributing to energy losses in the electrolysis process. As in V_{act}, there are anodic and cathodic contributions to V_{con}. However, the anodic contribution is much higher and therefore it will be the only one considered in this study. It can be modelled by the following expression [98]

$$V_{\mathrm{con}} = \frac{RT}{\alpha_a ZF} \ln\left(\frac{j_L}{j_L - I_{\mathrm{EL}}/A_{\mathrm{EL}}}\right) \tag{2.16}$$

where j_L is the limiting current density, namely the maximum current density that can be provided to the electrolyzer. These parameters are collected in Table 2.2.

Table 2.2 Characteristics parameters of the electrolyzer used in this work.

Electrolyzer parameter		Reference
Maximum current density, j_L (A·cm^{-2})	4.00	[100]
Anode exchange current density, $j_{0,a\,\mathrm{ref}}$ (A·cm^{-2})	$1.00 \cdot 10^{-7}$	[100]
Cathode exchange current density, $j_{0,c\,\mathrm{ref}}$ (A·cm^{-2})	$1.00 \cdot 10^{-3}$	[100]
Charge transfer coefficients, α_a, α_c	0.5	[101]
Activation energy, E_{exc} (J·mol^{-1})	$5.40 \cdot 10^{4}$	[66]
PEM conductivity at T_{ref}, σ_{ref} (S·cm^{-1})	$2.00 \cdot 10^{-2}$	[102]
PEM Activation energy for H$^+$ transport, E_{pro} (J·mol^{-1})	$1.89 \cdot 10^{4}$	[66]
PEM thickness, t_m(cm)	$1.83 \cdot 10^{-2}$	[102]
Electrolyzer cell effective area, A_{EL} (cm^2)	5.00	-
Reference temperature, T_{ref} (K)	353	[100]
Number of electrolytic cells, S_{cell}	6	-
Threshold voltage non-ideality factor, k	2.12	-

Ohmic losses occur due to the resistance to the flow of current within the electrolyzer. These losses arise from the resistance of the electrolyte, the electrodes, and other conductive materials in the system. As current flows through these components, energy is dissipated in the form of heat, which increases the overall energy consumption of the system. Of all the resistive contributions, the dominant one is the one corresponding to the membrane, which is the one we proceed to develop, disregarding the effect of the series resistance associated with other parts of the electrolyzer. The magnitude of ohmic losses is directly proportional to the current and the resistance within the system, as expressed in Eq. (2.17)

$$V_{\mathrm{ohm}} = \frac{I_{\mathrm{EL}} r_{\mathrm{ohm}}}{A_{\mathrm{EL}}} \tag{2.17}$$

where r_{ohm} is the electric resistance by unit of area of the PEM membrane to H$^+$ ions transport. This resistance by unit of area depends on the membrane thickness (t_m) and electric conductivity (σ) as follows

$$r_{\mathrm{ohm}} = \frac{t_m}{\sigma} \tag{2.18}$$

The conductivity can be modelled with an Arrhenius type expression:

$$\sigma = \sigma_{\mathrm{ref}} \exp\left[-\frac{E_{\mathrm{pro}}}{R}\left(\frac{1}{T} - \frac{1}{T_{\mathrm{ref}}}\right)\right] \tag{2.19}$$

where E_{pro} is the activation energy for proton transport in the membrane and σ_{ref} is the conductivity of the membrane at T_{ref}. Minimizing these losses is crucial for improving the overall efficiency of the electrolyzer.

Analogously to the PV module, the electrolyzer stacking is made of a number of series-connected electrolytic cells, sharing the same current (I_{EL}) and adding their individual voltages ($V_{\mathrm{EL},c}$) to the whole stacking ($V_{\mathrm{EL}} = V_{\mathrm{EL},c} \cdot S_{\mathrm{cell}}$) when all cells are identical, being S_{cell} the number of cells. Since V_{EL} depends on S_{cell} and considering that each electrolytic cell has its own $V_{\mathrm{th},c}$, the V_{th} of the electrolyzer is given by $V_{\mathrm{th}} = V_{\mathrm{th},c} S_{\mathrm{cell}}$. The parameters described above are collected in Table 2.2.

The purple line in Figure 2.4 depicts a typical current-voltage characteristic of the PEM electrolyzer, where I_{EL} is 0 for $V_{\mathrm{EL}} < V_{\mathrm{th}}$, but starts increasing once the threshold voltage V_{th} is exceeded. In our model, the electrolyzer contains 6 cells connected in series, what gives $V_{\mathrm{th}} = 8.33$ V, as shown in Figure 2.4. The electrolyzer used in our simulations has a nominal power of 65 $\mathrm{W_p}$, which makes a reasonable ratio between nominal PV to electrolyzer power for this application.

Once the current-voltage characteristic of the electrolyzer is determined, the next step is to calculate the production of H_2 and O_2. The generation rate of these gases is directly proportional to the electrolyzer current (I_{EL}) and the Faradaic efficiency (μ_F), as stated by Faraday law of electrolysis in Eqs. (2.20) and (2.21). Faradaic efficiency represents the ratio between the actual amount of H_2 (or any product) generated in an electrochemical reaction and the theoretical amount expected based on the charge passed through the system. It accounts for any side reactions or losses and is typically expressed as a percentage. In PEM electrolyzers, it is usually very high (around 99%), meaning nearly all the supplied electricity contributes to H_2 production.

The production rate of H_2 is expressed as

$$\dot{m}\mathrm{H}_2 = \frac{I_{\mathrm{EL}} S_{\mathrm{cell}} \mu_F}{2F} \tag{2.20}$$

Meanwhile, the production rate of O_2 is

$$\dot{m}\mathrm{O}_2 = \frac{I_{\mathrm{EL}} S_{\mathrm{cell}} \mu_F}{4F} \tag{2.21}$$

The cumulative H_2 production ($M\mathrm{H}_2$) is determined by integrating the instantaneous H_2 production rate over the entire year as expressed in Eq. (2.22). This integration accounts for the variations in operating conditions, such as solar irradiance and temperature, which affect the current of the electrolyzer I_{EL} and the Faradaic efficiency μ_F, ensuring an accurate estimation of the total H_2 generated throughout the annual cycle.

$$M\mathrm{H}_2 = \frac{S_{\mathrm{cell}}}{2F} \int I_{\mathrm{EL}} \, \mu_F \, dt \tag{2.22}$$

2.1.4 Battery model

Indirect configuration may also incorporate batteries to store surplus energy generated by the PV module. The battery is used to store energy and power the electrolyzer during periods when PV energy is insufficient, thereby extending H_2 production throughout the year. Specifically, a lithium-ion battery is connected between the PS and the PEM electrolyzer through a regulator that prioritizes power transfer to the load, i.e., H_2 production, over battery charging. Consequently, the battery only charges if the PV module generates sufficient energy to power the electrolyzer at its nominal operating point (65 W), and the state of charge (SOC) of the battery is below its maximum capacity. The SOC of the battery is defined as:

$$SOC = \frac{C_{\mathrm{bat}}}{C_{\mathrm{max}}} \tag{2.23}$$

where C_{bat} is the energy stored in the battery at a given time and C_{max} is the maximum energy storage capacity. In this case, the SOC is maintained within a range of 0.2 to 1 to prevent both overcharging and deep discharging, ensuring the battery operates efficiently and maintains its longevity. Additionally, the battery will provide energy whenever the 200 $\mathrm{W_p}$ PV module is unable to supply the required 65 W for the electrolyzer and its SOC is above its minimum 0.2 value. This occurs under two main conditions: (1) during nighttime and (2) during daytime when solar generation falls below 65 W. In such cases, the battery compensates for the shortfall, ensuring the electrolyzer operates at its nominal power. If the available battery energy is insufficient to fully meet this demand, it supplies as much as possible, provided the SOC remains above the minimum threshold. If the SOC reaches its lower limit, the battery stops discharging to prevent damage. Conversely, if the battery reaches full charge and the PV module continues generating surplus energy beyond the electrolyzer needs, the excess is directed to the grid. Under no circumstances is grid energy used to power the electrolyzer in this study. Charging efficiency and discharge efficiency of 100% are assumed, i.e. no losses are assumed in the process of transforming electrical to chemical energy and vice versa. The detailed study of the behavior of the battery is outside the scope of the Thesis and this paradigm of ideal behavior is chosen for its simplicity.

The maximum battery capacity C_{max} has been optimized to maximize the profitability of the system over the lifespan of the PEM electrolyzer. This optimization is essential, as the battery constitutes a considerable upfront investment. If not properly sized, the added cost could outweigh the economic benefits, potentially rendering the indirect configuration with battery financially unfeasible. Optimization of the battery is discussed in subsection 2.2.2.

2.2 Optimization

2.2.1 Optimization of the PV module

In the direct configuration, the operation current and voltage of the PV generator and the electrolyzer are the same ($V_{\text{PV}} = V_{\text{EL}}, I_{\text{PV}} = I_{\text{EL}}$) and are determined by the point where both current-voltage characteristics intersect. Because the $I_{\text{PV}} - V_{\text{PV}}$ characteristic changes with G_t and T, in general, $V_{\text{PV}} \neq V_{\text{MPP}}$ and $I_{PV} \neq I_{\text{MPP}}$ and the PV generator supplies suboptimal power ($P_{\text{PV}} < P_{\text{MPP}}$) to the electrolyzer, as seen in Figure 2.4. This will ultimately lead to lower H_2 production than in the indirect case, since the generation of H_2 is proportional to I_{EL}, which equals I_{PV}, but is lower than I_{MPP} most of the hours of the year, under the direct scheme.

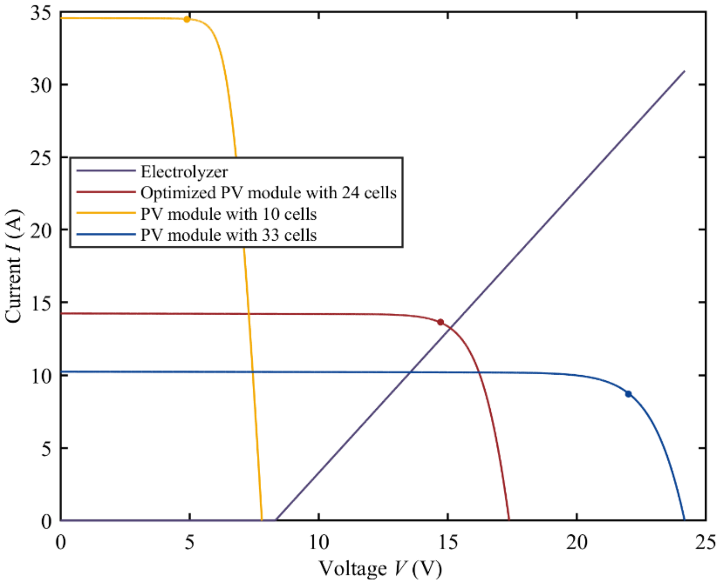

Figure 2.6 $I - V$ curves of the 65 W_p electrolyzer (purple curve) and three 200 W_p PV modules illuminated at STC. The red line corresponds to the optimized PV module, the yellow line represents a module with 10 cells, and the blue line corresponds to a module with 33 cells. The electrolyzer operates at the intersection point of its $I - V$ curve with the curve of each module. Dots on every $I - V$ curve of PV module represent MPP.

In this respect, the selection of the solar cell area and the number of series-connected cells in the PV module is a crucial design consideration that can greatly impact the performance of the electrolyzer under the direct coupling strategy. Given that the total module area A is fixed (at 1 m^2 in this case), increasing the number of cells N_S in the module leads to a reduction in the individual cell area A_c, while decreasing the number of cells results in larger individual cell area. If the number of cells is low, each cell occupies a large area and considering they are all connected in series, the module voltage V_{PV} decreases for a given power. In extreme cases, this voltage may not even exceed the threshold voltage V_{th} required to initiate electrolysis, making H_2 production impossible. This situation is depicted in Figure 2.6, where the $I - V$ curve of a 200 W_p module with 10 cells (yellow line in Figure 2.6) illuminated at STC conditions does not intersect the $I - V$ curve of the electrolyzer (purple line). This indicates that, the way the PV module biases the electrolyzer in direct configuration, it does not generate sufficient voltage to activate the H_2 production.

On the other hand, if the number of cells is too high, each cell becomes smaller, leading to an increase in V_{PV}, but a decrease in I_{PV}. Since H_2 production is directly proportional to the current, this scenario would result in a lower production rate. This case is also illustrated in Figure 2.6, where the 200 W_p PV module with 33 cells (blue line) at STC supplies the electrolyzer (purple line) with a lower current compared to the 200 W_p PV module with 24 cells (red line). The current supplied to the electrolyzer under the direct coupling configuration corresponds to the one obtained by the intersection point between the $I - V$ characteristics of the PV module and the electrolyzer.

Because direct coupling presents this suboptimal biasing of the PV module disadvantage, to make a fair comparison, we have optimized N_S and A_c, while preserving the nominal power rating of the module (200 W_p measured at STC), so that the electrolyzer produces the maximum H_2 throughout the entire typical meteorological year (TMY) at the selected location described in subsection 2.1.1.

The hydrogen production over the course of a year has been calculated for the direct coupling of a 65 W_p electrolyzer with 200 W_p PV modules of different N_S and A_c, featuring 20% efficiency and a total area of 1 m^2. For each configuration, the cell area was adjusted according to the number of series-connected cells in the module. The goal is to determine the design of the optimal module, defined as the one that maximizes annual hydrogen production.

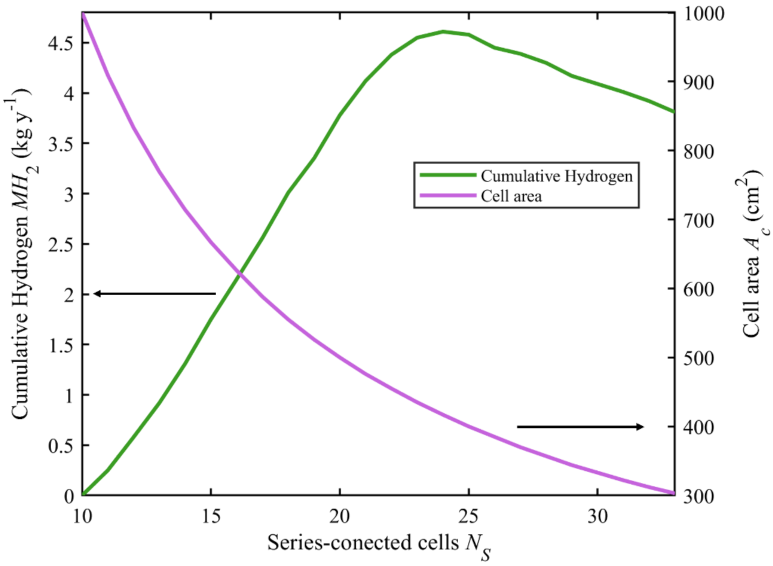

Figure 2.7 Yearly accumulated H_2 production on the direct coupling with different number of cells N_S and cell area A_c in the 200 W_p PV module. The maximum H_2 production is obtained for a PV module of 24 cells with an area of 417 cm^2 each.

Figure 2.7 shows the annual production of H_2 for the direct configuration as a function of N_S. It also shows the corresponding cell area A_c that must be chosen to preserve the 200 W_p module output power at STC once N_S has been fixed. The maximum annual PV production under the direct configuration results to be 4.61 $\mathrm{kg} \cdot \mathrm{y}^{-1}$ and is obtained for a module with N_S = 24 cells and a cell area A_c= 417 cm^{-2}. Although the modules containing between 23 and 27 cells exhibit hydrogen production values that are close to the maximum levels, with outputs of 4.55, 4.61, 4.60, 4.55 and 4.45 $\mathrm{kg} \cdot \mathrm{y}^{-1}$ respectively, Figure 2.7 clearly illustrates a significant sensitivity of annual H_2 production to the design of the module in the direct coupling configuration. The most noticeable reduction in production occurs as the number of cells N_S decreases, with the system eventually reaching zero H_2 production for a 200 W_p module consisting of only 10 cells or less. This behavior is caused by an insufficient V_{PV} when $N_s < 11$ so that $V_{\mathrm{PV}} < V_{\mathrm{th}}$ at all times during the year. This emphasizes the role that module configuration plays in optimizing H_2 generation under the direct coupling strategy, as even relatively small differences in design can have a substantial impact on performance.

Figure 2.7 shows how the choice of optimal values for N_S and A_c leads to an $I_{\mathrm{PV}} - V_{\mathrm{PV}}$ curve that, at STC, intersects with the $I_{\mathrm{EL}} - V_{\mathrm{EL}}$ curve at 15.10 V, a value close to V_{MPP} (14.83 V). This result is explained by the fact that, at the chosen location, G_t close to STC (1,000 $\mathrm{W} \cdot \mathrm{m}^{-2}$) are common, as depicted in Figure 2.4. However, during the green H_2 system operation throughout its entire lifetime, it will be likely that the meteorological conditions of the different years differ significantly from those of the TMY used to obtain a maximized annual H_2 production, resulting in a reduction in its generation for this optimization. However, as we cannot predict the meteorological data, the results here calculated are the best-case scenario for the direct coupling strategy. An illustrative case is shown in Figure 2.4, where at low G_t (200 and 600 $\mathrm{W} \cdot \mathrm{m}^{-2}$), the intersection between the $I_{\mathrm{EL}} - V_{\mathrm{EL}}$ and $I_{\mathrm{PV}} - V_{\mathrm{PV}}$ curves results in an operating point far from P_{MPP}, thus leading to underused PV power and, consequently, to a reduced H_2 production.

This demonstrates that even when a PV module is optimized to maximize H_2 production throughout the year, the direct coupling configuration struggles to perform effectively when operating under conditions different from those used in its optimization.

2.2.2 Optimization of the battery

The optimal battery capacity $C_{\max}$ is the one that maximizes profitability in the indirect setup, considering both the battery cost and the utilization rate of PV energy, which is the ratio of the energy provided by the battery to the electrolyzer and the total PV energy of the indirect configuration.

For the simulation testing, batteries with capacities of 1,800 Wh, 1,350 Wh, 900 Wh, and 450 Wh were selected. These specific values were chosen because they closely align with industry standards, making them relevant for practical applications. Additionally, they provided a well-distributed range for an initial performance assessment, allowing for a comprehensive evaluation of how different storage capacities influence system efficiency and overall hydrogen production. This selection serves as a foundation for further optimization and comparison with alternative configurations.

The simulation of the H_2 production process has been conducted for the indirect configuration with batteries, considering the four different battery capacities mentioned above. To assess profitability, it is essential to evaluate both the costs and benefits of the process. While a more detailed explanation on how these costs and benefits are calculated will be provided in Section 2.3, this subsection presents the net benefit directly obtained for the indirect configuration with different battery capacities. Additionally, other factors such as SOC are analyzed to provide a deeper understanding of why a specific battery capacity is the most suitable for H_2 production under these conditions and with this setup.

Figure 2.8 illustrates the SOC variation throughout the year for different battery capacities: 450 Wh (Figure 2.8a), 900 Wh (Figure 2.8b), 1,350 Wh (Figure 2.8c), and 1,800 Wh (Figure 2.8d). These graphs provide valuable insight into battery performance with different storage capacities, helping to assess how each capacity influences energy availability and overall system efficiency.

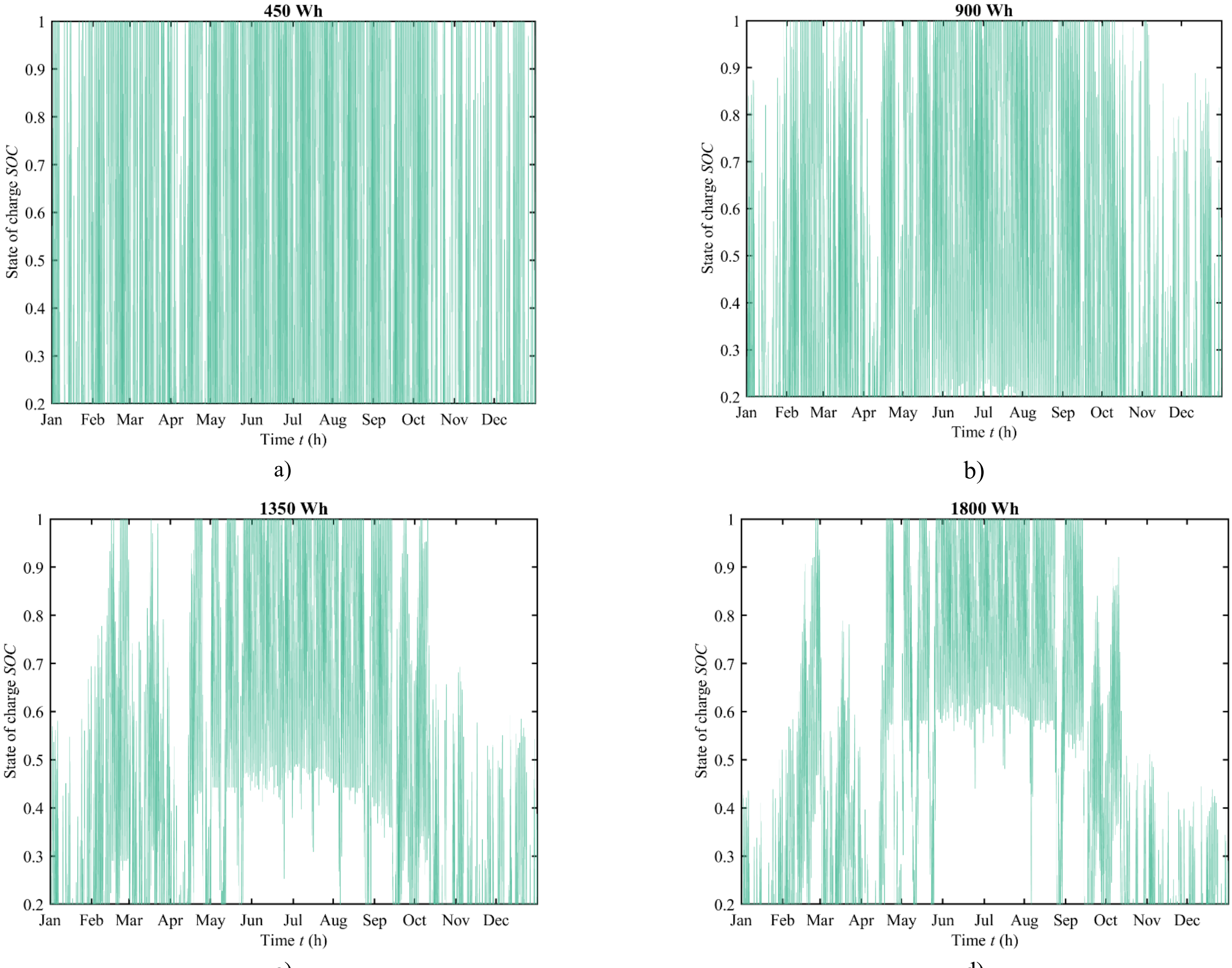

a) b) c) d)

Figure 2.8 State of charge (SOC) throughout the year for batteries with $C_{\max}$ of a) 450 Wh b) 900 Wh c) 1,350 Wh d) 1,800 Wh.

Figure 2.8a shows that the SOC of the 450 Wh battery undergoes full charge and discharge cycles repeatedly throughout the year. This indicates that the battery capacity is being fully utilized but often reaches the maximum SOC, implying that a significant portion of the PV energy is lost due to the inability to store it. Figure 2.8b presents the SOC of the 900 Wh battery, which still shows a large number of complete charge-discharge cycles throughout the year, except for the winter months, when it presents a SOC far from the maximum. In most cases, the minimum SOC value within each cycle reaches zero, meaning that the battery is not large enough to provide all the required energy when needed.

However, it is observed that during the spring and summer months, the battery remains charged for a longer period compared to the autumn and winter months. This behavior is not seen with the 450 Wh battery. Figure 2.8c illustrates the SOC profile of the 1,350 Wh battery, revealing a more pronounced seasonal effect. During the central months of the year, the battery remains fully charged without significant discharge. Additionally, in autumn and winter, when the battery does discharge, it struggles to recharge efficiently. Once depleted, the SOC does not easily return to full capacity, unlike the 450 Wh and 900 Wh batteries. These effects become even more pronounced with the 1,800 Wh battery, as shown in Figure 2.8d, further emphasizing the increasing difficulty in maintaining an optimal charge-discharge balance as capacity increases.

This behavior illustrates that for high capacities (1,350 and 1,800 Wh), the battery is not fully utilized for a significant portion of the year. This underutilization could have an impact on profitability, as the cost of the battery increases with its capacity. If a battery remains charged for extended periods without being discharged efficiently, the investment in a larger capacity may not translate into proportional benefits. On the contrary, a small capacity (450 Wh) reaches its charge limit easily, wasting Wh that cannot be stored. Additionally, it discharges completely just as easily, making it unable to meet the energy needs of the electrolyzer for long.

Therefore, finding an optimal balance between battery size, utilization, and cost is crucial to maximizing the economic viability of the indirect configuration.

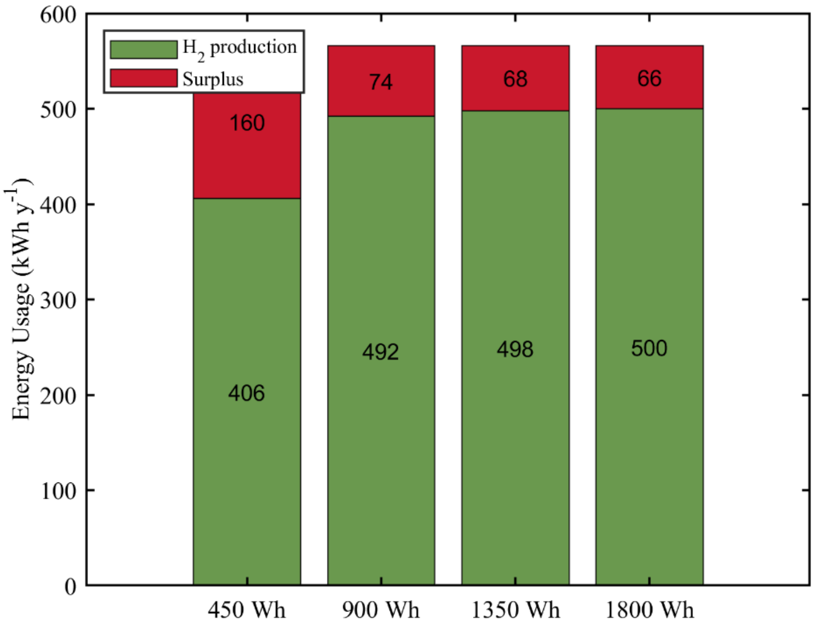

Figure 2.9 Energy use distribution in the indirect configuration with batteries of 450, 900, 1,350 and 1,800 Wh. Green represents the amount of energy allocated to hydrogen production, accounting for energy supplied directly by the PV module as well as by the battery when solar resources are insufficient. Red indicates excess energy that is fed into the grid.

Figure 2.9 illustrates the energy utilization in the indirect configuration with batteries of varying capacities. The green part of the bars represents the amount of energy allocated to hydrogen production, encompassing both the energy supplied directly by the PV module and the energy provided by the battery when solar resources are insufficient. This ensures a continuous supply for hydrogen generation even during periods of low solar availability. In contrast, red represents the excess energy that cannot be utilized for hydrogen production and is instead fed into the grid. Ideally, the available PV energy is primarily allocated to H_2 production and then to the battery if not fully charged; however, any excess energy is redirected to the grid. The energy used for H_2

production comes from both the PV module and, when possible, the battery. Since the PV module and the electrolyzer remain the same across all four setups, the total annual energy generated by the PV modules remains constant. However, the way this energy is utilized depends on the capacity of the battery.

Figure 2.9 demonstrates that as battery capacity increases, a greater amount of energy is allocated to H_2 production. This trend is particularly noticeable when comparing the energy directed toward H_2 production with a 450 Wh battery (406 $\mathrm{kWh} \cdot \mathrm{y}^{-1}$) and a 900 Wh battery (492 $\mathrm{kWh} \cdot \mathrm{y}^{-1}$). However, when the capacity increases to 1,350 Wh and 1,800 Wh, the energy used for H_2 production only rises slightly, reaching 498 $\mathrm{kWh} \cdot \mathrm{y}^{-1}$ and 500 $\mathrm{kWh} \cdot \mathrm{y}^{-1}$, respectively. This represents only a marginal increase in energy utilization for H_2 production, considering the substantial increase in battery capacity.

Naturally, this energy distribution directly impacts hydrogen production. Over the course of a year, the indirect configuration with different battery capacities produces 7.95 kg, 9.64 kg, 9.75 kg, and 9.81 kg of H_2 for the 450 Wh, 900 Wh, 1,350 Wh, and 1,800 Wh batteries, respectively. This behavior aligns with the observations regarding battery SOC. As previously explained, when battery capacity is too large, the system does not utilize the stored energy efficiently, leading to diminishing returns in H_2 production despite increased storage capacity.

Once the annual H_2 production, the amount of energy sold to the grid, and the cost of each battery have been determined, the net benefit of the indirect configuration with different battery capacities can be calculated. The net benefits have been calculated for a production period of nine years, as this is the estimated lifespan of PEM electrolyzers [45,103,104]. This timeframe provides a realistic assessment of the long-term economic viability of the indirect configuration with different battery capacities, ensuring that the analysis aligns with the expected operational lifespan of key components of the system. The main input data and the net benefit results are summarized in Table 2.3. This analysis provides a clear comparison of the economic performance of each setup, helping to identify the most cost-effective battery capacity for maximizing profitability in the indirect configuration. Both the total costs and net benefits in Table 2.3 are referred to the year 9. The total cost includes both capital expenditure (CAPEX) and operational expenditure (OPEX), with the latter being the same across all four case studies. Consequently, the cost differences related to battery capacity are reflected solely in the CAPEX.

Table 2.3 Maximum capacity of the battery, H_2 production, total cost, and Net benefits in year 9 of the configurations. The prices of H_2 (P_{H2}) and surplus energy (P_{Ex}) remain stable over the years, which are 10 $€ \cdot \mathrm{kg}^{-1}$ and 0.05 $€ \cdot \mathrm{kWh}^{-1}$ respectively [105,106].

Capacity (Wh)	H_2 production ($\mathrm{kg} \cdot \mathrm{y}^{-1}$)	Total cost (€)	Net benefit (€)
450	7.65	341.70	446.07
900	9.64	394.43	506.79
1,350	9.75	447.16	461.29
1,800	9.81	499.90	412.48

Table 2.3 further indicates that the 900 Wh battery provides the highest net profitability for the indirect configuration after 9 years. This outcome is attributed to the fact that, while higher battery capacities lead to increased H_2 production, the increment is not substantial enough to offset the higher initial cost of larger batteries. For those reasons, the battery selected for the comparative analyses between direct and indirect configurations has a capacity of 75 Ah and 12 V, equating to 900 Wh.

2.3 Performance of configurations

2.3.1 Comparative H_2 production

In the direct configuration, the PV generator and electrolyzer operate at the same current and voltage ($V_{\mathrm{PV}} = V_{\mathrm{EL}}, I_{\mathrm{PV}} = I_{\mathrm{EL}}$), determined by their intersecting current-voltage characteristics. The indirect configurations include a PS with two steps: the MPPT and the DC-DC converter. The MPPT locks V_{MPP} and I_{MPP} in real time, extracting P_{MPP} from the PV generator despite the fluctuating G_t and T conditions. The DC-DC converter adjusts this $V_{\mathrm{MPP}}I_{\mathrm{MPP}}$ product to match the operating current and voltage values corresponding to such electrolyzer input power, defined by $V_{\mathrm{EL}}I_{\mathrm{EL}}$, with an efficiency η_{DC} so that:

$$\eta_{\mathrm{DC}} V_{\mathrm{MPP}} I_{\mathrm{MPP}} = V_{\mathrm{EL}} I_{EL} \tag{2.24}$$

and ensuring the $V_{\mathrm{EL}}, I_{\mathrm{EL}}$ pair fits the electrolyzer current-voltage characteristics. In this study, the DC-DC converter is assumed to have a constant efficiency of 95% for the sake of simplicity. In the indirect configuration, the PV module does not need to be optimized because the PS ensures maximum production for any 200 W_p PV module design, independently of the values chosen for N_s and A_c. However, we will consider the same PV module configuration as in the direct coupling (N_s= 24 and A_c = 417 cm^{-2}) for the sake of an appropriate comparison.

Figure 2.10 shows the cumulative annual H_2 production (MH_2) for the three configurations studied. The direct configuration yields the least H_2, producing 4.61 kg per year. The indirect configuration without batteries produces a total of 5.41 kg of H_2 per year, which is 17.4% more than the direct configuration. As observed in Figure 2.10, both the direct and indirect configurations without batteries exhibit a relatively similar trend, with increased production rates in spring and summer (corresponding to the central part of the horizontal axis), due to higher G_t at the study location. It is observed that the MH_2 is relatively similar during the first few months (approximately, the first 1,400 hours) of the year, which correspond to the wintertime. After the first 1,400 h, the difference in MH_2 is wider as the year progresses, with a clear advantage of the indirect configuration over the direct one.

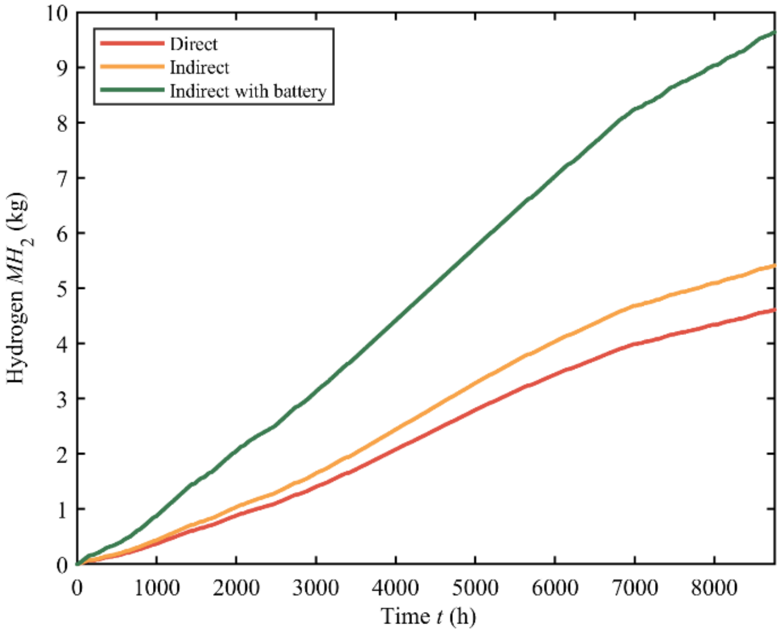

Figure 2.10 H_2 kilograms accumulated during the year (MH_2) for the direct and indirect (with and without battery) coupling configurations for a module PV Power of 200 W_p.

As shown in Figure 2.10, the indirect configuration with 900 Wh batteries produces the highest H_2 annually as shown in Figure 2.10, yielding 9.64 kg. This is 109% more than the direct configuration and 78.2% more than the indirect configuration without batteries. Similar to the other configurations, H_2 production is higher in the spring and summer months, however, in this case, the increase is much more pronounced, and H_2 production is significantly higher than in the configurations without batteries throughout the entire year. The noticeable increase in the H_2 production rate of the system incorporating batteries during the spring and summer months is attributed to the numerous hours when the PV module generates more than 65 W, in which case, the energy is stored, to contribute to the operation of the electrolyzer later that day, extending its operation and, consequently, its total hydrogen production. Consequently, the battery reaches its maximum SOC nearly every day during these months, as seen previously in Figure 2.8b.

Once the annual H_2 production has been determined for the three configurations, the overall efficiency (η_{global}) of the process can be evaluated. η_{global} is defined as the ratio between the energy content of the produced hydrogen (E_{H2}) and the total incident solar energy on the PV module throughout the year (E_{in}), as expressed in Eq. (2.25). This metric provides insight into how effectively the system converts available solar energy into stored chemical energy in the form of H_2.

$$\eta_{\mathrm{global}} = \frac{E_{\mathrm{H2}}}{E_{\mathrm{in}}} \tag{2.25}$$

where E_{H2}, represented as the product of $M\mathrm{H}_2$, the molecular weight of H_2 and $\Delta G_{R,0}$ (the total Gibbs free energy content of the produced H_2, $\Delta G_{R,0} = 237.23\ \mathrm{kJ \cdot mol^{-1}}$), and E_{in} is the solar energy received on the PV module ($E_{\mathrm{in}} = 2.79\ \mathrm{MWh \cdot m^{-2}}$ calculated from the hourly irradiance of the TMY at this location and under this tilt angle). Table 2.4 presents the cumulative amount of H_2 produced by each configuration over one year, the energy contained in the produced H_2, and the overall efficiency of each configuration.

Table 2.4. Comparison of different performance data between direct and indirect, with and without battery, coupling configurations.

Parameters	Direct	Indirect	Indirect (Battery)
Annual solar energy received, E_{in} ($\mathrm{kWh \cdot m^{-2}}$)	2,790	2,790	2,790
Hydrogen produced, $M\mathrm{H}_2$ ($\mathrm{kg \cdot y^{-1}}$)	4.61	5.41	9.64
Hydrogen energy content, E_{H2} ($\mathrm{kWh \cdot y^{-1}}$)	152	178	318
Energy efficiency, η_{global} (%)	5.6	6.6	11.8

Table 2.4 shows that the overall efficiency of the H_2 production process for the direct configuration is 5.6%, as the energy stored in the produced H_2 reaches 152 kWh per year. The inclusion of a power stage (MPPT and DC-DC converter) increases the H_2 energy output to 178 kWh per year, raising the overall efficiency to 6.6%. Finally, incorporating a 900 Wh battery to the indirect configuration further boosts the stored H_2 energy to 318 kWh per year, achieving a maximum efficiency of 11.8%.

In terms of energy efficiency, the indirect configuration with a battery proves to be the most effective, whereas the direct configuration is the least efficient of all. It should be recalled at this point that the module used has been designed to perform optimally in the direct coupling configuration, which means that η_{global} has been calculated for the best-case direct coupling scenario and would be lower if a non-optimized PV module were used while η_{global} would remain the same for the indirect coupling case.

2.3.2 Comparative energy production and usage

The configurations can also be compared based on PV energy production and energy utilization. For clarity, we define usable energy production as occurring when the $I_{\mathrm{PV}} - V_{\mathrm{PV}}$ and $I_{\mathrm{EL}} - V_{\mathrm{EL}}$ characteristics intersect at a point where $I \times V > 0$. Additionally, we will assume that the primary priority for the produced energy is powering the electrolyzer. Once the electrolyzer operates at its nominal power, any excess energy will be directed towards charging the battery, if one is present in the configuration. This approach ensures that H_2 production is maximized before allocating surplus energy to storage, optimizing the overall system performance. In this way, electricity will only be fed into the grid when the electrolyzer is operating at its nominal power and the battery is fully charged. The amount of energy supplied to the grid will be determined by subtracting the energy used for electrolysis from the total PV energy produced. This ensures that the system prioritizes H_2 production and energy storage before exporting any surplus electricity.

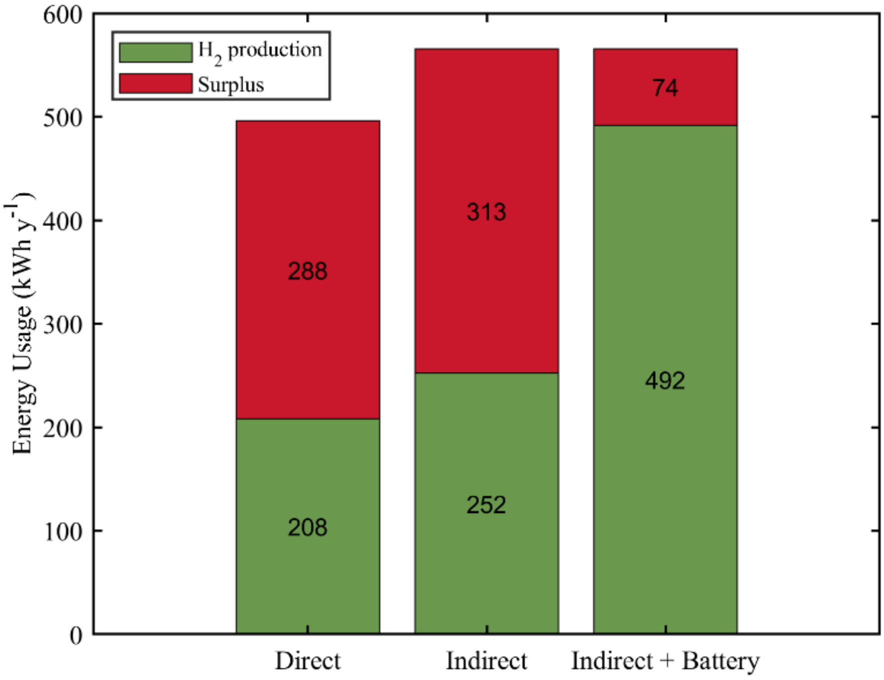

Figure 2.11 Energy production and usage in a year for the three configurations. All three configurations include a 200 W_p PV module and 65 W_p PEM electrolyzer while the indirect with battery also includes a 900 Wh battery.

Figure 2.11 illustrates the energy distribution for each configuration. The total bar height represents the total energy produced by the PV generator, while the green fraction indicates the energy utilized for H_2 production and the red fraction represents the surplus energy fed into the grid. This visualization highlights how each configuration manages energy allocation, emphasizing the proportion directed toward electrolysis versus the excess energy that remains unused for H_2 generation.

The direct configuration generates 496 $\mathrm{kWh \cdot y^{-1}}$, whereas the indirect configurations (both with and without a battery) produce 565 $\mathrm{kWh \cdot y^{-1}}$. In direct configuration, the intersection between $I_{\mathrm{PV}} - V_{\mathrm{PV}}$ and $I_{\mathrm{EL}} - V_{\mathrm{EL}}$ often deviates significantly from the MPP of the PV module because there is no MPPT, meaning that the PV generator fails to operate at optimal efficiency. As a result, the direct configuration system consistently produces less energy throughout the year, even though the indirect configurations experience additional energy loss due to the non-ideal efficiency of the power stage.

Regarding energy usage, Figure 2.11 shows that the direct configuration allocates 208 $\mathrm{kWh \cdot y^{-1}}$ to H_2 production, while 288 $\mathrm{kWh \cdot y^{-1}}$ is considered surplus because it exceeds the nominal 65

W capacity of the electrolyzer. This means that only 41.9% of the total produced energy is utilized for H_2 generation, with the remaining 58.1% being fed into the grid. For the indirect configuration without batteries, 252 $\mathrm{kWh}\cdot\mathrm{y}^{-1}$ is used for H_2 production, while 313 $\mathrm{kWh}\cdot\mathrm{y}^{-1}$ is surplus energy, corresponding to 44.6% and 55.4% of the total produced energy, respectively. Compared to the direct configuration, the indirect setup shows a slight increase in the percentage of energy used for H_2 production. However, the difference remains relatively small, indicating that while power conditioning improves solar energy utilization by optimizing the operating point of the system, a significant portion of the energy generated is still not directed toward H_2 production. This suggests that, despite the advantages of indirect configuration, the ability to fully harness the available energy for a green hydrogen production system remains limited.

The indirect configuration with batteries uses 492 $\mathrm{kWh}\cdot\mathrm{y}^{-1}$ for H_2 production and has only 74 $\mathrm{kWh}\cdot\mathrm{y}^{-1}$ as surplus, representing 86.9% and 13.1% of the produced energy, respectively. Figure 2.11 shows the indirect coupling with battery presents a substantial increase in energy utilization for H_2 production, demonstrating the role of the battery in improving system efficiency. By storing excess energy that would otherwise be fed into the grid and later supplying it to the electrolyzer when solar availability is low, the battery effectively minimizes energy waste. As a result, the indirect configuration with batteries achieves a much higher percentage of energy directed toward H_2 generation, ensuring a more stable and continuous operation of the electrolyzer. This explains why H_2 production is substantially greater in the battery configuration, as shown in Figure 2.10.

While the indirect configuration with a 900 Wh battery maximizes energy efficiency by significantly increasing the proportion of PV energy used for H_2 production, its economic feasibility must also be carefully evaluated. The integration of a battery introduces additional costs related to its purchase, maintenance, and eventual replacement, which impact the overall profitability of the system. Therefore, assessing the trade-off between the increased H_2 yield and the associated costs is essential to determine whether the benefits outweigh the financial investment and the increased complexity of the system. A comprehensive economic analysis will provide insight into the long-term viability of this configuration and its competitiveness compared to other H_2 production strategies.

2.3.3 Comparative economic viability

To perform a comprehensive economic feasibility study of the three configurations, we will take the full operational lifespan of the PEM electrolyzer as 80,000 hours, according to specialized literature [45,103,104], since it is the common element among all configurations that has the greatest impact on CAPEX, representing the highest cost. In any case, although the photovoltaic module could have a relatively close impact on cost, its durability is guaranteed, at least, for more than double the hours (over 20 years), as offered by most major commercial suppliers. As a first step, we will calculate the costs associated with each configuration. The costs (C) include CAPEX and OPEX, multiplied by the number of years (ny):

$$C = \mathrm{CAPEX} + ny \cdot \mathrm{OPEX} \tag{2.26}$$

CAPEX includes not only the costs of the main components for each configuration but also those associated with the energy balance of system (EBOS) and the structure balance of system (SBOS). These two categories encompass all auxiliary elements required to ensure the proper operation, safety, and reliability of the green hydrogen production system.

The EBOS refers to all electrical and electronic components necessary for the functioning of the system, excluding those that are part of the core production unit itself. This includes elements such as electrical infrastructure, power distribution systems, control and automation systems, cabling, transformers, and other essential electrical equipment that facilitate efficient energy management and integration.

On the other hand, the SBOS comprises the physical and structural components required to support, protect, and house the entire system. This includes structural frameworks, mounting and support systems, piping and plumbing for hydrogen and cooling fluids, ventilation systems, safety mechanisms, fire protection, and site preparation activities such as foundations and enclosures. The SBOS ensures mechanical stability, durability, and compliance with safety regulations, providing a robust infrastructure for long-term operation.

Together, EBOS and SBOS are fundamental for enabling a fully operational green hydrogen production system, as they integrate all the necessary auxiliary infrastructure to ensure efficiency, safety, and reliability throughout the lifecycle of the system.

Table 2.5. Cost per power unit, lifespan and total cost of the components used in the different configurations.

Component	Cost	Lifespan (h)	Unit	Cost (€)
200 W_p PV module	0.345 $(\text{€} \cdot \text{W}^{-1})$[107]	$2.19 \cdot 10^5$	1	69.0
65 W_p Electrolyzer	1.071 $(\text{€} \cdot \text{W}^{-1})$[108]	$8.7 \cdot 10^4$	1	69.6
PS	0.045$(\text{€} \cdot \text{W}^{-1})$[107]	$1.31 \cdot 10^5$	1	16.1
Battery	0.12 $(\text{€} \cdot \text{Wh}^{-1})$[109]	$1.31 \cdot 10^5$	1	105.5
Regulator	0.1395$(\text{€} \cdot \text{W}^{-1})$[110]	$1.31 \cdot 10^5$	1	27.9
EBOS	0.16 $(\text{€} \cdot \text{W}^{-1})$[107]	-	1	32.6
SBOS	0.12 $(\text{€} \cdot \text{W}^{-1})$ [107]	-	1	23.8
OPEX	0.025 $(\text{€} \cdot \text{W}^{-1} \cdot \text{y}^{-1})$ [107]	-	1	5.0

Table 2.5 presents a detailed breakdown of the costs associated with each individual main component of the system, including the PV module, electrolyzer, PS, and battery. In addition to these key components, the table also accounts for the costs related to the energy balance of system, the structure balance of system, and the OPEX of the system. The cost estimations for SBOS and EBOS per unit of power are based on the installed PV power, serving as a reference for standardization across configurations. Furthermore, Table 2.5 provides a cost per power unit analysis, expressed in euros per watt $(\text{€} \cdot \text{W}^{-1})$, for the PV module, electrolyzer, and PS, while the cost of the battery is given in euros per watt-hour $(\text{€} \cdot \text{Wh}^{-1})$ to account for its energy storage capacity. These cost estimations represent a conservative, potentially underestimated figure. For simplicity, they do not incorporate additional expenses related to engineering design, land acquisition, labor costs, permits, taxes, or other miscellaneous project-related expenditures. While these factors can significantly impact the overall investment, their exclusion allows for a more streamlined comparison of the core system costs across different configurations.

Table 2.5 also defines the lifespan and total cost of the various system components. While all configurations include OPEX, SBOS, and EBOS in their costs, the specific components vary depending on the configuration. In direct configuration, the system consists only of the PV module and the electrolyzer, representing the simplest setup. The indirect configuration without batteries includes an additional component: the PS, which regulates energy conversion and distribution. Finally, the indirect configuration with batteries is the most comprehensive, incorporating all the elements presented in Table 2.5 including the energy storage unit, which enhances the flexibility and reliability of the system.

The gross benefits (B_g) are also accounted in this study, which depend on two sources of income: the annual amount of H_2 produced (M_{H2}) and the surplus PV energy fed into the grid (Ex). The gross benefits can be calculated using Eq. (2.27)

$$B_g = ny \cdot [(M_{\text{H2}} \cdot P_{\text{H2}}) + (Ex \cdot P_{\text{Ex}})] \tag{2.27}$$

To simplify the economic feasibility study, we assume that the prices of H₂ (P_{H2}) and surplus energy (P_{Ex}) remain stable over the years, which in this study have been defined as 10 $€ \cdot \mathrm{kg}^{-1}$ and 0.05 $€ \cdot \mathrm{kWh}^{-1}$ respectively [105,106]. To assess the economic viability of each configuration over the 9-year lifespan of the PEM electrolyzer, we calculate the net benefits (B_n), which are obtained by subtracting the total costs (C) from the gross benefits (B_g). The configuration with the highest B_n at the end of year 9 will be considered the most economically profitable.

$$B_n = B_g - C = ny \cdot [(M_{H2} \cdot P_{\mathrm{H2}}) + (Ex \cdot P_{\mathrm{Ex}})] - [\mathrm{CAPEX} + ny \cdot \mathrm{OPEX}] \qquad (2.28)$$

In the small-scale examples of the three configurations used in our study, the initial costs are as follows: the direct configuration has an initial cost of €200, the indirect configuration without batteries is priced at €216, and the indirect configuration with a 900 Wh battery amounts to €349.

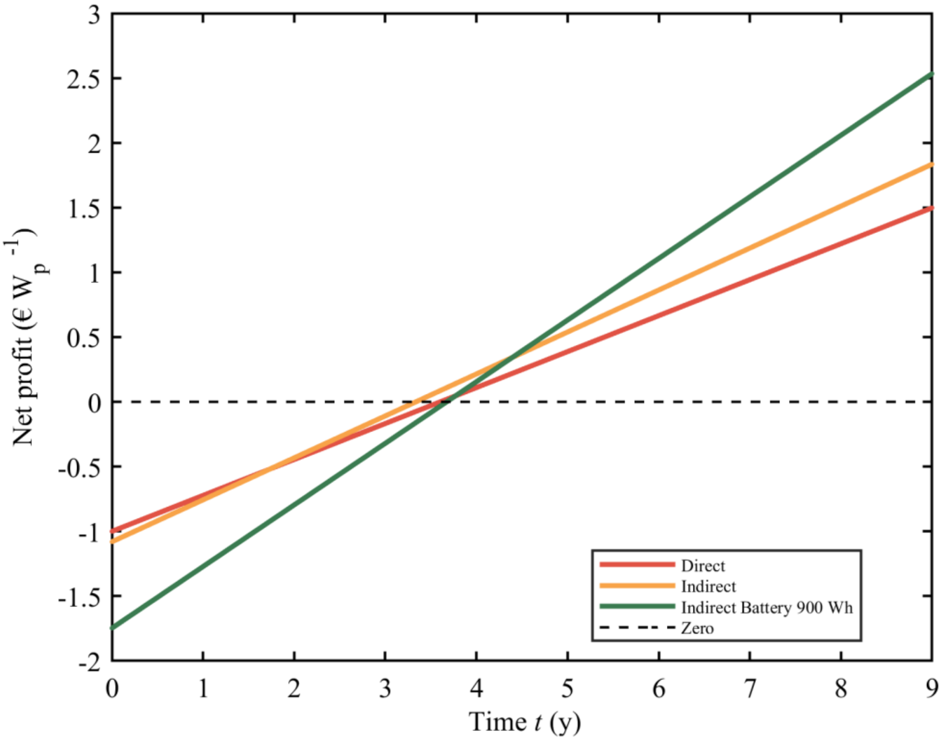

Figure 2.12 Net profit evolution per unity of PV power ($€ \cdot \mathrm{W}^{-1}$) of the three configurations throughout the 9-year lifespan of the electrolyzer.

Figure 2.12 shows the net benefits per unit of PV power ($€ \cdot \mathrm{W}^{-1}$), overtime for the different configurations throughout the 9-year operational lifespan of the PEM electrolyzer. The evolution of these net benefits reflects the financial performance of each configuration. A configuration is considered profitable when its benefits move from negative to positive, crossing the zero line, as depicted in Figure 2.12. Figure 2.12 also demonstrates that all configurations become profitable by the end of the study. In fact, each of the three configurations reaches profitability after the third year. Despite the higher initial cost of the indirect configuration without battery compared to the direct one, the former produces more annual H₂, as reflected in Figure 2.10, and feeds more surplus electricity to the grid, as shown in Figure 2.11. This results in a faster rate of profit generation for the indirect configuration. In fact, by year 9, the indirect configuration without battery becomes more profitable than the direct configuration, generating 1.83 $€ \cdot \mathrm{W}^{-1}$ and 1.49 $€ \cdot \mathrm{W}^{-1}$, respectively.

The indirect configuration with a 900 Wh battery is the most expensive from the start, as reflected in Figure 2.12, primarily due to the high cost of the battery, which is the most expensive individual component in the system. Despite this higher initial cost, it emerges as the most profitable configuration by the end of year 9, generating 2.53 $€ \cdot \mathrm{W}^{-1}$. This profit per unit of PV power is primarily driven by the ability of the battery to store surplus energy, which improves the overall efficiency, energy utilization of the system and long-term economic returns.

If the lifetime of the electrolyzer is less than 80,000 hours, the gap in net profitability between the different configurations narrows, as shown in Figure 2.12. From year 0 to year 1, direct configuration is the most profitable. However, from year 2 to year 4, the indirect configuration without batteries becomes the most profitable. This shift in profitability reflects how the configurations perform over time, with direct configuration initially providing higher returns, but the indirect configuration without batteries gaining an advantage as the system progresses. This is why the findings of this article are valid if the PEM electrolyzers have a lifespan of more than 4 years, as this is the time frame within which all configurations become profitable, according with the results from Figure 2.12.

Thus, after comparing H_2 production, PV energy generation, energy usage, and economic profitability across the three configurations and taking into account the costs of the various components selected for the S-H system and the prices of the products obtained from it, it is clear that the indirect configuration with batteries represents the most efficient and economically viable option. This configuration optimizes the entire hydrogen production process by maximizing the utilization of solar PV energy and ensuring better long-term profitability.

2.3.4 Impact of PV power reduction

So far, it has been considered that all the cells of the PV module are identical and, therefore, produce the same power. However, it is important to acknowledge that the presence of malfunctioning PV cells can occur due to various factors, such as physical damage or partial shading caused by buildings, trees or surface contamination. Under such conditions, the PV power output and, consequently, the H_2 generation are reduced. The impact of this effect can vary depending on factors such as the size of the shaded area, the time of the year, the electrical configuration of the PV cells in the module, the presence of bypass diodes (which have been intentionally avoided from the discussion in this work for simplicity).

We will here compare the impact of PV power reduction on the H_2 production for the direct and indirect configuration without battery. Including the indirect configuration with batteries would not provide a fair comparison for the direct configuration, as the presence of batteries in the indirect setup would introduce additional storage capacity, affecting the overall system performance. This would create an imbalance in the analysis, as direct configuration, lacking a storage system, would be at a disadvantage.

The PS power loss impacts the H_2 production of the indirect configuration in the same amount. Furthermore, the existence of the PS will always minimize the impact of any other source of PV power loss by making the H_2 loss almost equivalent. The study of the effect of power loss on H_2 production will be illustrated by removing cells from the originally optimized 24-cell module one by one, so each removed cell represents a generic malfunctioning produced by any of the factors detailed above. Assuming that all cells provide the same power to the PV module, the withdrawal of a cell leads to an 8.33 W_p decrease in the nominal PV power. Since the cells are connected in series, the decrease in generated power is at the expense of the reduction of the module V_{OC} (in the range of -0.73 V/malfunctioning cell). This significant drop is due to V_{PV} falling below the threshold voltage of 8.33 V, which makes it impossible to produce H2 efficiently. Notice that this number of cells that produce no H2 differs from the number obtained in the calculations showed in Figure 2.7 because, in that case, the power of the module was preserved to 200 Wp even if the number of cells changed.

Table 2.6 shows the dependence of H_2 production on the number of functioning cells for both configurations. In both cases, as the number of functioning cells decreases, hydrogen production decreases. However, the decrease in hydrogen production is more pronounced in the direct configuration than in the indirect one. In the direction configuration, H_2 production becomes impossible when fewer than 12 cells are operational, highlighting the vulnerability of the configuration to partial cell failures. As the number of malfunctioning cells increases, performance in the direct coupling configuration deteriorates rapidly, with hydrogen production losses reaching up to 100% when 13 cells fail, which is, there are 11 functioning cells in the PV module.

This significant drop is due to V_{PV} falling below the threshold voltage of 8.33 V, which makes it impossible to produce H_2 efficiently. Notice that this number of cells that produce no H_2 differs from the number obtained in the calculations showed in Figure 2.7 because, in that case, the power of the module was preserved to 200 W_p even if the number of cells changed.

Table 2.6 H_2 yearly production, voltage and power characteristics of the PV module with different numbers of functional cells. "Number of cells" indicate the number of cells functioning in the module, e.g., 20 cells means there are 4 cells malfunctioning on the module.

Number of Cells (nominal module power loss %)	V_{OC} (V)	V_{MPP} (V)	P_{MPP} (W)	Direct H_2 (kg · y^{-1})	Direct H_2 loss (%)	Indirect H_2 (kg · y^{-1})	Indirect H_2 loss (%)
24 (0%)	17.38	14.83	200	4.61	0	5.41	0
23 (4.1%)	16.68	14.21	191.7	4.35	5.64	5.24	3.15
22 (8.3%)	15.97	13.62	183.3	3.95	14.32	5.07	6.28
21 (12.5%)	15.26	13.01	175.1	3.57	22.56	4.90	9.47
20 (16.7%)	14.56	12.41	166.7	3.12	32.32	4.73	12.94
19 (20.9%)	13.84	11.78	158.4	2.77	39.98	4.56	15.88
18 (24.9%)	13.13	11.12	150.1	2.39	48.15	4.39	18.78
17 (29.2%)	12.42	10.54	141.7	2.20	52.28	4.22	21.97
16 (33.3%)	11.71	9.98	133.4	1.79	61.17	4.05	25.00
15 (37.5%)	10.98	9.35	125.1	1.46	69.33	3.88	28.28
14 (41.6%)	10.24	8.71	116.7	0.97	78.96	3.71	31.42
13 (45.9%)	9.45	8.08	108.4	0.81	82.43	3.54	34.55
12 (50.0%)	8.69	7.42	100.1	0.42	90.89	3.37	37.84
11 (54.1%)	8.05	6.86	91.74	0	100	3.20	40.74
10 (58.3%)	7.32	6.19	83.38	0	100	2.99	44.02

In contrast, the indirect coupling configuration shows a linear reduction in H_2 production as cells malfunction, with H_2 loss increasing proportionally to the number of cells that fail. This indicates that the indirect configuration is less sensitive to the number of non-functional cells compared to the direct configuration, making it a more robust option in situations where partial shading or degradation of the PV module occurs over time. The results highlight the challenges of the direct coupling configuration, especially in real world scenarios where partial shading or aging effects might cause cell malfunctions. Therefore, the indirect coupling configuration may be a more reliable choice for ensuring consistent H_2 production throughout the lifetime of the module.

2.3.5 Impact of the DC-DC converter efficiency

The performance of the indirect coupling configuration is highly influenced by the efficiency of the DC-DC converter, which is assumed to be 95% in the model used in this study. However, as the efficiency of the DC-DC converter decreases, annual H_2 production also declines. If the efficiency drops significantly, the H_2 production levels in the indirect configuration may approach those of the direct coupling configuration.

In this section, we will examine the impact of η_{DC} on hydrogen production in the indirect coupling configuration. To do so, we have calculated the annual hydrogen production for DC-DC converters with varying η_{DC} values. As in 2.3.4, this comparison has been made exclusively between the direct coupling configuration and the indirect coupling configuration without batteries.

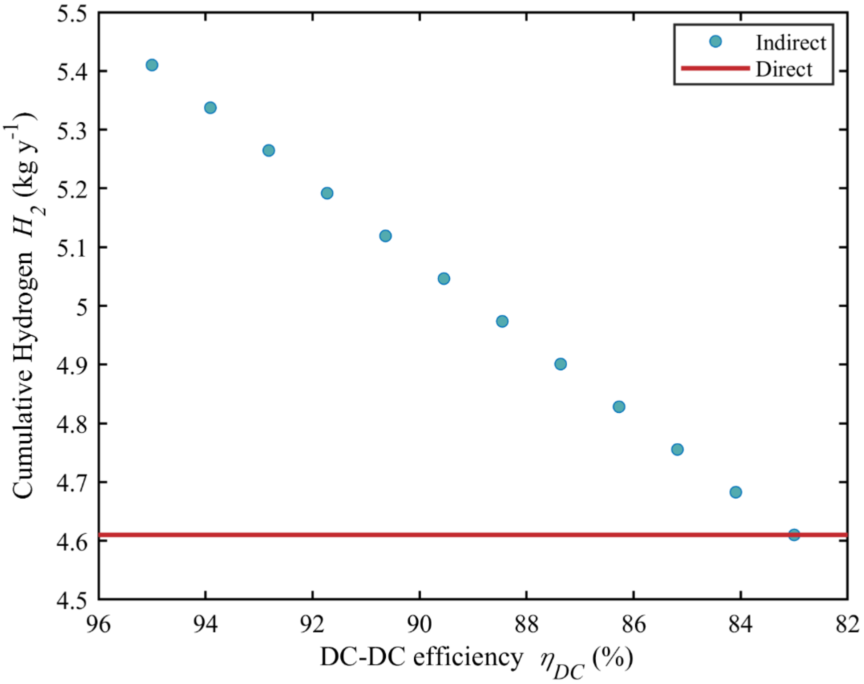

Figure 2.13 H_2 yearly production for DC-DC converters of different efficiency (η_{DC}).

Figure 2.13 illustrates the expected linear reduction of the annual H_2 production with η_{DC} ($6 \cdot 10^{-2}$ $\mathrm{kg} \cdot \mathrm{y}^{-1}$ for every 1% decrease in η_{DC}). It is also observed from Figure 2.13 that H_2 production in the indirect coupling configuration equals that of the direct coupling ($4.61\ \mathrm{kg} \cdot \mathrm{y}^{-1}$) when η_{DC} is 83%, a value well below the standards used in conventional commercial DC-DC converters. In fact, for a DC-DC converter design to be considered valid, its efficiency must exceed 90% [78], so a scenario with efficiencies and H_2 production as low as in the direct coupling is unlikely to occur in the indirect coupling despite the use of the PS. This result reinforces that indirect coupling will always generate more H_2 than direct coupling under the same irradiance conditions, even when the DC-DC converter has efficiencies within today's industrial standards.

2.4 Summary

Different PV modules were designed to optimize H_2 production in the direct coupling between the module and a 65 W PEM electrolyzer. All modules had a nominal power of 200 W_p (under STC), a total area of 1 m^2, and an efficiency of 20%. The differences lay in the number of series-connected cells and the cell area, such that a higher number of series-connected cells corresponded to a smaller cell area. The optimal module consists of 24 series-connected cells, each with an area of 417 cm^2. As for the PEM electrolyzer, it consists of six series-connected cells. Hydrogen production begins once the electrolyzer is polarized above 8.33 V.

The inclusion of a battery in the indirect configuration has been studied. The battery capacity was optimized based on two criteria: maximizing net benefit at the end of the electrolyzer's lifespan and ensuring efficient use of the stored energy. In other words, the battery should neither fully charge and discharge constantly nor remain in periods where stored energy is not utilized for hydrogen production. Capacities of 400, 900, 1,350, and 1,800 Wh were analyzed, with the optimal capacity being 900 Wh.

We calculated the annual hydrogen production for three different configurations: direct, indirect, and indirect with a 900 Wh battery, yielding 4.61 kg, 5.41 kg, and 9.64 kg per year, respectively. Moreover, the overall process efficiency has also been determined for each configuration, with values of 5.6%, 6.6%, and 11.8%, respectively.

The energy utilization among the three configurations has also been compared. The direct configuration generates 496 kWh per year, while the other two configurations produce 565 kWh. The lower energy output of the direct configuration is due to the absence of a power conditioning stage. In terms of energy allocation to hydrogen production, the direct configuration utilizes 41.9%, the indirect configuration 44.6%, and the indirect configuration with a battery achieves 86.9%.

The more components a configuration has, the higher its CAPEX and total cost, as OPEX remains the same for all three configurations studied. The direct configuration has the lowest cost, followed by the indirect configuration, while the most expensive is the indirect configuration with a battery. All configurations become profitable from year 3 onward. In year 9, the direct configuration generates net benefits of 1.49 $€ \cdot \mathrm{W}^{-1}$, the indirect configuration of 1.83 $€ \cdot \mathrm{W}^{-1}$, and the indirect configuration with a battery 2.53 $€ \cdot \mathrm{W}^{-1}$.

Therefore, the indirect configuration with a 900 Wh battery is the one that produces the most hydrogen in a year, has the highest efficiency, allocates the most energy to hydrogen production, and is the most profitable (in year 9) among the three configurations studied.

The indirect configuration also shows higher resilience to module power losses. For instance, with 13 dysfunctional solar cells, H_2 production in direct configuration collapses entirely, whereas the indirect configuration only reduces production by 40.7%.

The PS does not have 100% efficiency, meaning that not all the electrical energy generated by the PV module in the indirect configuration is converted into hydrogen. However, even considering that the efficiency is not 100%, for the hydrogen production in the indirect configuration to match that of the direct configuration, the PS efficiency would need to fall below industrial standards. Specifically, for the two configurations to produce the same amount of hydrogen, the PS efficiency would need to be 83%.

Chapter 3. Direct air capture thermodynamics

The growing concern about climate change driven by the increasing concentration of CO_2 in the atmosphere has spurred research into various technologies and methods for capturing and separating CO_2 from the air [111,112]. The ability to efficiently extract CO_2 is crucial for advancing the mitigation of the adverse effects associated with global warming [113,114].

In this context, this chapter explores the minimum energy required to extract one ton of CO_2 from the air, without focusing on specific methods. As a preliminary step toward a potential CO_2 electrolyzer, a thermodynamic study is conducted to determine the minimum energy cost, and therefore also economic cost, under various scenarios and to understand the underlying fundamental processes. If this cost is excessively high, developing a CO_2 electrolyzer may not be viable.

In the first scenario, we assume that extraction occurs at constant pressure and temperature, specifically $101{,}325\ \mathrm{Pa}$ and $298.15\ \mathrm{K}$, which corresponds to the average atmospheric pressure and temperature, also known as standard conditions. This case likely represents the most realistic model, where CO_2 extraction takes place on a moderate scale, ensuring that neither atmospheric pressure nor temperature is significantly affected by the capturing process. This approach, developed in subsection 3.1, leads to a result of $4.97 \cdot 10^{8}\ \mathrm{J \cdot ton^{-1}}$, originating from the minimum thermodynamic work required to counteract the entropy decrease associated with separating a gas, CO_2 in this case, from a mixture.

This analysis prompts a deeper examination of the concept of entropy of mixing, within which certain systems—such as those underlying the so-called Gibbs paradox—can be formulated where entropy of mixing is zero, as studied in both subsections 3.2 and 3.3. This consideration allows us to investigate whether such systems could apply to CO_2 extraction from the atmosphere. In this regard, we conclude that they are not applicable.

3.1 Thermodynamic study of CO_2 capture from air at constant pressure and temperature

Let us consider an initial volume of air, V_0, (system 0) at standard conditions of pressure, P, and temperature, T ($P = 101{,}325\ \mathrm{Pa}$ and $T = 298.15\ \mathrm{K}$ respectively) which also correspond to the standard conditions usually assumed for the atmosphere (Figure 3.1) which in the process will also act as thermal and pressure reservoir. The volume V_0 of air is defined as it contains 1 ton of CO_2 at a concentration of 400 ppm.

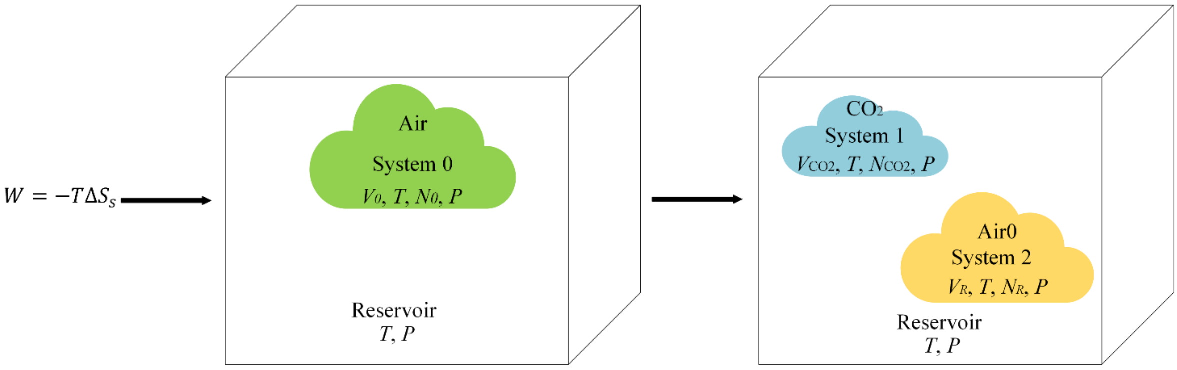

Figure 3.1 Schematic representation of a direct air capture (DAC) process. All systems have the same pressure P and temperature T because the capture process is assumed to take place in equilibrium with the atmosphere also acting as thermal and pressure reservoir.

System 0 contains N_{CO2} mol of $\mathrm{CO_2}$ and N_R mol of the other gases present in air (mainly $\mathrm{N_2}$ and $\mathrm{O_2}$). In the capturing process, the air (system 0) is separated into N_{CO2} mol of $\mathrm{CO_2}$ (system 1) and N_{R} mol of the remaining components, which form Air0 (system 2). The separation process will be considered quasi-static (that is, occurring through equilibrium states) and the gases will be treated as ideal gases. Hence, for ideal gases in equilibrium, the following equation of state must be satisfied [115]

$$PV = NRT \tag{3.1}$$

where R is the universal gas constant (R=$8.21 \cdot 10^{-5}$ $\mathrm{m^3 \cdot atm \cdot mol^{-1} \cdot K^{-1}}$ = $8.31 \cdot 10^{-3}$ kJ· $\mathrm{mol^{-1} \cdot K^{-1}}$). From Eq. (3.1), the volume V_0 of system 0 can be expressed as

$$V_0 = \frac{(N_{\mathrm{CO2}} + N_R)RT}{P} = \frac{N_0 RT}{P} \tag{3.2}$$

where

$$N_0 = N_{\mathrm{CO2}} + N_R = xN_0 + (1 - x)N_0 \tag{3.3}$$

where x accounts for the proportion of 400 parts per million, that is $x = 400/10^6 = 4 \cdot 10^{-4}$. In summary, the volume V_0 represents the volume of air that contains 1 ton of $\mathrm{CO_2}$ at a concentration of 400 ppm. Thus, the volume occupied by 1 ton of $\mathrm{CO_2}$ after being separated from air (system 1) is

$$V_{\mathrm{CO2}} = \frac{N_{\mathrm{CO2}} RT}{P} = 5.56 \cdot 10^2 \ \mathrm{m^3} \tag{3.4}$$

and the volume occupied by the components of system Air0 (system 2) is

$$V_R = \frac{N_R RT}{P} = 1.39 \cdot 10^6 \ \mathrm{m^3} \tag{3.5}$$

Values of N_{CO2}, N_R and N_0 are collected in Table 3.1.

The internal energy of a system, U, in thermodynamic equilibrium is a function of the extensive parameters, those whose value depends on the amount of matter or the size of the system, such as entropy, S, volume, and the number of moles, N [116] (for a single component system)

$$U = U(S, V, N) \tag{3.6}$$

a small change, dU, in this internal energy is given by

$$dU = \left(\frac{\delta U}{\delta S}\right)_{V,N} dS + \left(\frac{\delta U}{\delta V}\right)_{S,N} dV + \left(\frac{\delta U}{\delta N}\right)_{S,V} dN = TdS - PdV + \mu dN \tag{3.7}$$

where the partial derivatives define the intensive parameters temperature, T, pressure, P, and chemical potential, μ

$$T = \left(\frac{\delta U}{\delta S}\right)_{V,N} \tag{3.8}$$

$$-P = \left(\frac{\delta U}{\delta V}\right)_{S,N} \tag{3.9}$$

$$\mu = \left(\frac{\delta U}{\delta N}\right)_{S,V} \tag{3.10}$$

The internal energy is also a homogeneous function of first order of its extensive parameters, meaning that if all the extensive parameters are scaled by a factor λ, the energy of the system U will scale by the same factor as in Eq. (3.11) [115]

$$U(\lambda S, \lambda V, \lambda N) = \lambda U(S, V, N) \tag{3.11}$$

Following the properties of first-degree homogeneous functions, U then can also be written as

$$U(S, V, N) = TS - PV + \mu N \tag{3.12}$$

which is known as the Euler relation.

To calculate the work necessary for the CO_2 separation, we state first energy conservation so that

$$W = \Delta U_S + \Delta U_{\mathrm{RV}} \tag{3.13}$$

where U_S is the energy of the system under study and U_{RV} is the energy of the reservoir. Since a thermal and pressure reservoir, by definition, can only exchange entropy and volume with the system it interacts with, we have, from Eq. (3.12)

$$\Delta U_{\mathrm{RV}} = T\Delta S_{\mathrm{RV}} - P\Delta V_{\mathrm{RV}} \tag{3.14}$$

so that the work applied (3.12) can be rewritten as

$$W = \Delta U_S + T\Delta S_{\mathrm{RV}} - P\Delta V_{\mathrm{RV}} \tag{3.15}$$

For the interchange process assumed reversible (since these are the processes leading to minimum work) we have that any change in entropy experienced by the system must balance the change in entropy in the reservoir

$$\Delta S_{\mathrm{RV}} = -\Delta S_S \tag{3.16}$$

and since also any change in the volume of the system must be balanced by the same change in the reservoir, we also have

$$\Delta V_{\mathrm{RV}} = -\Delta V_S \tag{3.17}$$

in this way, Eq. (3.15) can be rewritten in terms of the changes in entropy and volume that the system undergoes.

$$W = \Delta U_S - T\Delta S_S + P\Delta V_S \tag{3.18}$$

The energy of ideal gases depends solely on temperature and the number of particles [115] so that, for example, for a diatomic gases we would have

$$\Delta U_S = \frac{5}{2}N_{\mathrm{CO2}}RT + \frac{5}{2}N_R RT - \frac{5}{2}(N_{\mathrm{CO2}} + N_R)RT = 0 \tag{3.19}$$

where the first two terms correspond to the energy of system 1 and system 2 and the third term corresponds to the energy of system 0. As a result, there is no change in energy in the system when transitioning from the initial state to the final state so that the work can be written as

$$W = -T\Delta S_S + P\Delta V_S = -T\Delta S_S \tag{3.20}$$

since $\Delta V_S = V_{\mathrm{CO2}} + V_R - V_0 = 0$ as proven by Eqs. (3.2), (3.4) and (3.5). That is, under these operating conditions, the external work required to separate the CO_2 from the other components of the air corresponds to the heat that the system transfers to the reservoir [115] associated to the entropy transfer ΔS_S. In order to calculate this entropy change, we need to resort to the Gibbs theorem which is explained below.

3.1.1 Gibb's theorem

The entropy, S_i, of a single component ideal gas consisting of N_i mols of component i occupying a volume V_i at temperature T is given by [115]:

$$S_i = N_i\left(\frac{S_i^0}{N^0}\right) + N_i\int_{T^0}^{T}\frac{c_{v,i}(T')}{T'}dT' + N_iR\ \ln\left(\frac{V_i}{V^0}\frac{N^0}{N_i}\right) \tag{3.21}$$

where N^0, V^0 and T^0 are some values for the number of moles, volume and temperature that we set as reference (therefore, when later on we introduce more components in the gas, these values will remain the same). S_i^0 is the entropy of a gas made of the component i at these reference values. $c_{v,i}$ is the specific heat of the gas at constant volume, that depends only on the temperature because we are considering ideal gases. Since, unless stated otherwise, we will be dealing with processes at constant temperature, we can choose this working temperature as our temperature of reference $(T = T^0)$ for which S_i^0 must also correspond to so that Eq. (3.21) simplifies to

$$S_i = N_i\left(\frac{S_i^0}{N^0}\right) + N_iR\ \ln\left(\frac{V_i}{V^0}\frac{N^0}{N_i}\right) \tag{3.22}$$

Gibbs theorem states that for a multi-component ideal gas, its entropy, S, equals the sum of the entropy of its individual components as given as if all the components would have the same volume $V_i = V$, corresponding this volume to the actual volume the multicomponent ideal gas occupies [115,117] so that

$$S = \sum_i S_i = \sum_i N_i\left(\frac{S_i^0}{N^0}\right) + \sum_i N_iR\ \ln\left(\frac{V}{V^0}\frac{N^0}{N_i}\right) \tag{3.23}$$

However, in our study, the separated gases do not occupy the same volume once they are separated, as $V_R \neq V_{\mathrm{CO2}} \neq V_0$. Instead, when the gases are separated, they maintain the same pressure as when mixed. To reflect this condition in the entropy of the ideal multicomponent gas, S, it is sufficient to replace V by $\frac{NRT}{P}$ in Eq. (3.23)

$$S = \sum_i S_i = \sum_i N_i\left(\frac{S_i^0}{N^0}\right) + \sum_i N_iR\ \ln\left(\frac{N^0RT}{PV^0}\right) - \sum_i N_iR\ln\left(\frac{N_i}{N}\right) \tag{3.24}$$

where N is the total mol of the mixture. Since also $\frac{RT}{P} = \frac{V_i}{N_i}$, comparing with Eq. (3.23), Eq. (3.24) demonstrates that the entropy of a mixture of ideal gases is equal to the sum of entropies that the individual gases would have if each were at the same temperature and pressure as the mixture, plus a correction term. This correction term is called the entropy of mixing and is given by

$$\Delta S_{\mathrm{mixing}} = -R\sum_i N_i\ln\left(\frac{N_i}{N}\right) \tag{3.25}$$

Therefore, we can specify the change in entropy that the system undergoes associated with the separation of CO_2 from the rest of the air components as:

$$\Delta S_S = S_{\mathrm{fi}} - S_{\mathrm{in}} = -R\sum_i N_i\ln\left(\frac{N}{N_i}\right) = -N_{\mathrm{CO2}}R\ln\left(\frac{N_0}{N_{\mathrm{CO2}}}\right) - N_RR\ln\left(\frac{N_0}{N_R}\right) \tag{3.26}$$

where N_0 accounts for the total mol of the system in the initial state ($N_0 = N_{\mathrm{CO2}} + N_R$). According to the expressions above, we have used that the entropies at the final and initial states, S_{fi} and S_{in} respectively are given by

$$S_{\text{fi}} = \sum_i N_i \left(\frac{S_i^0}{N^0}\right) + \sum_i N_i R \ \ln\left(\frac{N^0 RT}{PV^0}\right) \tag{3.27}$$

and

$$S_{\text{in}} = \sum_i N_i \left(\frac{S_i^0}{N^0}\right) + \sum_i N_i R \ \ln\left(\frac{N^0 RT}{PV^0}\right) - \sum_i N_i R \ln\left(\frac{N_i}{N}\right) \tag{3.28}$$

Once the expression of ΔS_S is known, the work involved in the separation of 1 ton of CO_2 from the rest of the air components can be determined by multiplying Eq. (3.26) by temperature, as stated in Eq. (3.20).

3.1.2 Calculation of the work

Considering that the molecular weight of CO_2 is $44.01\ \text{g} \cdot \text{mol}^{-1}$ [118], it is calculated that 1 ton of pure CO_2 contains $N_{\text{CO2}} = 22{,}722$ mol. The number of mol of the rest of the air components considered in these calculations is detailed in Table 3.1. The presence of other gases in the air such as Ar are considered incorporated into the concentration of N_2 for simplicity, without changing the result since they are still considered ideal gases.

It is important to note that, since $N_0 \gg N_{\text{CO2}}$ and $N_0 > N_R$ as seen in Table 3.1, the entropy change associated with the separation of CO_2 from the air, calculated with Eq. (3.25), is negative. As confirmed by Eq. (3.20), a decrease in entropy (ΔS_S) of the system indicates that work must be applied on the system.

Table 3.1 Number of mol N_{N2}, N_{O2} , N_{CO2}, whose sum results in the composition of system 0 (N_0), while the sum of the first two defines the composition of system 2 (N_R)

Number of mol	
CO_2, N_{CO2}	$2.27 \cdot 10^4$
O_2, N_{O2}	$1.19 \cdot 10^7$
N_2, N_{N2}	$4.49 \cdot 10^7$
System 0, $N_0 = N_{\text{N2}} + N_{\text{O2}} + N_{\text{CO2}}$	$5.68 \cdot 10^7$
Air0, $N_R = N_{\text{N2}} + N_{\text{O2}}$	$\sim 5.68 \cdot 10^7$

This answers one of the questions posed at the beginning of the chapter: the process of separating CO_2 from air at constant P and T requires the application of work on the initial system (system 0). However, although work is applied to the system, the total internal energy remains constant ($\Delta U_S = 0$), and this work is released as heat ($-T\Delta S_S$) to the surrounding environment that acts as reservoir. Eq. (3.26) reveals that the work to be applied depends solely on the amount of CO_2 and air to be separated (N_{CO2} y N_R). Considering the values from Table 3.1, at a constant pressure of 101,325 Pa and a temperature of 298.15 K, a minimum work of $-T\Delta S_S = W = 4.97 \cdot 10^8$ J is required to extract one ton of CO_2 from air.

Having established this thermodynamic minimum, it is illustrative to contextualize this energy consumption by comparing it with practical values reported in the literature for CO_2 separation methods operating under constant P and T. Comparing it with other DAC methods that involve variations in temperature or pressure would be inappropriate, as these processes do not occur under the same conditions. In this context, a DAC system operating under constant P and T conditions is the one studied by Wang et al. [119], which is based on electrochemical processes.

The process starts with an aqueous solution of K_2SO_4 (chamber 1) sandwiched by two selective membranes, one cation exchange membrane, such as Naffion 551, allowing K^+ ions passing through towards chamber 3, and an anion exchange membrane, such as AMI-7001, allowing SO_4^{-2} ions to pass through chamber 2, where the anode is located. At this anode, 2 water molecules are oxidized releasing 4 protons to the aqueous solution, one oxygen molecule to the air and 4 electrons to the electric circuit:

$$2H_2O \rightarrow 4H^+ + O_2 + 4e^- \qquad \text{(R.4)}$$

The SO_4^{-2} and H^+ ions diffuse then from chamber 2 to chamber 4. The solar generator raises the energy of the electrons released at the anode and pumps them to the cathode located in chamber 3. At this cathode, these electrons reduce H_2O to produce hydrogen and OH^- ions:

$$4H_2O + 4e^- \rightarrow 4\,OH^- + 2H_2 \qquad \text{(R.5)}$$

The OH^- and K^+ ions from chamber 1 combine with CO_2 to produce K_2CO_3 or $KHCO_3$.

$$2CO_2 + 2K^+ + 2\,OH^- \rightarrow 2KHCO_3 \qquad \text{(R.6)}$$

$$CO_2 + 2K^+ + 2\,OH^- \rightarrow K_2CO_3 + H_2O \qquad \text{(R.7)}$$

K_2CO_3 and $KHCO_3$ diffuse towards chamber 4 where they encounter H^+ and SO_4^{-2} ions that diffused from chamber 2 and the following reactions, releasing CO_2, takes place:

$$K_2CO_3 + 2H^+ + SO_4^{-2} \rightarrow CO_2 + H_2O + K_2SO_4 \qquad \text{(R. 8)}$$

$$2KHCO_3 + 2H^+ + SO_4^{-2} \rightarrow 2CO_2 + 2H_2O + K_2SO_4 \qquad \text{(R. 9)}$$

The resulting K_2SO_4 can be then recycled into chamber 1. According to their analysis, this method consumes 383 kJ per mol of captured CO_2. Considering N_{CO2}, this translates to a required energy of $W = 870.5 \cdot 10^4\ \mathrm{kJ \cdot ton^{-1}}$, representing an energy consumption 17 times higher than the thermodynamic minimum calculated before.

The discrepancy between the energy consumption estimated in our analysis and that reported in Wang method lies in the fact that our thermodynamic analysis is based on an ideal theoretical limit, which does not account for the losses inherent to practical operations or the deviations from ideality characteristic of real systems [120,121]. These deviations include factors such as the limited energy efficiency of equipment, design constraints in process engineering, and the unavoidable irreversibilities in their operation [122]. In experimental methods like the one described by Wang et al., these additional practical contributions are always present, which explains why experimentally observed values are higher compared to ideal theoretical calculations.

In summary, DAC is a process that, under constant P and T, requires work to be applied to the system. To capture one ton of CO_2 from air at 298.15 K and 101,325 Pa, a minimum work of $4.97 \cdot 10^8\ \mathrm{J \cdot ton^{-1}}$ is required.

The discussion that follows focuses on whether DAC always requires an external input of work or if, under conditions different from those considered in the previous thermodynamic analysis, it could be carried out through a process not requiring the application of work. In this context, we review first an ideal gas separation process, which can be used also to prove the Gibbs theorem above, that does not require the application of work and discuss whether it is of practical applicability to the separation of CO_2 from air. In another section we will discuss another process known as the Gibbs paradox.

3.2 Zero entropy process gas separation

The minimum work calculated in the previous section assumed that the CO_2 extraction process was carried out at constant pressure and temperature which, in other words, implied that the final pressure and temperature of the extracted CO_2 were the same as the atmospheric ones. Application of some work was needed then to account for the decrease in entropy. It is possible, however, to conceive gas separation processes in which the entropy does not increase along the process, what implies that the separation process could be achieved without the application of any work. In the next paragraphs we describe one of these processes, which was in fact imagined by Gibbs, to prove his theorem used in the previous section. The question which will be answered later is whether this process is of practical applicability.

In the following argument, we will use the description provided by Callen in his book *Thermodynamics and an introduction to thermostatistics* [115] with slight modifications to adapt it to our case. A cylinder (Figure 3.2) with a total volume of $2V_0$ is divided into four chambers (denoted as α, β, γ, δ) by a fixed central wall and two movable walls. The two movable walls are coupled together in such a way that the distance between them is always half the length of the cylinder ($V_\alpha = V_\gamma$ and $V_\beta = V_\delta$). In the initial state (Figure 3.2a), one of the movable walls coincides with the left end of the cylinder, and the other coincides with the central wall, so that $V_\alpha = V_\gamma = 0$. The β chamber, with volume V_0, is filled with a mixture of N_A mol of an ideal gas A and N_B mol of an ideal gas B (in our case A could be CO_2 and B what we have designated as air0, that is the rest of the components of air without CO_2). In the δ chamber, vacuum is created, and its volume is V_0. The entire system is kept at temperature T. The left movable wall is permeable to gas A but not to gas B, while the fixed wall is permeable to gas B but not to gas A. The right movable wall is impermeable to both gases.

Next, the coupled movable walls slide quasi-statically to the right (Figure 3.2b) until the final state is reached, where $V_\beta = V_\delta = 0$ y $V_\alpha = V_\gamma = V_0$ (Figure 3.2c). The α chamber contains now only pure gas A, and the γ chamber contains only pure gas B. In this way, the initial mixture, with volume V_0, is separated into its pure components, A and B, each occupying a volume of V_0.

As mentioned earlier in subsection 3.1, the energy of an ideal gas depends solely on its temperature and the number of mol present in the system, which remain constant between the initial and final state of the system. Thus, the energy of the system stays the same throughout the experiment. According to Eq. (3.20), since there is no change in energy, the work done in moving the coupled walls is equal to $-T\Delta S_S$.

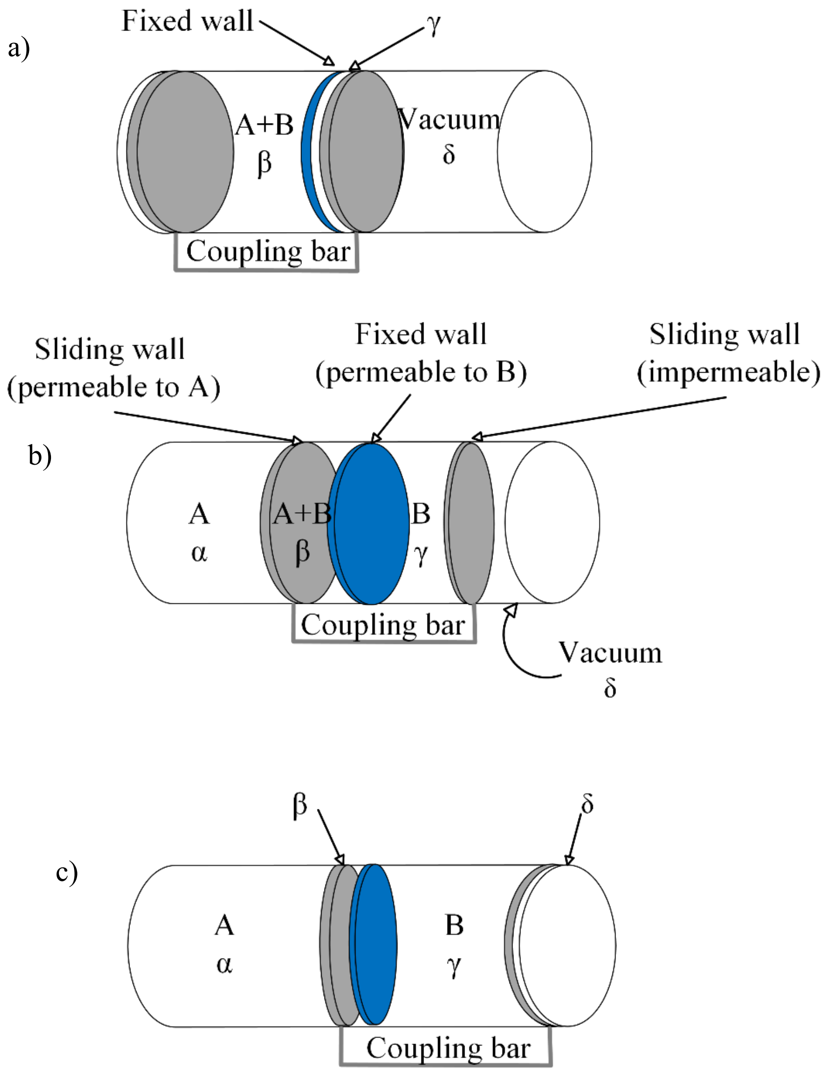

Figure 3.2 Separation of a mixture of ideal gases, demonstrating Gibbs theorem.

If $P_{A,\alpha}$ is the pressure in chamber α due to the presence of component A (the only one existing in this chamber), $P_{B,\beta}$ is the pressure in chamber γ due to the presence of component B (the only one existing in this chamber) and $P_{A+B,\beta}$ is the pressure in chamber β (in which both components A and B are present), the net force, *F*, acting on the movable walls per unit of area as they move is given by

$$F = P_{A,\alpha} - P_{A+B,\beta} + P_{B,\gamma} \tag{3.29}$$

where $P_{A,\alpha} - P_{A+B,\beta}$ is the net force per unit of area at the left movable wall and $P_{B,\gamma}$ is the net force per unit of area at the right wall. The two net forces add because they are attached to each other by the coupling bar. Notice also that the net force at the right wall is only $P_{B,\gamma}$ because there is vacuum at the other side of the wall. The total pressure $P_{A+B,\beta}$ can be decomposed, by definition of the concept of partial pressure, as the sum of the partial pressures of the components involved

$$P_{A+B,\beta} = P_{A,\beta} + P_{B,\beta} \tag{3.30}$$

Therefore, Eq. (3.29) can be written as

$$F = P_{A,\alpha} - P_{A,\beta} - P_{B,\beta} + P_{B,\gamma} \tag{3.31}$$

For an ideal gas, the chemical potential of component *i* in the gas is expressed as

$$\mu_i = \mu_i^0(T^0) + RT_R \ln\left(\frac{P_i}{P^0}\right) \tag{3.32}$$

where μ_i^0 is its standard chemical potential at a pressure of reference P^0 and temperature of reference T^0 and P_i is its partial pressure. We will assume the same temperature and pressure of reference for all components. Since the left wall is permeable only to component A and the left wall is permeable only to component B, in equilibrium, the following equalities between chemical potentials must hold

$$\mu_{A,\alpha} = \mu_{A,\beta} \tag{3.33}$$

$$\mu_{B,\gamma} = \mu_{B,\beta} \tag{3.34}$$

Substituting (3.32) in these equalities, we obtain that

$$P_{A,\alpha} = P_{A,\beta} \tag{3.35}$$

$$P_{B,\beta} = P_{B,\gamma} \tag{3.36}$$

from which, substituting in (3.31), results in $F = 0$. Hence, the work used to separate the gases is also zero and, consequently, no change in entropy accompanies the process. The entropy of the original mixture of A and B, in a common volume V_0, is precisely equal to the entropy of pure A and pure B, each in a separate volume V_0. This is Gibbs' theorem. This proof of Gibbs' theorem demonstrates that the separation of gases composing a mixture can occur without any change in entropy and without accompanying work.

The results of the experiment used to illustrate the Gibbs theorem and the gas separation analyzed in section 3.1 present significant differences due to several reasons. The first reason lies in the operating conditions of the two gas separation processes, particularly the initial vacuum applied in chamber γ for the experiment described in this section- a condition not considered in section 3.1. The second reason concerns the experimental design itself. While both experiments share the same objective, their approaches and configurations differ. For instance, the experiment in this section employs membranes that are selectively permeable to only one type of gas, a factor not accounted for in section 3.1.

The experiment used in this subsection is correct in the sense that no change in entropy or energy is observed between the initial and final states of the gas system. Therefore, the separation process of gases A and B does not require the application of work on the system, nor does it generate usable work. However, the fact that the system includes a vacuum chamber implies that energy was required to create it. It is important to highlight that the work necessary to create this vacuum has not been considered in the application of the Gibbs theorem.

3.3 The Gibbs paradox

The Gibbs paradox refers to the following. As internal energy, entropy is also accepted to be a first order homogeneous function of its extensive variables so that for a single component system we have that

$$S(\lambda U, \lambda V, \lambda N) = \lambda S(U, V, N) \tag{3.37}$$

Hence, if we, for example, simply split the system into two identical subsystems so that

$$\lambda = 1 = \frac{1}{2} + \frac{1}{2} \tag{3.38}$$

then Eq. (3.37) can also be written as

$$S(U,V,N) = \left(\frac{1}{2}+\frac{1}{2}\right)S(U,V,N) = S\left(\frac{1}{2}U,\frac{1}{2}V,\frac{1}{2}N\right) + S\left(\frac{1}{2}U,\frac{1}{2}V,\frac{1}{2}N\right) \tag{3.39}$$

Physically this implies that, in the particular case in which we mix two gases consisting of the same indistinguishable components initially separated by an impermeable wall (Figure 3.3), the entropy of mixing disappears. Therefore, the concept of entropy of mixing must be also related to the distinguishability or not of the particles of the gas to the observer.

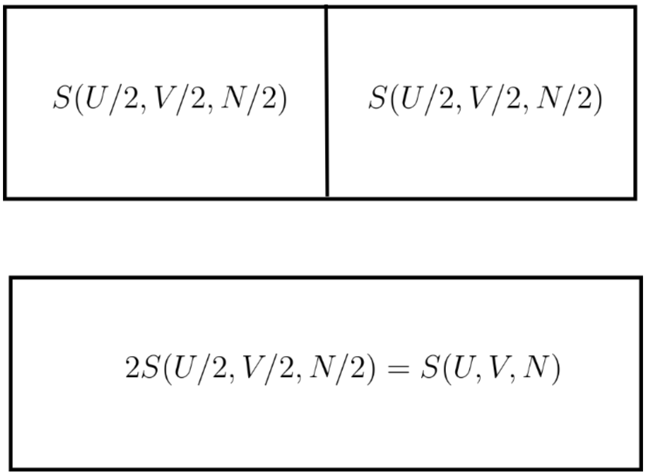

Figure 3.3 Illustration of how the mixing of two gases consisting of the same type of identical particles (top figure) leads to no entropy of mixing because of the first order homogeneity of the entropy function.

The solution to the Gibbs paradox is still a topic of debate. For example, in *Thermodynamics: Foundations and Applications* [123], is discussed how the paradox is solved by questioning in the first place the validity of the homogeneity of the entropy function when the number of particles involved is small. In this respect, when the number of particles is small, even if the particles are identical, the observer could still be able to distinguish them by their position, something that would become increasingly difficult as the number of particles increases.

Either way, this example suggests that the problem associated with the Gibbs paradox only emerges when the particles are indistinguishable, which is not the case for the CO_2 separation problem, and/or when the number of particles involved is small, which is not our case either.

The importance of sections 3.1 and 3.2 lies in emphasizing that the energy involved in the gas separation process, whether it is CO_2 from air or any other mixture, critically depends on the conditions under which the separation takes place. This means that the results obtained in sections 3.1 and 3.2 are not universally applicable, as they are conditioned by specific values of pressure and temperature and a given setup. Any modification of these conditions can significantly alter the energy required for the process, highlighting the importance of contextualizing the results within a concrete thermodynamic framework. In this section, it has been shown that the capacity to distinguish gases also plays a significant role in gas separation processes. Therefore, both the external conditions of the system and the ability of the observer are essential factors that determine not only the energy associated with gas separation but also how this energy is understood and quantified. This approach underscores the inherent complexity of separation processes and the need to interpret the results within a well-defined theoretical and experimental framework.

3.4 Economy of direct air capture

The study of the thermodynamics involved in the gas separation process, and specifically in the separation of CO_2 from air, is important for understanding the physical foundations and quantifying the magnitude of the energy challenge we face. This analysis allowed us in the previous sections to determine the theoretical limits of the work required for such separation, identify the factors that affect efficiency, and assess feasibility from a fundamental perspective. However, this thermodynamic approach alone is not sufficient, as these separation processes must be translated into real technologies that can be implemented at an industrial scale.

In the industrial sector, gas separation processes such as CO_2 capture not only have technical implications but also economic ones. Each unit of energy consumed by a separation system carries an associated cost that directly impacts the economic viability of the process [124,125]. In certain scenarios, these technologies could generate economic benefits, either through energy recovery or the valorization of the products obtained [126,127]. Therefore, complementing the thermodynamic analysis with an economic assessment enables the evaluation of both the technical feasibility and economic sustainability of the proposed technologies.

Conducting an economic analysis allows for identifying which separation processes have the potential to be profitable and scalable, particularly in direct CO_2 capture from the air, where energy costs are high due to the low atmospheric concentration of this gas. This approach also helps to prioritize research and development investments, optimize technological designs, and develop strategies to reduce operational and energy costs over time. Only through this integration of thermodynamics and economics will it be possible to effectively address the CO_2 capture challenge and move towards technological solutions that are both technically and economically viable.

From an economic perspective, assuming a levelized cost of electricity (LCOE) of $35\ € \cdot \mathrm{MWh}^{-1}$ for PV sources [128] and an energy consumption of $4.97 \cdot 10^{8}\ \mathrm{J} \cdot \mathrm{ton}^{-1}$ (or $0.138\ \mathrm{MWh} \cdot \mathrm{ton}^{-1}$) as calculated in 3.1.2, the minimum estimated cost of CO_2 capture is approximately $5\ € \cdot \mathrm{t}^{-1}$, obtained by multiplying the energy cost by the consumption. This calculation considers only the minimum energy requirement established by thermodynamic laws, without accounting for inefficiencies or losses associated with practical operations. Nevertheless, this result allows us to conclude that, from a purely thermodynamic standpoint, direct air capture does not introduce an inherently prohibitive energy cost. To put this energy consumption into context, in 2007 the average energy consumption of gold mines was $52\ \mathrm{MWh}$ per kilogram of gold [129], while the average energy consumption for one kilogram of platinum is approximately $37\ \mathrm{MWh}$ [130]. This fact emphasizes that the main economic or technical barriers to implementing large-scale DAC do not arise from thermodynamic limitations, but rather from the operational, technological, and efficiency challenges faced by real-world systems.

A Sherwood diagram is a tool primarily used in chemical and environmental engineering to analyze the economic feasibility of separation or capture processes of compounds, including gases [131]. This type of diagram graphically represents the economic cost of separating or extracting a chemical compound as a function of its relative concentration in a system [132]. This type of diagram shows how the economic costs associated with separation increase drastically as the concentration of the compound to be separated decreases, highlighting the inherent difficulty of extracting components from diluted mixtures [132]. The Sherwood diagram not only illustrates the relationship between economic viability and concentration, but it is also a useful tool for comparing different separation technologies applied to the same substance from mixtures with the same composition. For example, it allows for the analysis and comparison of DAC methods used to separate CO_2 from the air, highlighting their differences in terms of efficiency and costs.

Figure 3.4 shows a Sherwood diagram that includes a line based on data reported by Grübler A. in *Technology and Global Change* (Cambridge Univ Press, Cambridge, UK, 1998). A line in the form $PD = A/C$ can be plotted for each set of separated materials, where PD represents the price (in dollars per kilogram), C is the initial concentration of the input stream (i.e., the mass of the product per mass of the mixture), and A is a separation constant with units of dollars per kilogram of the initial mixture. Dahmus and Gutowski note that A is approximately $1\ \$ \cdot \mathrm{kg}^{-1}$of the initial mixture for separating organics, around $0.01\,\$ \cdot \mathrm{kg}^{-1}$ for separating metals, and about $0.001\,\$ \cdot \mathrm{kg}^{-1}$for separating pollutants from mixed gas streams. Using the estimated separation constant for pollutants in mixed gas streams ($A = 0.001\,\$ \cdot \mathrm{kg}^{-1}$), we can estimate the cost per unit of CO_2 to separate CO_2 from various mixed streams [132]. This is the line that has been represented in the plot.

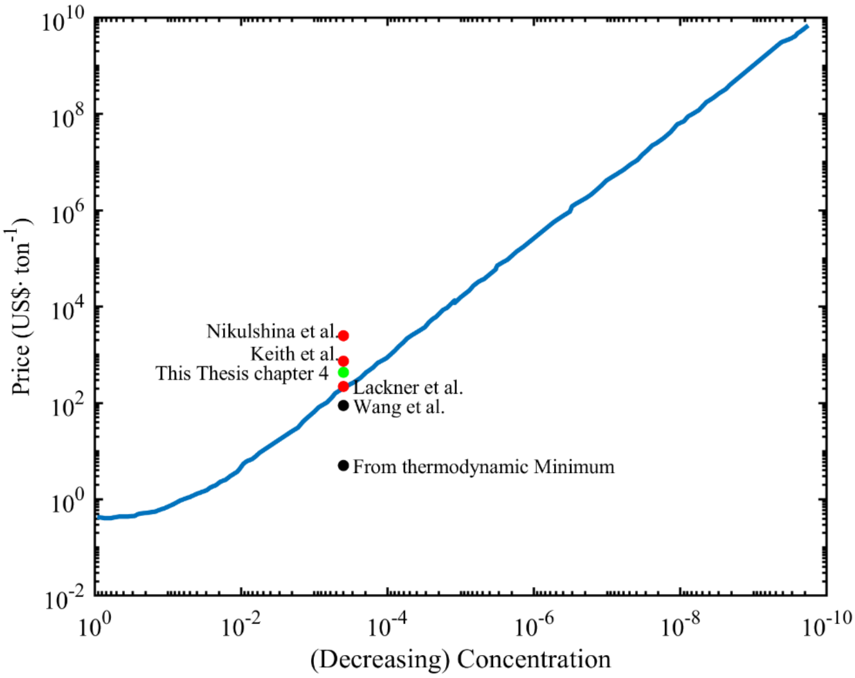

Figure 3.4 A Sherwood plot illustrates the relationship between the concentration of CO_2 in a feed stream of air and the cost of removing 1 ton of CO_2 from it. The blue line (PD) represents the theoretical cost for separating pollutants from mixed gas streams, while the red dots indicate the reported costs of real DAC technologies from literature. The black dots correspond to the cost using the method reported by Wang et al. and the thermodynamic analysis presented in subsection 3.1. The green dot represents the energy cost of the DAC method based on IPDA, as detailed in chapter 4 of this Thesis, excluding CAPEX and OPEX expenses.

This line (PD) is merely an estimate of the cost for gases in a mixed gas stream as a function of their concentration. It does not necessarily reflect the actual costs of real gas separation processes such as DAC. The red dots in Figure 3.4 represent the cost per ton of CO_2 captured using technologies reported in the literature. Specifically, the method proposed by Nikulshina et al. incurs a cost of $2{,}485\,\$ \cdot \mathrm{ton}^{-1}$, Keith et al. method results in a cost of $736\,\$ \cdot \mathrm{ton}^{-1}$, and the approach reported by Lackner et al. involves a cost of $220\,\$ \cdot \mathrm{ton}^{-1}$. All three methods involve a higher cost per ton of CO_2 captured compared to the line based on Grübler A. data, particularly the methods by Nikulshina et al. [133] and Keith et al [134]. In contrast, the method proposed by Lackner et al [135]. incurs a cost similar to what is predicted by the line that represents PD.

Figure 3.4 also presents the cost in dollars per ton of CO_2 captured through the method detailed in subsection 3.1 and the method reported by Wang, which are the black dots. To convert the energy consumption of each method into an economic cost [9], the LCOE for solar photovoltaic energy was used [128]. Considering the energy consumption for separating 1 ton of CO_2, the process detailed in subsection 3.1 would lead to a cost of $5.4\,\$ \cdot \mathrm{ton}^{-1}$, whereas the method proposed by Wang et al. would incur an approximate cost of $89\,\$ \cdot \mathrm{ton}^{-1}$, which is about 17 times higher. This significant increase in cost stems solely from higher energy consumption, as in both cases, the economic cost is assumed to be directly proportional to the energy cost. As shown in Figure 3.4, the cost of these two methods is significantly lower than both the P line and the costs reported by the methods in the literature. There are two common reasons to explain this. First, both our analysis and that of Wang et al. consider only the inherent energy consumption for CO_2 separation. In real systems, however, the energy consumption is typically higher because the total energy required for the entire process is taken into account, not just the energy specific to the separation stage. For instance, essential processes such as CO_2 compression or air pumping, which are critical in practical applications, are excluded from these calculations and would significantly increase both the overall energy demand and economic cost. Second, neither method accounts for the CAPEX associated with the initial investment or equipment, as is done in the methods reported in the literature.

Furthermore, the method reported by Wang et al. was developed at a laboratory scale. Scaling it up to an industrial system capable of capturing tons of CO_2 would require additional components and systems that are not considered in laboratory-scale experiments, leading to significantly higher costs. Similarly, the result from the analysis in subsection 3.1 is based on an idealized system, does not correspond to any specific technology, and overlooks inefficiencies or losses associated with real-world operation.

3.5 Summary

The minimum thermodynamic energy cost for extracting one ton of CO_2 from the air, with a concentration of 400 ppm, under standard conditions is $4.97 \cdot 10^8$ J. Assuming the electricity cost of $35\,€ \cdot \mathrm{MWh}^{-1}$, this results in a cost of $5\,€ \cdot \mathrm{ton}^{-1}$ or $5.4\,\$ \cdot \mathrm{ton}^{-1}$. From a purely thermodynamic standpoint, direct air capture does not introduce an inherently prohibitive energy cost.

Considering the atmosphere as an ideal gas, this energy cost is not associated with a change in the energy of the system, as the final energy of the gases involved remains equal to the initial energy. Instead, it corresponds to the work required to compensate for the entropy decrease associated with gas separation (mixing entropy).

However, there are models in which gas separation occurs without a decrease in entropy. One such model is the one used in thermodynamics to demonstrate Gibbs' theorem. However, this model is not practically applicable to the case of CO_2 separation from the atmosphere, as it requires prior system preparation, where one of the chambers used must initially be in a vacuum.

The mixing entropy would also vanish if CO_2 were indistinguishable from the other air molecules, leading to the so-called Gibbs paradox, which remains apparently unresolved in thermodynamics. However, this is not applicable to our case, as CO_2 is distinguishable from the other gas molecules, and the number of molecules involved is very large.

While the cost of $5.4\,\$ \cdot \mathrm{ton}^{-1}$ may not seem inherently prohibitive, it is important to note that this result accounts only for the minimum energy involved in the system and excludes inefficiencies and the technological implementation costs. The findings reported in the literature indicate that currently established technologies in the market have significantly higher costs than calculated. According to the literature, these costs range from \$220 to \$2,475 per ton of CO_2. Thus, the current challenge lies in developing techniques with energy consumption as close as possible to the theoretical minimum, while ensuring costs are low enough to enable the adoption and widespread implementation of DAC technologies in the market.

Chapter 4. Direct air capture system with IPDA and its thermodynamic analysis

Amines, like other chemical compounds, are used as sorbents in DAC systems due to the relative simplicity of their operation, which—as described in Chapter 1—is based on heating–cooling cycles. Given the wide variety of available amines, research aimed at identifying those that can optimize the capture process is gaining momentum.

In Chapter 1 we also hinted the experiments led by the group of Kikkawa et al. from the Department of Chemistry at the Graduate School of Science, Tokyo Metropolitan University. In these experiments they proposed a hypothesis suggesting that when amines used for CO_2 capture form an insoluble reaction product, the separation of CO_2 is facilitated, improving the overall process efficiency [57]. To test this hypothesis, the study investigated various amine compounds and compared their performance with a conventional amine absorption system using ethanolamine—typically employed under high CO_2 concentration conditions—and an aqueous KOH solution. The study by Kikkawa et al. evaluated CO_2 removal efficiency (η_{cap}) in a system where a low CO_2 concentration gas stream was introduced. It was found that diamine, organic molecules containing two amine groups, exhibited a high η_{cap} as CO_2 absorbents [57]. Among the tested diamines, isophorone diamine (IPDA; 3-(aminomethyl)-3,5,5-trimethylcyclohexylamine), presented in Figure 4.1, demonstrated the highest capture efficiency. The experiments were conducted using N_2 streams with varying CO_2 concentrations, ranging from 400 ppm (0.04% by volume) to 30% by volume. As a result of the reaction, a carbamic acid (CA1) was formed, which precipitated due to its insolubility in IPDA. The reaction took place at 298 K. This liquid-solid phase separation phenomenon for CO_2 removal was observed in various solvents, including H_2O and dimethyl sulfoxide (DMSO) [57].

Once CO_2 is captured from the air, the question arises: what should be done about it? In industry, this approach falls under the concept of CCUS, meaning that the captured CO_2 can either be utilized or stored [137,138].

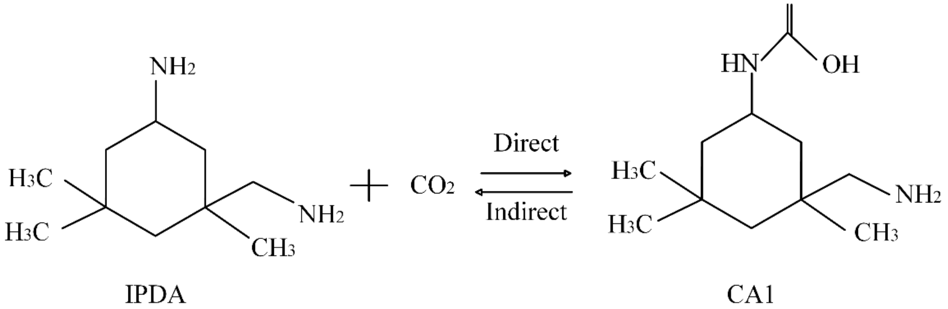

Figure 4.1 Reaction of IPDA and CO_2 to form CA1, which dissociates into IPDA and CO_2 when heated above 303 K. The carbon atom of CO_2 bonds with the most accessible nitrogen atom of IPDA, thereby capturing the CO_2.

In the case of solar fuel production, the goal of DAC is the subsequent use of the captured CO_2. In this regard, industrial methods based on amines rely on increasing temperature to dissociate the DAC product molecule, resulting in a concentrated CO_2 gas stream [139,140]. The method proposed by Kikkawa follows the same principle, as shown in Figure 4.1. However, CA1 begins to release CO_2 at a lower temperature (303 K) than conventional MEA-based systems [57]. Another significant advantage of using IPDA is that it maintains its capture efficiency over at least five cooling-heating cycles, meaning the same amount of IPDA can be reused five times without a decrease in performance. This reference study is the first demonstration of a potential DAC system with a CO_2 removal efficiency exceeding 90% and the ability to be reused. The study reports capture efficiency above 99% for more than 100 hours [57]. For all these reasons, we have decided to experimentally replicate the DAC system presented in the study of Kikkawa et al. Our objective is to reproduce the experiment to achieve a similar capture efficiency, verifying the reported results. However, in our experiment, we aim to determine the capture efficiency for a range of volumetric flow rates that were not considered in the original study. Additionally, we seek to confirm whether CO_2 desorption begins at a temperature close to 303 K. These verifications are necessary because, besides being a recent and novel approach, the nature of the experiment suggests that it may be sensitive to the physical characteristics of the elements used in the process, such as the containers, the depth of the solution, and the air bubbling configuration.

This chapter provides a detailed explanation of the DAC method based on IPDA, which has been implemented in the IES-UPM laboratory and is inspired by the research of Kikkawa et al., as described in subsection 4.1. In subsection 4.2, the DAC process is systematically divided into seven distinct stages, allowing for a thorough thermodynamic analysis of each step. Subsection 4.3 focuses on the experimental procedures used to determine both the capture efficiency of the process and the temperature at which CO_2 desorption occurs. Moving forward, subsection 4.4 presents the thermodynamic analysis of the seven stages, calculating the energy requirements and identifying key factors influencing the overall performance of the system.

4.1 DAC system based on IPDA

The DAC system used in our study, depicted in Figure 4.2, consists of four main components: an air compressor, a volumetric flow controller, a volumetric flow meter, and a reactor containing the IPDA solution in DMSO.

The reactor consists of a glass tube sealed with an airtight stopper that has two perforations, through which two plastic tubes are inserted. One tube is submerged in the IPDA solution, while the other remains above the liquid, avoiding direct contact with the solution as shown in Figure 4.2a. This setup allows air to enter through the submerged tube, ensuring direct interaction between the dissolved CO_2 in the air and the IPDA. Meanwhile, the tube that remains above the liquid enables the release of unreacted gases, primarily N_2, O_2, and residual CO_2.

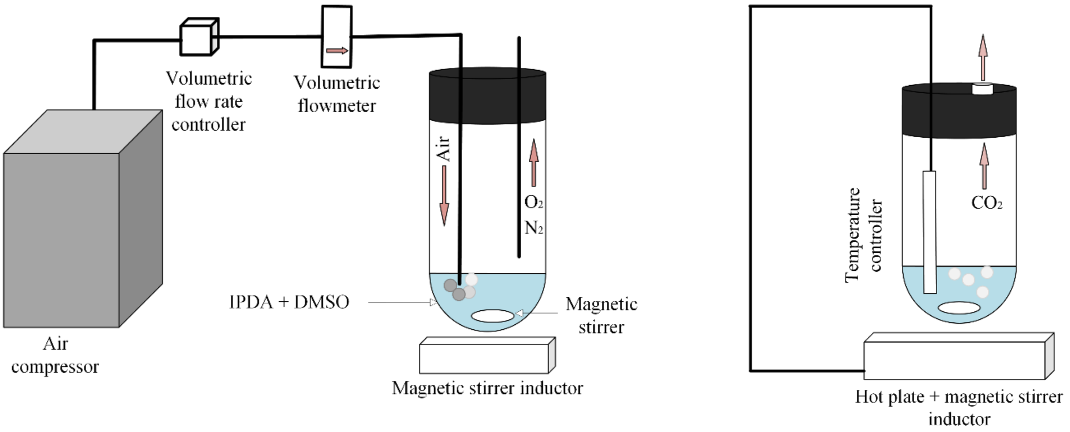

a) b)

Figure 4.2 a) Diagram of the experimental system used in the DAC based on IPDA. The system consists of an air compressor, a flow controller, a flowmeter, and the reactor with isophorondiamine (IPDA) that captures CO_2 to form the corresponding carbamic acid (CA1) b) Diagram of the reactor heating system for desorbing the CO_2 trapped by IPDA. The system includes a hot plate with a temperature controller inserted into the reactor.

First, a precise and known amount of IPDA is introduced using a micropipette. Then, DMSO is added in a 10:1 ratio to serve as the solvent for the reaction. The resulting solution is a transparent, colorless liquid. Additionally, a magnetic stirrer is placed in the reactor to promote the homogeneity of the solution during the reaction.

Next, the two plastic tubes are inserted through the holes in the airtight stopper. This assembly is then placed on an analytical scale, and its weight is recorded. The experiment begins when the air inlet tube is connected to the gas circuit, which consists of the air compressor, the flow rate controller, and the flowmeter. Once the air compressor is turned on, the volumetric flow rate (Ø) of the air is adjusted to the desired value, and the air is bubbled through the solution for the selected duration of the experiment. This duration must be sufficient to ensure that the air bubbling stops once all the IPDA in the solution has reacted or when a significant amount has reacted. As the reaction progresses, the solution, initially transparent and colorless, becomes increasingly turbid and acquires a whitish tone. Over time, a white precipitate (CA1) forms and settles at the bottom of the reactor. This phenomenon allows the air tube to continue bubbling through the IPDA and DMSO solution, as the precipitate does not obstruct the gas circulation in the system. Once the experiment concludes, the reactor is disconnected from the gas circuit and weighed again. The weight difference from the initial measurement (before the reaction) reflects the amount of CO_2 captured by the IPDA.

The second part of the experiment involves heating the reactor after the CO_2 capture reaction has concluded to analyze the desorption process. To implement this phase, the plastic tubes are removed from the system, and a temperature sensor/controller is inserted through one of the holes in the stopper. This sensor is connected to a hot plate, which heats the reactor and regulates the heating temperature (Figure 4.2b). As the reactor heats up, the white solid gradually transforms into a colorless liquid (IPDA), and bubbles appear in the solution, which are assumed to be desorbed CO_2. This confirms that, upon heating, CA1 dissociates into IPDA (a colorless liquid) and CO_2 (a gas that forms bubbles). This part of the experiment determines the temperature at which the dissociation of CA1 into CO_2 and IPDA becomes visibly noticeable, which is useful for estimating the energy consumption required for heating in this DAC method. It is important to note that the experimental setup does not analyze the nature or flow rate of the desorbed gas during this stage. Instead, the onset of desorption is identified through visible changes in the solution, such as bubbling and variations in turbidity. As a result, unlike in the experiment conducted by Kikkawa, this approach does not allow for precise determination of the exact minimum temperature at which the desorption reaction begins.

4.2 Thermodynamic analysis of the DAC system

The objective of this study is to determine, through a thermodynamic analysis, the energy consumption required to capture one ton of CO_2 using the DAC method based on the use of IPDA. Essentially, this objective aligns with the one proposed in the analysis of subsection 3.1 in the previous chapter. However, there are three differences between the two approaches.

The first difference lies in the fact that the analysis presented in subsection 3.1 was general in nature, since it only considered the initial and final states of the system without accounting for intermediate states. In contrast, the analysis developed here, which is detailed in subsection 4.4, includes the results of the thermodynamic analysis of the intermediate stages. This distinction is significant because an analysis limited to the initial and final states does not provide information about the energy transferred during intermediate states, effectively canceling out certain positive and negative energy transfer terms corresponding to these intermediate processes and leaving them unaccounted for. As a result, valuable information related to the total energy involved in the actual DAC process is lost. This difference can lead to a significant discrepancy in the analysis of energy exchanges occurring throughout all the stages of the experiment, as some of these energy transfers may result in losses for the system.

The second difference between both analyses is that the analysis in subsection 3.1 was not linked to any specific DAC method, while the analysis in subsection 4.4 focuses specifically on the method based on the use of IPDA. This difference directly affects the definition of the system in each analysis. In the analysis of subsection 3.1, no detailed definition of the system was provided, whereas in the analysis of subsection 4.4, one is given. Additionally, in the latter analysis, the system changes depending on the stage of the process. This aspect will be addressed in more detail when explaining the stages of the analysis described in subsection 4.4.

The third and final difference between both analyses concerns the operating conditions. In the analysis of subsection 3.1, the process occurred at constant pressure and temperature. In contrast, the DAC process analyzed in subsection 4.4 includes heating and cooling stages, which means the temperature varies throughout the process.

The seven stages of the thermodynamic analysis in which the DAC process based on the use of IPDA has been divided are described below (Figure 4.3). The system and the reservoir vary in each stage of the process, and will be specified in detail in each of them. For clarity, the system is defined as everything that is not labeled as the reservoir (R) in Figure 4.3.

The initial system consists of an IPDA solution in DMSO (A in Figure 4.3) that is in equilibrium with the reservoir, that in our case corresponds to the atmosphere in standard conditions. The system is separated from the reservoir by an impermeable and movable membrane, represented by a black dotted line in Figure 4.3, preventing any exchange of matter between the system and the reservoir. For clarity, the system and the reservoir will be separated by this membrane throughout the seven stages of the process. From now on, any membrane we refer to will not be the one separating the system from the reservoir.

- Stage 1 (Introduction of air with CO_2): Stage 1 involves the introduction of air into the system. Once the air has been introduced, the system consists of this introduced air and the IPDA-DMSO solution, both at the temperature (T_{RV}) and pressure (P_{RV}) of the reservoir. At the end of this stage, the introduced air and the IPDA-DMSO solution are considered separated by an impermeable, immobile adiabatic membrane, represented by a blue dashed line in Figure 4.3.
- Stage 2 (Chemical reaction for CO_2 capture): In Stage 2, the “blue dashed” membrane separating the air from the IPDA solution is removed. This results in the chemical reaction between the CO_2 in the air and the IPDA, leading to the formation of CA1, represented by C in Figure 4.3. It is in this stage that the CO_2 capture process takes place. Once the reaction is complete, the system consists of CA1, CO_2-free air (denoted as air0 from now on, as shown in Figure 4.3), and the original DMSO. All components of the system are at the temperature and pressure of the reservoir, as it is assumed that the chemical reaction has taken place at equilibrium with the temperature and pressure reservoir.
- Stage 3 (Separation of CO_2-free air): This stage involves separating the air0 phase from the CA1 using, for example, an impermeable adiabatic membrane, represented by a dashed black line in Figure 4.3. The system still consists of air0, CA1, and DMSO, all of which are at the temperature and pressure of the reservoir.
- Stage 4 (Heating): This stage involves heating CA1 and DMSO until it reaches the CO_2 desorption temperature, T_{CO2}. At the end of this stage, the system consists of air0, CA1, and DMSO at the pressure of the reservoir but at temperature T_{CO2} (Figure 4.3).
- Stage 5 (Desorption of CO_2): This stage involves the chemical reaction of CO_2 desorption, where CA1 transforms into IPDA and CO_2. At the end of this stage, the system consists

of air0 at the pressure and temperature of the reservoir, as well as IPDA, DMSO, and CO_2 at pressure of the reservoir but at temperature T_{CO2} (Figure 4.3).

- Stage 6 (Separation of CO_2): This stage involves separating CO_2 from the rest of the components. The separation is carried out with an adiabatic and impermeable membrane, represented by dashed black lines in Figure 4.3. One membrane separates air0 from CO_2, and the other separates CO_2 from the IPDA solution. The system consists of air0 at the pressure and temperature of the reservoir, as well as CO_2 and the IPDA-DMSO solution at the pressure of the reservoir and temperature T_{CO2} (Figure 4.3).
- Stage 7 (Cooling): This stage consists of cooling the IPDA, DMSO and CO_2 from the desorption temperature T_{CO2} down to the reservoir temperature T_{RV}. At the end of this stage, the system consists of air0, CO_2, and the IPDA-DMSO solution, all at the pressure and temperature of the reservoir. The membranes from the previous stage remain unchanged.

The objective of this thermodynamic analysis is to quantify the energy involved in the DAC process based on diamine. The analysis will determine also the energy exchanged by the system (ΔU_S) and the reservoir (ΔU_{RV}) for each stage of the process. However, since the details of the calculations can distract us from this objective, we summarize in Figure 4.4 the results and advance their discussion.

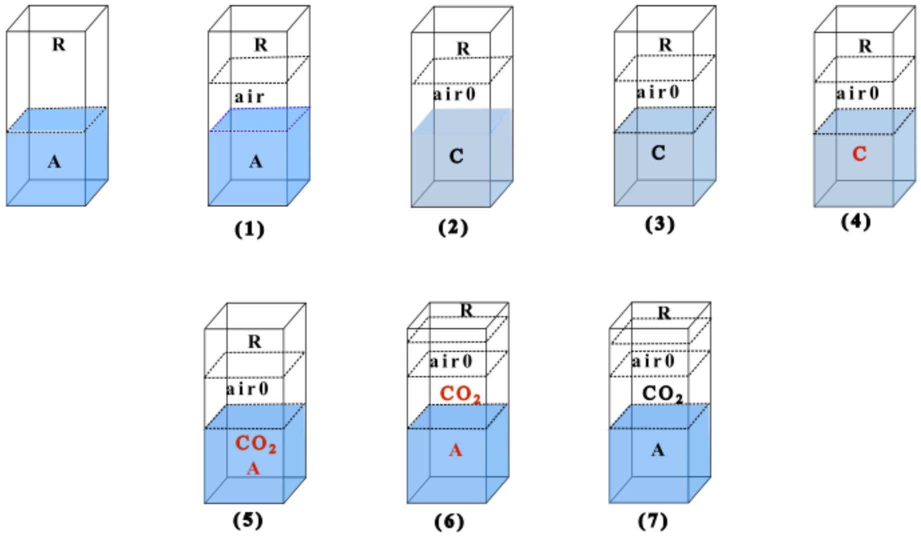

Figure 4.3 Stages of the DAC process based on the IPDA reaction: (1) introduction of air with CO_2, (2) chemical reaction for CO_2 capture, (3) separation of CO_2-free air (air0), (4) heating (5) CO_2 desorption, (6) separation of CO_2, and (7) cooling.

Figure 4.4 presents a bar graph showing the energy exchange associated with each stage of the process, except for stages 3 and 6, for which energy values were not determined because they were considered negligible compared to those of the other stages. Further details on this analysis will be provided in subsections 4.4.3 and 4.4.6.

Figure 4.4 shows that stage 1 (air introduction) involves energy consumption of $2.10 \cdot 10^{10}\ \mathrm{J} \cdot \mathrm{ton}^{-1}$, while stage 4 (CA1 heating) consumes $6.27 \cdot 10^{9}\ \mathrm{J} \cdot \mathrm{ton}^{-1}$. Stage 5 ($CO_2$ desorption reaction) involves $1.26 \cdot 10^{10}\ \mathrm{J} \cdot \mathrm{ton}^{-1}$. Stages 2 and 7, corresponding to the CA1 formation reaction and the cooling of CO_2 and IPDA, respectively, involve the least energy change, with values of $-9.80 \cdot 10^{9}\ \mathrm{J} \cdot \mathrm{ton}^{-1}$ and $-3.62 \cdot 10^{8}\ \mathrm{J} \cdot \mathrm{ton}^{-1}$. The negative sign indicates that stages

2 and 7 release energy instead of consuming it. However, we will consider this energy cannot be reused. The energy of stages 2 and 7 is represented in red in Figure 4.4.

The total energy of the DAC process is the sum of energy from stages 1 to 7. The total energy exchanged amounts to $5.00 \cdot 10^{10}\ \mathrm{J \cdot ton^{-1}}$, of which $3.99 \cdot 10^{10}\ \mathrm{J \cdot ton^{-1}}$ is consumed energy and $1.02 \cdot 10^{10}\ \mathrm{J \cdot ton^{-1}}$ are energy losses. The ratio between the consumed energy ($3.99 \cdot 10^{10}\ \mathrm{J \cdot ton^{-1}}$) and the total energy ($5.00 \cdot 10^{10}\ \mathrm{J \cdot ton^{-1}}$) is 79.8%. This means that 79.8% of the total energy involved in this DAC process is allocated to energy consumption, while, at best, the remaining 20.2% can be used to power other stages of the process. This suggests that although recovering and reusing the energy released in these stages could optimize the overall efficiency of the process, its impact on the overall efficiency of the process would be minimal.

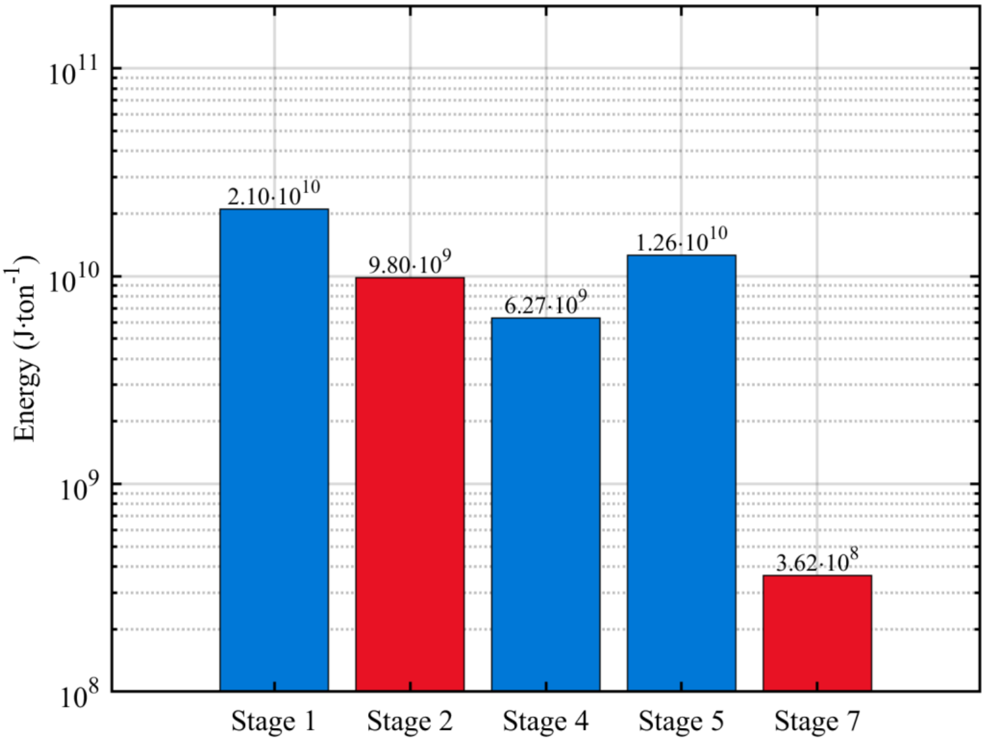

Figure 4.4 Energy exchange at the different stages of the DAC process for capturing 1 ton of CO_2. The energies of stages 3 and 6 are not shown because their value is considered negligible compared to that of the other stages. The energy for stages 2 and 7 is negative but is considered non-recoverable.

4.3 Experimental results

4.3.1 Determination of capture efficiency

Each of the experiments related to CO_2 capture lasted 24 hours and were carried out using the same amounts of IPDA and DMSO in all reactions: 0.5 and 5 mL, respectively. In these experiments, the CO_2 capture efficiency (η_{cap}) was evaluated at volumetric flow rates ($\emptyset$) of 20, 30, 40, 50, 60, and 70 $\mathrm{mL \cdot min^{-1}}$. The capture efficiency is defined as the ratio of CO_2 molecules captured over a period of time (N_{cap}) to the number of CO_2 molecules passing through the solution during that same period (N_D).

$$\eta_{\mathrm{cap}} = \frac{N_{\mathrm{cap}}}{N_D} \tag{4.40}$$

To determine N_{cap}, a differential weighing of the reactor with all the reagents was performed both before the reaction began and after the 24-hour reaction period during which the CO_2 capture reaction took place. Since CO_2 is the only component of the air that reacts with IPDA [57], any change in weight (Δm_{CO2}) was considered exclusively as CO_2 absorbed when CA1 was formed. Therefore, N_{cap}, expressed in mol, was determined as the ratio of Δm_{CO2} to the molecular weight of CO_2 (M_{CO2})

$$N_{\text{cap}} = \frac{\Delta m_{\text{CO2}}}{M_{\text{CO2}}} \tag{4.41}$$

On the other hand, the volume of air passing through the reactor (V_{air}) was simply the integral of the volumetric flow rate with respect to time, such that

$$V_{\text{air}} = \int_{0\ \text{h}}^{24\ \text{h}} \emptyset \, dt \tag{4.42}$$

To determine the amount of CO_2 moles passing through the reactor over 24 hours, V_{air} must be considered, according to

$$N_D = \frac{V_{\text{air}}\, x}{V_m} \tag{4.43}$$

where $x = 4 \cdot 10^{-4}$ is the concentration of CO_2 in air (400 ppm) [141], and V_m is the molar volume of CO_2 under standard conditions. V_m is defined as the volume occupied by one mole of gas, assuming it behaves as an ideal gas. Once the moles of CO_2 captured and those passing through the reactor are determined, the CO_2 capture efficiency can be calculated. The differential weight change Δm_{CO2} was experimentally determined three times for each volumetric flow rate (20-70 $\text{mL} \cdot \text{min}^{-1}$). Table 4.1 shows the average of the differential weight change ($\overline{\Delta m_{\text{CO2}}}$) and the average mol of CO_2 captured ($\overline{N_{\text{cap}}}$) for each flow rate.

As seen in Table 4.1, there is a relationship between the flow rate and several of the parameters recorded. The bubbling system operated without leaks and was assumed to be impermeable to air molecules. Therefore, an increase in flow rate resulted in an increase in the air volume (V_{air}) and moles of CO_2 passing through the reactor (N_D). A growing trend of $\overline{\Delta m_{\text{CO2}}}$ and $\overline{N_{\text{cap}}}$ was also observed as the volumetric flow rate increased. The increase in flow rate led to a larger volume of air flowing through the reactor, thereby increasing the amount of CO_2 in contact with the IPDA. With more CO_2 available in the same time interval, the formation of a larger amount of CA1 was favored.

Table 4.1. Values of $\emptyset$, V_{air} y N_D, and average values of Δm_{CO2}, N_{cap} y η_{cap}. Each test with a given flow rate was performed three times.

Parameter						
Flow rate, $\emptyset$ ($\text{mL} \cdot \text{min}^{-1}$)	20 ± 3	30 ± 3	40 ± 3	50 ± 3	60 ± 3	70 ± 3
Weight, $\overline{\Delta m_{\text{CO2}}}$ (g)	$(2.2 \pm 0.1) \cdot 10^{-2}$	$(3.3 \pm 0.1) \cdot 10^{-2}$	$(3.7 \pm 0.1) \cdot 10^{-2}$	$(4.3 \pm 0.1) \cdot 10^{-2}$	$(5.1 \pm 0.1) \cdot 10^{-2}$	$(5.1 \pm 0.1) \cdot 10^{-2}$
Captured CO_2, $\overline{N_{\text{cap}}}$ (mol)	$(4.9 \pm 0.2) \cdot 10^{-4}$	$(7.4 \pm 0.2) \cdot 10^{-4}$	$(8.3 \pm 0.2) \cdot 10^{-4}$	$(9.8 \pm 0.2) \cdot 10^{-4}$	$(1.2 \pm 0.2) \cdot 10^{-3}$	$(1.2 \pm 0.2) \cdot 10^{-3}$
Air volume, V_{air} (L)	29 ± 3.6	43 ± 3.6	58 ± 3.6	72 ± 3.6	86 ± 3.6	101 ± 3.6
Bubbled CO_2, N_D (mol)	$(5.2 \pm 0.5) \cdot 10^{-4}$	$(7.8 \pm 0.7) \cdot 10^{-4}$	$(1.0 \pm 0.5) \cdot 10^{-3}$	$(1.3 \pm 0.1) \cdot 10^{-3}$	$(1.6 \pm 0.2) \cdot 10^{-3}$	$(1.8 \pm 0.1) \cdot 10^{-3}$
Efficiency, $\overline{\eta_{\text{cap}}}$ (%)	96 ± 1.2	95.3 ± 0.9	80.3 ± 0.7	75.5 ± 0.6	74.2 ± 0.5	63.9 ± 0.4

Figure 4.5 illustrates the influence of flow rate on capture efficiency in the experiments, showing a decrease in capture efficiency as the flow rate increased. This decrease in capture efficiency became more pronounced as the flow rates increased, which directly stems from the trend observed in $\overline{\Delta m_{\text{CO2}}}$ and $\overline{N_{\text{cap}}}$ (Table 4.1). Specifically, it is observed that the capture efficiency

was almost the same for 20 and 30 $\mathrm{mL \cdot min^{-1}}$, with values of 96% and 95.3%, respectively. For 40, 50, and 60 $\mathrm{mL \cdot min^{-1}}$, the capture efficiency is 80.3%, 75.5%, and 74.2%, respectively. The lowest capture efficiency, 63.9%, was achieved with 70 $\mathrm{mL \cdot min^{-1}}$.

Two explanations can justify this trend. The first is directly related to the diffusion of CO_2 molecules from the air bubbles into the IPDA and DMSO solution. When flow rates were high, the air bubbles spent less time in contact with the IPDA solution because they were displaced more quickly by the incoming gas, which flowed at high speed [142]. This meant that, in a given air bubble, CO_2 had less time to diffuse into the IPDA solution, and therefore, the probability that it would react to form CA1 was lower than it could be. In other words, the amount of $\overline{N_{\mathrm{cap}}}$ was lower than expected for the entire N_D, which translated into a decrease in η_{cap} as the flow rate increased. The reduction in η_{cap} described by this explanation could, to some extent, be mitigated with a different geometry and arrangement of the capture system components, such as the shape and volume of the reactor or the position of the air inlet, so that the air bubbles would have enough travel distance along the dissolution column to ensure that they do not limit the reaction, even at high flow rates.

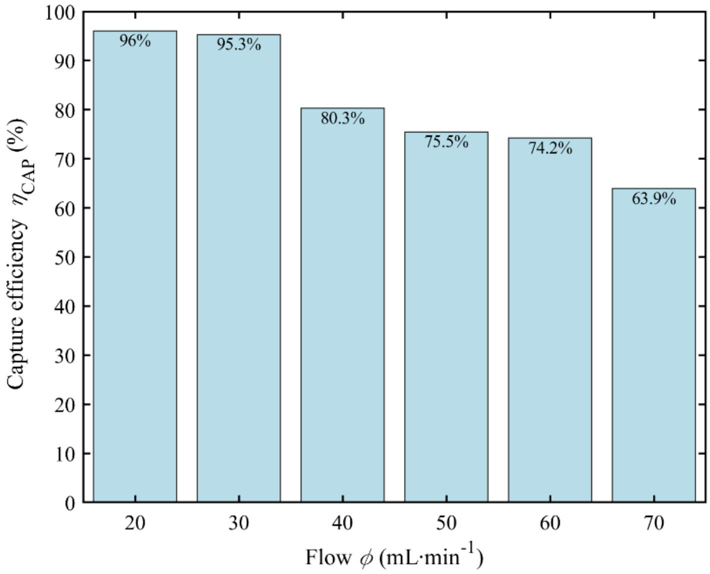

Figure 4.5 Average capture efficiency ($\overline{\eta_{\mathrm{cap}}}$) obtained with different flow rates.

The other explanation is related to the geometry of the reactor. The laboratory tests were carried out in a glass container, through which a tube was inserted to bubble air directly into the IPDA solution. Additionally, a second tube was introduced which, without touching the solution, allowed the exit of air components that did not react with the IPDA. With this design, it was observed that flow rates of 20-30 $\mathrm{mL \cdot min^{-1}}$ were laminar, meaning there was little turbulence in the IPDA solution. However, for flow rates above 40 $\mathrm{mL \cdot min^{-1}}$, turbulence was generated in the IPDA solution, causing some of the solution to adhere to the walls above the solution level, forming droplets. In these cases, the IPDA remaining on the walls of the reactor was not in direct contact with the air bubbling into the reactor, which reduced the amount of solution available to react with the CO_2 from the air, thus decreasing the amount of CO_2 ultimately captured and reducing η_{cap}. In addition to this, there was an additional effect whereby, at very high flow rates, the turbulence was so intense that part of the CA1 and the IPDA and DMSO solution even exited the reactor through the gas exhaust tube, as shown in Figure 4.6. The added problem with this effect was that the CA1 and droplets of the IPDA and DMSO solution that exited through the tube were not part of the mass measured at the end of the experiment on the analytical balance. As a result, Δm_{CO2} was lower, and therefore the measured N_{cap} was also smaller, leading to a capture efficiency η_{cap} that was measured lower than the actual value.

For all these reasons, the very low value of η_{cap} at a flow rate of $70\ \mathrm{mL\cdot min^{-1}}$ can be considered influenced by a measurement artifact and, therefore, not valid. At the same time, it cannot be ruled out that this type of artifact may have had some small influence on the measurements made at flow rates of 50 and $60\ \mathrm{mL\cdot min^{-1}}$, although no clear remnants of particles around (or outside) the reactor were observed in these cases. In this scenario, a different geometry and arrangement of the experiment could also eliminate or minimize the influence of potential experimental errors.

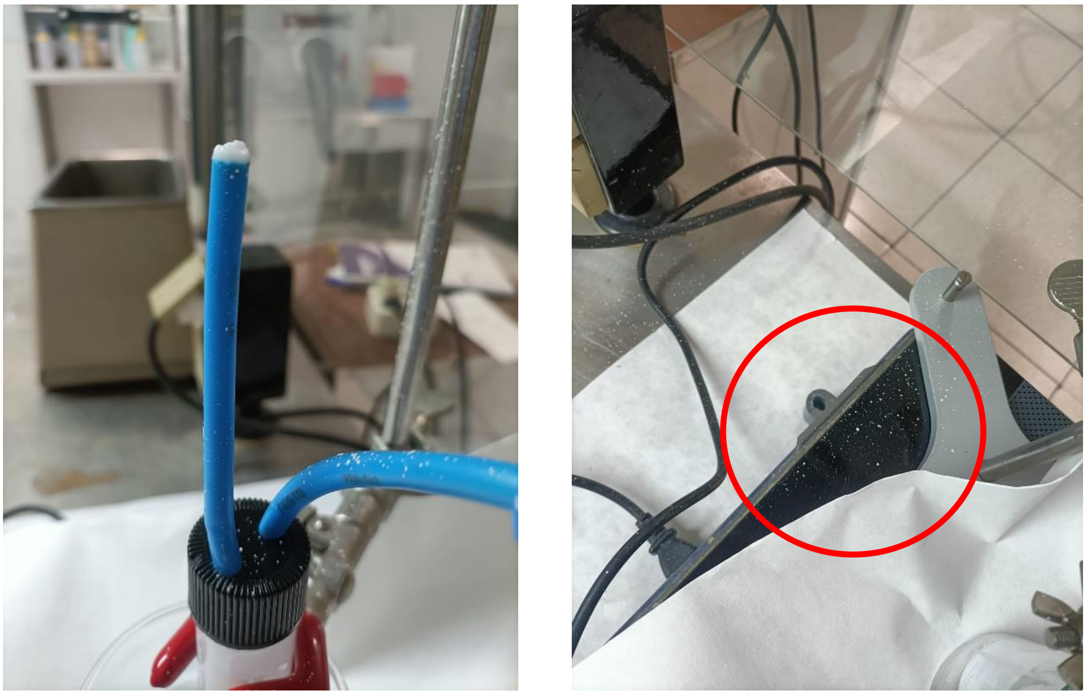
a) b)

Figure 4.6 a) Evacuation tube of reactive gases covered with CA1 formed during the reaction and displaced toward the exit by the turbulence generated in the solution due to the flow rate of $70\ \mathrm{mL\cdot min^{-1}}$ b) White specks corresponding to remnants of CA1 expelled from the reactor due to the turbulence.

The average capture efficiencies corresponding to flow rates of 20 and $30\ \mathrm{mL\cdot min^{-1}}$ in this experiment were in the same order as those reported by the creators of this technology for a flow rate of $20\ \mathrm{mL\cdot min^{-1}}$ [57]. Meanwhile, those corresponding to higher flow rates were clearly lower, which is likely due to the geometry of the reactor used in these experiments, as previously explained. Our experiment not only confirmed that the CO_2 capture efficiency was similar to the values reported by the developers of this technology for a flow rate of $20\ \mathrm{mL\cdot min^{-1}}$ [57], but also demonstrated that the capture efficiency was indeed dependent on the volumetric flow rate at which the air was introduced into the reactor, an aspect not investigated in the original study.

4.3.2 Determination of CO_2 desorption temperature

S. Kikkawa et al. heated the system and found that CO_2 begins to desorb from CA1 at a minimum temperature, T_{CO2}, of 303 K [57]. Additionally, they measured the CO_2 desorption rate during heating —i.e., the rate at which the CA1 dissociation reaction occurs— by monitoring the outgoing CO_2 flow using a calibrated CO_2 flowmeter. Their experiments revealed a relationship between the desorption rate and T_{CO2} within a study range of 303–333 K: the higher the T_{CO2}, the greater the desorption rate.

To verify whether T_{CO2} in this process matched the value reported by Kikkawa et al., a CO_2 release experiment was conducted by heating the reactor in our laboratory. All heating tests were performed using systems with an initial amount of 0.5 mL of IPDA and 5 mL of DMSO, through which air was bubbled at a flow rate of 20 $\mathrm{mL \cdot min^{-1}}$ for 24 hours. Determining T_{CO2} is necessary for assessing the energy consumption required to heat CA1 in the process. This energy consumption corresponds to the heat (Q) supplied to the reactor, which is directly proportional to the temperature difference (ΔT) between the reactor's initial temperature and, in this case, the CO_2 desorption temperature. For simplicity, let us assume that once this temperature is reached, the solution remains at that temperature, without any additional energy input, until the complete conversion of CA1 into IPDA and CO_2 is achieved

$$Q = \sum m_i \, C_{p,i} \Delta T \tag{4.44}$$

where $C_{p,i}$ is the specific heat capacity at constant pressure of a substance, and m_i is the mass of the substance. Constant pressure has been assumed because the heat is supplied with the atmosphere acting as pressure reservoir. Eq. (4.44) also assumes that heat supplied is entirely delivered to the substance without losses.

In the experiments conducted, no instruments were used to directly measure the presence or volumetric flow rate of the CO_2 released from the system due to the unavailability of such equipment. Instead, the onset of CA1 dissociation and the subsequent release of CO_2 were identified through visual observation, specifically by the appearance of bubbles in the system. Thus, T_{CO2} is defined as the temperature at which bubbles first appear in the reactor.

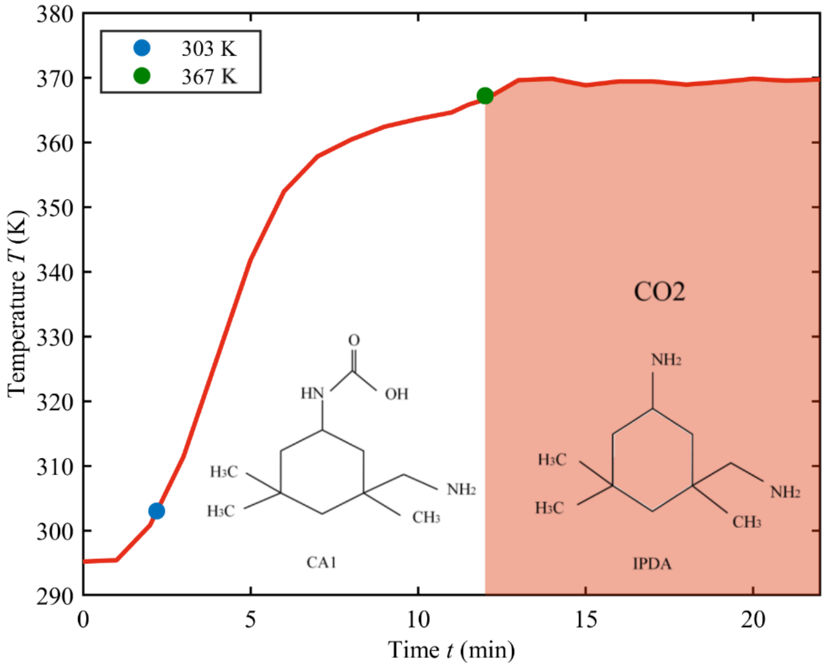

Figure 4.7 Temperature profile of the first reactor heating. The reactor was bubbled for 24 hours with a volumetric flow rate of 20 $\mathrm{mL \cdot min^{-1}}$. The shaded temperature interval indicates the points at which the CA1 dissociation reaction occurs, during which both CA1 and CO_2 are present.

Figure 4.7 plots a red line representing the temperature profile of the reactor during heating. The desorption temperature T_{CO2} reported by Kikkawa et al. is marked with a blue dot. Additionally, the figure includes an orange-shaded area, indicating the time interval in which the dissociation reaction of CA1 occurs, leading to its transformation into IPDA and CO_2. Meanwhile, the white area below the curve represents the phase in which only CA1 is present. The desorption reaction concludes when no more CO_2 bubbles are generated, and the white precipitate (CA1) is completely converted into a colorless solution (IPDA).

The first CO_2 bubbles were detected starting at 367 K as indicated in Figure 4.7, which represents a temperature increase of 64 K compared to the value reported by S. Kikkawa et al.

Due to the discrepancy with the literature results [57], the reactor heating was repeated following the same procedure and under the same pressure conditions. To ensure the reproducibility of these results, the heating process was carried out 10 times, all of which demonstrated a desorption temperature T_{CO2} in the range of 365.1-367.0 K as depicted in Figure 4.8 that shows the CO_2 desorption temperatures recorded during the 10 heating sessions conducted in the laboratory, represented individually as blue points. The red line indicates the average desorption temperature, $\overline{T_{CO2}}$ = 366.2 K. The standard deviation of the measurements from the average was calculated as 0.7 K. Since the average desorption temperature is to be used, it is necessary to determine the associated error. This error is defined as the ratio of the standard deviation to the square root of the number of measurements, which in this case is 10. Therefore, the average CO_2 desorption temperature is expressed as $\overline{T_{CO2}} = 366.2 \pm 0.2$ K.

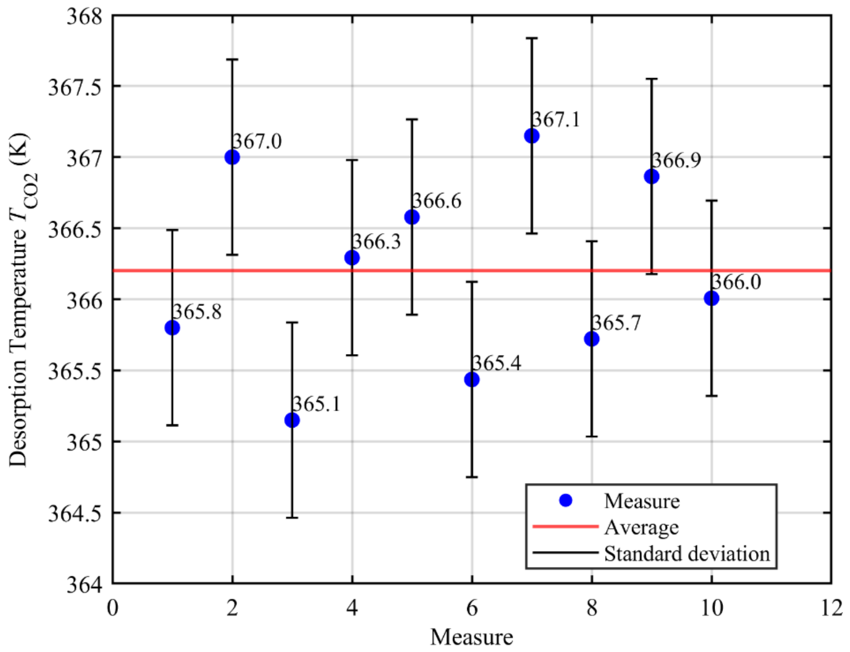

Figure 4.8 Measured T_{CO2} values in the laboratory. The average of these temperature values $\overline{T_{CO2}}$ (red line) and the standard deviation of each measurement with respect to the average are also shown.

These results are not intended to contradict the findings of S. Kikkawa et al., but rather to reflect the temperature and pressure conditions at which visible changes occur in the reactor during heating. However, the use of a CO_2 flow meter would allow for much greater precision in measuring $\overline{T_{CO2}}$, as the reaction likely begins before CO_2 bubbles become visible in the reactor.

4.4 Results of the thermodynamic analysis

Before conducting a thorough analysis of the energy involved in each stage of the DAC process, it is pertinent to present an introduction to the thermodynamics underlying any process. This thermodynamic foundation will provide a common reference framework, allowing for a consistent understanding and evaluation of the various energy transformations that occur in each step of the process. Furthermore, this preliminary approach will facilitate a detailed and contextualized interpretation of the results.

Let us recall from Chapter 2 that internal energy (U) is a homogeneous first-order function of the extensive parameters: entropy (S), volume (V), and quantity of matter (N). This property of energy allows us to derive the Euler equation, Eq. (3.12), which we recall next for convenience.

$$U = TS - PV + \mu N \tag{4.45}$$

The product of the chemical potential, μ, and N is known as the Gibbs free energy or Gibbs potential (G)

$$G = \mu N \tag{4.46}$$

The Gibbs potential is a natural function of pressure, temperature, and the amount of substance, making it particularly useful in the analysis of processes occurring at constant pressure and temperature. Once the Gibbs free energy is defined, Eq. (4.45) can be rewritten as

$$U = TS - PV + G \tag{4.47}$$

In this manner, an infinitesimal change in energy (dU) can be expressed as

$$dU = d(TS) - d(PV) + dG \tag{4.48}$$

In an isobaric and isothermal process, the energy change can be expressed as

$$\Delta U = T\Delta S - P\Delta V + \Delta G \tag{4.49}$$

Energy is a state function, therefore it is a property that depends only on the state and not on the path taken to reach that state. Hence, the change in energy between the two states can be expressed as ΔU.

We will consider our system is in equilibrium with a temperature and pressure reservoir (e.g., the atmosphere). We will analyze the energy change in both the system and the reservoir as they transition from an initial state to a final state, denoted as ΔU_S and ΔU_{RV}, respectively.

In our analysis, the energy change in the system ΔU_S results from external energy input, either in the form of work (W) or heat (Q) or both. At the same time, the system can exchange energy with the reservoir. Thus, the overall energy balance of the system and reservoir can be expressed as

$$Q + W = \Delta U_S + \Delta U_{\mathrm{RV}} \tag{4.50}$$

Reservoirs only exchange extensive properties, namely N, S and V. In our study, the pressure and temperature reservoir are characterized by a fixed value of its temperature and pressure. Also, it can only exchange entropy and volume with the system. In a process occurring at constant pressure and temperature, the exchange of entropy and volume can be incorporated into the overall energy balance as

$$Q + W = \Delta U_S + T_{\mathrm{RV}}\Delta S_{\mathrm{RV}} - P_{\mathrm{RV}}\Delta V_{\mathrm{RV}} \tag{4.51}$$

Now, let us assume that the process is reversible. This implies that any change in entropy experienced by the reservoir will be exactly opposite to that of the system. The same happens for the volume. Assuming the process occurs at the pressure and temperature of the reservoir, the energy balance can be expressed as

$$Q + W = \Delta U_S - T_{\mathrm{RV}}\Delta S_S + P_{\mathrm{RV}}\Delta V_S \tag{4.52}$$

Eq. (4.52) holds for any process involving the system and the reservoir kept at constant pressure and temperature, even when the system does not evolve at constant pressure and temperature, such as in heating or cooling processes. However, if the system is assumed in equilibrium with the reservoir along each quasi-static transformation, the system will also evolve at constant pressure ($P_S = P_{\mathrm{RV}}$) and temperature ($T_S = T_{\mathrm{RV}}$) that equal to the ones of the reservoir. In this case, Eq. (4.52) can be rewritten as

$$Q + W = \Delta U_S - T_S \Delta S_S + P_S \Delta V_S = \Delta G_S \tag{4.53}$$

Eq. (4.53) serves as the foundation for expressing the energy changes experienced by the system and the reservoir in the different stages of the thermodynamic analysis of the DAC process. For processes occurring at constant pressure and temperature, we will use Eq. (4.53) that offers two paths to calculate it: through the change in the Gibbes free energy (right hand side of the equation) or through the direct calculation of the internal energy change, entropy and volume.

Next, the energy balance for each stage of the DAC process is detailed. The thermodynamic analyses of all seven stages of the process anticipated above will be studied to determine the energy involved in each of them.

4.4.1 Stage 1: Introduction of air with CO_2

The first stage consists of introducing air (containing CO_2) by doing some work W_1 into the system, which at its initial stage is considered to consist only of the solution of IPDA in DMSO. The air is considered not to react yet with the IPDA at this stage for which an impermeable, adiabatic and non-movable membrane is considered to separate the air from the IPDA in DMSO system. Also, we will neglect the impact of the gravitational field that would increase the pressure at which the air is introduced with respect to the atmospheric pressure of the reservoir by a factor $\rho g h$ being ρ the density of the IPDA-DMSO solution, g the acceleration of the gravitational field and h the height with respect to the surface of the solution at which the air is introduced. Besides, this term is highly experiment dependent and the results can be corrected for this term if considered necessary.

Once the air is introduced, the system consists of air and the IPDA solution, both separated by the membrane. This stage occurs at the pressure and temperature of the reservoir (which coincides with that of the system), 101,325 Pa and 298.15 K, respectively. No heat is supplied to the system at this stage ($Q_1 = 0$). The energy balance for this stage is based on Eq. (4.53) and leads to

$$W_1 = \Delta U_{S,1} + \Delta U_{\mathrm{RV},1} = \Delta U_{S,1} - T_{\mathrm{RV}} \Delta S_{S,1} + P_{\mathrm{RV}} \Delta V_{S,1} = \Delta G_{S,1} \tag{4.54}$$

Eq. (4.54) reveals that part of the energy supplied to the system as work in this stage remains within the system ($\Delta U_{S,1}$), another part is exchanged as heat with the reservoir ($T_{\mathrm{RV}} \Delta S_{S,1}$), and a fraction is used as work to increase the system volume ($P_{\mathrm{RV}} \Delta V_{S,1}$). Next, each energy component of this stage is calculated.

4.4.1.1 Energy retained by the system ($\Delta U_{S,1}$)

In this analysis, air is considered an ideal gas, primarily composed of N_2 and O_2, which account for approximately 79% and 21% of its composition, respectively [143]. In addition to these main components, air contains smaller proportions of argon (Ar), H_2O vapor, and CO_2 in decreasing order. For simplicity, air will be considered as consisting of three components: N_2, O_2, and CO_2 (400 ppm [143]). Accordingly, Ar and H_2O vapor molecules can be considered grouped together with N_2 in the calculations that follow since they will be considered to perform as N_2 under this simplification.

Let us recall from section 3.1 that the energy of an ideal gas depends exclusively on temperature and the amount of the gas [144]. For a gas mixture, its energy is expressed as follows

$$U = \left(\sum_{i} N_i c_i \right) RT \tag{4.55}$$

where R is the ideal gas constant (8.31 $\mathrm{J \cdot K^{-1} \cdot mol^{-1}}$), N_i is the amount of a certain gas in the mixture measured in moles, and c_i is a constant that depends on the gas. For monatomic ideal gases, the constant c_i takes a value of 3/2, while for diatomic ideal gases such as N_2 and O_2, it can be approximated as 5/2. In this analysis, we will also use the value of 5/2 for CO_2. The energy of the air introduced into the system in stage 1 can be expressed as the sum of the energy of its constituent gases

$$U_{\mathrm{air}} = \frac{5}{2} \sum_{i} N_i \, RT \tag{4.56}$$

Given the composition of air, the amount of its components introduced into the system to reach one ton of CO_2 is listed in Table 4.2. This table also includes the energy values associated with each gas and the total energy of the air (U_{air}) at 298.15 K, calculated using Eq. (4.56)

Since the air has an intrinsic internal energy (U_{air}), its introduction into the system results in a change in the energy of the system, $\Delta U_{S,1}$. This change in energy corresponds to the internal energy of the introduced air. Therefore, the energy retained by the system when introducing the air containing one ton of CO_2 is $\Delta U_{S,1} = U_{\mathrm{air}} = 2.11 \cdot 10^{11} \mathrm{J \cdot ton^{-1}}$.

Table 4.2. Values of N_{N2}, N_{O2}, N_{CO2}, U_{N2}, U_{O2}, U_{CO2} y U_{air} to capture one ton of CO_2 at 298 K.

Parameter	
Amount of N_2, N_{N2} (mol)	$44.9 \cdot 10^6$
Amount O_2, N_{O2} (mol)	$11.9 \cdot 10^6$
Amount CO_2, N_{CO2}(mol)	$22.7 \cdot 10^3$
Total amount, N_T (mol)	$5.68 \cdot 10^7$
Energy of N_2, U_{N2} (J)	$1.66 \cdot 10^{11}$
Energy of O_2, U_{O2} (J)	$4.43 \cdot 10^{10}$
Energy of CO_2, U_{CO2} (J)	$1.41 \cdot 10^8$
Energy of air, U_{air} (J)	$2.11 \cdot 10^{11}$

4.4.1.2 Increase in volume ($P_{\mathrm{RV}} \Delta V_{S,1}$)

The introduction of air results in an increase in the volume of the system ($\Delta V_{S,1}$) because, in addition to containing IPDA and DMSO at their initial stage, it now also contains N_2, O_2, and CO_2. It is important to note that this process occurs at the constant pressure of the reservoir (P_{RV}), meaning that this change in the system volume, $\Delta V_{S,1}$, involves the realization of work [145] on the reservoir due to the expansion of this gas.

To determine the work $P_{\mathrm{RV}} \Delta V_{S,1}$, we can use one equation of state of ideal gases, Eq. (3.1), which, in the context of our system, is expressed as [146]

$$P_{\mathrm{RV}} \Delta V_{S,1} = N_T R T_{\mathrm{RV}} \tag{4.57}$$

Although the goal is to determine the work exerted on the system $P_{\mathrm{RV}} \Delta V_{S,1}$, determining the volume of air $\Delta V_{S,1}$ introduced into the system in such a way that it contains 1 ton of CO_2 at a concentration of 400 ppm can be useful to illustrate the magnitude of the process and contextualize its scale. By solving for $\Delta V_{S,1}$ in Eq. (4.57), we obtain

$$\Delta V_{S,1} = \frac{N_T R T_{\mathrm{RV}}}{P_{\mathrm{RV}}} \tag{4.58}$$

Considering the values of N_{N2}, N_{O2} and N_{CO2} listed in Table 4.2, the volume of air introduced into the system is calculated as $\Delta V_{S,1} = 1.39 \cdot 10^9$ L. Therefore, the work exerted on the reservoir (W) in this stage can be determined as $W = P_{\mathrm{RV}} \Delta V_{S,1} = 1.39 \cdot 10^{11} \mathrm{J} \cdot \mathrm{ton}^{-1}$.

4.4.1.3 Heat exchange ($T_{\mathrm{RV}} \Delta S_{S,1}$)

In an isothermal thermodynamic process, the heat exchanged by the system is related to the change in entropy experienced by the system ($T\Delta S$) [145], as occurs in this stage of the DAC process. The sign convention for heat in thermodynamics states that heat is positive when the system receives heat. Conversely, negative heat implies that the system supplies the heat [145]. In this stage, the change in entropy $\Delta S_{S,1}$ is associated with the introduction of the air species into the system, as the entropy of the IPDA and DMSO in the system remains constant during the introduction of air. Thus, the introduction of new species increases the total entropy of the system, which, according to Eq. (4.54), implies that the system releases heat to the reservoir.

Let us recall that Gibbs' theorem states that the entropy of a mixture of ideal gases is the sum of the entropies of the individual gases if they occupy the same volume as the mixture at a given temperature [145]. Therefore, we will consider that stage 1 is a mixing process in which the initial state of the system has an entropy associated with the IPDA solution (S_0). In the final state of this stage, the system has the entropy corresponding to the sum of S_0 and the entropy of the mixed gases of the air (S_1). The entropy associated with the IPDA solution remains constant between the initial and final states of this stage. Thus, the change in entropy in stage 1 coincides with the entropy of air (S_1), a multicomponent ideal gas. Let us recall from chapter 2, that the entropy of a multicomponent ideal gas is expressed as

$$\begin{aligned}\Delta S &= (S_1 + S_0) - S_0 = S_1 \\ &= \sum_i N_i \left(\frac{S_i^0}{N^0}\right) + \sum_i N_i R \ln\left(\frac{RT}{V^0}\frac{N^0}{P}\right) - \sum_i N_i R \ln\left(\frac{N_i}{N}\right)\end{aligned} \tag{4.59}$$

where N_i, is the amount of a single component of the gas mixture, N^0 is the amount of a component in a reference state, V^0 is the volume occupied by the component in the reference state, S_i^0 is the entropy of the component in the reference state, and N is the total amount (in mol) of the gas mixture. Specifically, the entropy change in this stage of the process is given by

$$\begin{aligned}\Delta S_{S,1} = {} & N_{\mathrm{CO2}}\frac{S^0_{\mathrm{CO2}}}{N^0} + N_{\mathrm{O2}}\frac{S^0_{\mathrm{O2}}}{N^0} + N_{\mathrm{N2}}\frac{S^0_{\mathrm{N2}}}{N^0} + N_{\mathrm{CO2}} R \ln\left(\frac{N^0 RT}{PV^0}\right) + N_{\mathrm{O2}} R \ln\left(\frac{N^0 RT}{PV^0}\right) \\ & + N_{\mathrm{N2}} R \ln\left(\frac{N^0 RT}{PV^0}\right) - N_{\mathrm{CO2}} R \ln\left(\frac{N_{\mathrm{CO2}}}{N}\right) - N_{\mathrm{O2}} R \ln\left(\frac{N_{\mathrm{O2}}}{N}\right) \\ & - N_{\mathrm{N2}} R \ln\left(\frac{N_{\mathrm{N2}}}{N}\right)\end{aligned} \tag{4.60}$$

As the reference states, we chose 1 mol of gas under standard conditions. Thus, N^0 is 1, and V^0 24.4 L for all components of the mixture. The values of the standard entropies for each individual gas, which are taken from reference [147], and the values of N_i are collected in Table 4.3.

Table 4.3. Values of S^0_{N2}, S^0_{O2}, S^0_{CO2}, N_{N2}, N_{O2} , and N_{CO2} needed to determine $\Delta S_{S,1}$ of the first stage of the DAC process based on IPDA.

Parameter	Nitrogen (N_2)	Oxygen (O_2)	Carbon dioxide (CO_2)
Amount, N_i (mol)	$4.49 \cdot 10^7$	$1.19 \cdot 10^7$	$2.27 \cdot 10^4$
Entropy, S_i^0 ($\mathrm{J} \cdot \mathrm{mol}^{-1} \cdot \mathrm{K}^{-1}$)	192 [147]	205 [147]	214 [147]

According to Eq. (4.60), the introduction of air in stage 1 ($V = 1.39 \cdot 10^9$ L of air at 298.15 K and 101,325 Pa) leads to an increase in entropy $\Delta S_{S,1} = 1.11 \cdot 10^9 \text{ J} \cdot \text{K}^{-1}$. The heat associated with this entropy increase is $Q = T_{\text{RV}} \Delta S_{S,1} = 3.30 \cdot 10^{11} \text{ J} \cdot \text{ton}^{-1}$.

The total energy provided to the system in stage 1 ascends to: $\Delta G_{S,1} = 2.10 \cdot 10^{10} \text{ J} \cdot \text{ton}^{-1}$. The total energy is broken down as follows: a portion of the energy is used to increase the energy of the system ($\Delta U_{S,1} = 2.11 \cdot 10^{11} \text{ J} \cdot \text{ton}^{-1}$), another portion of the energy is used as work ($P_{\text{RV}} \Delta V_{S,1}$) to increase the volume of the system ($P_{\text{RV}} \Delta V_{S,1} = 1.39 \cdot 10^{11} \text{ J} \cdot \text{ton}^{-1}$), and another portion of the energy is transferred as heat from the reservoir to the system ($T_{\text{RV}} \Delta S_{S,1} = 3.30 \cdot 10^{11} \text{ J} \cdot \text{ton}^{-1}$). Figure 4.9 shows the distribution of energy components $\Delta U_{S,1}, P_{\text{RV}} \Delta V_{S,1}$, and $T_{\text{RV}} \Delta S_{S,1}$ relative to the total energy change $\Delta G_{S,1}$ in stage 1 of the DAC process.

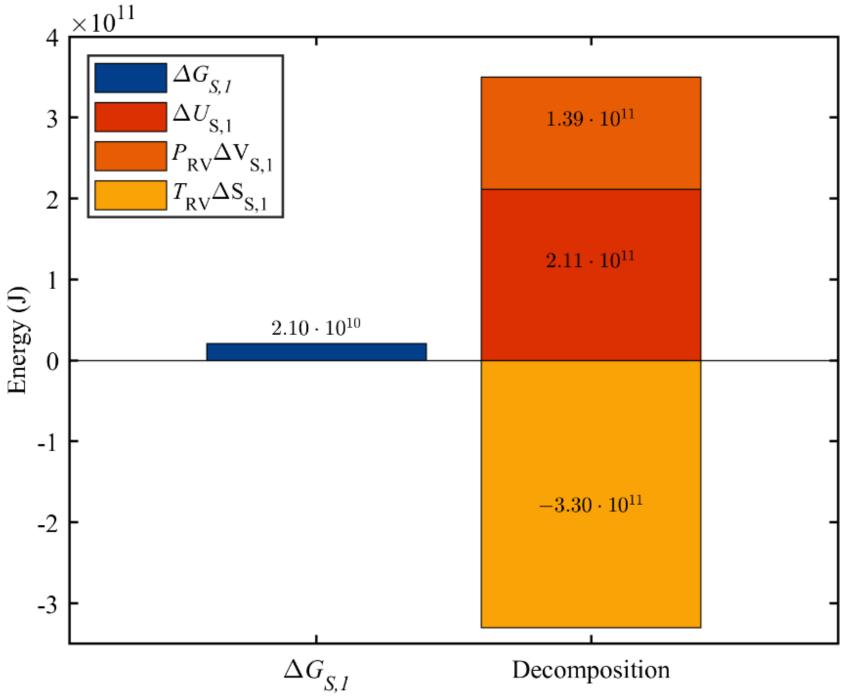

Figure 4.9 Contributions of the different energy components ($\Delta U_{S,1}, P_{\text{RV}} \Delta V_{S,1}, T_{\text{RV}} \Delta S_{S,1}$) in the air introduction stage of the DAC process based on IPDA.

4.4.2 Stage 2: Chemical reaction for CO2 capture

The initial system consists of air and the IPDA solution separated by the impermeable membrane, adiabatic and non-movable membrane we mentioned in the previous section. This membrane is removed at this stage and the system is assumed to evolve quasi-statically, and at constant pressure and temperature, to a new final equilibrium state. At the end of this stage, the system consists of CA1, CO2-free air (air0), unreacted IPDA and DMSO. In this stage, no work is supplied to the system, thus $W_2 = 0$ but some heat might we interchanged with the system. The overall energy balance is expressed as

$$Q_2 = \Delta U_{S,2} + \Delta U_{\text{RV},2} = \Delta U_{S,2} - T_{\text{RV}} \Delta S_{S,2} + P_{\text{RV}} \Delta V_{S,2} = \Delta G_{S,2} \tag{4.61}$$

Recall from Eq. (4.53) that the Gibbs free energy of a system is expressed as: $\Delta G_S = \Delta U_S - T_{\text{RV}} \Delta S_S + P_{\text{RV}} \Delta V_S$. Considering this, Eq. (4.61) has been expressed also in terms of the change in Gibbs free energy of the system. It is important to note that in this stage, the change in Gibbs free energy ($\Delta G_{S,2}$) has two contributions: one associated with the chemical reaction, which we will denote as $\Delta G_{r,2}$ and another derived from the absence of CO2 in air0, ΔG_{air}. This latter contribution is simply the difference in Gibbs free energy between air0, G_{air0}, and the air introduced into the system, G_{air}, which differ because the former does not contain CO_2. Keeping this in mind, Eq. (4.61) can be rewritten as:

$$Q_2 = \mathit{\Delta} U_{S,2} + \mathit{\Delta} U_{\text{RV},2} = \Delta G_{r,2} + \Delta G_{\text{air}} \tag{4.62}$$

The term ΔG_{air} represents the variation in the free energy of the air when separating CO_2 from the rest of its components. In other words, it does not refer to the chemical reaction itself but rather to how the energy of the components that do not participate in the reaction changes.

The objective of this subsection is to calculate $\Delta G_{r,2}$ and ΔG_{air}, whose sum reflects the energy change in stage 2 of the DAC process. Since the reaction occurs under standard pressure and temperature conditions, we calculate the standard Gibbs free energy of reaction ($\Delta G^0_{r,2}$). This standard Gibbs free energy of reaction $\Delta G^0_{r,2}$ is defined as the difference between the standard Gibbs free energies of formation (ΔG^0_f) of the products and reactants [116].

$$\Delta G^0_{r,2} = \sum_{\text{Prod}} \Delta G^0_f - \sum_{\text{React}} \Delta G^0_f \tag{4.63}$$

However, it is difficult to directly determine ΔG^0_f for many organic molecules like IPDA because it requires measuring changes in other thermodynamic properties associated with the formation of a molecule from its constituent elements in their most stable forms under standard conditions. This is why a thermodynamic analysis is necessary to determine $\Delta G^0_{r,2}$.

Let us recall that the Euler equation of thermodynamics Eq. (4.45) can be expressed in terms of the Gibbs potential as

$$U = T_{\text{RV}} S - P_{\text{RV}} V + G \tag{4.64}$$

Reordering the Eq. (4.64) to clear Gibbs' potential, we get

$$G = U - T_{\text{RV}} S + P_{\text{RV}} V \tag{4.65}$$

At this point, it is relevant to introduce the concept of enthalpy (H), defined as the partial Legendre transform of energy and that replacing volume as an independent variable with pressure, such that $H = H(S, P, N)$. Thus, enthalpy can be expressed as

$$H = P_{\text{RV}} V + U \tag{4.66}$$

Therefore, Eq. (4.65) is rewritten as

$$G = H - T_{\text{RV}} S \tag{4.67}$$

The change in Gibbs free energy (ΔG) in an isothermal process at the temperature of the reservoir, such as the reaction between IPDA and CO_2, can be then also expressed as

$$\Delta G = \Delta H - T_{\text{RV}} \Delta S \tag{4.68}$$

Eq. (4.68) allows for determining the standard Gibbs free energy of formation (ΔG^0_f) of the reactants and products of the reaction based on their respective enthalpies (ΔH^0_f) and entropies of formation (ΔS^0_f). Under standard pressure (P^0) and temperature (T^0), which coincide with those of the reservoir, these can be expressed as follows

$$\Delta G^0_f = \Delta H^0_f - T_{\text{RV}} \Delta S_f{}^0 \tag{4.69}$$

For many chemical compounds, tabulated values of ΔH_f^0 and ΔS_f^0 are available in the literature, but this is not the case for many organic compounds such as IPDA and CA1. Various methods allow for estimating ΔH_f^0 and ΔS_f^0 values based on the contributions of different functional groups within a molecule (a specific set of atoms that has characteristic chemical properties and determines its behavior and reactivity) [148–151]. Determining ΔH_f^0 and ΔS_f^0 of a compound by summing its functional groups can lead to an inaccurate estimation because functional groups may interact in a non-additive manner. In other words, the ΔH_f^0 and ΔS_f^0 of a compound may not simply be the sum of the ΔH_f^0 and ΔS_f^0 of its individual functional groups. This approximation can result in significant errors in calculations, as it does not account for specific interactions (such as hydrogen bonding and dispersion forces) between functional groups.

However, computational chemistry methods exist to determine ΔH_f^0, ΔS_f^0, and ΔG_f^0 for organic compounds while accounting for interactions between functional groups within the same molecule. The choice of the most suitable method depends on several factors, including the availability of computational resources, the desired accuracy, and the nature of the system under study. These methods can quickly and efficiently predict the thermodynamic properties of compounds, offering flexibility to study a wide range of chemical systems and reaction conditions. Additionally, they enable detailed investigation of molecular interactions at the atomic and molecular levels [152–154].

4.4.2.1 Determination of $\Delta G_{r,2}^0$

Density functional theory (DFT) is a computational quantum-mechanical modeling method used in physics, chemistry, and materials science to investigate the electronic or nuclear structure of the ground state of various systems, including atoms, molecules, and condensed phases [155]. With this theory, the properties of a many-electron system can be determined using functionals of the electronic density, which are functions whose arguments are other functions.

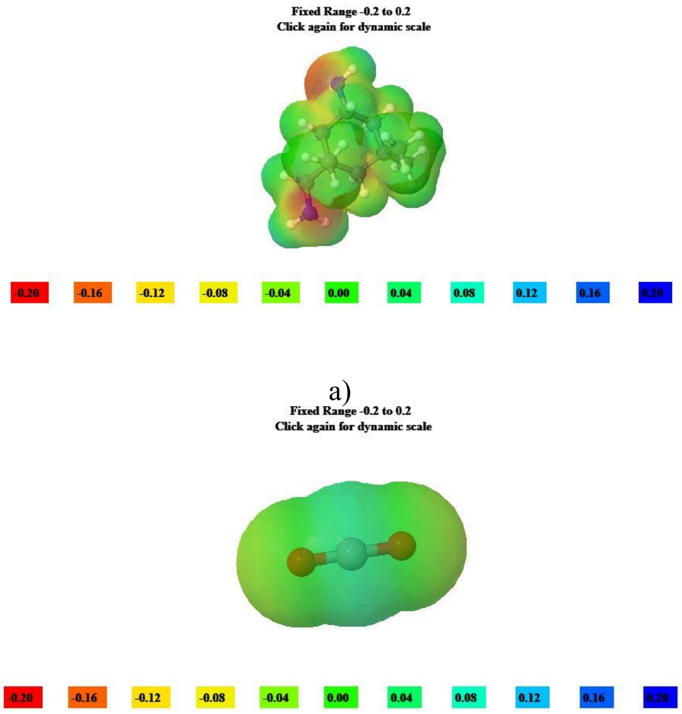

a)

b)

Figure 4.10 Electrostatic potential map of the molecule of (a) IPDA and (b) CO_2. Regions of high negative charge density are represented in warm colors (red-yellow), while regions of high positive charge density are represented in blue [156].

In the case of DFT, these functionals depend on the spatially varying electronic density or specific molecular regions, as illustrated in the examples shown in Figure 4.10 The electronic density distribution within a molecule helps to identify the regions most prone to react [156]. In the case of IPDA, represented in Figure 4.10a, the nitrogen atoms in the amino group exhibit a higher electron density, whereas in the CO_2 molecule, represented in Figure 4.10b, the carbon atom has a significantly lower electron density. This implies that the nitrogen atoms, with their excess electrons, have an affinity for the electron-deficient carbon in CO_2. As a result of this difference in electronic density, an interaction is established between the nitrogen in IPDA and the carbon in CO_2, leading to the formation of CA1.

As is common in many-body electronic structure calculations, the nuclei of the molecules or groups being treated are considered fixed (the Born-Oppenheimer approximation), generating a static external potential V in which the electrons move. A stationary electronic state is then described by a wave function $\Psi(r1, ..., rN)$ that satisfies the time-independent many-electron Schrödinger equation

$$\hat{H}\Psi = \left[\hat{T} + \hat{V} + \hat{U}\right]\Psi = E\Psi \tag{4.70}$$

Where, for the system of N electrons, $\hat{H}$ is the Hamiltonian, E is the total energy, $\hat{T}$ is the kinetic energy, $\hat{V}$ is the potential energy of the external field due to the positively charged nuclei, and $\hat{U}$ is the electron-electron interaction energy. The operators $\hat{T}$ and $\hat{U}$ are called universal operators because they are the same for any system of N electrons, while $\hat{V}$ depends on the system. This many-particle Eq. (4.70) cannot be separated into simpler single-particle equations due to the interaction term $\hat{U}$.

There are many sophisticated methods to solve the many-body Schrödinger equation based on the expansion of the wave function in Slater determinants, which are used to generate antisymmetric wave functions that describe the collective states of multiple fermions (such as electrons) and that satisfy the Pauli exclusion principle. While the simplest is the Hartree-Fock method, more sophisticated approaches are generally classified as post-Hartree-Fock methods [157]. However, the problem with these methods is the enormous computational effort, which makes it practically impossible to apply them efficiently to larger and more complex systems. In this case, DFT provides an attractive alternative, as it is much more versatile, offering a way to systematically map the many-body problem, through the $\hat{U}$ operator, into a single-body problem without $\hat{U}$. In DFT, the key variable is the electron density n, which for a normalized Ψ (the probability of finding the particle in the entire space being 1) is given by

$$n(r) = N \int d^3 r_2 \cdots \int d^3 r_N \Psi^*(r, r_2, \dots, r_N)\Psi\,(r, r_2, \dots, r_N) \tag{4.71}$$

where N is the total number of electrons in the system, d^3r represents the differential volume in a three-dimensional space (the molecule), and r_i is the position vector in the three-dimensional space of electron *i*. Eq. (4.71) can be inverted, that is, for a given ground-state density $n_0(r)$, it is possible, in principle, to calculate the corresponding ground-state wave function $\Psi_0\,(r, r_2, \dots, r_N)$. In other words, Ψ is a function of n_0

$$\Psi_0 = \Psi[n_0] \tag{4.72}$$

and, consequently, the expected value of an observable $\hat{O}$ in its ground state is a function of n_0. In particular, the energy of the ground state (E_0) is a function of n_0.

$$E_0 = E[n_0] = \left\langle \Psi[n_0] \middle| \hat{T} + \hat{V} + \hat{U} \middle| \Psi[n_0] \right\rangle \tag{4.73}$$

Eq. (4.73) can also be written as a function of n. Recall that the functionals $T[n]$ and $U[n]$ are universal, while $V[n]$ is a non-universal functional, as it depends on the system being studied. To minimize E_0, it is necessary to obtain n_0, and to do so, the functionals $[n]$, $U[n]$, and $V[n]$must be minimized. The minimization of $E[n]$ can be solved by applying the method of Lagrange undetermined multipliers.

DFT has a disadvantage in that, except for the simplest cases, the functional that relates the electron density to the energy of the system is not exactly known. However, in recent decades, methods have been developed that hybridize DFT with Hartree-Fock field theory, so that the simplicity of DFT and computational efficiency are maintained, while improving its ability to predict thermodynamic properties [158]. Hybrid functionals are a class of approximations to the energy functional in DFT that incorporate part of the exact exchange from Hartree-Fock theory along with the rest of the energy [159]. A hybrid functional is generally constructed as a linear combination of the Hartree-Fock exchange functional and other terms. Depending on the proportion of this combination, different methods are distinguished. Some of these methods that use hybrid functionals are B3LYP, PBE0, M06, and wB97X-D. This study provides an overview of each of them, including the modifications they introduce with respect to DFT, as well as their advantages and limitations.

Note that the functionals combined by each of the methods are complex, so the mathematical aspects of each one are not discussed in detail, but rather the linear combination of them. Finally, the values of ΔH_f^0 and ΔS_f^0 for IPDA and CA1 are calculated using these methods, and an average value of ΔG_r^0 is calculated.

4.4.2.2 B3LYP method

The B3LYP method uses the exchange-correlation functional $(E_{\mathrm{xc}}^{B3LYP})$, combining linearly the DFT energy functional, the Hartree-Fock energy functional (E_x^{HF}), and the energy functionals of Becke (E_x^{B}), and Lee-Yang-Parr (E_c^{LYP}) [158] as follows

$$E_{\mathrm{xc}}^{B3LYP} = (1-a)E_X^{LSDA} + aE_x^{HF} + bE_x^{B} + (1-c)E_c^{LSDA} + cE_c^{LYP} \tag{4.74}$$

where $a = 0.20$, $b = 0.72$ y $c = 0.81$ [158]. B3LYP uses a combination of approximations to describe both exchange energy and electron correlation. It is typically employed with Gaussian-type basis functions, such as ground-state wave functions or molecular orbitals commonly used in computational chemistry. However, its flexibility allows adaptation to other types of basic functions depending on the specific application. B3LYP is the most widely used hybrid DFT approach because it can accurately predict molecular structures, spectroscopic properties, chemical kinetics, and thermodynamic properties, among others. However, B3LYP is not reliable for modeling systems where non-covalent interactions are significant [160]. Nevertheless, in the reaction studied here, such interactions do not occur, so this does not pose a limitation for determining thermodynamic parameters.

4.4.2.3 PBE0 method

On the other hand, the PBE0 hybrid method mixes E_x^{HF} with the exchange energy and Perdew-Burke-Ernzerhof functionals (E_x^{PBE}) and (E_c^{PBE}) [161] as follows

$$E_{\mathrm{xc}}^{PBE0} = \frac{1}{4}E_x^{HF} + \frac{3}{4}E_x^{PBE} + E_c^{PBE} \tag{4.75}$$

Like the B3LYP method, PBE0 is typically used with Gaussian-type basis functions, although it can be adapted to other types of functions. This method has proven to be particularly effective in describing molecular structures and reaction energies, providing more accurate results than B3LYP in some cases [161]. Like B3LYP, PBE0 may have limitations in describing non-covalent interactions, such as hydrogen bonding. Additionally, PBE0 is usually more computationally expensive than B3LYP due to the inclusion of the exact Hartree-Fock correction.

4.4.2.4 M06 method

The M06 method was designed to provide a better description of a variety of chemical systems, including proton transfer reactions, hydrogen bonds, and systems with charge transitions [162]. This method uses a combination of approximations to describe exchange energy and electron correlation and mixes these functions with different orders of gradient, allowing it to capture a wide range of molecular behaviors. Generally, the linear combination is expressed as [163]

$$E_{\mathrm{xc}}^{M06} = \frac{X}{100} E_x^{HF} + (1 - \frac{1}{100}) E_x^{DFT} + E_c^{DFT} \tag{4.76}$$

Where X is the percentage of Hartree-Fock exchange in the hybrid functional, and E_x^{DFT} is the local DFT exchange energy (B3LYP or PBE0). The value of X represents the weight assigned to the contribution of Hartree-Fock exchange energy. This parameter determines the proportion in the linear combination and can vary depending on the specific version of the M06 method. The M06 method provides accurate results for a variety of chemical systems, including organic, inorganic, and organometallic molecules [162]. Additionally, the M06 method has been extended into specific variants, such as M06-2X and M06-L, which are designed to address specific challenges in describing certain types of systems or properties. On the other hand, M06 can be more computationally expensive compared to the previous methods.

4.4.2.5 wB97X-D method

wB97X-D is a DFT method that combines the Perdew-Burke-Ernzerhof (PBE) approximation for exchange energy with an empirical dispersion (D) correction developed by Grimme, known as the D3 correction [164]. The wB97X-D method provides an accurate description of a wide range of molecular properties, including structures, reaction energies, and bonding properties, while also accounting for dispersion interactions.

$$E_{\mathrm{xc}}^{wB97X-D} = (1 - w_D) E_{\mathrm{xc}}^{PBE} + w_D E_{\mathrm{xc}}^{D3} \tag{4.77}$$

Where E_{xc}^{D3} is the empirical dispersion correction obtained using Grimme's D3 method, and w_D is the weight assigned to the empirical dispersion correction, which determines the proportion of the D3 correction in the linear combination and may vary depending on the specific version of the wB97X-D method. This is the most recent method among all those mentioned and, therefore, addresses the deficiencies present in the other methods [164].

4.4.2.6 $\Delta G_{r,2}^0$ obtained from the different methods

In this study, the calculations of ΔH_f^0 and ΔS_f^0 for IPDA, CO_2, and CA1 were performed using the four hybrid DFT methods mentioned above. This type of analysis is often carried out using commercial computational chemistry software, such as Gaussian [1]. However, in this study, a different approach was chosen: simulations were conducted using an online software known as GAMESS/Psi4 [2] [165]. The choice was based on the accessibility and ease of use of the online software, without incurring additional costs associated with obtaining a Gaussian software license.

---

[1] https://gaussian.com

[2] https://chemcompute.org/psi4/status

Table 4.4. Values of ΔH_f^0, ΔS_f^0, ΔG_f^0 for CO_2, IPDA, and CA1 according to DFT hybrid methods B3LYP, PBE0, M06, and wB97X-D. Value of the Gibbs energy of the rection, ΔG_r^0, calculated with the above-mentioned methods. Values of ΔH_f^0, ΔS_f^0 for CO_2 in the literature are also collected.

Method	Parameter	CO_2	IPDA	CA1
Reference [166]	ΔH_f^0 $(\mathrm{kJ \cdot mol^{-1}})$	-394	-	-
	ΔS_f^0 $(\mathrm{J \cdot mol \cdot K^{-1}})$	214	-	-
B3LYP	ΔH_f^0 $(\mathrm{kJ \cdot mol^{-1}})$	-386	-383	-1253
	$\Delta S_f^0 (\mathrm{J \cdot mol \cdot K^{-1}})$	218	451	527
	ΔG_f^0 $(\mathrm{kJ \cdot mol^{-1}})$	-451	-517	-1,410
	$\Delta G_{r,2}^0$ $(\mathrm{kJ \cdot mol^{-1}})$		-442	
PBE0	$\Delta H_f^0 (\mathrm{kJ \cdot mol^{-1}})$	-393	-383	-1268
	$\Delta S_f^0 (\mathrm{J \cdot mol \cdot K^{-1}})$	213	455	517
	ΔG_f^0 $(\mathrm{kJ \cdot mol^{-1}})$	-456	-519	-1,422
	$\Delta G_{r,2}^0 (\mathrm{kJ \cdot mol^{-1}})$		-447	
M06	$\Delta H_f^0 (\mathrm{kJ \cdot mol^{-1}})$	-393	-383	-1268
	$\Delta S_f^0 (\mathrm{J \cdot mol \cdot K^{-1}})$	213	455	515
	ΔG_f^0 $(\mathrm{kJ \cdot mol^{-1}})$	-456	-519	-1,421
	$\Delta G_{r,2}^0 (\mathrm{kJ \cdot mol^{-1}})$		-446	
wB97X-D	$\Delta H_f^0 (\mathrm{kJ \cdot mol^{-1}})$	-393	-383	-1261
	$\Delta S_f^0 (\mathrm{J \cdot mol \cdot K^{-1}})$	213	451	515
	ΔG_f^0 $(\mathrm{kJ \cdot mol^{-1}})$	-456	-517	-1,414
	$\Delta G_{r,2}^0 (\mathrm{kJ \cdot mol^{-1}})$		-441	
Averages	$\overline{\Delta H_f^0}$ $(\mathrm{kJ \cdot mol^{-1}})$	-391±2	-383±1	-1263±3
	$\overline{\Delta S_f^0}$ $(\mathrm{J \cdot mol \cdot K^{-1}})$	214±1	453±1	519±6
	$\overline{\Delta G_f^0}$ $(\mathrm{kJ \cdot mol^{-1}})$	-454±1	-518±1	519±2
	$\overline{\Delta G_{r,2}^0}$ $(\mathrm{kJ \cdot mol^{-1}})$		-444±3	

Table 4.4 presents the $\Delta G_{r,2}^0$ value obtained with each DFT method. These values represent the free energy of the CO_2 capture reaction from the air, calculated from Eq. (4.67) using the ΔG_f^0 values for each molecule according to each method. As observed in Table 4.4, the ΔH_f^0 and ΔS_f^0values for CO_2 calculated with the PBE0, M06, and wB97X-D methods are consistent with each other and closely match the data found in the literature. Therefore, they can be considered reliable values, as they have been experimentally determined. The difference in ΔH_f^0 calculated by the PBE0, M06, and wB97X-D methods compared to the experimental value is 0.06 $\mathrm{kJ \cdot mol^{-1}}$, corresponding to an error of only $1.52 \cdot 10^{-5}$ $\mathrm{kJ \cdot mol^{-1}}$. Regarding ΔS_f^0, the difference is 1.21 $\mathrm{J \cdot mol \cdot K^{-1}}$, with an error of $5.66 \cdot 10^{-4}$ $\mathrm{J \cdot mol \cdot K^{-1}}$. In the case of the B3LYP method, the ΔH_f^0 and ΔS_f^0 values deviate more from the reference values, specifically by 7.59 $\mathrm{kJ \cdot mol^{-1}}$ and 4.55 $\mathrm{J \cdot mol \cdot K^{-1}}$, which corresponds to a relative error of $1.92 \cdot 10^{-3}$ $\mathrm{kJ \cdot mol^{-1}}$ and $2.13 \cdot 10^{-3}$ $\mathrm{J \cdot mol \cdot K^{-1}}$, respectively.

The four methods calculate similar ΔH_f^0 values for IPDA and CO_2, with the ΔH_f^0 of the CA1 molecule being significantly lower. This indicates that CA1 requires more energy to form from its constituent elements than IPDA. Although the exact values vary slightly between the different calculation methods, the general trend that CA1 has a lower ΔH_f^0 than IPDA is maintained in all cases. This suggests that this difference is not an anomaly of a particular method but a consistent feature of the molecules in question.

Since no specific information is available regarding the uncertainty associated with each individual calculation method or experimental validation data, to provide a single ΔH_f^0 value for IPDA and CA1, it is most appropriate to give the average value $\overline{(\Delta H_f^0)}$ and the associated uncertainty, defined as the standard deviation of ΔH_f^0 for each compound. Thus, $\overline{\Delta H_f^0}$ (IPDA) $=$ $-383\ \pm 1\ \mathrm{kJ\cdot mol^{-1}}$ and $\overline{\Delta H_f^0}$ (CA1) $=\ -1{,}263\ \pm 3\ \mathrm{kJ\cdot mol^{-1}}$ The same procedure will be followed for ΔS_f^0 and $\Delta G_{r,2}^0$.

Regarding ΔS_f^0, it seems that the calculation methods produce similar entropy values for IPDA (Table 4.4), which suggests a consistent trend across all methods. Concerning CA1, the calculation methods also show a consistent trend in entropy (Table 4.4). The fact that ΔS_f^0 for CA1 is higher than that for IPDA means that the formation of CA1 involves greater dispersion of energy or a higher number of possible configurations for the particles compared to the formation of IPDA. In general, solids (such as CA1) tend to have lower entropies than liquids (such as IPDA), but there are exceptions, and this may be the result of differences in molecular structure, the number of atoms, or functional groups [116]. The average entropy values are $\overline{\Delta S_f^0}(\mathrm{IPDA}) =$ $453\ \pm 1\ \mathrm{J\cdot mol^{-1}\cdot K^{-1}}$ and $\overline{\Delta S_f^0}(\mathrm{CA1}) =\ 519\ \pm 6\ \mathrm{J\cdot\ mol^{-1}\cdot K^{-1}}$.

Regarding ΔG_r^0, the methods show a consistent trend, with values between -441 and -447 $\mathrm{kJ\cdot mol^{-1}}$. Therefore, the average value of the free energy of the DAC reaction is $\overline{\Delta G_{r,2}^0} =\ -444\ \pm$ $3\ \mathrm{kJ\cdot mol^{-1}}$. Since the value of $\overline{\Delta G_{r,2}^0}$ is negative, it can be deduced that the CO_2 capture reaction with IPDA is spontaneous, which implies that the formation of CA1 is thermodynamically favorable under standard conditions. Since the stoichiometry of the reaction is 1:1, it is enough to calculate the product of $\overline{\Delta G_{r,2}^0} =\ -444\ \pm 3\ \mathrm{kJ\cdot mol^{-1}}$ and N_{CO2} to calculate the energy during the CO_2 capture reaction for 1 ton of CO_2. Specifically, the energy of the chemical reaction at this stage is $\Delta G_{r,2} = -1.01\cdot 10^{10}\ \mathrm{J\cdot ton^{-1}}$.

4.4.2.7 Determination of ΔG_{air}

According to Eq. (4.62), in addition to calculating $\Delta G_{r,2}$, it is necessary to determine ΔG_{air} in order to obtain the full energy of stage 2, $\Delta G_{S,2}$. From Eq. (4.53) we obtain that ΔG_{air} can be expressed as

$$\Delta G_{\mathrm{air}} = G_{\mathrm{air0}} - G_{\mathrm{air}} = \Delta U_{\mathrm{air}} - T_{\mathrm{RV}}\Delta S_{\mathrm{air}} + P_{\mathrm{RV}}\Delta V_{\mathrm{air}} \tag{4.78}$$

This stage involves the actual separation of CO_2 from the other components of air. Therefore, the changes in energy, entropy, and volume are referenced specifically to the separation of CO_2 from the remaining air components. Since this step takes place at the reservoir temperature, the term $T_{\mathrm{RV}}\Delta S_{\mathrm{air}}$ is exactly the same as calculated in subsection 3.1.2 that corresponded to the entropy of mixing of CO_2 in air. Thus, $T_{\mathrm{RV}}\Delta S_{\mathrm{air}} = 4.97\cdot 10^8\ \mathrm{J\cdot ton^{-1}}$. The terms ΔU_{air} and $P_{\mathrm{RV}}\Delta V_{\mathrm{air}}$, that in the ideal case studied in chapter 3 were null, now will be different from zero, and could be visualized as corrections to the entropy of mixing since the final stage of CO_2 is not that of an ideal gas, but it is trapped in the CA1 molecule.

The changes in energy, ΔU_{air}, and volume, ΔV_{air}, of the air are then exclusively due to the absence of CO_2 in air0. In this sense, ΔU_{air} corresponds to the loss of energy associated with the energy content of 1 ton of CO_2, as listed in Table 4.2: $\Delta U_{\mathrm{air}} = -U_{\mathrm{CO2}} = -1.41\cdot 10^8\ \mathrm{J\cdot ton^{-1}}$.

The term $P_{\mathrm{RV}}\Delta V_{\mathrm{air}}$ is related to the volume decrease caused by the removal of CO_2. Assuming that air behaves as an ideal gas both before and after CO_2 separation, the term $P_{\mathrm{RV}}\Delta V_{\mathrm{air}}$ can be calculated using: $P_{\mathrm{RV}}\Delta V_{\mathrm{air}} = -N_{CO2}RT_{\mathrm{RV}}$. Considering that one ton of CO_2 corresponds to 22,722 mol, the associated volume decrease gives $P_{\mathrm{RV}}\Delta V_{\mathrm{air}} = -5.63\cdot 10^7\ \mathrm{J\cdot ton^{-1}}$.

Therefore, the change in Gibbs free energy, calculated by Eq. (4.78), is $\Delta G_{\text{air}} = G_{\text{air0}} - G_{\text{air}} = 2.99 \cdot 10^8\ \text{J} \cdot \text{ton}^{-1}$.

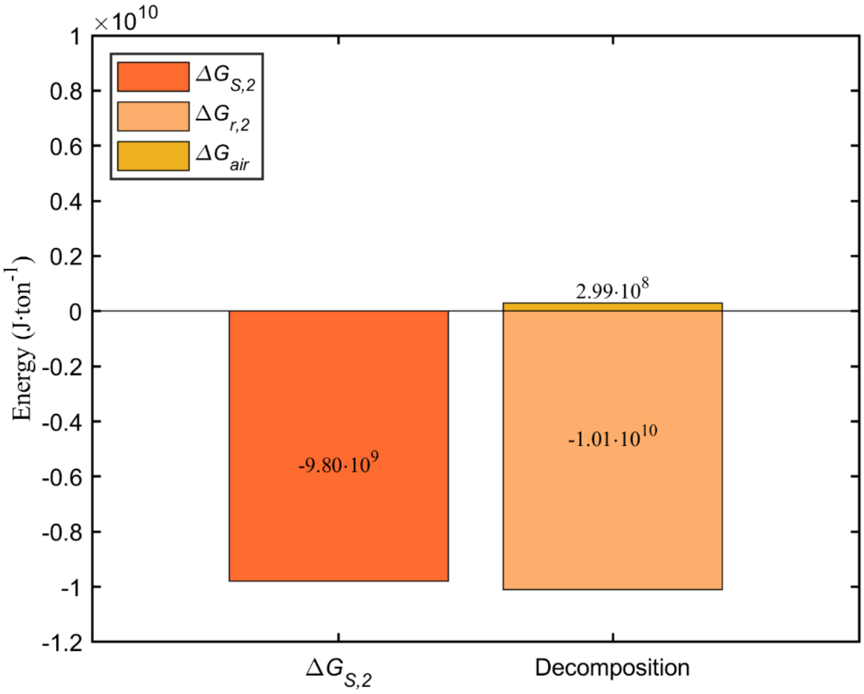

Figure 4.11 Contributions of the different energy components ($\Delta G_{r,2}, \Delta G_{\text{air}}$) in the reaction of CO_2 and IPDA.

Figure 4.11 shows how the energy of stage 2 is decomposed, with $\Delta G_{r,2}$ liberating $-1.01 \cdot 10^{10}\ \text{J} \cdot \text{ton}^{-1}$ and ΔG_{air} consuming $2.99 \cdot 10^8\ \text{J} \cdot \text{ton}^{-1}$. According to Eq. (4.61), in stage 2, $\Delta G_{\text{S},2} = Q_2 = \Delta G_{r,2} + \Delta G_{\text{air}}$, which is equivalent to $\Delta G_{\text{S},2} = Q_2 = -9.80 \cdot 10^9\ \text{J} \cdot \text{ton}^{-1}$, as depicted in Figure 4.11.

The negative sign of Q_2 indicates that the system does not consume energy but rather releases it, in this case, in the form of heat. In an ideal scenario, this energy could be harnessed by connecting the system to an electrochemical cell. However, it is assumed that the energy from this stage is lost as heat. Note that the energy released in this stage, Q_2, is due to the fact that the energy associated with the capture of CO_2, ΔG_{air}, is lower than the energy released by the reaction between IPDA and CO_2, $\Delta G_{r,2}$. In other words, the energy required for the separation of CO_2 is supplied by the chemical reaction itself. The condition $\Delta G_{\text{S},2} = 0$ defines the thermodynamic limit for CO_2 capture from air. that is, if ΔG_{air} ($2.99 \cdot 10^8\ \text{J} \cdot \text{ton}^{-1}$) exceeds $\Delta G_{r,2}$, the chemical reaction is no longer able to supply the energy required for CO_2 separation, and therefore, CO_2 cannot be captured from air under such conditions.

4.4.3 Stage 3: Separation of CO_2-free air (air0)

At the end of stage 2, the CO_2 from air has been absorbed leading to the formation of CA1. We have therefore a system composed of CA1 and air0 (CO_2-free air), and DMSO. From a strictly thermodynamic point of view the question that arises is what the degree of mixture we have among these components. If we assume some degree of mixture among them, following similar arguments to the ones used in chapter 2 to calculate the entropy of mixing between ideal gases, we should calculate their entropy of mixing and from this value to calculate the work necessary to separate air0 from the rest of the components. The task would not be easy since, this time, the components involved cannot all be dealt with as ideal gases (such as for example CA1, which is a solid, and IPDA, which is a liquid) and we lack a similar formula to Gibbs entropy of mixing for this case. Also, the degree of mixing is unknown, and we could in fact well assume that since CA1 is a solid, DMSO is a liquid, and air0 is a gas, no air0 is dissolved into CA1 or DMSO and bubbles up freely outside of the mixture thanks to its lower density. In this case, it would be Earth's gravitational field the one that would be assisting in providing the necessary work for the separation, work that in our introductory general description was assumed to be done by the displacement across the mixture of an idealized impermeable CO_2 membrane. With all these considerations we will not include this work in our calculations, either by assuming that it is not necessary because air0 is not mixed from CA1 nor IPDA from start or because Earths gravitational field provides the necessary work.

4.4.4 Stage 4: Heating

Initially the system consists of CA1 and DMSO at the pressure and temperature of the reservoir. Stage 4 consists of heating exclusively CA1 and DMSO until reaching the CO_2 desorption temperature, T_{CO2}. After the heating, the system consists of CA1 and DMSO at the temperature T_{CO2} and at the pressure of the reservoir. We assume that the work done on the system is zero, so $W_4 = 0$. In this stage we assume that the reservoir is only a pressure reservoir, thus, there is no entropy exchange between the system and the reservoir ($T_{\mathrm{RV}} \Delta S_{S,4} = 0$). Additionally, we assume that the volume change is negligible since solids and liquids are being heated, and no phase transition to gases occurs ($P_{\mathrm{RV}} \Delta V_{S,4} = 0$). This means that $\Delta U_{\mathrm{RV},4}$ is cero. Thus, the overall energy balance of this stage can be expressed as

$$Q_4 = \Delta U_{S,4} \tag{4.79}$$

The energy change in this stage ($\Delta U_{S,4}$) depends only on the temperature change, the quantity of heated components (m_i), and the specific heat capacity at constant pressure (C_p) of the substance. In a multicomponent system such as ours, the heat supplied to the system is equal to the sum of the heats of each component of the system [167] so Eq. (4.79) transforms into

$$Q_4 = \Delta U_{S,4} = \sum m_i \, C_{p,i} \Delta T \tag{4.80}$$

The heat calculated corresponds to the energy required to raise the system from the standard temperature ($T_1 = T_{\mathrm{RV}}$) to the temperature at which the dissociation reaction initiates (T_{CO2}). At no point is heat intended to be supplied during the reaction itself

The $C_p$value of CA1 was determined using the four hybrid DFT methods mentioned in stage 2 of the process (B3LYP, PBE0, M06, and wB97X-D). In contrast, the C_p value of DMSO is available in the literature [168]. Table 4.5 presents these values, along with the mass of each species heated during this stage.

Table 4.5. Values of C_p and masses, m, of CA1 and DMSO to capture one ton of CO_2.

Parameter	
Heat capacity CA1, $\overline{C_{p,\mathrm{CA1}}}(\mathrm{J \cdot kg^{-1} \cdot K^{-1}})$	$1.22 \cdot 10^3$
Heat capacity DMSO, $C_{p,\mathrm{DMSO}}(\mathrm{J \cdot kg^{-1} \cdot K^{-1}})$ [168]	$1.91 \cdot 10^3$
mass DMSO, $m_{\mathrm{DMSO}}(\mathrm{kg})$	$4.50 \cdot 10^4$
mass CA1, $m_{\mathrm{CA1}}(\mathrm{kg})$	$4.87 \cdot 10^3$

Let us recall that it has been experimentally determined that $\bar{T}_{\mathrm{CO2}} = 366.2$ K, and since $T_1 = T_{\mathrm{RV}} = 298.15$ K, the temperature increase during heating is $\Delta T = 68.2$ K.

Using the data from Table 4.5 and ΔT, it is calculated that the heat required for the system to reach the temperature T_{CO2} is $Q_4 = 6.27 \cdot 10^9\ \mathrm{J} \cdot \mathrm{ton}^{-1}$.

4.4.5 Stage 5: Desorption of CO2

The initial system consists of CA1 and DMSO at T_{CO2}. During the transformation, all the components will be assumed in equilibrium with a pressure reservoir at the pressure of the ambient and a heat reservoir at T_{CO2}. Stage 5 consists of the chemical desorption reaction of CO_2, in which CA1 is converted back into IPDA and CO_2. This desorption reaction is the reverse of the one studied in Stage 2. After the reaction, the system consists of CO_2, IPDA, and DMSO at T_{CO2} and at the pressure of the ambient reservoir. Following the same reasoning as in previous sections, since no work is applied to the system, the energy balance for this stage can be expressed as

$$Q_5 = \Delta U_{S,5} + \Delta U_{\mathrm{RV},5} = \Delta U_{S,5} - T_{\mathrm{CO2}} \Delta S_{S,5} + P_{\mathrm{RV}} \Delta V_{S,5} = \Delta G_{S,5}^{T_{\mathrm{CO2}}} \tag{4.81}$$

Following the reasoning from Stage 2, the ideal approach would be to determine $\Delta G_{S,5}^{T_{\mathrm{CO2}}}$ in the same manner as the Gibbs free energy in that stage, $\Delta G_{S,2}$. However, the software used to calculate $\Delta G_{S,2}$ is not capable of determining ΔH_f, ΔS_f, and ΔG_f at the temperature T_{CO2}. Therefore, the challenge in this stage is to determine $\Delta G_{S,5}^{T_{\mathrm{CO2}}}$ based on the value of $\Delta G_{S,2}$. This problem can be addressed using the *Gibbs-Helmholtz* equation, which is useful in many processes where the variation of Gibbs free energy ΔG with temperature needs to be determined [169–171] and that is given by

$$\left(\frac{\partial(\Delta G/T)}{\partial T}\right)_P = -\frac{\Delta H}{T^2} \tag{4.82}$$

Note that we already know the ΔG of the forward reaction at T_{RV} and ambient pressure, which corresponds to the formation of CA1. In this stage, the goal is to determine the Gibbs free energy of the reverse reaction at a different temperature (T_{CO2}). Since Gibbs free energy is a state function, the change in Gibbs free energy for the reverse reaction (ΔG_{inv}) at standard conditions will have the same magnitude but the opposite sign as the forward reaction (ΔG_{dir}), which in this case corresponds to $\Delta G_{S,2}$ [116]

$$\Delta G_{\mathrm{inv}} = -\Delta G_{\mathrm{dir}} \tag{4.83}$$

Enthalpy, also a state function, is treated accordingly, thus $\Delta H_{\mathrm{inv}} = -\Delta H_{\mathrm{dir}}$. At constant pressure, Eq. (4.82) can be reordered as

$$\partial\left(\frac{\Delta G}{T}\right) = -\frac{\Delta H}{T^2} \partial T \tag{4.84}$$

Integrating Eq. (4.84) with respect to the temperature between T_{CO2} and T_{RV}, we obtain the following expression

$$\frac{\Delta G_{\mathrm{inv}}(T_{\mathrm{CO2}})}{T_{\mathrm{CO2}}} - \frac{\Delta G_{\mathrm{inv}}(T_{\mathrm{RV}})}{T_{\mathrm{RV}}} = \Delta H_{\mathrm{inv}} \left(\frac{1}{T_{\mathrm{CO2}}} - \frac{1}{T_{\mathrm{RV}}}\right) \tag{4.85}$$

By rearranging Eq. (4.85), we obtain an explicit expression to determine $\Delta G_{\mathrm{inv}}(T_{\mathrm{CO2}})$ as a function of parameters calculated earlier

$$\Delta G_{\mathrm{inv}}(T_{\mathrm{CO2}}) = \Delta G_{S,5}^{T_{\mathrm{CO2}}} = T_{\mathrm{CO2}} \Delta H_{\mathrm{inv}} \left(\frac{1}{T_{\mathrm{CO2}}} - \frac{1}{T_{\mathrm{RV}}}\right) + \frac{T_{\mathrm{CO2}} \Delta G_{\mathrm{inv}}(T_{\mathrm{RV}})}{T_{\mathrm{RV}}} \tag{4.86}$$

Table 4.6. Values of ΔG_{inv} and ΔH_{inv} in the simulations of stage 2 and used in Eq. (4.86) to calculate $\Delta G_{\mathrm{inv}}(T_{\mathrm{CO2}}) = \Delta G_{S,5}^{T_{CO2}}$.

Property	
Free energy of inverse reaction at T_{RV}, ΔG_{inv} $(\mathrm{kJ} \cdot \mathrm{mol}^{-1})$	444.13
Inverse reaction enthalpy at T_{RV}, $\Delta H_{\mathrm{inv}} (\mathrm{kJ} \cdot \mathrm{mol}^{-1})$	489

With the values ΔG_{inv} and ΔH_{inv} collected in Table 4.6, the energy for the desorption reaction has been determined as $\Delta G_{S,5}^{T_{\mathrm{CO2}}} = 554.53\ \mathrm{kJ} \cdot \mathrm{mol}^{-1}$. The positive sign of $\Delta G_{S,5}^{T_{\mathrm{CO2}}}$ indicates that the desorption reaction is non-spontaneous, meaning that it requires an external energy input to occur. The total energy required by the system to desorb 1 ton of CO_2 from CA1 is $\Delta G_{S,5}^{T_{\mathrm{CO2}}} = 1.26 \cdot 10^{10}\ \mathrm{J} \cdot \mathrm{ton}^{-1}$. It is noted that a 100% reaction efficiency has been assumed, meaning that all of the CA1 dissociates into CO_2 and IPDA.

4.4.6 Stage 6: Separation of CO_2

This stage is similar to stage 3 but with CO_2 playing the role air0 played in stage 3. If we assume a model by which at the end of stage 5, CO_2 would be separated from IPDA-DMSO there would be no need to apply any work. However, if we assume a more general model in which at the end of stage 5 CO_2 is mixed with IPDA-DMSO, the application of some work would be necessary to compensate for the entropy of mixing. However, even in this case, given CO_2 is a gas, this work is provided by the gravitational field that makes CO_2 bubble to the surface of the mixture. However, as we did in stage 3, we will also neglect this work.

4.4.7 Stage 7: Cooling

Initially, the system consists of IPDA, DMSO, and CO_2 at T_{CO2} and at the standard pressure of the reservoir. The system is set in contact with the pressure reservoir and is let to quasi-statically cool down from T_{CO2} to T_{RV} (standard temperature). No external work is supplied to the system ($W_7 = 0$) during this process. The overall energy balance of the system and the pressure reservoir during this stage is given by

$$Q_7 = \Delta U_{S,7} + \Delta U_{\mathrm{RV},7} \tag{4.87}$$

where

$$\Delta U_{S,7} = \sum m_i\, C_{p,i} \Delta T \tag{4.88}$$

with *i* corresponding to IPDA, DMSO, and CO_2 while the energy change in the reservoir is

$$\Delta U_{\mathrm{RV},7} = P_{\mathrm{RV}} \Delta V_{\mathrm{CO2}} \tag{4.89}$$

In this last equation we have assumed that the only relevant change in volume corresponds to CO_2, given it is gas, while we have neglected the change in volume of IPDA and DMSO during the transformation since they are a liquid mixture.

Introducing the values of Table 4.7 in Eq. (4.88) we obtain that the system changes its energy in $\sum m_i\, C_{p,i} \Delta T = -3.49 \cdot 10^{8}\ \mathrm{J} \cdot \mathrm{ton}^{-1}$. The negative sign indicates that the system releases this energy.

To determine the energy change in the reservoir, it is necessary to evaluate the volume change associated with the cooling of the CO_2, according to Eq. (4.89). Assuming that CO_2 behaves as an ideal gas, this volume change can be calculated using one of the ideal gas equations of state, so that

$$\Delta U_{\mathrm{RV},7} = P_{\mathrm{RV}} \Delta V_{\mathrm{CO2}} = N_{\mathrm{CO2}} R \Delta T \tag{4.90}$$

where ΔT is the temperature difference from T_{CO2} to T_{RV}. Considering that 22,722 mol of CO_2 are cooling down during this stage, the energy difference experimented by the reservoir is $\Delta U_{\mathrm{RV},7} = -1.29 \cdot 10^7\ \mathrm{J} \cdot \mathrm{ton}^{-1}$. This energy corresponds to the work performed by the reservoir on the system because of the volume reduction of the CO_2.

Table 4.7. Values of C_p and masses, m, of IPDA, DMSO, and CO_2 to cool down one ton of CO_2 from T_{CO2} to T_{RV}.

Parameter	
Heat capacity IPDA, $\overline{C_{p,\mathrm{IPDA}}}$ ($\mathrm{J} \cdot \mathrm{kg}^{-1} \cdot \mathrm{K}^{-1}$)	$1.31 \cdot 10^3$
Heat capacity CO_2, $\overline{C_{p,\mathrm{CO2}}}$ ($\mathrm{J} \cdot \mathrm{kg}^{-1} \cdot \mathrm{K}^{-1}$)	$0.85 \cdot 10^3$
Heat capacity DMSO, $C_{p,\mathrm{DMSO}}$ ($\mathrm{J} \cdot \mathrm{kg}^{-1} \cdot \mathrm{K}^{-1}$) [168]	$1.91 \cdot 10^3$
mass DMSO, m_{DMSO} (kg)	$4.50 \cdot 10^4$
mass IPDA, m_{IPDA} (kg)	$2.22 \cdot 10^4$
mass CO_2, m_{CO2} (kg) [147]	$1 \cdot 10^3$

According to Eq. (4.87), the total heat of this stage is $Q_7 = -3.62 \cdot 10^8\ \mathrm{J} \cdot \mathrm{ton}^{-1}$. The negative sign indicates that the stage does not consume energy but rather releases it. In the best case, the heat released in this stage could be used for other stages of the DAC process, for example, by incorporating a heat exchanger into the system. However, in this analysis, such integration is not considered, so Q_7 is assumed to be an energy loss.

4.5 Summary

In this chapter we have replicated the DAC system based on the use of IPDA proposed by the research group of Kikkawa et al., from the Department of Chemistry of the Graduate School of Science of the Tokyo Metropolitan University.

The capture efficiency, η_{cap}, of the process has been experimentally determined for air flow rates ranging from 20 to 70 $\mathrm{mL} \cdot \mathrm{min}^{-1}$ with increments of 10 $\mathrm{mL} \cdot \mathrm{min}^{-1}$. Unlike the reference article, which evaluated only a flow rate of 20 $\mathrm{mL} \cdot \mathrm{min}^{-1}$, this study analyzed different operating regimes. The efficiency was obtained through differential weighing, showing that the best performance is achieved with a flow rate of 20 $\mathrm{mL} \cdot \mathrm{min}^{-1}$, reaching a capture efficiency of 96%. A decrease in capture efficiency was observed as the volumetric airflow increased. The results for 70 $\mathrm{mL} \cdot \mathrm{min}^{-1}$ show the lower capture efficiency, 63.9%. The decrease in capture efficiency at higher flow rates is explained by two factors: reduced contact time between air and the solution, which limits CO_2 diffusion, and turbulence in the reactor that decreases the effective reaction volume and causes material loss, affecting the final measurements. This finding suggests the need for further research to assess the impact of the capture system's design and geometry on process efficiency.

The CO_2 desorption temperature, T_{CO2}, was also experimentally determined in our laboratory, obtaining a value of 366.2 K. This result differs from the value reported by Kikkawa et al. (303 K), showing a temperature difference of 63.2 K. This difference is likely due to differences in the CO_2 detection systems used: the experimental setup implemented by Kikkawa et al. included an FT/IR detector connected to the reactor to analyze CO_2 desorption. In our case, CO_2 desorption was identified by the appearance of bubbles in the CA1-DMSO mixture and a color change from white to transparent.

A thermodynamic analysis of the DAC process, divided into seven stages, was carried out with the objective of determining the energy involved in each stage. This analysis, was detailed through sections to 4.4.1 to 4.4.7 and allowed for the calculation of how much energy this DAC process requires to separate one ton of CO_2 from the air. The results were presented at the beginning of the chapter in Figure 4.4. The analysis allowed us to identify which of these stages involve energy consumption and which, on the contrary, release it. In addition, it makes it possible to quantify the energy involved in each of them, thus revealing the critical stages of the process.

In this respect, the introduction of air in Stage 1 increased the internal energy of the system in $2.11 \cdot 10^{11}\ \mathrm{J} \cdot \mathrm{ton}^{-1}$, in addition, the system performed work of $1.39 \cdot 10^{11}\ \mathrm{J} \cdot \mathrm{ton}^{-1}$ to expand its volume. Additionally, the reservoir transferred $3.30 \cdot 10^{11}\ \mathrm{J} \cdot \mathrm{ton}^{-1}$ to the system as heat. The energy consumption in stage 1 reached $2.10 \cdot 10^{10}\ \mathrm{J} \cdot \mathrm{ton}^{-1}$, making it the most energy-intensive stage of this DAC process.

The reaction of CO_2 and IPDA in Stage 2 separated CO_2 from the rest of components in air. The separation of CO_2 from air required $2.99 \cdot 10^{8}\ \mathrm{J} \cdot \mathrm{ton}^{-1}$ and the chemical reaction liberated $-1.01 \cdot 10^{10}\ \mathrm{J} \cdot \mathrm{ton}^{-1}$. Thus, in Stage 2, $9.80 \cdot 10^{9}\ \mathrm{J} \cdot \mathrm{ton}^{-1}$ net were released from the system.

The separation of CO_2-free air (air0) in Stage 3 required no work from our part, since the Earth's gravitational field was the one providing the necessary work for the separation.

The heating of CA1 and DMSO in Stage 4 from the temperature of the reservoir to the experimental temperature for the desorption of CO_2, 366.2 K, required the application of $6.27 \cdot 10^{9}\ \mathrm{J} \cdot \mathrm{ton}^{-1}$ to the system as heat. This stage was the third highest in energy demand within the DAC process.

The desorption reaction of CO_2 in Stage 5 required the application of $1.26 \cdot 10^{10}\ \mathrm{J} \cdot \mathrm{ton}^{-1}$ to the system in the form of heat, making this stage the second highest in energy demand within the DAC process. The reaction occurred at 366.2 K.

Like Stage 3, no external work was required in Stage 6, since the separation of CO_2 was driven by Earth's gravitational field.

The cooling of CO_2, IPDA, and DMSO in Stage 7 from 366.2 K to 298 K made the system release $3.49 \cdot 10^{8}\ \mathrm{J} \cdot \mathrm{ton}^{-1}$. Besides, the cooling was accompanied by a reduction in the volume of CO_2, which made the system release $1.29 \cdot 10^{7}\ \mathrm{J} \cdot \mathrm{ton}^{-1}$. In total, the system released $3.62 \cdot 10^{8}\ \mathrm{J} \cdot \mathrm{ton}^{-1}$ in Stage 7.

Accounting the energy of all the stages in this process, the capture of one ton of CO_2 involved $5.00 \cdot 10^{10}\ \mathrm{J} \cdot \mathrm{ton}^{-1}$. The energy consumption of this process, which corresponded to the sum of Stages 1, 4, and 5 reached $3.99 \cdot 10^{10}\ \mathrm{J} \cdot \mathrm{ton}^{-1}$, represented 79.8% of the total energy. Compared with the theoretical minimum calculated in Chapter 3 ($4.97 \cdot 10^{8}\ \mathrm{J} \cdot \mathrm{ton}^{-1}$) this result is around 80 times higher. Assuming a constant electricity price, an energy consumption 80 times higher would result in an energy cost that is also 80 times greater. In Chapter 3, it was calculated that the minimum cost of the energy required to capture one ton of CO_2 from air is approximately $5.4\ \$ \cdot \mathrm{ton}^{-1}$. Therefore, if the process consumes 80 times more energy, the corresponding energy cost would increase proportionally, reaching around $432\ \$ \cdot \mathrm{ton}^{-1}$. Figure 3.4 illustrates the difference between the energy cost of this DAC method and the one derived from the thermodynamic minimum calculated in Chapter 3.

Stages 2 and 7 released a total of $1.02 \cdot 10^{10}\ \mathrm{J} \cdot \mathrm{ton}^{-1}$, which represented the 20.2% of the total energy. This implies that, while recovering and reusing the energy released in stages 2 and 7 could contribute to improving the efficiency of the process, the overall impact would be marginal.

Chapter 5. Design, manufacture, and characterization of a CO_2 electrolyzer aimed at producing formic acid

The advancement of CCUS technologies supports a circular carbon economy, where CO_2 is not discarded but reintegrated into industrial processes [172]. By recycling and repurposing carbon, these solutions reduce waste and optimize resource use, aligning with the broader goal of achieving a more sustainable and efficient economic system. As mentioned in Chapter 1, CO2RR technologies are expected to play a pivotal role in the development and implementation of CCUS technologies.

CO2RR via electrolysis can be powered with renewable electricity to convert captured CO_2 into valuable carbon-based products, such as carbon monoxide (CO) [173], formic acid (HCOOH) [174], methanol (CH_3OH) [175], and ethylene (C_2H_4) [176], which can serve as chemical feedstocks or fuels. By leveraging electrochemical catalysts, CO2RR enables the production of sustainable fuels and industrial chemicals while reducing reliance on fossil resources. This technology not only helps to mitigate emissions but also integrates carbon utilization with renewable energy, creating a closed-loop carbon cycle that aligns with global decarbonization efforts.

To better implement CCUS technologies, there is a need to integrate CO2RR technologies into a market-driven industrial economy, selecting a specific product requires careful consideration of multiple factors, including energy consumption per unit produced, market size, and overall profitability. Additionally, the performance and properties of an electrolyzer, particularly its selectivity for generating a single desired product, are determined by its configuration and the materials used—both in its structural components and in the working medium. In fact, the lack of selectivity towards the production of a specific compound is the primary challenge this process faces [177,178]. Nevertheless, selectivity can be improved by carefully tuning key operational parameters, such as electrode composition, catalyst properties, electrolyte composition, and reactor design [178]. Advances in material science and process engineering are continuously expanding the possibilities for enhancing selectivity and efficiency in CO2RR. A deeper understanding of these factors is important to optimize efficiency and ensure the feasibility of large-scale deployment. Moreover, accurately characterizing electrolyzer performance plays a vital role in coupling these systems with renewable energy sources, such as photovoltaic solar power, where the resulting fuels could be classified as solar fuels.

In this framework, the understanding of the practical details involved in the operation of a CO_2 electrolyzer, and its limitations become necessary as a prior step towards the optimization of its performance in a photovoltaic context.

This chapter is devoted to improving this understanding. Hence, in section 5.1, we consider the possibility of production of different products from the electrochemical reduction of CO_2: methane (CH_4), CO, HCOOH, solid carbon (C), CH_3OH, C_2H_4 and n-propanol (C_3H_7OH). Each of these products has specific industrial applications and varying levels of conversion efficiency. To select the most suitable CO2RR technology, a thermodynamic analysis to assess the energy feasibility of each reaction was conducted, as well as a cost study to determine the most economically viable option for solar fuel production. Formic acid was selected as the most suitable product. Section 5.2 contains information on the components and the set-up of the electrolyzer, which has been decided to implement for its synthesis in the laboratory of the Instituto de Energía Solar. Section 5.3 contains the explanation of the design of our electrolyzer to transform CO_2 into HCOOH. Additionally, as detailed in section 5.3, we have developed and manufactured various components of the electrolyzer, which are reviewed in this section. In section 5.4 we detail the assembly of the electrolyzer. Finally, section 5.5 includes the electrical characterization of the electrolyzer and the analysis of the chemical species produced during the CO2RR using this device.

5.1 Most suitable product for CO2RR

We hereby conduct an economic profitability analysis associated with the production of one metric ton of different organic compounds to justify the selection of a target compound. Table 5.1 presents the chemical reactions for the formation of each product from CO_2, as well as their market price per ton. Additionally, it includes the cost of the electricity required to synthesize one ton of each compound. The profitability of each product was determined by calculating the difference between its market price and the energy cost required for its production. This energy cost was estimated considering the current LCOE of photovoltaic solar energy ($35\ € \cdot \mathrm{MWh}^{-1}$) [179] and the energy needed for the reaction to occur.

Let us consider that all the energy required for each chemical reaction is supplied in the form of electrical work at constant standard pressure and temperature. In this context, the amount of energy in the form of work, W, that must be provided to carry out the chemical reaction is determined by the change in Gibbs free energy (ΔG) [116] between products and reactants. Therefore, the change in standard Gibbs free energy associated to the chemical reaction (ΔG_r^0) is defined as the difference between the standard Gibbs free energy of formation (ΔG_f^0) of the products and the reactants, as stated in Eq. (4.63) from section 4.4.2 [116]:

$$\Delta G_r^0 = \sum_{\mathrm{Prod}} \Delta G_f^0 - \sum_{\mathrm{React}} \Delta G_f^0 \tag{4.66}$$

Table 5.1 provides the values of standard Gibbs free energy of formation for both the products and the reactants in each CO2RR. However, to determine the work required to produce one ton of each product, the molecular weight of each specific compound must be considered. Finally, the economic cost of supplying this work has been determined by multiplying it by the LCOE of photovoltaic solar energy, as collected in Table 5.1.

For clarification, let us consider, as an example, the formation of CO. The reaction is as follows

$$CO_2(g) + H_2O(l) \rightarrow CO(g) + O_2(g) + H_2(g) \tag{R.10}$$

The work required to carry out the reaction per mol of CO is determined by the change in Gibbs free energy:

$$W = \Delta G_f^0[\mathrm{CO}(g)] + \Delta G_f^0[\mathrm{O_2(g)}] + \Delta G_f^0[H_2\mathrm{(g)}] - \Delta G_f^0[\mathrm{CO_2(g)}] - \Delta G_f^0[\mathrm{H_2O(l)}] \tag{5.1}$$

where $\Delta_f G^0$ is the Gibbs energy of formation of the compound indicated in square brackets in standard conditions. The resulting figure, taking the data from Ref. [115] for CO is $\Delta W = 542.9\ \mathrm{kJ} \cdot \mathrm{mol}^{-1}$. Obtaining 1 ton of CO, rather than 1 mol (28.01 g), would require 5.4 MWh of energy. Considering the LCOE for utility-scale crystalline silicon solar systems [179] ($35\ € \cdot \mathrm{MWh}^{-1}$) producing 5.4 MWh of PV electricity would result in a minimum cost of approximately $189\ € \cdot \mathrm{t}^{-1}$. Comparing this cost to the current market price of CO, which is $184\ € \cdot \mathrm{t}^{-1}$ [180], we conclude that the production of CO from CO_2 and H_2O is not economically viable at present. This straightforward analysis leads to the conclusion that, given the current costs, it would not be feasible to produce CO as a solar fuel at competitive prices.

Table 5.1 Electricity cost per metric ton (t) of product assuming an electricity price of 35 $€ \cdot \text{MWh}^{-1}$ and that the minimum amount of energy allowed by thermodynamics is used to synthetize the product from CO_2 via the methods above stated. For the calculations the following data have been assumed: $\Delta G_f^0 = -394.359 \text{ kJ} \cdot \text{mol}^{-1}$ for CO_2(g); $\Delta G_f^0 = -237.19 \text{ kJ} \cdot \text{mol}^{-1}$ for H_2O(l); $\Delta G_f^0 = 0 \text{ kJ} \cdot \text{mol}^{-1}$ for O_2, H_2, and C [115].

Product	Reaction	Market price ($€ \cdot \text{t}^{-1}$)	$\Delta_f G^0$ ($\text{kJ} \cdot \text{mol}^{-1}$) [181]	W ($\text{kJ} \cdot \text{mol}^{-1}$)	Molar weight (g) [181]	Electr. cost ($€ \cdot \text{t}^{-1}$)	Economic margin ($€ \cdot \text{t}^{-1}$)	E^0_{cell} (V)
Carbon monoxide (CO)	$CO_2(g)+H_2O(l) \rightarrow CO(g)+O_2(g)+H_2(g)$	184 [180]	-137.3	542.9	28.01	189	-425	1.33
Methane (CH_4)	$CO_2(g)+4H_2(g) \rightarrow CH_4(g)+2H_2O(l)$	496 [182]	-50.72	808.0	16.04	490	-426	1.06
Formic acid (HCOOH)	$2H_2O(l)+2CO_2(g) \rightarrow 2HCOOH(l)+O_2(g)$	838 [183]	-385.8	491.5	46.03	104	302	1.43
Carbon (C)	$CO_2(g) \rightarrow C(s)+O_2(g)$	32 [184]	0	394.4	12.01	320	-719	1.64
Methanol (CH_3OH)	$4H_2O(l)+2CO_2(g) \rightarrow 2CH_3OH(l)+3O_2(g)$	555 [185]	-166.27	702.5	32.04	214	-91	1.20
Ethylene (C_2H_4)	$2CO_2(g)+2H_2O(l) \rightarrow C_2H_4(g)+3O_2(g)$	1135 [186]	-68.15	1194.9	27.05	431	272	1.15
n-Propanol (C_3H_7OH)	$6CO_2(g)+8H_2O(l) \rightarrow 2C_3H_7OH(l)+9O_2(g)$	1200 [187]	-161.90	3,940.1	60.09	638	130	1.13

Table 5.1 presents the results of the above calculations for several products. In the case of methane, the thermodynamic cost is estimated at 490 $€ \cdot \text{t}^{-1}$, compared to a market price of 496 $€ \cdot \text{t}^{-1}$ [182]. For formic acid, the thermodynamic cost is significantly lower, at 104 $€ \cdot \text{t}^{-1}$, while its market price reaches 838 $€ \cdot \text{t}^{-1}$ [183]. Similarly, methanol presents a thermodynamic cost of 214 $€ \cdot \text{t}^{-1}$, compared to a market price of 555 $€ \cdot \text{t}^{-1}$[185], while for ethylene, the cost reaches 431 $€ \cdot \text{t}^{-1}$ against a market price of 1135 $€ \cdot \text{t}^{-1}$ [186]. In the case of n-propanol, the estimated thermodynamic cost is 638 $€ \cdot \text{t}^{-1}$, whereas its market price is 1,200 $€ \cdot \text{t}^{-1}$ [187]. These figures indicate that, under ideal thermodynamic conditions, all these products could be produced at costs below current market prices, leaving a margin of 6 $€ \cdot \text{t}^{-1}$ for methane, 734 $€ \cdot \text{t}^{-1}$ for formic acid, 341$€ \cdot \text{t}^{-1}$ for methanol, 704 $€ \cdot \text{t}^{-1}$ for ethylene and 562 $€ \cdot \text{t}^{-1}$ for n-propanol to account for system inefficiencies, as well as CAPEX and OPEX expenses. On the other hand, the production of solid carbon results in a negative balance of -287.5 $€ \cdot \text{t}^{-1}$, as its estimated production cost is 319.5 $€ \cdot \text{t}^{-1}$, while its market value fluctuates around 32 $€ \cdot \text{t}^{-1}$ [184].

Assuming that the cost of capturing one ton of CO_2 using a diamine-based DAC system is 432 $\$ \cdot \text{ton}^{-1}$, we can assess the economic viability of producing various CO_2-derived products based on their ideal thermodynamic profit margins. To facilitate comparison, and assuming approximate parity between the euro and the dollar, a product is considered viable only if its profit margin exceeds the CO_2 capture cost. Based on the available data, formic acid (302 $€ \cdot \text{t}^{-1}$), ethylene (272 $€ \cdot \text{t}^{-1}$), and n-propanol (130 $€ \cdot \text{t}^{-1}$) all present sufficient margins to remain economically viable. In contrast, methane (-426 $€ \cdot \text{t}^{-1}$) and methanol (-91 $€ \cdot \text{t}^{-1}$) fall below the viability threshold, with methanol being close but still not sufficient. This analysis illustrates that for CO2RR to be economically feasible, particularly when using CO_2 from DAC, the chosen products must yield high enough value to offset the significant cost of CO_2 capture. Economic margin of each compound is collected on Table 5.1.

Before selecting a desired product, in addition to its minimum cost, it is also convenient to review some fundamental concepts of electrochemistry and electrolyzers: electrochemical reactions consist of two simultaneous half-reactions that occur at the electrodes of an electrochemical system, the electrolyzer. Oxidation takes place at the anode, where a chemical species loses electrons, while reduction occurs at the cathode, where a species gains electrons. These half-reactions are electrically coupled, meaning that the electrons released at the anode travel through an external circuit to the cathode, where they participate in the reduction process. In the CO_2 electrolyzer, the reaction at the anode is known as the oxygen evolution reaction (OER) and the reaction at the cathode is known as CO2RR. The feasibility of these half-reactions is determined by their thermodynamic potential, which establishes the theoretical minimum voltage required for the reaction to occur and can be calculated as follows:

$$E^0 = \frac{\Delta G_r^0}{zF} \tag{5.2}$$

where ΔG_r^0 denotes the standard Gibbs free energy of the reaction, z denotes the number of electrons transferred per molecule of product, and F denotes the Faraday constant (96,500 $\mathrm{C \cdot mol^{-1}}$). The cell potential ($E^0_{\mathrm{cell}}$) determines the overall electrochemical reaction in the electrolyzer and is given by:

$$E^0_{\mathrm{cell}} = E^0_{\mathrm{CO2RR}} - E^0_{\mathrm{OER}} \tag{5.3}$$

the value of E^0_{cell} represents the minimum thermodynamic voltage in which the overall reaction can occur. The OER occurs at a standard thermodynamic potential (E^0_{OER}) of 1.23 V versus the standard hydrogen electrode, while values of standard CO2RR (E^0_{CO2RR}) are found in the literature [58]. Values of E^0_{cell} for different CO2RR reactions are collected in Table 5.1. These reactions have similar E^0_{cell} while producing different species, meaning that operating at a given E^0_{cell} does not ensure the formation of a single product. Consequently, product selectivity cannot be achieved solely by tuning the working electrode voltage. Moreover, a specific E^0_{cell} does not correspond to a particular product and is not the only variable that explains the energy consumed to synthesize it, therefore, minimizing its value does not justify the selection of a particular product.

Beyond the profitability and electrochemical considerations, it is also essential to consider the market size of each product, as larger markets may offer greater economic opportunities. In this regard, methane has the largest market size at 250 $\mathrm{Mt \cdot y^{-1}}$ [188], followed by carbon monoxide at 150 $\mathrm{Mt \cdot y^{-1}}$[188], ethylene at 140 $\mathrm{Mt \cdot y^{-1}}$ [58], and methanol at 110 $\mathrm{Mt \cdot y^{-1}}$ [188]. In contrast, formic acid and n-propanol have significantly smaller market sizes, at 0.6 $\mathrm{Mt \cdot y^{-1}}$ [188] and 0.2 $\mathrm{Mt \cdot y^{-1}}$ [58], respectively. This suggests that, while certain products may have favorable margins, their overall economic impact will also depend on the scale of demand in their respective markets.

Furthermore, from a practical standpoint, there is a greater interest in liquid –rather than gaseous– products at ambient temperature due to their higher energy density and ease of handling. Higher energy density is an important factor in fuel applications, as it enables more efficient storage and transportation, making liquids more suitable for large-scale energy distribution compared to gaseous alternatives. In addition, liquids are generally easier and safer to transport, store, and integrate into existing infrastructure. In this context, methane, carbon monoxide, and ethylene, which are gaseous under standard conditions, pose additional challenges in terms of compression, liquefaction, and distribution. Conversely, products such as methanol, formic acid, and n-propanol, which remain liquid at ambient temperature, offer significant advantages in terms of logistics and industrial applicability, making them particularly attractive for energy and chemical production.

Having considered profitability, market size, and the ease of transporting liquid products, it can be concluded that formic acid production, despite its relatively small market size, remains a highly promising option. It is a profitable product and, the fact that it is a liquid at standard temperature and pressure, offers significant advantages in terms of handling, storage, and transportation. Its liquid state simplifies the logistical aspects of post-production use, making it more efficient to integrate into existing systems. These factors strongly support our choice, as they highlight both the economic and practical benefits of producing formic acid, even with the challenges presented by its market size. In addition, we aim to fabricate an electrolyzer inspired by the formic acid electrolyzer developed by Dioxide Materials [3], given the availability of the components that make up the electrolyzer. This approach is motivated by the practicality of using readily accessible materials, which should allow for easier reproduction and potential scaling of the system in the future.

5.2 Electrolyzer for formic acid production

In this subsection, we will describe the electrolyzer meant to produce HCOOH, its components, and its functioning. The electrolyzer design is based on the three-chamber electrolyzer concept, similar to the one developed, manufactured, and commercialized by the U.S. company Dioxide Materials [189]. However, on the one hand, due to the limited information provided by the company, and on the other hand, the need to implement a flexible design that allowed us to test different elements in the context of our collaboration with the Instituto de Catálisis y Petroleoquímica (ICP) at the Consejo Superior de Investigaciones Científicas (CSIC) in the framework of common research projects, many design choices have been made different from the commercial HCOOH electrolyzer. Such original design criteria have allowed us to adapt it to our research requirements, based on findings from scientific literature.

Figure 5.1 presents the exploded view of the three-chamber electrolyzer designed at IES-UPM. Each of the three chambers of the electrolyzer is associated with a different circuit: (1) the anode chamber, composed of the anodic bipolar plate, the anode, and the Nafion® membrane, linked to the H_2O circuit; (2) the cathode chamber, which includes the cathodic bipolar plate, the cathode, and the Sustainion® membrane, and is connected to the CO_2 circuit; (3) the middle chamber is associated with the produced HCOOH, which is contained in a circulating aqueous solution that gradually becomes enriched.

The H_2O introduced through the anodic bipolar plate reaches the anode and is converted into protons (H^+), electrons (e^-) and gaseous O_2, as shown in reaction (R.11) [97]. This reaction is known as the OER. Deionized water is introduced through Entrance 1 (Figure 5.1) from an external reservoir using a micropump. Once inside, water circulates through the serpentine channel of the anodic bipolar plate, which is in contact with the surface of the anode. The gaseous O_2 diffuses through the anode and is transported by the serpentine channel of the anodic bipolar plate, exiting the anode chamber along with the unreacted H_2O through Exit 1 (Figure 5.1). The H^+ ions pass through the Nafion® NM-117 membrane, which is selective for cation transport, allowing their migration to the middle chamber. The electrons generated in the anode travel to the cathode through an external circuit.

---

[3] https://dioxidematerials.com

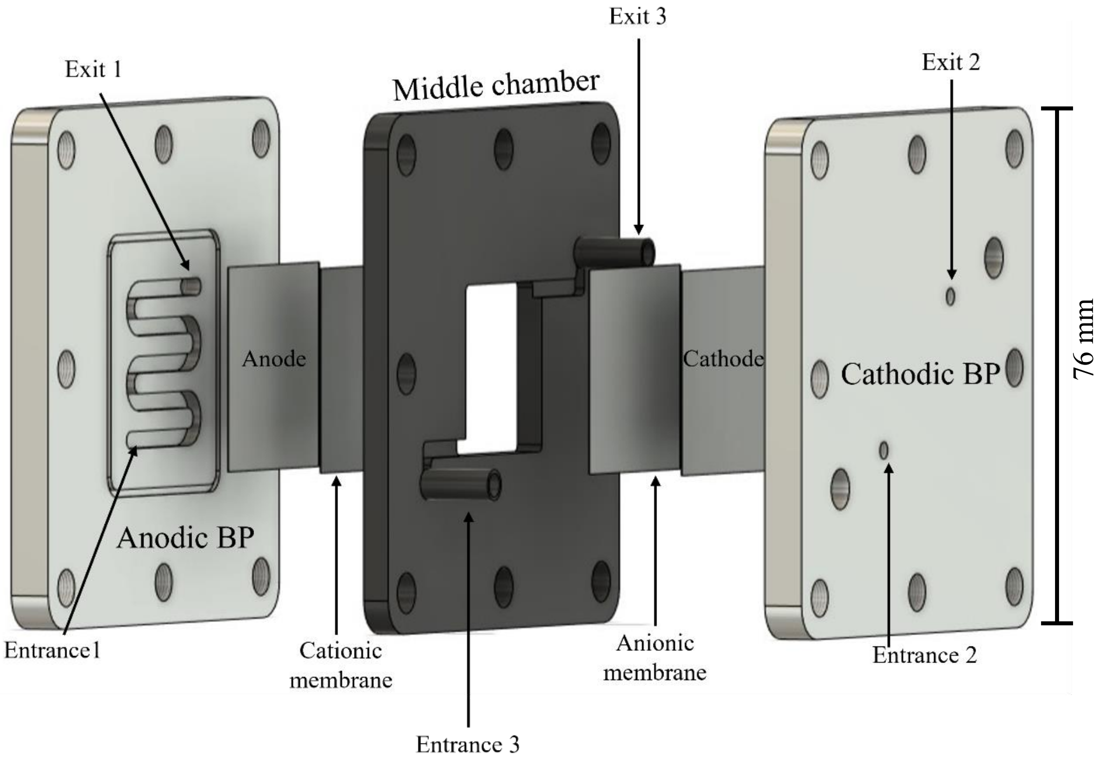

Figure 5.1 Depieced electrolyzer and its components from left to right: aluminum anodic bipolar plate, carbon cloth anode with RuO_2, Nafion® NM-117 membrane, PLA middle chamber, Sustainion® X37-FA membrane, silver cathode, and aluminum cathodic bipolar plate.

The reaction (R.11) and the flow path of the products are illustrated on the left side of Figure 5.2.

$$H_2O\ (l) \rightarrow \frac{1}{2} O_2(g) + 2H^+ + 2e^- \tag{R.11}$$

In the cathode, CO_2 captures the electrons generated in the oxidation reaction at the anode, which are conducted through the external circuit. Thus, CO_2 reacts with H_2O to produce formate ($HCOO^-$) and hydroxide (OH^-) anions as shown in reaction (R.12) [189]. CO_2 is introduced into the electrolyzer through Entrance 2 (Figure 5.1) from a CO_2 cylinder. Once inside, CO_2 circulates the serpentine channel of the cathodic bipolar plate, which is in direct contact with the cathode. The cathode remains moistened because it is also in close contact with the Sustainion® membrane, which is hydrated by water coming from the middle chamber. The formate ($HCOO^-$) and hydroxide (OH^-) anions migrate through the Sustainion® anionic membrane into the middle chamber. This part of the process is illustrated on the right side of Figure 5.2.

$$H_2O\ (l) + CO_2 + 2e^- \rightarrow HCOO^- + OH^- \tag{R.12}$$

In the cathode, as in any CO2RR reaction, multiple competing chemical reactions can take place [190]. In other words, besides the formation of formate anions, CO_2 can also be reduced to other compounds (CO-R in Figure 5.2). This phenomenon is common in CO2RR electrolyzers. Achieving the selective production of a single compound is one of the main challenges in the development of CO_2-based fuel production [190,191]. In section 5.5, it will be shown that, indeed, additional species have been produced at the cathode. More details on this will be provided in subsection 5.5. The thermodynamic potential of several CO2RR is collected in Table 5.1. This potential is related to the voltage at which the respective electrolyzer is biased. At the very least, so that the voltage in terminals is greater than that limit in order to produce that compound.

In the middle chamber, protons from the anode chamber react with the formate and hydroxide anions arriving from the cathode chamber. This reaction leads to the formation of formic acid and additional water (R.13) [189].

$$\mathrm{HCOO^- + OH^- + 2H^+ \rightarrow\ HCOOH\ (l) + H_2O\ (l)} \qquad \text{(R.13)}$$

Initially, the middle chamber is filled with water, which is introduced through Entrance 3 in Figure 5.1. The produced formic acid exits the middle chamber through Exit 3. Both Entrance 3 and Exit 3 are tubes that pass through the cathodic bipolar plate and are connected to a liquid tank. The liquid is recirculated through the middle chamber to gradually concentrate the formic acid in the water over time.

For the anode (R.11) and cathode (R.12) reactions to take place, they must be connected to an electrical power source capable of applying a voltage bias between them. These reactions will only occur once a certain threshold voltage is exceeded [192,193]. The threshold voltage of an electrochemical reaction is determined by the standard thermodynamic potential of the overall reaction (E^0_{cell}) and the overpotentials. In practice, the actual threshold voltage exceeds E^0_{cell} due to overpotentials arising from kinetic factors such as slow electron transfer, energy barriers at the electrode surface, and catalyst properties [194]. As explained in Chapter 2, there are three types of overpotentials: activation overpotential [195], concentration overpotential [196], and ohmic losses [197].

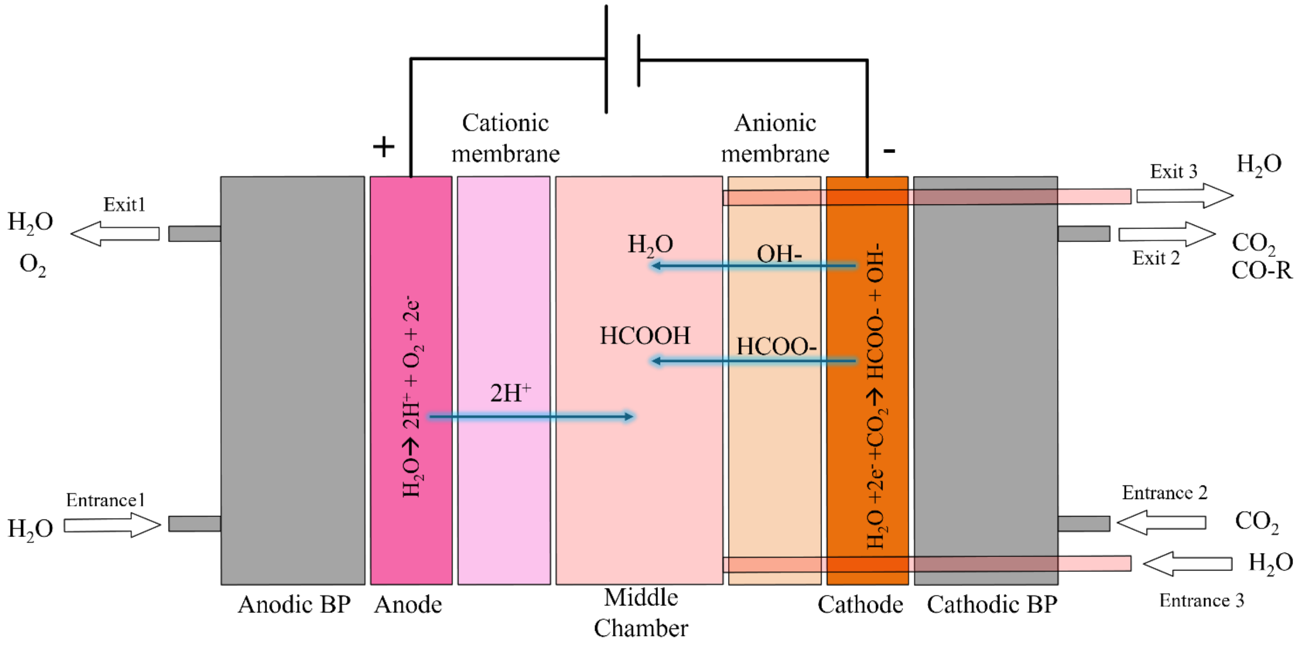

Figure 5.2 Diagram of the components and reactions in the three-chamber CO_2 electrolyzer for formic acid (HCOOH) production. The electrolyzer is connected to an electrical source, such as a PV array, which provides the required voltage bias to the electrodes.

Once the threshold voltage is surpassed, an electric current begins to flow through the electrolyzer, meaning that reactions at the anode and the cathode are occurring [198]. Within the electrolyzer, the electric current does not flow through the transport of electrons but rather through the movement of ions—protons, hydroxide ions, and formate ions—across the different chambers of the electrolyzer [189]. The production of the electrochemical reactions (R.11) and (R.12) per unit of time is greater the higher the current. This is because electric current is directly related to the number of electrons transferred in the reaction. As the current increases, more atoms or molecules participate in the reaction, which increases the production of the desired product. The reaction in the middle chamber (R.13) is not electrochemical like the reactions at the anode and cathode, meaning it does not require exceeding a specific voltage threshold to occur *per se*. In fact, it could occur if protons, formate, and hydroxide ions are present in the medium. However, in this electrolyzer, it depends on the reactions at the electrodes—meaning it will not take place until the voltage threshold at the electrodes of the three-chamber electrolyzer is surpassed.

The electrolyzer consists of the following components:

- Two bipolar plates (BPP): one anodic (Figure 5.3a) and one cathodic (Figure 5.3b). The BPP are electrically conductive, flat separators designed to accommodate the voltage of the power supply. They must minimize the addition of series resistance to the whole electrical electrolyzer circuit. Additionally, they provide mechanical strength to the electrolyzer, necessitating high mechanical and chemical stability [93]. The bipolar plates of this electrolyzer feature feedthroughs that connect to a milled serpentine channel within them as observed in Figure 5.3. These feedthroughs link the serpentine channels to the CO_2 circuit in the cathodic bipolar plate and to the H_2O circuit in the anodic bipolar plate. Both bipolar plates also have eight perforations around their perimeter to facilitate the assembly and tightening of the electrolyzer. Additionally, the cathodic bipolar plate has two extra feedthroughs compared to the anodic bipolar plate. These additional feedthroughs enable the connection to the central chamber of a closed-circuit water flow that will accumulate the production of HCOOH. Both bipolar plates are made of aluminum.

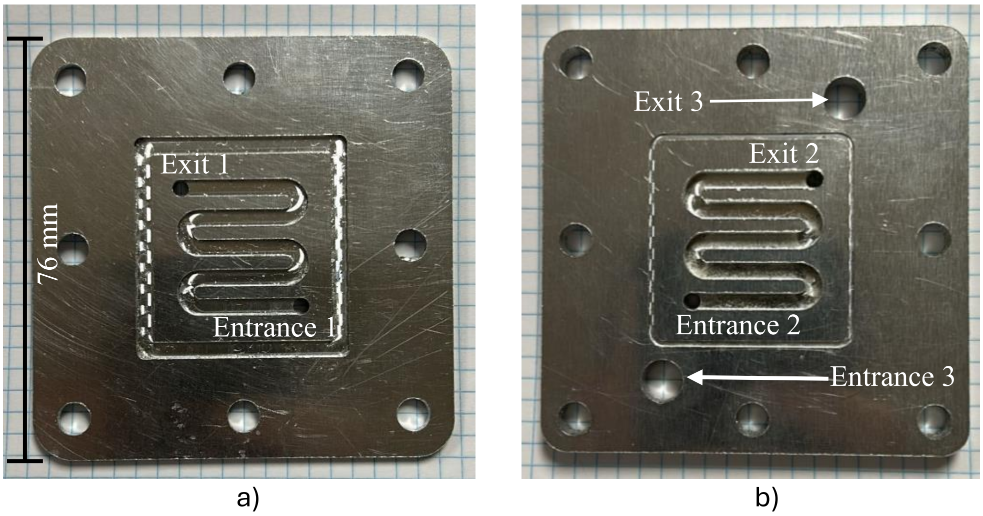

Figure 5.3 Bipolar plates made of aluminum for the three-chamber CO_2 electrolyzer to produce HCOOH.

- Anode. It consists of carbon cloth coated with ruthenium dioxide (RuO_2) because this functions as a gas diffusion layer (GDL), which is crucial for the proper operation of the system [199]. As will be seen In Chapter 5, reaction R.1 is the reaction that takes place at the anode of PEM electrolyzers for hydrogen production [36]. In PEM technology, iridium oxide (IrO_2) is typically used as a catalyst due to its high catalytic activity, corrosion resistance, and durability [200]. These properties make it an optimal catalyst for the anodic reaction in the formic acid electrolyzer and, in fact, it is the catalyst used in the commercial electrolyzer from Dioxide Materials [189]. However, this catalyst is one of the most expensive components in PEM electrolyzers [201], and it would also be a costly choice for our electrolyzer. Ruthenium belongs to the same group as iridium in the periodic table. Both RuO_2 and IrO_2 share similar properties, such as high electrical conductivity and good stability in acidic media [202]. However, RuO_2 is more abundant and less expensive than IrO_2, making it an attractive alternative as a catalyst in electrolyzers. A sample of the anode can be seen in Figure 5.4a.

- Cathode. It consists of cloth with silver particles (Ag), which serves as a common catalyst in CO2RR thanks to the easy synthesis, relatively low cost, and excellent catalytic activity [203]. A sample of the cathode can be seen in Figure 5.4b.

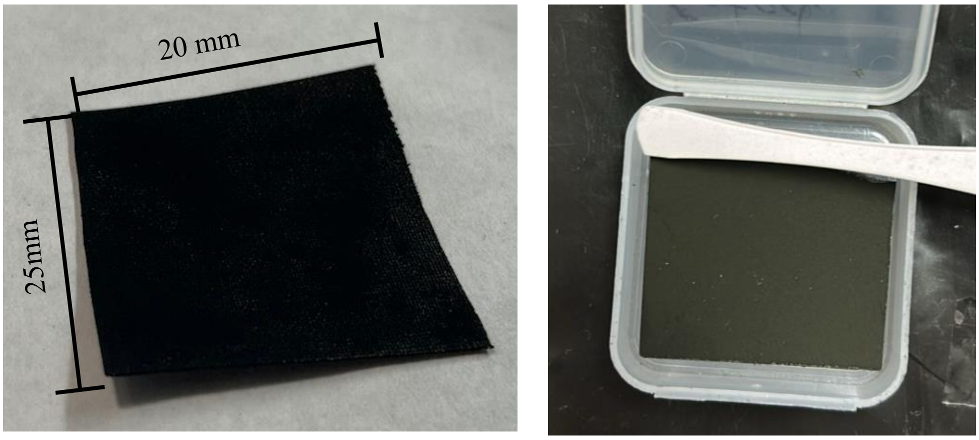

a) b)

Figure 5.4 a) Anode composed of carbon cloth with ruthenium oxide (RuO_2) deposition b) Cathode composed of carbon fibers with silver deposition, purchased from Dioxide Materials.

- Cationic membrane Nafion® (NM-117). On one side, it is in direct contact with the anode, while on the other, it interfaces with the middle chamber. This membrane is selectively permeable to cations, allowing only the protons generated at the anode to pass into the middle chamber [204]. Its chemical structure contains perfluorosulfonic acid functional groups. The NM-117 membrane can be seen in Figure 5.5a.
- Anionic membrane Sustainion® (X37-FA). On one side, it is in direct contact with the cathode, while on the other, it interfaces with the middle chamber. This membrane is selectively permeable to anions, allowing the formate and hidroxile ions generated at the cathode to pass into the middle chamber [189]. Its chemical structure contains perfluorosulfonic acid functional groups [189]. The X37-FA membrane can be seen in Figure 5.5b.

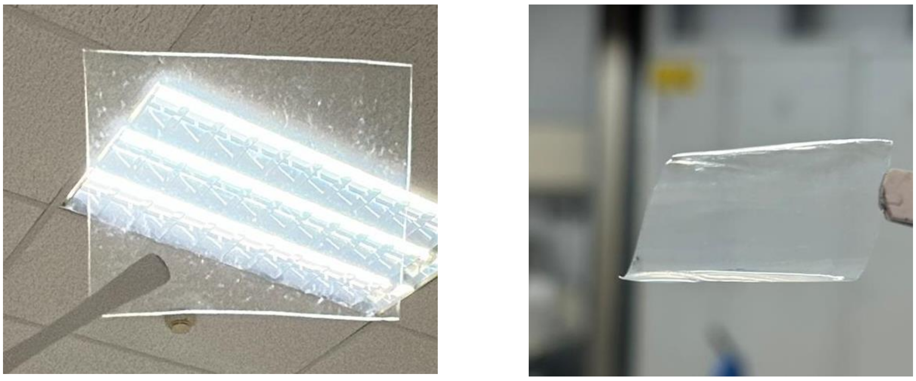

a) b)

Figure 5.5 a) Cationic membrane Nafion® NM-117 b) Anionic membrane Sustainion® X37-FA.

- Middle chamber. It is positioned between the cationic and anionic membranes, making contact with both. Inside, the protons generated at the anode react with the formate ions produced at the cathode to form HCOOH (R.13). This chamber was designed in our facilities and manufactured using 3D printing with polylactic acid (PLA). Additionally, it features two hollow protrusions that pass through the cathodic bipolar plate, as shown in Figure 5.6.

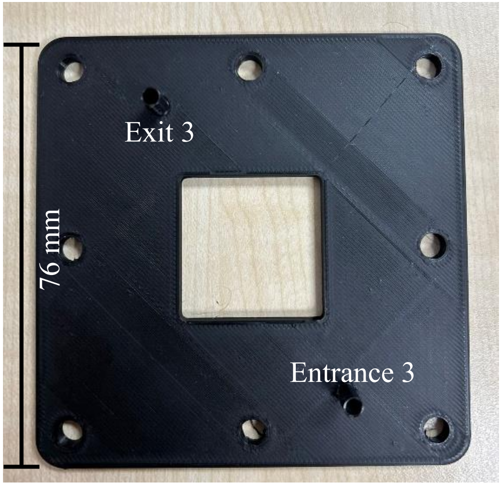

Figure 5.6 Middle chamber printed in polylactic acid (PLA), with an embedded circuit for water inlet and the outlet of water and formic acid. Its thickness is 2 mm.

5.3 Design and manufacture of the electrolyzer

All components of the electrolyzer, except for the silver cathode and the anionic and cationic membranes, were designed and manufactured at IES-UPM.

This section focuses on the design and processing of the components fabricated in our facilities, as well as the challenges encountered throughout the process, from the design to the assembly of the components.

5.3.1 Design and fabrication of bipolar plates

As mentioned, the design of the bipolar plates was inspired by the formic acid electrolyzer commercialized by Dioxide Materials. However, we introduced several modifications, including changes to the serpentine flow field, the thickness of the bipolar plates, the diameter of the holes, and the perimeter groove for our O-ring. Based on this inspiration, we developed a versatile design that allows for easy replacement of components such as electrodes and membranes suitable for research. To determine the morphology of the bipolar plates, we used a middle chamber purchased from the company. This chamber has a truncated square shape with 76 mm sides and rounded corners.

Since the bipolar plates are connected to the H_2O and CO_2 circuits, maintaining a constant cross-section from the entrance to the exit is essential to ensure optimal transport of the reactants. This maximizes the reaction surface area in contact with the anode and cathode. To achieve this, a serpentine-shaped flow channel was designed to fit within 5 cm^2 square. We chose this area because it is the area of electrodes used in the electrolyzer commercialized by Dioxide Materials. The serpentine path ends in an entrance and an exit circular feedthrough of 3mm diameter each, where connectors are later attached to integrate the plate into the circuit.

The bipolar plates also feature eight circular perforations that align with those of the middle chamber from Dioxide Materials as seen in Figure 5.7. These perforations facilitate the assembly of all the electrolyzer components and have a diameter of 6 mm. To ensure that there are no reactant leaks in the bipolar plates, an O-ring has been installed around the serpentine channel of each bipolar plate. To accommodate the O-ring, a perimetral groove was created in the bipolar plates with a diameter of 1.5 mm and a depth of 1 mm. The cathodic bipolar plate is identical to the anodic chamber, except for two additional circular feedthroughs, also 6 mm in diameter (see

Figure 5.7b). These extra feedthroughs are positioned along the same diagonal as the serpentine circuit feedthroughs for CO_2 and are designed to connect the middle chamber to its corresponding water reservoir without interfering with the CO_2 circuit.

For the initial design, alternative circuit configurations were considered, such as the one shown in Figure 5.7a, using different serpentine shapes. The goal of this exploration was to maximize the reaction surface area. However, it was found that the contact area between H_2O, CO_2, and the electrodes in the modified serpentine design was not significantly larger than in the original zigzag configuration, which did not justify the increased amount of bends in the circuit. Moreover, this design required certain sections of the serpentine channel to have a non-uniform cross-section, which led to suboptimal performance compared to the original zigzag design.

The bipolar plates were designed in Fusion software [4], where they were extruded to a thickness of 6 mm each, except for the feedthroughs and the serpentine channel. The serpentine was then extruded by 1.5 mm, resulting in the 3D model shown in Figure 5.7b.

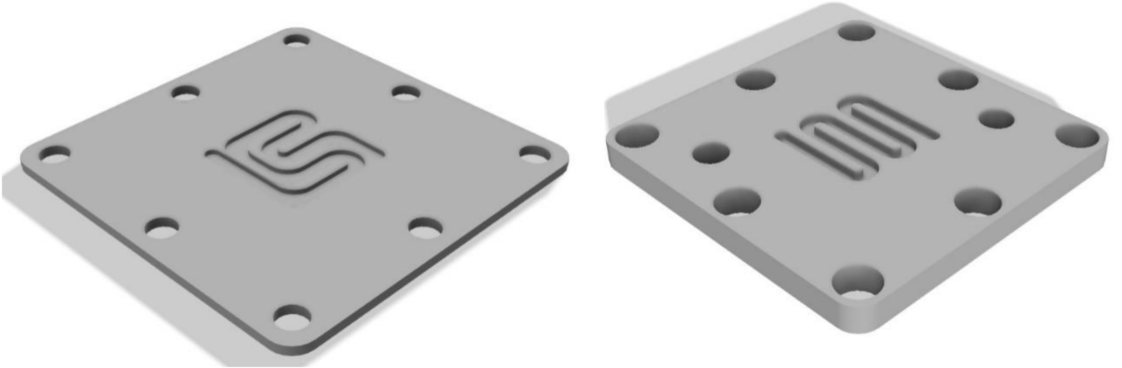
a) b)

Figure 5.7 a) 3D design of the bipolar plate with an alternative coil to maximize the contact area between the coil and the electrodes. b) 3D design of the cathodic bipolar plate with 6 mm extrusion.

In the Fusion software, it is possible to select the processing method for the designed 3D part. For our work, we used a computer numerical control (CNC) metal milling machine acquired through the company Orpi [5]. Specifically, we utilized the CNC milling machine KX3S-MACH. Within the Fusion's manufacturing module, various processing methods can be selected, including milling, turning, and additive manufacturing. For our CNC machine, milling was used as the primary machining process. Among the available milling options, 2D operations were chosen for roughing, pocketing, and contouring. Although 3D milling strategies exist, they were not necessary, due to the geometry of our part. However, drilling operations were employed to create the feedthroughs in the piece. For the 2D operations, different complete turns are programmed defining the trajectory of the 2D, but in different planes, each time at a deeper point, towards the inside of the plate. The manufacturing setup is created by defining the tool that will be used. This involves selecting the workpiece to be machined, setting the coordinate axis, and defining the orientation.

The parameters and tools of the milling machine depend on the material being processed. Our bipolar plates are made of aluminum and have a thickness of 6 mm. The milling cutters used were carbide with a single flute. The operating parameters were optimized to prevent aluminum from melting during machining, which could lead to surface imperfections on the workpiece. However, a detailed discussion of these optimizations falls outside the scope of this work. In some fabrication iterations, aluminum melting occurred, resulting in defects. This issue can arise due

---

[4] https://www.autodesk.com/es/solutions/fusion-360-3d-modeling

[5] https://orpi-sl.com

to factors such as a worn-out milling cutter, excessively high cutting speed, or inadequate cooling of the workpiece. To prevent melting during machining, an oil-based coolant or cutting fluid was used. Iterations were carried out to manufacture bipolar plates with aluminum sheets of different thicknesses (2 mm and 6 mm) and various designs. The final plates used were those shown in Figure 5.3: 6 mm aluminum bipolar plates featuring the serpentine design depicted in the figure.

5.3.2 Design and fabrication of middle chamber

The middle chamber was designed using the sketch of the bipolar plates in Fusion. However, instead of a serpentine channel, a square was designed with the same dimensions as the serpentine. This square is where reaction (R.13) takes place and is connected to the H_2O reservoir, which is independent of the H_2O reservoir in the anode chamber circuit. The connection is made through channels that end in the protrusions passing through the cathodic bipolar plate as shown in Figure 5.8a.

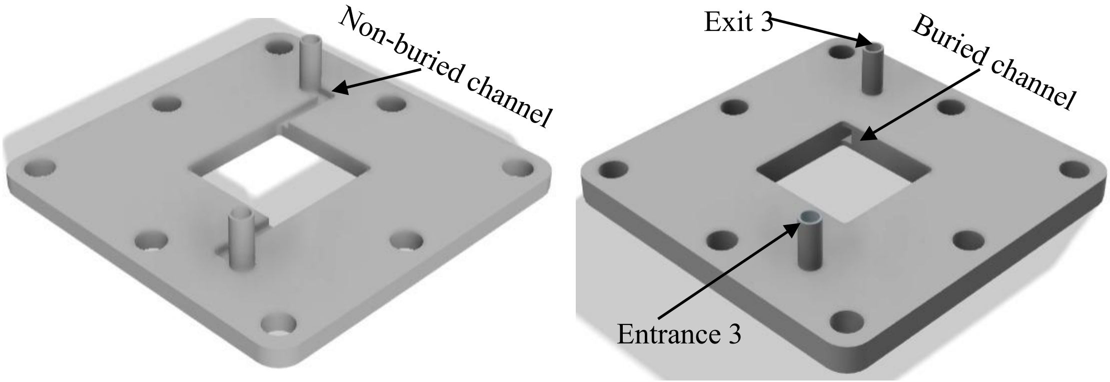

a) b)

Figure 5.8 a) 3D design of the middle chamber with exposed channels connecting to the H_2O reservoir. b) 3D design of the middle chamber with buried channels connecting to the H_2O reservoir.

With the first design (Figure 5.8a), leaks were observed in the middle chamber circuit when operating the electrolyzer, as water escaped from the channel connecting the middle chamber to the tubes passing through the cathodic bipolar plate. For this reason, and to prevent leaks and ensure no cross-contamination between different chambers of the electrolyzer, the middle chamber was redesigned with buried channels in a tunnel-like structure, as shown in Figure 5.8b.

Middle chambers with thicknesses of 1, 2, and 6 mm and the design of Figure 5.8b were tested. All of them performed well in terms of preventing leaks. However, the results of the electrolyzer characterization were significantly influenced by the thickness of the middle chamber. This aspect will be explored further in subsection 5.5.1.

Once the design of the middle chamber was completed in Fusion, a mesh was exported to the 3D printing processing software Cura [6]. In this software, the desired print quality was selected, ranging from 0.2 to 0.5 mm layer height. The system then converted the 3D design into a G-code file, which the printer processed while automatically adding the necessary support for printing. The 3D printer used for the manufacturing of the middle chamber was Creality Ender 3 [7].

Middle chambers were fabricated using PLA, acrylonitrile butadiene styrene (ABS), and polypropylene (PP). The PP middle chamber exhibited defects because the 3D printer was unable to produce it with good quality, resulting in holes forming on its surface, as marked in red circles in Figure 5.9a. On the other hand, the ABS middle chamber had a rough surface that could compromise the electrolyzer sealing, but this issue was resolved using an acetone vapor treatment,

---

[6] https://ultimaker.com/es/software/ultimaker-cura/

[7] https://www.creality.com/es/products/ender-3-3d-printer

which smoothed out the roughness. However, after the acetone vapor treatment, the ABS chambers developed slight warping, as shown in Figure 5.9b, which affected the proper assembly of the electrolyzer.

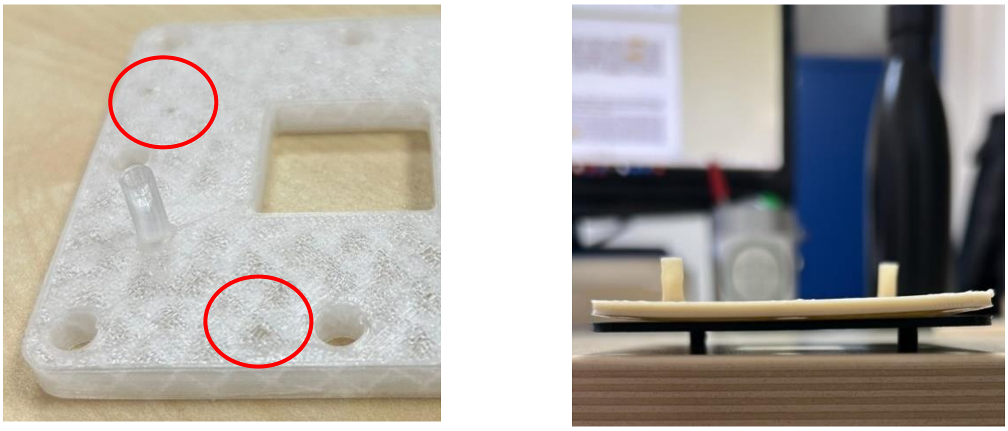
a) b)

Figure 5.9 a) Middle chamber made of PP with holes in the surface that could compromise the seal of the electrolyzer. b) Middle chamber made of ABS after treatment with acetone vapors to eliminate surface roughness. It has curvature compared to the flat surface of a PLA middle chamber.

For these reasons, it was decided that the best available material was PLA, as it did not present leakage issues in the electrolyzer. However, during the initial analyses of the compounds produced during the electrolyzer operation, lactic acid was detected, which we assumed was a product of PLA degradation during operation. To resolve this issue, the middle chamber was wrapped with Teflon tape, as depicted in Figure 5.10. Subsequent analyses revealed that coating PLA with Teflon successfully resolved the issue of PLA degradation into lactic acid. The incorporation of Teflon tape also improved the sealing of the electrolyzer.

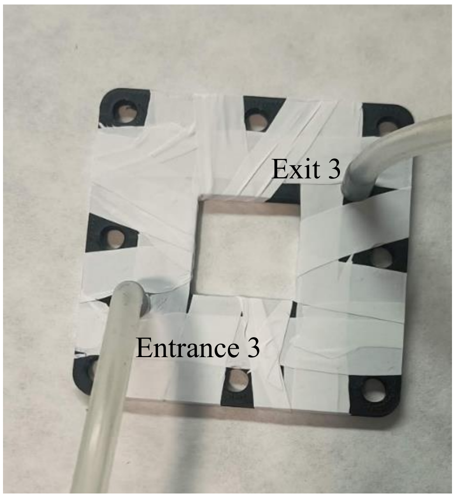

Figure 5.10 Middle chamber made of PLA with a Teflon tape coating to prevent PLA degradation in lactic acid. The middle chamber is coupled to the tubes that pass through the cathodic bipolar plate and connect it to the H_2O reservoir, which is recirculated in the middle chamber.

5.3.3 Anode design and fabrication

The anode used in the three-chamber electrolyzer for formic acid production is based on a carbon cloth that facilitates the diffusion of gaseous oxygen in reaction (R.4). We then deposited RuO_2 on this cloth, as described next, serving as the chemical compound that catalyzes reaction R.4.

The anode has the same dimensions as the serpentine of the anodic bipolar plate, which is 5 cm^2. For its preparation, a square piece of carbon cloth provided by the company Quintech was cut *in* *situ*, onto which a suspension of RuO_2 was deposited. The suspension was prepared by adding 30 mg of RuO_2 to 5 mL of iso-2-propanol (IPA) in a sealed container. The container was then placed in an ultrasonic bath for 30 minutes, after which the suspension was transferred into an airbrush. RuO_2 was applied using the airbrush, ensuring a homogeneous deposition across the entire surface of the carbon cloth. Once the entire suspension was deposited, the IPA was allowed to evaporate, leaving clusters of RuO_2 attached to the carbon cloth fibers. Figure 5.4a shows an example of the anode of the three-chamber electrolyzer with the RuO_2 already deposited.

5.3.4 Modification of cathode, Nafion and Sustainion membranes

The 25 cm^2 cathode sheet from Dioxide Material was cut *in situ*, just like the anode in the anodic chamber, ensuring it matched the dimensions of the serpentine area on the cathodic bipolar plate.

The cationic membrane (specific for H^+ protons) Nafion® NM-117 was purchased from the German company QuinTech. This membrane did not require any pretreatment before operating the three-chamber electrolyzer. The only modification made in our laboratory was cutting the Nafion® membrane *in situ* to match the shape of the carbon cloth anode with RuO_2. However, it was decided to make its surface approximately 1 cm^2 larger than the anode to ensure that its size exceeded that of the anode, preventing leaks between the middle chamber and the anodic chamber.

The anionic Sustainion® membrane (specific for OH^- and HCOO^- anions) was purchased through the company Dioxide Materials. The membrane was coated to a plastic liner to prevent its curling. Like the Nafion® membrane, it was cut into a square shape with an area approximately 1 cm^2 larger than the cathode to prevent leaks between the middle chamber and the cathodic chamber. However, this membrane was not ready for immediate use in the three-chamber electrolyzer because the compounds that permit the passage of anions were not activated.

For the activation of the Sustainion® membrane we followed the indications of Dioxide Materials:

- First, we carefully removed the Sustainion® membrane from its packaging, ensuring it not to damage it in its initial dry and brittle state.
- Instead of cutting the membrane to the exact electrode size, we prepared a slightly larger piece for soaking in an aqueous 1M potassium hydroxide (KOH) solution. Since the membrane initially curled in the solution, we placed small weights like Vickers on the edges of the liner to keep it flat.
- We then heated the KOH bath to 55 °C and maintained the membrane in the solution for approximately 1.5 to 3.5 hours. Over time, the membrane swelled and began to separate from the liner, typically after 2-3 hours. At this stage, we removed the weights and discarded the liner.
- After that, we let the membrane activate in a room temperature 1M KOH solution for 24 hours. Once the membrane was activated, we cleaned with abundant deionized water.
- Finally, we cut the Sustainion® membrane with a square shape of 6 cm^2.

5.3.5 Design and fabrication of connectors

In addition to the components that make up the electrolyzer, we at IES-UPM also designed and manufactured connection elements for the circuits of the anode and cathode chambers. To incorporate the connectors into the electrolyzer, we used tap tools to thread the feedthroughs that connect the serpentine channels in the bipolar plates with the outer face of the plates, meaning we tapped the holes machined in the serpentines. The connectors were designed using Fusion. In the initial sketch, three concentric circles were drawn: one representing the inner radius, which matched that of the serpentine channel; another defining the outer radius, where the fluid carrying tube would be attached; and finally, the threading radius, which allowed the connector to be screwed into the bipolar plates. Subsequently, two cylinders were extruded—one with threading and one without. The cylinder designated for external threading was selected to ensure a secure fit when screwed into the plate. Between the threaded and non-threaded sections, we added a larger-diameter cylinder that acts as an overhang, preventing leaks from the anode and cathode chambers to the exterior of the electrolyzer.

Figure 5.11 displays the 3D design of the connectors, both in their unrendered form (Figure 5.11a) and fully rendered (Figure 5.11b).


a) b)

Figure 5.11 3D design of the connector with the overhang: (a) without rendering and (b) rendered.

As with the design of the middle chamber, the connectors were exported and processed in Cura software for 3D printing. The only printing parameter modified was the quality setting, selecting the highest possible resolution of 0.2 mm layer height. PLA was used as the printing material.

5.4 Assembly of the electrolyzer

The electrolyzer was assembled by inserting screws through the eight holes in each bipolar plate. For the assembly, the components were arranged according to the schematic in Figure 5.1. To ensure the most airtight assembly possible, threading taps were used on all eight holes. The final thread size of the holes was M6.

To bias the electrodes of the electrolyzer, positive and negative voltages were applied to the bipolar plates in the anode and cathode chambers, respectively. Since the screws pass transversely through the electrolyzer and contact both bipolar plates, using metal screws could cause a short circuit. To prevent this, screws made of an insulating polymer were employed.

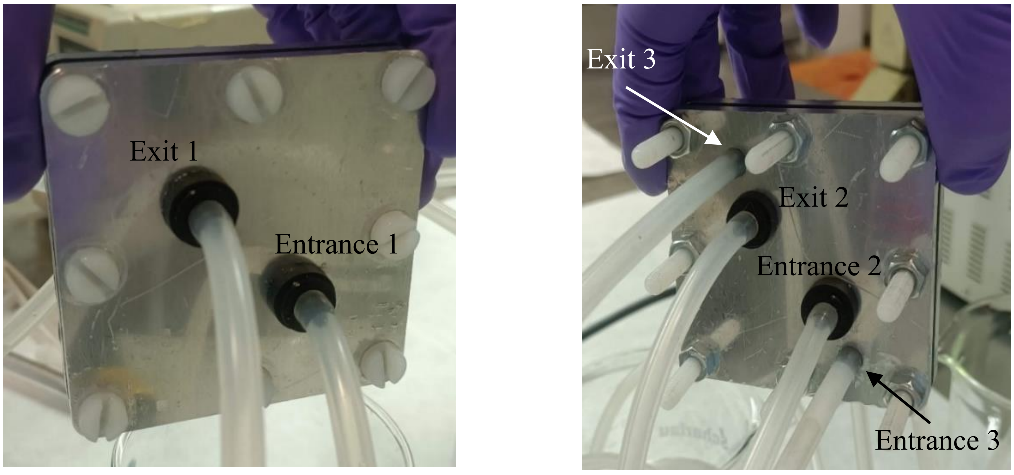

a) b)

Figure 5.12 a) Electrolyzer assembly viewed from the anodic bipolar plate. b) Viewed from the cathodic bipolar plate.

Figure 5.12 shows images of the three-chamber electrolyzer for formic acid production, viewed from the anode bipolar plate (Figure 5.12a) and from the cathode bipolar plate (Figure 5.12b). The three circuits of the electrolyzer are connected to their respective reservoirs with plastic tubes resistant to the chemicals flowing through them.

Once the electrolyzer was assembled, leak tests were performed before its characterization. The following subsections detail the leaks found and the solutions implemented to resolve them.

5.4.1 Leaks between chambers

To identify leaks between the chambers, water was passed through each chamber individually. One of the leaks detected occurred between the chambers when water was circulating solely through the cathode. It was observed that some of the water ended up flowing into the central chamber, which had been dried before this process. The middle chamber should not become wet when water is circulating through the cathode, as the Sustainion® membrane only allows anions to pass through it. The same issue was observed when water was circulated through the central chamber. This issue has occurred multiple times during the design refinement process, but it has not always been caused by the same factor.

One of the reasons was that the membrane was stored dry when the electrolyzer was not in operation. This type of membrane is highly sensitive to humidity and becomes very fragile once it is completely dry. If the dehydration level is high, it can break, which explains the water leakage between the central chamber and the cathode chamber after one hydration-dehydration process. Figure 5.13a shows an image of the Sustainion® membrane broken after leaving the assembled electrolyzer dry for several days. One solution to this problem was to keep the membrane hydrated between uses of the electrolyzer to prevent deterioration.

The other issue arose because, initially, the channel connecting the inlet and outlet of water in the middle chamber was designed in the same way as the one used in electrolyzers sold by Dioxide Materials. Thus, in the first versions of this middle chamber, part of the water circulation circuit was exposed, as shown in b. Consequently, the external part of the circuit was not fully sealed when assembling the electrolyzer, leading to leaks. To address this problem, the middle chamber was redesigned with a recessed channel, as shown in Figure 5.8.

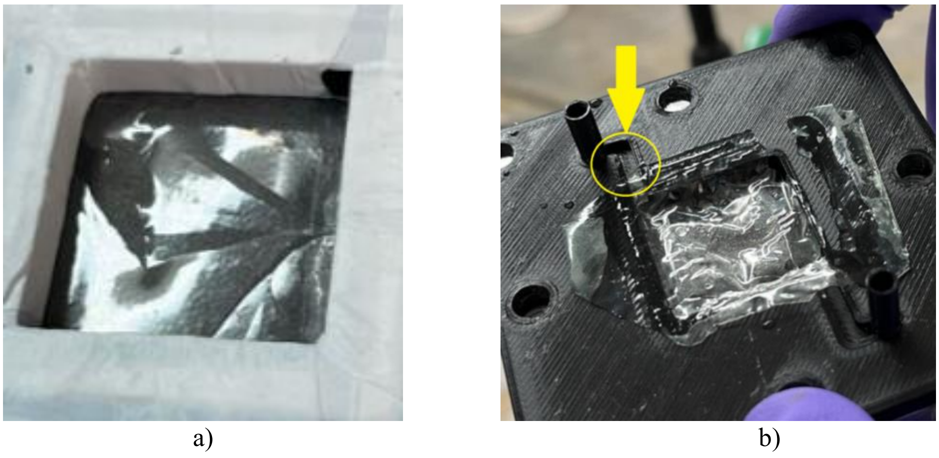
a) b)

Figure 5.13 a) Sustainion® membrane ruptured after being stored dry for several days. The ruptures in the membrane allow water to pass between the cathodic chamber and the middle chamber. b) Exposed channel of the central chamber that could lead to leaks between the central chamber and the cathodic chamber.

5.4.2 O-rings leaks

At first, the design of the bipolar plates did not include any type of O-ring, as the reference model did not feature one. However, after detecting leaks through the outer screws or the plate edge, it became necessary to add one. From that point on, various O-ring options were explored, with different diameters and sizes, and both round and flat cross sections. Ultimately, a circular-section silicone O-ring with a 2 mm diameter was chosen. The main challenge was placing the O-ring into the machined groove made by the CNC milling machine, primarily because their shapes were different, and the elasticity of the O-ring made it difficult to maintain the groove squared geometry. It was also not possible to machine a deeper groove, as the goal was for the O-ring to protrude slightly to create vacuum inside.

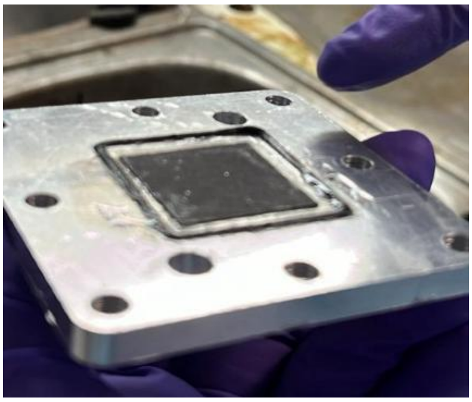

Figure 5.14 O-ring was installed in the groove surrounding the cathode of the cathodic bipolar chamber. The O-ring protrudes 1 mm from the surface of the cathodic bipolar plate.

Finally, the chosen solution was to glue the O-ring to the groove in the bipolar plate using instant adhesive (cyanoacrylate). Pressure was then applied for a certain period, allowing the O-ring to adhere while maintaining the desired shape. Figure 5.14 shows how the round O-ring conforms to the groove geometry of the bipolar plate after applying the adhesive.

5.4.3 Leaks in the connectors

After the connectors were manufactured and put into use, occasional water leakage in the form of droplets was observed. These leaks were due to the precision limitations of 3D printing. As a result, small gaps remained between the connector thread and the bipolar plate thread. To address this issue, a circular flange was added around the connectors, providing a surface for a circular flat gasket made of plastic to fit underneath. This design ensures that the flange presses the gasket firmly against the bipolar plate, creating a tighter seal. Although this solution significantly improved the system watertightness, the threading would wear down each time the connectors were removed [205]. Consequently, connectors needed to be replaced relatively frequently, as worn threads increased the risk of water leakage.

5.4.4 Electrical connections

The water circulated through the anode chamber and the water circulated through the middle chamber requires pumping from two separate water reservoirs. To achieve this, two micro pumps with a maximum pumping capacity of 3 liters per minute were used. These pumps operate within a voltage range of 3 to 12 V and have a maximum current of 0.65 A.

To bias the electrolyzer and measure the current at different voltages, a Keithley 2400 source meter was used. To connect the power supply to the electrolyzer, terminals that screw onto the bolts passing through the electrolyzer were used. The positive terminal of the power source was connected to the anode, while the negative terminal was connected to the cathode. Figure 5.15 illustrates the three-chamber electrolyzer connected to the power supply that biases it.

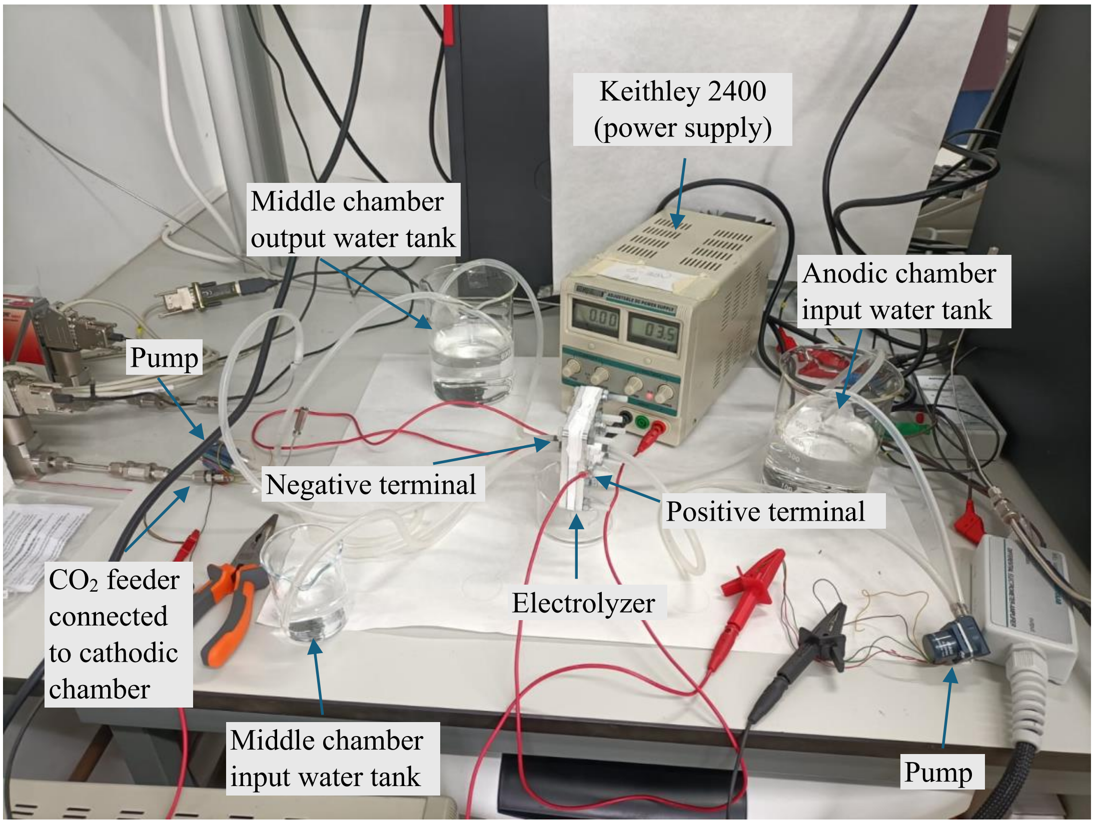

Figure 5.15 Three-chamber electrolyzer in operation. The electrolyzer is biased by a Keithley 2400 voltage source. Pumps circulate water through the anode circuit and the middle chamber circuit, drawing from two separate water reservoirs.

5.5 Characterization of the electrolyzer

5.5.1 Electrical characterization

The electrical characterization consisted of applying a voltage sweep from 0 to 10 V while measuring the current flowing through the electrolyzer, in order to get the current voltage ($I - V$) characteristic of the electrolyzer. The $I - V$ characteristics were obtained under different conditions. First, the $I - V$ characteristic of the electrolyzer was measured with the components of the electrolyzer lightly tightened and without H_2O in any of its circuits. Then, the $I - V$ characteristic was measured with all components fully tightened and without H_2O in any of its circuits. Next, the measurement was performed with all components fully tightened and with H_2O flowing through the anode chamber. Finally, the $I - V$ characteristic was measured with the electrolyzer fully tightened with H_2O flowing through both the anode chamber and the middle chamber. None of these experiments were performed feeding CO_2 to the cathode chamber of the electrolyzer. These experiments were carried out in electrolyzers with middle chambers of 2 mm and 6 mm in thickness.

Figure 5.16a shows the experimental $I - V$ characteristics of the electrolyzer with a 6 mm middle chamber. The $I - V$ characteristic of the electrolyzer with all elements lightly tightened is represented by blue dots, the fully tightened electrolyzer by green dots, the fully tightened electrolyzer with H_2O in the anode circuit by orange dots, and the fully tightened electrolyzer with H_2O in both the anodic and the middle chamber by red dots. Figure 5.16a shows that the $I - V$ characteristics of the first three experiments indicate good electrical insulation, as the current remains below the detection limit throughout the measured voltage range (it is to be noted that the blue and green dots are not visible because they remain behind the orange ones in the figure).

In contrast, the fully tightened electrolyzer with H_2O in both the anodic and the middle chamber exhibits currents on the order of 10^{-5} A when biased up to 10 V.

The corresponding $I - V$ curves were fitted to the following model,

$$\begin{cases} I = 0 \text{ for } V < E^0 \\ I = \frac{1}{R_E}(V - E^0) \text{ for } V > E^0 \end{cases} \tag{5.4}$$

obtaining the results that will be discussed in the next paragraphs. With this model, R_E will approximately correspond to the series resistance of the electrolyzer for the given operation conditions. Since the threshold voltage has not been experimentally determined, only the series resistance value of the electrolyzer will be provided.

The best-fit line for the $I - V$ characteristic of the electrolyzer, featuring a 6 mm middle chamber filled with H_2O in both the anode and middle chamber, yields an almost infinite resistance $R_E = 1.0 \cdot 10^3$ kΩ according to the model in Eq. (5.4). The first three experiments, conducted without H_2O in the middle chamber, do not conduct due to the absence of electrolytes in this section. As a result, even though electrolytes could form at the electrodes, the lack of a conductive medium in the middle chamber prevents their transport throughout the electrolyzer, leading to an open circuit. When H_2O is added to the middle chamber, the electrolyzer begins to conduct due to its presence. However, its electrical behavior does not resemble that of a typical electrolyzer, for instance, it conducts below the threshold voltage. Under these conditions, the electrolyzer behaves like a series resistor, with a resistance within the range of deionized water [206]. At this point, we have no way to confirm that the passage of current through the electrolyzer is due to chemical reactions because we have not analyzed the potential species that could be produced by the electrolyzer.

Figure 5.16b shows the $I - V$ characteristics of the electrolyzer with a 2 mm middle chamber under the same conditions as in the previous case. The figure reveals that this electrolyzer does not conduct when loosely tightened (blue dots) as expected from the lack of a conductive channel throughout the different parts of the assembly. The rest of the $I - V$ characteristics of this electrolyzer follow the same trend (no current is detected) up to approximately 1 V (it has to be noted that measurements with 1 V voltage steps are made). However, a change in the trend appears above 2 V, where the current starts flowing through the circuit. Once the electrolyzer starts conducting above a particular threshold voltage, its $I - V$ behavior resembles that of a series resistance. The series resistance was determined following the same procedure used in the previous experiment. The best-fit line for the $I - V$ characteristic of the fully tightened electrolyzer with a 2 mm middle chamber (green dots) gives $R_E = 7.8$ kΩ. Meanwhile, for the fully tightened electrolyzer with H_2O in the anodic chamber (orange dots) the series resistance is $R_E = 6.5$ kΩ. The increase in current, along with the decrease in series resistance, might be due to the presence of H_2O in one of the electrolyzers chambers. Finally, for the electrolyzer with H_2O in both the anodic and middle chambers (red dots) the series resistance is $R_E = 2.9$ kΩ. The increase in current could be attributed to the presence of water in both chambers. In fact, under these conditions, currents of up to 3 mA are reached at 10 V. The values of series resistance and current are collected in Table 5.2.

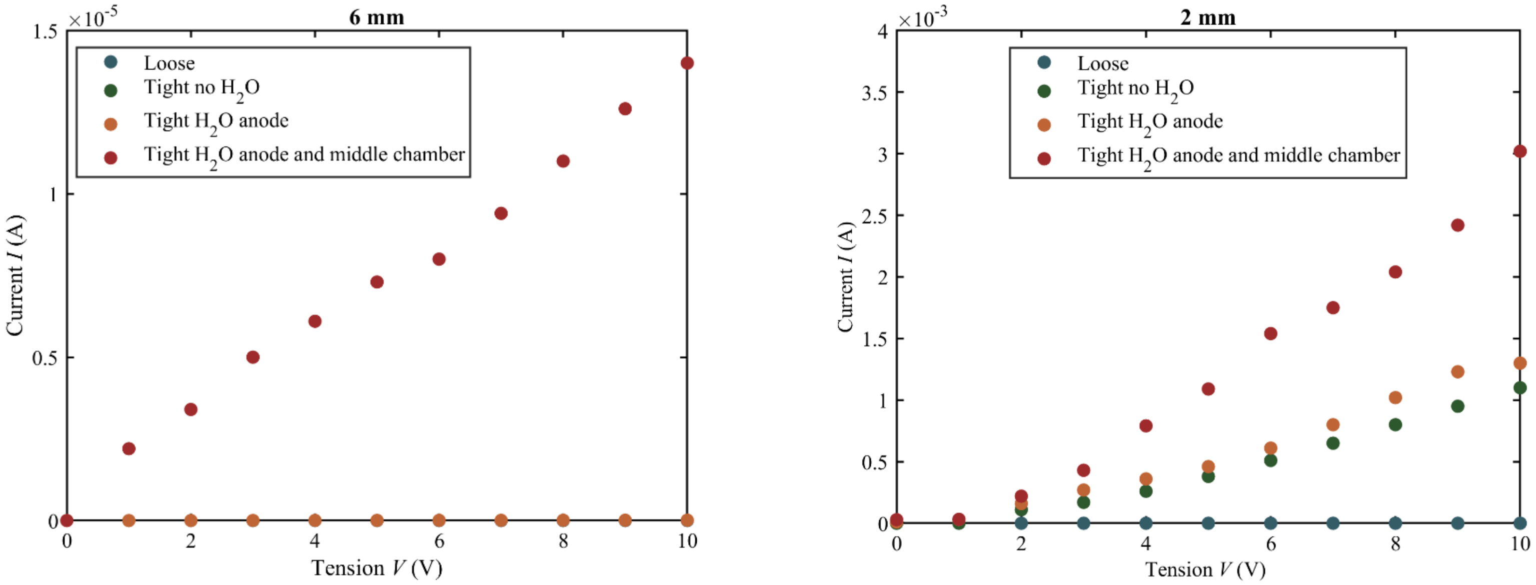

a) b)

Figure 5.16 $I - V$ curves of the electrolyzer in different scenarios: with the components loosely tightened (loose), with all components tightened (tight no H_2O), passing water through the anode chamber (tight H_2O anode), and passing water through both the anode and the middle chamber. (tight H_2O anode and middle chamber). The electrolyzer is biased between 0 and 10 V with a middle chamber thickness of a) 2 mm and b) 6 mm. Area of the electrodes was 5 cm^2.

Under these conditions, the passage of current through the electrolyzer could be due to chemical reactions occurring at both the anode and the cathode. At the anode, the OER can take place because H_2O is available, and its 1.23 V thermodynamic potential is exceeded. At the cathode, H_2O is present due to direct contact with the humid Sustainion® membrane, but CO_2 is not directly supplied. However, entrance 2 is exposed to air, which contains CO_2, meaning that CO_2 from the air could potentially be reduced at the cathode.

Table 5.2 Values of series resistance (R_E) of different electrolyzers with middle chambers of 2 and 6 mm working under different conditions. No CO_2 was fed to the electrolyzer.

Electrolyzer	Series resistance, R_E (kΩ)
6 mm tight H_2O in anode and middle chamber	$1.0 \cdot 10^3$
6 mm with H_2O and CO_2	4.9
2 mm tight without H_2O	7.8
2 mm tight H_2O in anode	6.6
2 mm tight H_2O in anode and middle chamber	2.9
2 mm with H_2O and CO_2	1.6

Anyways, both OER and CO2RR, which enable the flow of ions that account for the electric current, should take place simultaneously; therefore, neither can occur independently. At this point, we have no way to confirm that the passage of current through the electrolyzer is due to chemical reactions because we have not analyzed the potential species that could be produced by the electrolyzer.

Next, the $I - V$ curves of the electrolyzer were measured with all components tightly assembled, using H_2O in both the anode and middle chamber, and with CO_2 flowing through the cathode chamber. The electrical characterization was performed for electrolyzers with middle chamber thicknesses of 2 mm and 6 mm. In both cases, the electrolyzer was biased from 0 to 10 V in 1 V increments, while the CO_2 flow rate was maintained at 20 mL · min^{-1} because it is the minimum flow rate permitted in our setup. Figure 5.17 presents the experimental $I - V$ characteristics of both electrolyzers. In both cases, the presence of CO_2 in the cathode increased the current once a certain voltage threshold is exceeded. For the electrolyzer with a 6 mm middle chamber, the series resistance decreased from almost infinity ($1 \cdot 10^3$ kΩ), i.e. meaning that the electrolyzer behaves almost as an open circuit when no CO_2 is supplied to the cathode and therefore, no anions allow to close the electrical circuit, to 4.9 kΩ when the constant flow of CO_2 feeds the CO2RR reaction, resulting in a current increase from $1.45 \cdot 10^{-5}$ A to $1.75 \cdot 10^{-3}$ A at 10 V, representing a two orders of magnitude increase. In the case of the electrolyzer with a 2 mm chamber, the series resistance decreased from 2.9 kΩ to 1.6 Ω, leading to a current increase from $3.02 \cdot 10^{-3}$ A to $5.44 \cdot 10^{-3}$ A when biased at 10 V. Values of series resistance were determined according to Eq. (5.4) and are collected in Table 5.3.

Table 5.3 Values of series resistance (R_E) of electrolyzers with middle chambers of 2 and 6 mm working with H_2O at the anodic and middle chamber and with CO_2 fed in the cathodic chamber. The flow rate of CO_2 was 20 mL $\cdot$ min^{-1}.

Electrolyzer	Series resistance, R_E (kΩ)
6 mm with H_2O and CO_2	4.9
2 mm with H_2O and CO_2	1.6

Since CO_2 was present in the cathode and H_2O was available in both the anode and the middle chamber, it was assumed that the current passing through the electrolyzer was supplied by the CO2RR for $HCOO^-$ and OH^- formation at the cathode (R.12) while OER (R.11) occurred at the anode. As mentioned before, these reactions take place simultaneously once the standard cell potential E^0_{cell} of 1.43 V is exceeded (as indicated in Table 5.1) and both CO_2 and H_2O are supplied to the cathode and anode respectively. Note that the reaction voltage is considered without accounting for overpotentials.

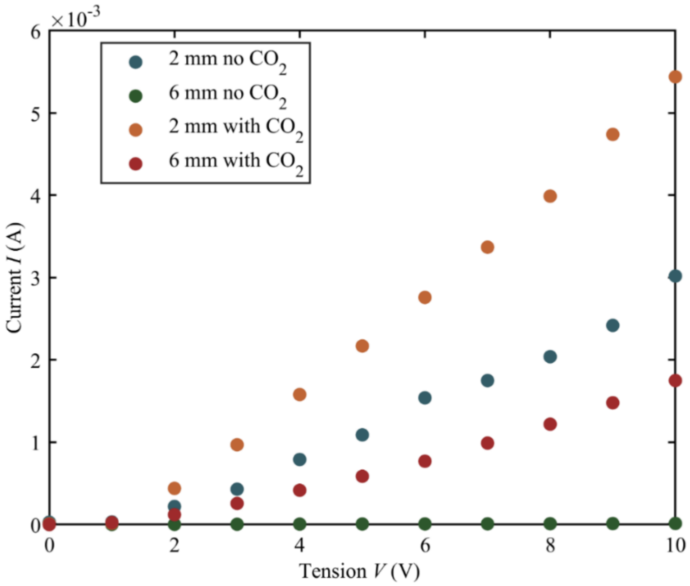

Figure 5.17 $I - V$ curves of the electrolyzer with a middle chamber of thicknesses 2 mm with a CO_2 flow rate of 20 mL $\cdot$ min^{-1} (orange dots) and without CO_2 (blue dots). Besides, the electrolyzer with a middle chamber of thickness 6 mm with a CO_2 flow rate of 20 mL $\cdot$ min^{-1} (red dots) and without CO_2 (green dots). The anodic and middle chamber are fed with H_2O in all cases. A voltage bias was applied from 0 to 10 V with 1 V intervals. The area of the electrodes was 5 cm^2.

In principle, a higher volumetric flow rate of CO_2 should lead to a higher current at the cathode. CO_2 is the reactant at the cathode, so increasing its flow rate could enhance its availability at the electrode interface. However, this behavior is not necessarily linear. Beyond a certain flow rate, the current may stabilize or even decrease if limitations in CO_2 adsorption on the cathode surface are reached, if gas bubbles form and hinder contact with the electrode, or if the system experiences efficiency losses due to other factors such as voltage drop or variations in flow distribution [196].

Figure 5.18a illustrates the impact of CO_2 volumetric flow rate on the $I - V$ characteristics of the electrolyzer equipped with a 2 mm middle chamber. The results reveal distinct trends across different voltage ranges. In the low-voltage region, from 0 to 2 V, an increase in CO_2 flow rate leads to a higher current response. This suggests that a greater availability of CO_2 enhances the electrochemical process in this range, with the maximum current observed at a flow rate of 100 $\mathrm{mL \cdot min^{-1}}$. Between 3 and 6 V, the trend shifts, and the highest current is achieved with CO_2 flow rates in the range of 40-60 $\mathrm{mL \cdot min^{-1}}$. This indicates that at intermediate voltages, an optimal balance between CO_2 supply and electrochemical reaction efficiency is reached within this specific flow rate range. At higher voltages, from 6 to 10 V, the current reaches its peak at lower CO_2 flow rates, specifically between 30 and 40 $\mathrm{mL \cdot min^{-1}}$. However, when the electrolyzer was biased at 10 V, the highest current was obtained with a CO_2 volumetric flow rate of 50 $\mathrm{mL \cdot min^{-1}}$. This suggests that, at high voltages, the abundance of CO_2 may not be necessary to achieve maximum current or could even hinder the electrochemical process. Possible explanations include changes in reaction mechanisms, mass transport limitations, or increased competition between different electrochemical pathways. These findings highlight the complex interplay between CO_2 flow rate and electrolyzer performance, emphasizing the importance of optimizing operating conditions to maximize efficiency across different voltage ranges.

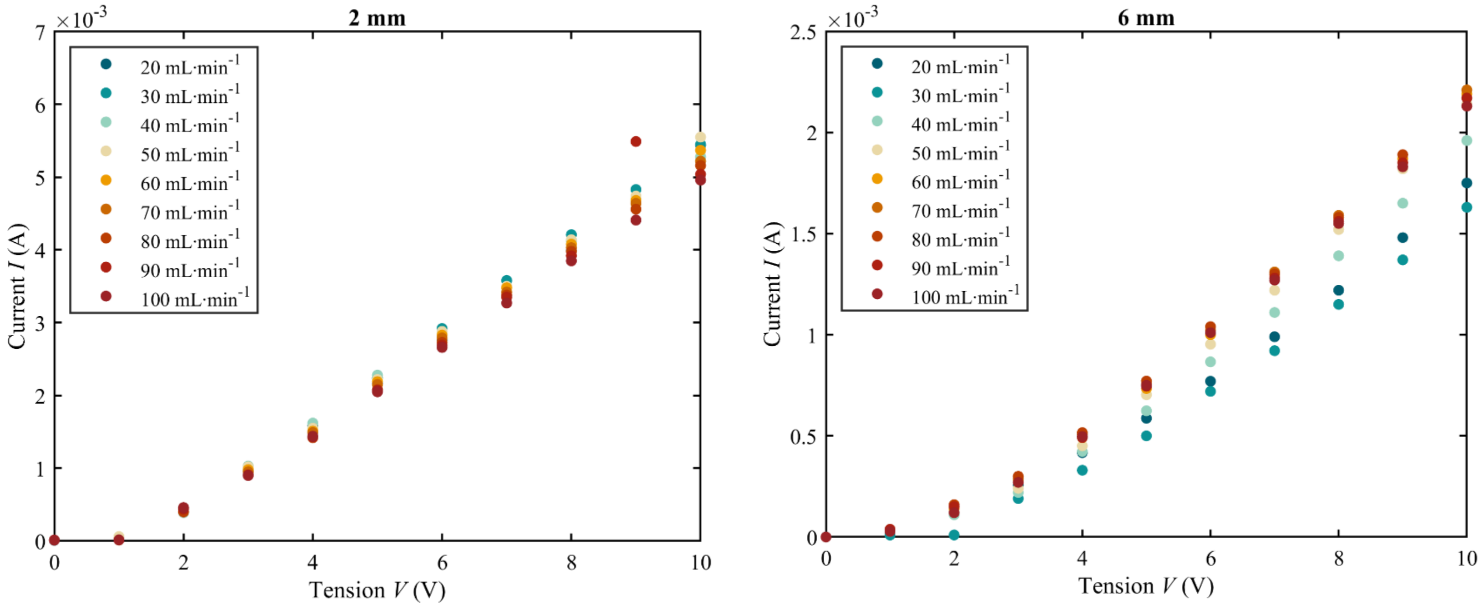

a) b)

Figure 5.18 $I - V$ curves of the three-chamber electrolyzer with different volumetric flow rates of CO_2 (from 20 to 100 $\mathrm{mL \cdot min^{-1}}$) in the cathodic circuit a) Electrolyzer with 2 mm thick chamber b) Electrolyzer with 6 mm thick chamber. The area of the electrodes was 5 cm^2.

Figure 5.18b illustrates the impact of CO_2 volumetric flow rate on the $I - V$ characteristics of the electrolyzer equipped with a 6 mm middle chamber. It is observed that, across the entire voltage range, higher CO_2 flow rates consistently result in higher current. This suggests that, unlike the behavior seen with the 2 mm chamber, an increased supply of CO_2 continuously enhances the electrochemical reaction throughout the tested voltage range. This increase in current with the CO_2 volumetric flow rate in the electrolyzer with a 6 mm middle chamber could be explained by a phenomenon related to the pressure exerted on the Sustainion® membrane and its proximity to the Nafion® membrane. As the CO_2 flow rate increases, the pressure on the cathode and, consequently on the Sustainion® membrane increases. This additional pressure causes the Sustainion® membrane to move closer to the Nafion® membrane in the anode chamber, which could facilitate the electrical interaction between the two membranes, thus reducing the series resistance of the electrical circuit.

From Figure 5.16, Figure 5.17, and Figure 5.18 we can observe that thinner the middle chamber the lower the resistance. We believe that the reduction in resistance as the middle chamber thickness decreases is due to the contact between the membranes. When operating with the electrolyzer with a 6 mm chamber, the anion and cation exchange membranes do not make physical contact. In contrast, with the 2 mm chamber, the membranes do come into contact. It should be noted that, when no CO_2 is fed into the cathode, the electrolyzer with the 6 mm middle chamber has a series resistance of $1 \cdot 10^3$ kΩ, which is a value in the order of pure water [206]. This series resistance is considerably smaller (2.9 kΩ) when operating the electrolyzer with 2 mm middle chamber. This leads us to think that in the electrolyzer with the 6 mm chamber, due to the greater distance between the membranes, an additional potential drop occurs, which could limit performance. However, when the CO_2 volumetric flow rate increases, the pressure exerted on the Sustainion® membrane appears to favor its approach toward the Nafion® membrane, reducing this potential drop and consequently increasing the current.

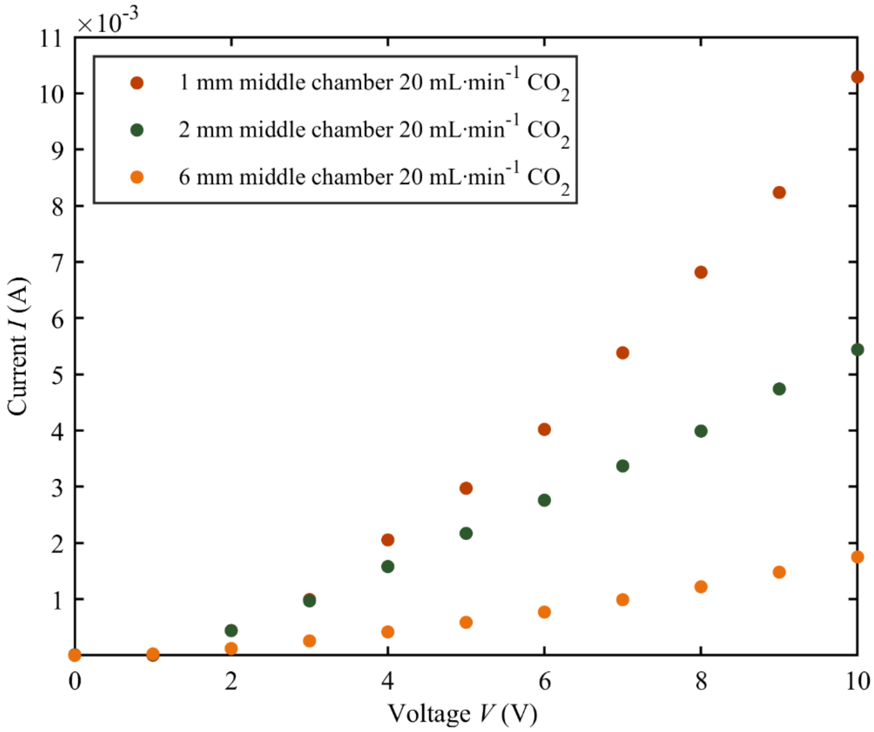

Figure 5.19 $I - V$ curves of the electrolyzer with middle chambers of thicknesses 1 mm (red dots), 2 mm (green dots), and 6 mm (yellow dots). A voltage bias was applied from 0 to 10 V with 1 V intervals. All the electrolyzers were fed with a CO_2 flow rate of 20 $\mathrm{mL \cdot min^{-1}}$.

Next, we fabricated a middle chamber with a thickness of 1 mm and characterized the electrolyzer with this new middle chamber as well to see if the current rose as expected. The electrical characterization was performed for middle chamber thicknesses of 1 mm, 2 mm, and 6 mm. In all three cases, the electrolyzer was biased from 0 to 10 V in 1 V intervals and the flow of CO_2 was 20 $\mathrm{mL \cdot min^{-1}}$. We chose this flow rate because with it we reported the highest current among all conditions and configurations. Figure 5.19 presents the $I - V$ characteristics of the three electrolyzers. From Figure 5.19, we can observe that all three $I - V$ characteristics follow the same trend: the current remains nearly zero between 0 and 1 V. Beyond a certain voltage, let us suppose E^0_{cell}, the current starts to flow through the electrolyzer. In Figure 5.19, it can be observed that the thinner the middle chamber, the higher the current of the electrolyzer. At a voltage of 10 V, the current of the electrolyzer with the 1 mm middle chamber (red dots), $10.3 \cdot 10^{-3}$ A, is nearly five times higher than that of the electrolyzer with the 6 mm chamber (yellow dots), which is $1.75 \cdot 10^{-3}$ A and almost twice that of the electrolyzer with the 2 mm middle chamber (green dots), which is $5.44 \cdot 10^{-3}$ A.

The value of series resistance for the electrolyzer with the 1 mm thick middle chamber is determined according to Eq. (5.4) and it is equal to $R_E = 0.8\ \mathrm{k\Omega}$.

According to Faraday's law of electrolysis, the production of chemical products in electrochemical reactions increases with higher current. Therefore, using an electrolyzer with higher conductivity is generally preferable, as it would, in principle, enhance both the efficiency and the yield of the reaction. However, this holds true only if the current flows in series rather than in parallel.

Last, we considered the addition of soluble salt in the middle chamber in order to increase the current passing through the electrolyzer. To test this hypothesis, we introduced 20 mL of a 1M aqueous solution of potassium bicarbonate ($KHCO_3$) into the middle chamber. This addition aims to raise the conductivity of the system and facilitate ionic transport within the electrolyzer. When potassium bicarbonate dissolves in water, it releases potassium (K^+) and bicarbonate (HCO_3^-) ions, which enhance the conductivity of the solution. Figure 5.20 illustrates the impact of $KHCO_3$ on the $I - V$ curve of the electrolyzer with a middle chamber thickness of 1 mm. This thickness was selected as it allows for the highest current. As before, the system was biased from 0 to 10 V in 1 V increments. The volumetric flow rate of CO_2 was set at $20\ \mathrm{mL \cdot min^{-1}}$.

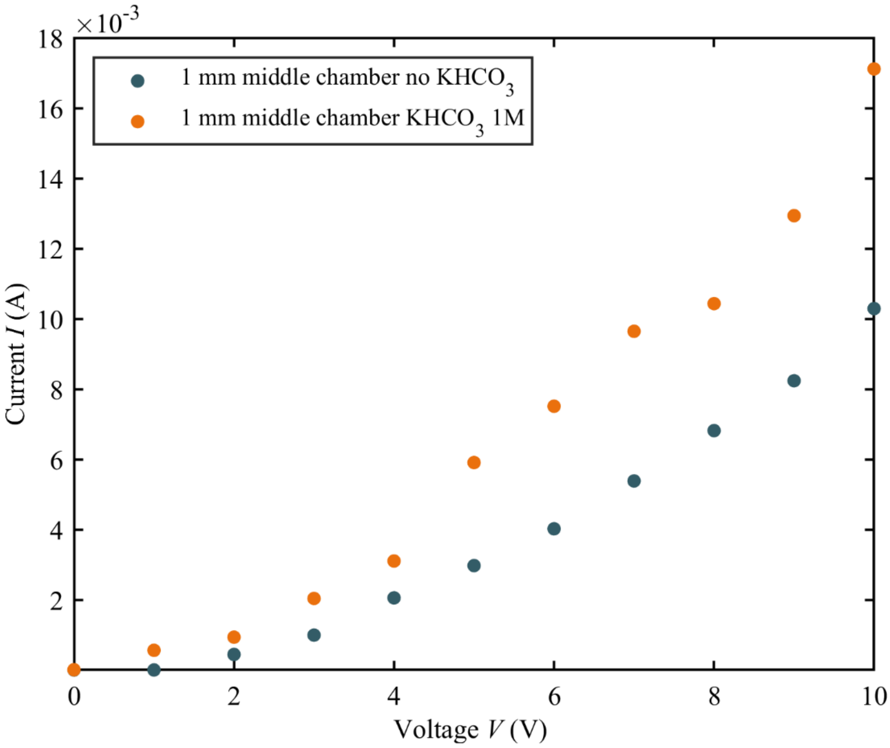

Figure 5.20 $I - V$ curves of the electrolyzer with water in the 1 mm middle chamber (blue dots) and with a 1M $KHCO_3$ solution in the 1 mm middle chamber. A voltage bias was applied from 0 to 10 V with 1 V intervals. The electrolyzer was fed with a CO_2 flow rate of $20\ \mathrm{mL \cdot min^{-1}}$.

Figure 5.20 shows that the current passing through the electrolyzer is higher at all voltage values when $KHCO_3$ is added to the middle chamber. When $KHCO_3$ is added, the increase in current becomes more pronounced as the voltage bias of the electrolyzer rises. Notably, at 1 V, the electrolyzer without $KHCO_3$ in the middle chamber does not conduct, whereas the one with $KHCO_3$ does. This conduction at 1 V occurs because the presence of ions from $KHCO_3$ in the middle chamber enables current transport when a voltage is applied across the electrolyzer terminals. At 10 V, the current increases from 10.3 mA to 17.1 mA, representing a 66% increase at that voltage. With these conditions, the electrolyzers a series resistance of 0.6 kΩ.

At first, we thought that the decrease in series resistance was due to the presence of more ions in the middle chamber, which would facilitate the reactions at the electrolyzer electrodes. However, potassium and carbonate ions do not participate in (R.1) or (R.12), meaning their presence neither enhances nor hinders the reactions. Therefore, the increase in current, or decrease in resistance, cannot be attributed to electrochemical reactions. Instead, the addition of $KHCO_3$ in the middle chamber can be seen as analogous to introducing a parallel circuit, leading to a reduction in resistance. This experiment helps determine whether the middle chamber is the primary factor affecting the series resistance of the electrolyzer. When $KHCO_3$ was added, the resistance decreased from 0.8 kΩ to 0.6 kΩ, representing a 25% reduction. If the series resistance is the sum of the electrolyte resistance and the resistance of the middle chamber, the fact that adding an electrolyte only reduces the resistance by 25% implies that electrolyte resistance is not the primary contributor. Instead, it suggests that the resistance of the middle chamber plays a more significant role in the total resistance of the system.

Having observed the effects of the middle chamber thickness and the CO_2 volumetric flow rate, we can determine the optimal operating conditions for our three-chamber electrolyzer. The best conditions will be those that result in the highest current related to chemical OER in the anode and the desired CO2RR in the cathode. Therefore, the optimal configuration regarding the electrical behavior of the electrolyzer found with respect to all the variants tested in this work is the one with a 1 mm thick middle chamber, and a CO_2 flow rate of $20\ \mathrm{mL \cdot min^{-1}}$.

So far, all characterizations performed on the different versions of our electrolyzer have focused exclusively on its electrical properties. However, these data have not yet been correlated with the highly relevant results of the production of various solar fuel species that may be generated in the system. Therefore, the following section will explore this aspect in detail, providing a more comprehensive analysis of the performance of the electrolyzer.

5.5.2 Chemical production

We have analyzed the products generated by the three-chamber electrolyzer using gas chromatography (GC) and high-performance liquid chromatography (HPLC). This analytical stage was carried out at the ICP-CSIC.

Both GC and HPLC operate on the same fundamental principle: a mixture of compounds is passed through a fixed column containing a stationary phase and each compound interacts differently with this phase, causing them to travel through the column at different speeds. This results in each compound takes a specific amount of time to exit the column, a parameter known as the retention time. Since each substance has a characteristic retention time under given conditions, it can be identified based on how long it takes to pass through the column [207,208].

In GC, the sample is vaporized and carried by an inert gas, such as helium or nitrogen, through a column coated with a stationary phase. Compounds are separated based on their volatility and interactions with the column, with more volatile substances eluting faster than those with stronger interactions [208]. In HPLC, the sample is dissolved in a liquid solvent and pumped through a packed column containing a solid stationary phase [209]. The separation occurs due to differences in polarity and solubility, with some compounds interacting more strongly with the stationary phase and, therefore, taking longer to elute [209].

In both techniques, the retention time is a crucial factor for identifying compounds, as each chemical species has a unique retention time under specific chromatographic conditions. By comparing retention times to known reference compounds, it is possible to determine the composition of a sample accurately. Beyond identifying compounds, both techniques also allow for quantification by measuring the intensity of the detector response for each compound. The area under each peak in the chromatogram (a graph with its x-axis representing time and y-axis showing the signal intensity) is proportional to the concentration of the compound in the sample [208,209]. By comparing these areas to those obtained from known standard solutions, it is possible to determine the precise amount of each component present in the sample. This makes GC and HPLC essential tools for both qualitative and quantitative chemical analysis.

In our initial experiments at the ICP-CSIC, we focused on using HPLC as the analytical tool. The procedure involved biasing the electrolyzer within a voltage range from 1 to 5 V, with intervals of 0.5 V. As the electrolyzer was biased at each specific voltage, we collected a few milliliters of the flow coming from the middle chamber into glass vials. This flow was the result of the electrochemical reactions taking place in the middle chamber during the experiment.

The reason for collecting the flow at each voltage step was to analyze the components present in the middle chamber at different bias levels. By tracking the changes in the composition of the flow as the voltage was varied, we aimed to determine the specific voltage at which HCOOH would start to form, if it was indeed being produced. This allowed us to correlate the electrochemical conditions with the formation of specific products, providing valuable insights into the reaction dynamics within the system.

Formic acid was not detected at any of the voltages tested during the experiments. This could either be due to issues with the HPLC equipment, or it may indicate that HCOOH was not produced at a concentration higher than 1 mM, which is the detection limit of their HPLC.

Additionally, it has been observed that formate stability is very low [210]. Even when the samples are frozen immediately after collection, no formate is detectable upon analysis the following day. The samples were generated at the IES-UPM and then transported frozen to the ICP-CSIC for analysis the next day. This storage and transport method could be affecting the results, and it suggests that formate decomposition may be contributing to the absence of HCOOH detection, despite the expected formation under the experimental conditions.

What was detected, however, was lactic acid. We believe that this product is the result of the degradation of the PLA from the middle chamber when the electrolyzer is subjected to a voltage bias. The lactic acid was found at all voltage values to which the electrolyzer was biased, indicating that its formation is linked to the electrochemical conditions applied to the system. To verify whether lactic acid was a product of the CO2RR or the degradation of the middle chamber, we wrapped the chamber with Teflon tape to electrically isolate it. This is shown in Figure 5.10. The result was that once the middle chamber was covered with Teflon, no lactic acid was found in the solution from the chamber, confirming that this product very likely originated from the degradation of the middle chamber rather than from the CO2RR process.

As HPLC did not allow us to detect the presence of HCOOH, we decided to conduct the analysis using the gas chromatography system depicted in Figure 5.21. In gas chromatography, the species to be analyzed can be introduced into the system in two different ways, depending on whether the sample is in the gas or liquid phase. Each method provides complementary information about the products generated in the electrolyzer, allowing for a more complete characterization of the system.

The first method consists of injecting gases directly into the chromatograph. To do this, we connected the outlet of the CO_2 circuit at the cathodic chamber to the inlet of the chromatograph, enabling us to analyze the gaseous products generated by reactions taking place in the cathode during electrolysis. This approach was particularly useful for detecting compounds that might have been generated by CO2RR, but, for instance, could not be able to pass through the Sustainion® membrane and be present in the liquid phase, or, alternatively, could be somehow lost if only the liquid from the middle chamber was analyzed.

The second method involves manually injecting liquid samples obtained from the aqueous circuit flowing through the middle chamber into the chromatograph. In this case, the liquid is preheated to ensure its complete evaporation before it passes through the chromatographic column. This step is essential because gas chromatography requires all components to be in the vapor phase for proper separation and analysis. We applied this method to determine whether formic acid was generated in the middle chamber of the electrolyzer. By analyzing the liquid phase, we were able to detect and quantify dissolved products that might not have been observed in the gas-phase analysis.

Using both techniques together provided a more comprehensive understanding of the electrochemical processes taking place in the electrolyzer. The combination of gas and liquid injections allowed us to identify different reaction products and confirm their presence in either phase, ensuring a more reliable characterization of the system.

Figure 5.21 Image of the gas chromatograph available at the ICP-CSIC, used to analyze the production of formic acid in our three-chamber electrolyzer.

5.5.2.1 Analysis of gaseous products

For the gas chromatography tests, we biased the electrolyzer at a voltage of 3.5 V, as this is the voltage at which the efficiency of formic acid production is maximized, as reported by the literature [189]. We used the electrolyzer with the 2 mm middle chamber for this experiment.

Table 5.4 Peak height values in the chromatogram (u^2) and concentration (ppm) of the species detected in the gas outlet of the three-chamber electrolyzer, using volumetric flow rates of 10, 30, and 50 $\mathrm{mL \cdot min^{-1}}$.

Measurement	CO_2 flow ($\mathrm{mL \cdot min^{-1}}$)	H_2 (u^2)	H_2 (ppm)	CH_4 (u^2)	CH_4 (ppm)
0	10	$5.38 \cdot 10^3$	8.2	-	-
1	30	$2.01 \cdot 10^4$	31.8	-	-
		$3.43 \cdot 10^4$	52.6	-	-
2	50	$3.87 \cdot 10^4$	59.3	$7.28 \cdot 10^3$	9.8
		$4.94 \cdot 10^4$	75.8	-	-

We first analyzed the gases generated on the cathodic chamber. To achieve this, we conducted three tests, each with a different volumetric CO_2 flow rate: 10, 30, and 50 $\mathrm{mL \cdot min^{-1}}$. One measurement was taken for 10 $\mathrm{mL \cdot min^{-1}}$ and two measurements were taken for the rest flow rates. The reason for testing different flow rates was to determine whether the production of species increased with the volumetric flow rate. Table 5.4 shows the gases detected at the outlet of the gas chromatograph and their respective proportions.

By using this technique, we identified the formation of hydrogen (H_2), methane (CH_4), and carbon monoxide (CO) at the cathode, confirming that gas-phase reactions were taking place in addition to those occurring in solution. In the case of CO, we were unable to quantify it accurately due to leaks in the system. We also observed H_2 formation and its concentration seemed to increase slightly over successive injections within the same series. This suggests that the products might have been accumulating in the large final vessel, leading to higher detected concentrations over time. In the test at 50 $\mathrm{mL \cdot min^{-1}}$, we detected 9.8 ppm of CH_4, but only in one of the measurements. This isolated detection suggests that methane may be forming in very small amounts, potentially below the detection limit in most injections. Another possibility is that the signal was caused by a transient event, such as the release of accumulated gas in the system or a momentary fluctuation in the reaction conditions.

Since the results obtained from the first GC measurements did not allow for clear conclusions about the reactions occurring at the cathode, additional experimental campaigns were conducted. The retention times of gases typically generated at the cathode and used as reference for the evaluation of the data obtained from the characterization of CO2RR reactions are listed in Table 5.5. These retention times are approximate due to variations in experimental conditions.

Table 5.5 Retention time of common gas species produced on the cathode during CO2RR

Product	Retention time (min)
Hydrogen (H_2)	~3.7
Carbon monoxide (CO)	~4.8
Methane (CH_4)	~6.2
Ethylene (C_2H_4)	~11.2

In the new GC measurements, volumetric flow rates of 40 and 80 $\mathrm{mL \cdot min^{-1}}$ were used. Figure 5.22 shows the chromatogram of the sample analyzed while operating the electrolyzer at a volumetric flow rate of 40 $\mathrm{mL \cdot min^{-1}}$.

Figure 5.22 shows that the most detected compound in the GC was the CO_2 that did not react at the cathode of the electrolyzer, as it corresponds to the highest peak in the chromatogram. The gas chromatograph was able to detect the formation of H_2, CO, CH_4, and ethylene (C_2H_4) in the gas outlet of the cathodic chamber. These products were identified based on their retention times, which matched those reported in Table 5.5. CO was the most detected compound, followed by H_2, CH_4 and C_2H_4. It is consistent with the results that H_2 and CO are generated in higher proportions than CH_4 and C_2H_4, given that, starting with CO_2 as the reactant, the former two products require less energy to form than the latter. Specifically, CH_4 formation involves the removal of two oxygen atoms from the CO_2 molecule, while C_2H_4 formation requires the chaining of two carbon atoms and the complete removal of oxygen atoms from the CO_2 molecule. In contrast, the formation of CO only necessitates the removal of a single oxygen atom from CO_2. Additionally, the production of H_2 is commonly observed in reactions where water reduction is present, as in the case of the cathode, which is moistened with water from the middle chamber.

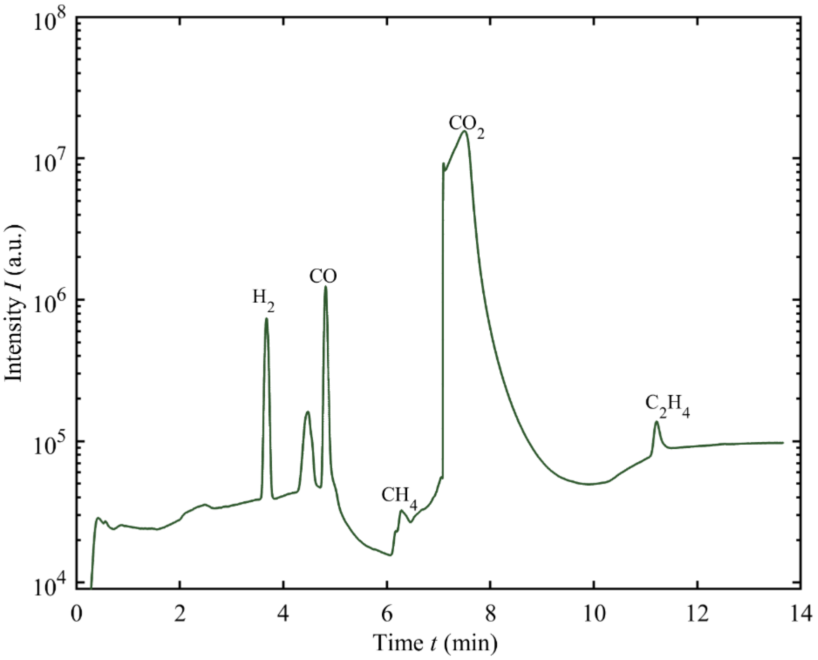

Figure 5.22 Chromatogram of the gas outlet from the three-chamber electrolyzer. A volumetric CO_2 flow rate of 40 mL · min^{-1} was used. The peaks indicate that H_2, CO, CH_4, and C_2H_4 were generated at the cathode of the electrolyzer. The CO_2 that did not react was also detected in the GC.

Figure 5.23 shows the chromatogram of the sample analyzed while operating the electrolyzer at a volumetric flow rate of 80 mL · min^{-1}. This experiment was conducted to determine whether doubling the volumetric CO_2 flow rate results in the same products and whether the amount of product generated doubles in proportion to the available CO_2.

The chromatogram presented in Figure 5.23 shows that CO_2, CO, CH_4, and C_2H_4 have been detected. In this case, H_2 is not detected, either because it is not produced at the cathode or because its production is below the detection limit of the chromatograph. In this case, CO is the most detected product and is therefore understood to be the most abundantly generated, followed by CH_4, with a small amount of C_2H_4 detected last. The products generated under these conditions differ from those observed in Figure 5.22. Moreover, the production of the detected species does not double compared to the amounts produced when a flow rate of 40 mL · min^{-1} was used. It can be observed in Figure 5.23 that the peak corresponding to CH_4 increases when using a CO_2 flow rate of 80 mL · min^{-1}. However, the peak corresponding to C_2H_4 is less intense in Figure 5.23 than in Figure 5.22.

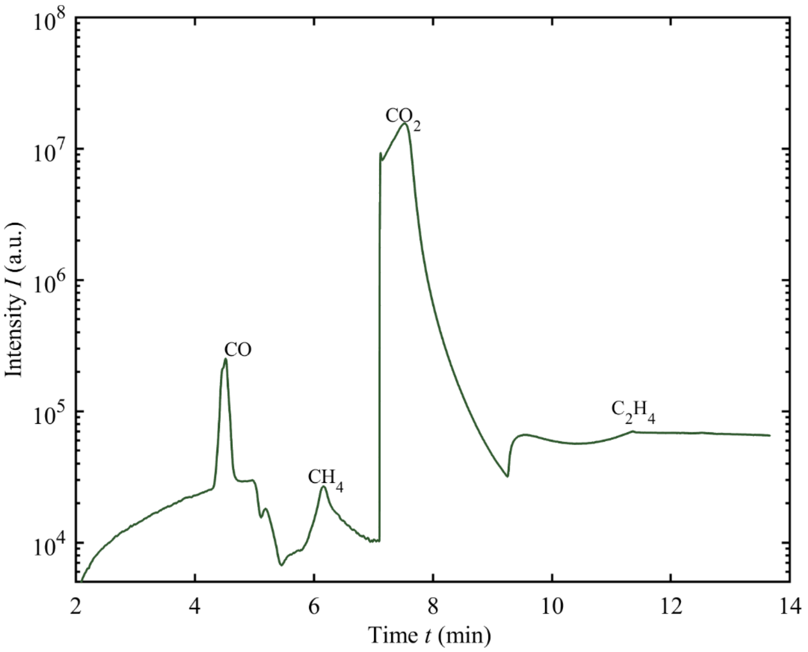

Figure 5.23 Chromatogram of the gas outlet from the three-chamber electrolyzer. A volumetric CO_2 flow rate of 80 $\mathrm{mL \cdot min^{-1}}$ was used. The peaks indicate that CO, CH_4, and C_2H_4 were generated at the cathode of the electrolyzer. The CO_2 that did not react was also detected in the GC.

On one hand, these results are satisfactory because they provide clear evidence that the current observed in the $I - V$ characteristics of the three-chamber electrolyzer is directly linked to the chemical reactions taking place at the electrodes. This supports the hypothesis that the observed electrical behavior is a direct consequence of the electrochemical processes occurring in the system. On the other hand, the detection of gaseous species at the cathode serves as further confirmation that the electrolyzer could not only produce HCOOH but also generate additional chemical compounds. This suggests a more complex reaction pathway at the cathode, leading to the formation of various products. Besides, the disparity in the results regarding the gas output from the cathodic chamber highlights the strong dependence of the electrochemical reactions on the operating conditions of the electrolyzer. This suggests that achieving consistent and reproducible results is challenging.

5.5.2.2 Analysis of liquid products

To determine whether HCOOH is generated in the middle chamber of the electrolyzer, several aliquots from this chamber were analyzed. The liquid samples were collected after operating the electrolyzer with a 2 mm middle chamber, a volumetric flow rate of 40 $\mathrm{mL \cdot min^{-1}}$, and a voltage bias of 3.5 V. Despite the 1 mm middle chamber offering the best electrical conductivity performance, electrolyzer samples with this configuration could not be analyzed due to time constraints. To improve conductivity through the central chamber of the electrolyzer, 1M aqueous solution of $KHCO_3$ was used . The retention times of liquid typically generated during CO2RR reactions are listed in Table 5.6 as reference for the comparison of the characterization results obtained with this technique. These retention times, again, are approximate due to variations in experimental conditions.

Figure 5.24 shows the chromatogram of the liquid sample extracted from the central chamber. The only peak that can be associated with a compound, based on the retention times listed in Table 5.6, is H_2O, which corresponds to the tailing peak extending approximately from 8.50 to 11.50.

There is a peak around minute 6 that could not be definitively associated with any specific compound. This unidentified peak suggests the possible presence of an unknown substance or a mixture of compounds that elute at a similar retention time. Further analysis, such as mass spectrometry or comparison with additional reference standards would be required to determine its exact nature. The absence of identifiable peaks corresponding to the products listed in Table 5.6 does not necessarily imply that no reactions are occurring within the middle chamber. It is possible that reactions are taking place, but the concentration of the resulting products is below the detection limit of the chromatograph.

Besides, note that the liquid injected into the gas chromatograph was introduced as an aliquot and analyzed one day after the electrolyzer operation. The electrolyzer was operated in a day, during which the gases formed at the cathode were analyzed in situ, and a fraction of liquid from the central chamber was isolated. Since different chromatographic columns are required for gas and liquid analysis, the column had to be changed before measuring the liquid sample.

Table 5.6 Retention time of common liquid species produced on CO2RR reactions.

Product	Retention time (min)
Acetaldehyde	1.82-2.03
Formaldehyde	2.05-2.13
Acetone	2.45-2.65
Methanol	3.43-3.65
Isopropanol	4.05-4.50
Ethanol	4.20-4.50
1-Propanol	7.80-8.20
Water	8.50-11.50
Allyl alcohol	10.28-10.35
Acetic acid	14.23-14.40
Formic acid	15.25-15.50

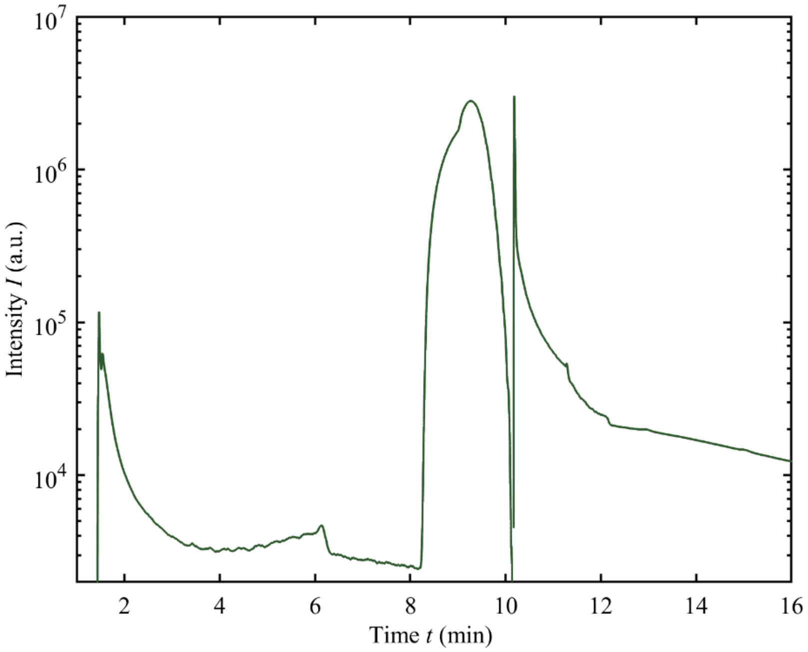

Figure 5.24 Chromatogram of the middle chamber outlet. A volumetric CO_2 flow rate of 40 $\mathrm{mL \cdot min^{-1}}$ was used as well as a 0.1 M aqueous solution of $KHCO_3$ to improve the conductivity in the middle chamber.

The results from the gas chromatograph analyses confirm that CO2RR reactions are indeed occurring at the cathode of the three-chamber electrolyzer. However, the formation of HCOOH in the middle chamber has not yet been detected, which is the primary objective of this section. To obtain more precise results, it would be necessary to analyze the liquid sample *in situ*, without waiting to replace the gas column with the liquid column. This would help prevent the possible degradation of any HCOOH formed in the middle chamber. Additionally, it would be advisable to operate the electrolyzer for several hours and analyze the samples after a longer period. This approach would allow any HCOOH that forms to accumulate, potentially increasing its concentration and making detection more feasible.

5.6 Summary

A CO_2 electrolyzer for HCOOH production has been implemented based on the model commercialized by Dioxide Materials. After assessing profitability, market size, and ease of transport, it is concluded that despite its relatively small market, HCOOH production remains a highly promising option.

At IES-UPM, the bipolar plates, middle chamber, and anode have been designed and manufactured in-house, while the remaining components were sourced pre-manufactured. The bipolar plates were developed to maximize the contact area between the electrodes and the corresponding reactants.

The complete assembly of the electrolyzer has been carried out, along with the design of the connectors that integrate it with the reactant circuits. To prevent leaks, an O-ring has been incorporated into the bipolar plates. Additionally, the middle chamber has been designed and 3D-printed with embedded circuits to ensure proper sealing between the central chamber and the anodic and cathodic chambers.

The behavior of the electrolyzer with middle chamber thicknesses of 2 mm and 6 mm was analyzed, evaluating the effect of assembly pressure. The results indicate that higher applied pressure leads to a greater current flow once the electrolyzer is biased. It was observed that the presence of H_2O in both the middle and anodic chambers increases the current compared to the electrolyzer operating under dry conditions. The presence of CO_2 at the cathode was found to increase the current passing through the electrolyzer. This suggests that the OER at the anode and the CO2RR at the cathode are occurring simultaneously. The best-fit line for the $I - V$ characteristic of these electrolyzers yielded the series resistance of $1.6\ \mathrm{k\Omega}$ and $4.9\ \mathrm{k\Omega}$, respectively.

The effect of CO_2 volumetric flow at the cathode on the electrical behavior of the electrolyzer was also studied. For the 2 mm middle chamber, higher volumetric flow resulted in lower current. In contrast, for the 6 mm chamber, the opposite behavior was observed. It is hypothesized that in the latter case, increased volumetric flow brings the cationic and anionic membranes closer together, enhancing current conduction. This suggests that a thinner middle chamber promotes higher current flow. Consequently, a 1 mm thick middle chamber was fabricated and the correspondent electrolyzer was electrically characterized. The best-fit line for the $I - V$ characteristic of this electrolyzers yielded a series resistance of $0.8\ \mathrm{k\Omega}$. Further work will be necessary to evaluate the performance of this last design regarding the production of fuels.

It has been demonstrated that the presence of a $KHCO_3$ solution in the middle chamber increases the current by creating a parallel conduction pathway. However, it cannot be confirmed that this current increase translates into a higher production of chemical species.

The analysis of the generated products confirmed the formation of gases at the cathode, including H_2, CO, CH_4, and C_2H_4. These gaseous products were analyzed in situ using a gas chromatograph at the cathode outlet.

Additionally, the liquid product from the middle chamber was analyzed to determine whether HCOOH was present. The analysis of the liquid product from the middle chamber revealed the presence of lactic acid. We believe this originated from the degradation of the PLA that constitutes the middle chamber. To address this issue, the chamber was covered with Teflon tape, after which lactic acid was no longer detected. The analysis of liquids was not performed in situ, as the samples were examined more than a day after their production. As a result, no HCOOH was detected. It is hypothesized that the lack of detection may be due to its decomposition over time. Conducting in situ analysis and increasing the concentration of the solution circulating through the middle chamber could help confirm the presence of HCOOH.

Chapter 6. Conclusions and future lines of work

6.1 Conclusions

RES are essential for reducing future CO_2 emissions, but their intermittency and the difficulty of electrifying some sectors limit their standalone effectiveness.

To tackle both ongoing and historical CO_2 emissions, RES must be complemented with different strategies: i.e., green H_2, which enables decarbonization in hard-to-electrify sectors that still emit CO_2, and CCUS technologies, which are essential for actively removing CO_2 already present in the atmosphere.

Indirect coupling between a PV system and a PEM electrolyzer for green H_2 production outperforms direct coupling. Given the same solar resource and identical PV and electrolyzer components, indirect configuration produces more H_2 within a year. This is mainly because the PV system generates more energy under indirect coupling, thanks to the MPPT included in the PS. Additionally, indirect configuration effectively uses a larger portion of the available energy for H_2 production. The overall efficiency of indirect configuration is higher than that of direct configuration.

Under cell malfunction scenarios, indirect configuration maintains partial H_2 production while direct configuration fails entirely. Direct configuration only surpasses the indirect in H_2 output with PS efficiencies than realistic industrial conditions.

The addition of a battery to the indirect configuration enables further optimization of the system performance under real operating conditions. Indirect configuration with optimized battery presents the biggest H_2 production, share of energy used for H_2 production, and overall efficiency, which in this study achieves 11.8%.

Indirect configuration with optimized battery presents the highest initial costs but is the most profitable after 9 years of operation, the lifetime spam of the electrolyzer. Direct configuration presents the lowest initial capital cost and is the least profitable after 9 years of operation.

The performance of S-H depends not only on individual components, but on how well the entire system is configured to operate as a cohesive whole. Strategic integration, through both electrical design and energy storage, emerges as the key to unlocking the full potential of green H_2 production.

From a purely theoretical standpoint, the minimum energy required to capture one ton of CO_2 from ambient air is $4.97 \cdot 10^5\ \mathrm{kJ} \cdot \mathrm{ton}^{-1}$. This energy does not arise from a change in the system's internal energy, but rather from the entropy reduction associated with gas separation. Assuming the electricity cost of PV, this energy requirement translates to 5.4 $ to capture 1 ton of CO_2 from air.

Although some theoretical models suggest that entropy penalties in gas separation can be avoided under idealized conditions, these scenarios are not physically realistic or applicable to practical DAC systems. Therefore, in real-world CO_2 capture, the entropy cost is unavoidable.

The significant gap between the cost to separate CO_2 derived from the theoretical minimum and the actual performance of current DAC technologies reveals that the main barrier for the deployment of DAC technologies is not physical, but technological. Closing this gap depends on innovation rather than theoretical breakthroughs.

The experiments presented in Chapter 4 demonstrate that the efficiency of the DAC method proposed by Kikkawa et al., which utilizes IPDA, is highly sensitive to the air flow rate; capture efficiency decreases as flow rate increases. This reduction is attributed to two main factors: a shorter contact time between the air and the absorbent solution, and increased turbulence within the reactor, which reduces the effective reaction volume and leads to material losses.

The experimental CO_2 desorption temperature was higher than the reported by Kikkawa et al. The discrepancy likely stems from differences in CO_2 detection methods: while Kikkawa's setup included an FT/IR detector directly connected to the reactor, the present study identified desorption by visual indicators such as bubbling in the CA1-DMSO mixture and a color change from white to transparent.

The thermodynamic analysis of the IPDA-based DAC process reveals that separating one ton of CO_2 from air requires $3.99 \cdot 10^{10}$ J. This energy consumption is roughly 80 times higher than the theoretical minimum, corresponding to an approximate cost of 432 $ per ton of CO_2 captured.

It is possible to predict whether a chemical reaction can independently drive CO_2 separation from air by comparing the Gibbs free energy of the capture reaction ($\Delta G_{r,2}$) with the energy required for separation (ΔG_{air}). If $\Delta G_{r,2}$ is more negative than ΔG_{air}, then the reaction can theoretically supply all the necessary energy without any external input.

The overall separation process releases 20.2% of the total energy, originating from the chemical reaction between CO_2 and IPDA, as well as the cooling of CO_2, IPDA, and DMSO. This released energy could potentially be harnessed to power energy-intensive stages within the DAC process.

The economic viability of CO_2-derived products from electrochemical CO2RR, especially when using CO_2 captured from DAC, depends critically on generating a profit margin high enough to offset the significant cost of CO_2 capture. Only products with sufficiently high margins, such as formic acid, ethylene, and n-propanol, are economically viable under these conditions, while others like methane and methanol are not.

The performance of the three-chamber formic acid electrolyzer improves significantly with optimized assembly pressure and internal operating conditions. Higher assembly pressure enhances contact between internal layers and improves conductivity, while the addition of water in the middle and anodic chambers increases current by facilitating better ionic transport. Furthermore, injecting CO_2 into the cathode further boosts the current.

Middle chamber geometry has a critical effect on the electrolyzers performance. Thinner chambers consistently led to lower series resistance, improving overall conductivity and reducing energy losses. These results demonstrate that optimizing the physical dimensions of the middle chamber is essential to improving the system's energy efficiency.

The electrochemical performance under different CO_2 flow rates highlights that chamber thickness significantly influences system behavior. Increased CO_2 flow reduced current in the thinner chamber but improved it in the thicker one, likely due to enhanced membrane contact from physical compression. This indicates that the interaction between gas flow and chamber geometry must be carefully balanced to optimize performance

The use of $KHCO_3$ solution in the middle chamber increases current, possibly by creating an additional conduction pathway, although further analysis is needed to determine whether this improves chemical yield.

Gas chromatography confirms the generation of gaseous products at the cathode (H_2, CO, CH_4, C_2H_4), validating the occurrence of CO2RR.

Formic acid is not detected in the analysis of liquid samples, most likely due to degradation over time, as samples are not analyzed in situ.

Covering PLA middle chamber with Teflon tape prevents middle chamber degradation into lactic acid.

6.2 Future lines of work

This Thesis is based on two fundamental pillars. The first is the optimization of green H_2 production processes, aimed at reducing CO_2 emissions in sectors where emissions are substantial and where the direct integration of renewable energy sources is not easily achievable. The second focuses on the development of CCUS technologies to reduce atmospheric CO_2 concentrations and convert this compound into value-added products, thus fostering a circular economy. Each of these pillars has enabled the study of a wide range of topics, both because the scope of the Thesis is genuinely broad and because it can be approached from multiple perspectives due to its multidisciplinary nature.

Many of the questions raised during the initial conceptualization of this Thesis have been answered throughout its development, as well as others that emerged during the research process. However, many new questions have also arisen, questions that open the door to future investigations and could contribute to a deeper and broader understanding of the full scope of this work.

- The scientific community considers that PEM electrolysis could benefit from elevated operating temperatures. Once the threshold voltage was surpassed, higher temperatures could enable the electrolyzer to reach greater current densities while operating at lower voltages. Thus, we think that studying the coupling of solar-to-hydrogen systems with processes that emit waste heat could be advantageous, as the residual heat from these processes could be used to raise the temperature of the PEM electrolysis, thereby reducing the voltage required for its operation. A detailed study of how increased electrolysis temperature affects hydrogen production could lead to the design of more efficient hydrogen production systems, thus promoting the implementation of these systems at an industrial scale.
- In both Chapters 3 and 4, we determined the energy required to separate 1 ton of CO_2 from the air. While Chapter 3 provides a general overview, Chapter 4 focuses on calculating this energy for a specific technology. In any case, the thermodynamic analyses developed in both chapters assume that the atmosphere, which acts as a reservoir of pressure and temperature throughout the CO_2 separation process, maintains a constant pressure. During the development of these analyses, we questioned what would happen if the atmosphere's pressure and temperature were not assumed to be constant nor CO_2 concentration as CO_2 itself is extracted. We believe that an analysis based on this assumption would be illustrative and provide further insight into the thermodynamics related to CO_2 extraction.
- In Chapter 4, we determined the energy consumption associated with the separation of 1 ton of CO_2 from the atmosphere using the DAC method based on IPDA. The consumption of this method highly depends on the temperature of CO_2 desorption. We believe that a lower temperature for CO_2 desorption would result in lower energy consumption. Let us recall that the CO_2 desorption temperature was experimentally determined using a method based on the visual observation of bubble formation in the DMSO solution. For this reason, we believe that coupling a system capable of detecting CO_2 at the DAC reactor outlet would be beneficial, as it would allow for a more accurate determination of the temperature at which CO_2 begins to desorb. With this new temperature, the energy involved in separating 1 ton of CO_2 could be recalculated.
- In Chapter 4 we demonstrated that energy requirements also depended on the amount of DMSO used in the DMSO-IPDA solution. We believe that using bigger amounts of DMSO,

which was used during the laboratory experiments, could result in a higher heat application during the system's heating process. It is important to remember that the heat applied to reach the CO_2 desorption temperature depends on the amount of material being heated, with more heat required as the quantity increases. Therefore, we believe it would be beneficial to determine the optimal amount of DMSO, ensuring it is sufficient to dissolve all the IPDA while minimizing the heat required to reach the CO_2 desorption temperature.

- The CO_2 electrolyzer described in Chapter 5 of this Thesis consists of several components that can be modified. For example, testing new materials or design of the components to study how these affect the performance of the CO_2 electrolyzer. Regarding the use of alternative materials, a titanium bipolar plate could be employed, similar to the one used in the formic acid electrolyzer commercialized by Dioxide Materials. An anode using IrO_2 as a catalyst could also be considered, instead of the RuO_2 used in laboratory experiments. Additionally, it would be valuable to assess how different anion and cation exchange membranes affect the electrolyzer performance. Finally, a middle chamber made of material that does not degrade during operation could also be implemented. Regarding the design of the electrolyzer, a more conventional configuration could be considered—one that does not require a middle chamber or two membranes, as these components introduce series resistance into the system.
- The anode used to operate the electrolyzer consisted of a carbon cloth on which 30 mg of RuO_2 was deposited. Another line of research could consist of the catalytic activity of the anode as a function of the amount of RuO_2 deposited in the anode and, in this way, observe how it affects the performance of the electrolyzer.
- We could, as well, try new ways to seal all the components of the electrolyzer in order to prevent leaks during its operation. Namely, new shapes for the O-ring integrated onto the bipolar plates.
- During the electrical characterization of the electrolyzer, we could use narrower voltage steps in order to better determine the threshold voltage of the electrolyzer. With this new threshold voltage, we could propose a new model to predict the behavior of the electrolyzer, as we have done with the PEM electrolyzer for hydrogen production. Once we could model the behavior of the CO_2 electrolyzer, we could study the different configurations of the PV modules and the electrolyzer.
- As hinted in Chapter 5, the electrolyzer containing the middle chamber of 1 mm presented the higher current of all the electrolyzers tested in laboratory. However, the chemical production studies were carried out with the electrolyzer containing the middle chamber of 2 mm. Another line of future work could consist of analyzing the chemical products generated by the electrolyzer when using a middle chamber of 1 mm.
- As previously commented in Chapter 5, the analysis of the liquid products of the electrolyzer could be carried out simultaneously to the electrolyzer operation. This way, we could prevent the potential decomposition of formic acid.
- Given the known CAPEX and OPEX figures for the mature PEM technology, it would be possible to estimate the capital and operational costs of the CO_2 electrolyzer. This would allow for a more comprehensive assessment of the economic viability of each of the products analyzed.

References

[1] B. Ayvaz, A. O. Kusakci, G. T. Temur, *GS* **2017**, *7*, 436–452.

[2] Y. Hu, R. Li, L. Du, S. Ren, J. Chevallier, *Energy Policy* **2022**, *170*, 113252.

[3] L. J. R. Nunes, *Environments* **2023**, *10*, 66.

[4] F. I. Dinul, H. Nurdin, D. Rahmadiawan, Nasruddin, I. A. Laghari, T. Elshaarani, *jerel* **2023**, *2*, 28–34.

[5] K. Nemire, *Ergonomics in Design: The Quarterly of Human Factors Applications* **2014**, *22*, 3–3.

[6] M. Peichl, M. A. Arain, J. J. Brodeur, *Agricultural and Forest Meteorology* **2010**, *150*, 1090–1101.

[7] K. Calvin, D. Dasgupta, G. Krinner, A. Mukherji, P. W. Thorne, C. Trisos, J. Romero, P. Aldunce, K. Barrett, G. Blanco, W. W. L. Cheung, S. Connors, F. Denton, A. Diongue-Niang, D. Dodman, M. Garschagen, O. Geden, B. Hayward, C. Jones, F. Jotzo, T. Krug, R. Lasco, Y.-Y. Lee, V. Masson-Delmotte, M. Meinshausen, K. Mintenbeck, A. Mokssit, F. E. L. Otto, M. Pathak, A. Pirani, E. Poloczanska, H.-O. Pörtner, A. Revi, D. C. Roberts, J. Roy, A. C. Ruane, J. Skea, P. R. Shukla, R. Slade, A. Slangen, Y. Sokona, A. A. Sörensson, M. Tignor, D. Van Vuuren, Y.-M. Wei, H. Winkler, P. Zhai, Z. Zommers, J.-C. Hourcade, F. X. Johnson, S. Pachauri, N. P. Simpson, C. Singh, A. Thomas, E. Totin, P. Arias, M. Bustamante, I. Elgizouli, G. Flato, M. Howden, C. Méndez-Vallejo, J. J. Pereira, R. Pichs-Madruga, S. K. Rose, Y. Saheb, R. Sánchez Rodríguez, D. Ürge-Vorsatz, C. Xiao, N. Yassaa, A. Alegría, K. Armour, B. Bednar-Friedl, K. Blok, G. Cissé, F. Dentener, S. Eriksen, E. Fischer, G. Garner, C. Guivarch, M. Haasnoot, G. Hansen, M. Hauser, E. Hawkins, T. Hermans, R. Kopp, N. Leprince-Ringuet, J. Lewis, D. Ley, C. Ludden, L. Niamir, Z. Nicholls, S. Some, S. Szopa, B. Trewin, K.-I. Van Der Wijst, G. Winter, M. Witting, A. Birt, M. Ha, J. Romero, J. Kim, E. F. Haites, Y. Jung, R. Stavins, A. Birt, M. Ha, D. J. A. Orendain, L. Ignon, S. Park, Y. Park, A. Reisinger, D. Cammaramo, A. Fischlin, J. S. Fuglestvedt, G. Hansen, C. Ludden, V. Masson-Delmotte, J. B. R. Matthews, K. Mintenbeck, A. Pirani, E. Poloczanska, N. Leprince-Ringuet, C. Péan, *IPCC, 2023: Climate Change 2023: Synthesis Report. Contribution of Working Groups I, II and III to the Sixth Assessment Report of the Intergovernmental Panel on Climate Change [Core Writing Team, H. Lee and J. Romero (Eds.)]. IPCC, Geneva, Switzerland.*, Intergovernmental Panel On Climate Change (IPCC), **2023**.

[8] X. Dong, M. Yue, Y. Jiang, X.-M. Hu, Q. Ma, J. Pu, G. Zhou, **2020**, DOI 10.5194/acp-2020-1128.

[9] A. Dosio, L. Mentaschi, E. M. Fischer, K. Wyser, *Environ. Res. Lett.* **2018**, *13*, 054006.

[10] N. W. Priambodo, J. Raharjo, M. Rokhmat, *IJEEP* **2022**, *12*, 457–465.

[11] G. Rothenberg, *Sustainable Chemistry for Climate Action* **2023**, *2*, 100012.

[12] Global Energy Review: CO2 Emissions in 2021(International Energy Agency). **2021**.

[13] Y. Zhao, H. Ding, X. Lin, L. Li, W. Liao, Y. Liu, *Front. Environ. Sci.* **2021**, *9*, 754192.

[14] X. Li, B. Yu, *Energy Policy* **2019**, *133*, 110913.

[15] Global Wind Report (Global Wind Energy Council). **2025**.

[16] D. Feldman, V. Ramasamy, R. Fu, A. Ramdas, J. Desai, R. Margolis, *U.S. Solar Photovoltaic System and Energy Storage Cost Benchmark (Q1 2020)*, **2021**.

[17] O. Bamisile, C. Acen, D. Cai, Q. Huang, I. Staffell, *Renewable and Sustainable Energy Reviews* **2025**, *208*, 115073.

[18] A. Garrod, A. Ghosh, *Front. Energy* **2023**, *17*, 704–726.

[19] M. Amir, R. G. Deshmukh, H. M. Khalid, Z. Said, A. Raza, S. M. Muyeen, A.-S. Nizami, R. M. Elavarasan, R. Saidur, K. Sopian, *Journal of Energy Storage* **2023**, *72*, 108694.

[20] O. Y. Edelenbosch, A. F. Hof, M. Van Den Berg, H. S. De Boer, H.-H. Chen, V. Daioglou, M. M. Dekker, J. C. Doelman, M. G. J. Den Elzen, M. Harmsen, S. Mikropoulos, M. A. E. Van Sluisveld, E. Stehfest, I. S. Tagomori, W.-J. Van Zeist, D. P. Van Vuuren, *Nat. Clim. Chang.* **2024**, *14*, 715–722.

[21] Y. E. Chew, B. S. How, J. Sunarso, I. Moser, V. Andiappan, *Process Integr Optim Sustain* **2025**, DOI 10.1007/s41660-025-00494-y.

[22] D. Guilbert, G. Vitale, *Clean Technol.* **2021**, *3*, 881–909.
[23] M. K. Singla, P. Nijhawan, A. S. Oberoi, *Environ Sci Pollut Res* **2021**, *28*, 15607–15626.
[24] D. D. T. Ferraren-De Cagalitan, M. L. S. Abundo, *Renewable and Sustainable Energy Reviews* **2021**, *151*, 111413.
[25] F. Swennenhuis, V. de Gooyert, H. de Coninck, *Energy Research & Social Science* **2022**, *88*, 102598.
[26] D. R. Nhuchhen, S. P. Sit, D. B. Layzell, *Applied Energy* **2022**, *317*, 119180.
[27] N. Rambhujun, M. S. Salman, T. Wang, C. Pratthana, P. Sapkota, M. Costalin, Q. Lai, K.-F. Aguey-Zinsou, *MRS Energy & Sustainability* **2020**, *7*, 33.
[28] S. Atilhan, S. Park, M. M. El-Halwagi, M. Atilhan, M. Moore, R. B. Nielsen, *Current Opinion in Chemical Engineering* **2021**, *31*, 100668.
[29] F. Schenke, J. Hoelzen, C. Minke, A. Bensmann, R. Hanke-Rauschenbach, *Energy Conversion and Management: X* **2023**, *20*, 100435.
[30] A. Rabiee, A. Keane, A. Soroudi, *Renewable Energy* **2021**, *163*, 1580–1587.
[31] J. A. Faria, *Current Opinion in Green and Sustainable Chemistry* **2021**, *29*, 100466.
[32] J. Go, J. Byun, K. Orehounig, Y. Heo, *Applied Energy* **2023**, *337*, 120742.
[33] B. Lee, L. R. Winter, H. Lee, D. Lim, H. Lim, M. Elimelech, *ACS Energy Lett.* **2022**, *7*, 3032–3038.
[34] S.-Y. Ahn, K.-J. Kim, B.-J. Kim, G.-R. Hong, W.-J. Jang, J. W. Bae, Y.-K. Park, B.-H. Jeon, H.-S. Roh, *Renewable and Sustainable Energy Reviews* **2023**, *186*, 113635.
[35] F. S. AlHumaidan, M. Absi Halabi, M. S. Rana, M. Vinoba, *Energy Conversion and Management* **2023**, *283*, 116840.
[36] D. G. Bessarabov, H. Wang, H. Li, N. Zhao, Eds. , *PEM Electrolysis for Hydrogen Production: Principles and Applications*, CRC Press, Boca Raton, Florida, **2016**.
[37] N. Ma, W. Zhao, W. Wang, X. Li, H. Zhou, *International Journal of Hydrogen Energy* **2024**, *50*, 379–396.
[38] S. Shiva Kumar, H. Lim, *Energy Reports* **2022**, *8*, 13793–13813.
[39] H. P. C. Buitendach, R. Gouws, C. A. Martinson, C. Minnaar, D. Bessarabov, *Results in Engineering* **2021**, *10*, 100216.
[40] M. Carmo, D. L. Fritz, J. Mergel, D. Stolten, *International Journal of Hydrogen Energy* **2013**, *38*, 4901–4934.
[41] S. A. Grigoriev, V. N. Fateev, D. G. Bessarabov, P. Millet, *International Journal of Hydrogen Energy* **2020**, *45*, 26036–26058.
[42] S. Zorica, M. Vukšić, T. Betti, *International Journal of Electrical Power & Energy Systems* **2019**, *111*, 237–247.
[43] S. Marini, P. Salvi, P. Nelli, R. Pesenti, M. Villa, M. Berrettoni, G. Zangari, Y. Kiros, *Electrochimica Acta* **2012**, *82*, 384–391.
[44] J. Brauns, T. Turek, *Processes* **2020**, *8*, 248.
[45] O. Schmidt, A. Gambhir, I. Staffell, A. Hawkes, J. Nelson, S. Few, *International Journal of Hydrogen Energy* **2017**, *42*, 30470–30492.
[46] M. Rashid, M. K. A. Mesfer, H. Naseem, M. Danish, **n.d.**, *4*.
[47] A. Hauch, R. Küngas, P. Blennow, A. B. Hansen, J. B. Hansen, B. V. Mathiesen, M. B. Mogensen, *Science* **2020**, *370*, eaba6118.
[48] A. Villalba-Herreros, R. d'Amore-Domenech, A. Crucelaegui, T. J. Leo, *ACS Sustainable Chem. Eng.* **2023**, *11*, 4716–4726.
[49] S. Thielges, B. Olfe-Kräutlein, A. Rees, J. Jahn, V. Sick, R. Quitzow, *Front. Clim.* **2022**, *4*, 943387.
[50] Ifeanyi Onyedika Ekemezie, Wags Numoipiri Digitemie, *Eng. sci. technol. j.* **2024**, *5*, 949–961.
[51] A. Sodiq, Y. Abdullatif, B. Aissa, A. Ostovar, N. Nassar, M. El-Naas, A. Amhamed, *Environmental Technology & Innovation* **2023**, *29*, 102991.
[52] E. Hanson, C. Nwakile, V. O. Hammed, *Results in Surfaces and Interfaces* **2025**, *18*, 100381.
[53] A. Dott, D. G. Gavrilis, A. Drews, A. Werner, *Chem Eng & Technol* **2023**, *46*, 891–900.

[54] M. F. Shehzad, H. Ishaq, C. Crawford, *International Journal of Hydrogen Energy* **2023**, *48*, 39216–39224.

[55] S. Fujikawa, R. Selyanchyn, *MRS Bulletin* **2022**, *47*, 416–423.

[56] Wags Numoipiri Digitemie, Ifeanyi Onyedika Ekemezie, *Financ. account. res. j.* **2024**, *6*, 408–420.

[57] S. Kikkawa, K. Amamoto, Y. Fujiki, J. Hirayama, G. Kato, H. Miura, T. Shishido, S. Yamazoe, *ACS Environ. Au* **2022**, *2*, 354–362.

[58] C. P. O'Brien, R. K. Miao, A. Shayesteh Zeraati, G. Lee, E. H. Sargent, D. Sinton, *Chem. Rev.* **2024**, *124*, 3648–3693.

[59] Carbon Engineering. (Accessed: April 2025).

[60] A. Mraoui, B. Benyoucef, L. Hassaine, *International Journal of Hydrogen Energy* **2018**, *43*, 3441–3450.

[61] G. M. Sriramagiri, W. Luc, F. Jiao, K. Ayers, K. D. Dobson, S. S. Hegedus, *Sustainable Energy Fuels* **2019**, *3*, 422–430.

[62] L. Phan Van, L. Hieu Hoang, T. Nguyen Duc, *International Journal of Hydrogen Energy* **2023**, *48*, 25231–25249.

[63] X. Gu, Z. Ying, X. Zheng, B. Dou, G. Cui, *Renewable Energy* **2023**, *209*, 53–62.

[64] X. Hu, L. Xu, X. Lin, M. Pecht, *Joule* **2020**, *4*, 310–346.

[65] M. Biswal, S. Sabyasachi, *International Journal of Engineering Research and* **2012**, *2*.

[66] R. García-Valverde, N. Espinosa, A. Urbina, *International Journal of Hydrogen Energy* **2011**, *36*, 10574–10586.

[67] V. K. Bupesh Raja, I. Raja, R. Kavvampally, *J. Phys.: Conf. Ser.* **2021**, *2129*, 012011.

[68] M. Scarfogliero, S. Carmeli, F. Castelli-Dezza, M. Mauri, M. Rossi, G. Marchegiani, E. Rovelli, in *2018 International Conference of Electrical and Electronic Technologies for Automotive*, IEEE, Milan, **2018**, pp. 1–6.

[69] M. J. Lacey, A. Yalamanchili, J. Maibach, C. Tengstedt, K. Edström, D. Brandell, *RSC Adv.* **2016**, *6*, 3632–3641.

[70] L. Arriaga, W. Martinez, U. Cano, H. Blud, *International Journal of Hydrogen Energy* **2007**, *32*, 2247–2252.

[71] Z. Yang, J. Lin, H. Zhang, B. Lin, G. Lin, *Fuel Cells* **2018**, *18*, 543–550.

[72] B. Paul, *International Journal of Hydrogen Energy* **2008**, *33*, 490–498.

[73] F. Gutiérrez-Martín, A. B. Calcerrada, A. de Lucas-Consuegra, F. Dorado, *Renewable Energy* **2020**, *147*, 639–649.

[74] R. E. Clarke, S. Giddey, F. T. Ciacchi, S. P. S. Badwal, B. Paul, J. Andrews, *International Journal of Hydrogen Energy* **2009**, *34*, 2531–2542.

[75] M. Kavya, S. Jayalalitha, *Arch Computat Methods Eng* **2021**, *28*, 2447–2457.

[76] A. González Del Valle, P. García-Linares, A. Martí, *Adv Energy and Sustain Res* **2024**, 2400210.

[77] F. Gutiérrez-Martín, J. A. Díaz-López, A. Caravaca, A. J. Dos Santos-García, *International Journal of Hydrogen Energy* **2024**, *52*, 995–1006.

[78] Rohde & Schwarz. Verifying DC-DC converter efficiency **2023**. https://www. rohde-schwarz.com/fi/applications/verifying-dc-dc-converter-efficiency-application-card_56279-836096.html.

[79] A. González Del Valle, P. García-Linares, A. Martí, *Energy Conversion and Management* **2024**, *315*, 118751.

[80] *PVGIS-SARAH2*. European Commission. (Accessed: March 2023)

[81] G. Ciulla, V. Lo Brano, V. Di Dio, G. Cipriani, *Renewable and Sustainable Energy Reviews* **2014**, *32*, 684–696.

[82] F. Ghani, *Renewable Energy* **2014**.

[83] H. K. Mehta, H. Warke, K. Kukadiya, A. K. Panchal, *IEEE J. Photovoltaics* **2019**, *9*, 803–810.

[84] V. J. Chin, Z. Salam, K. Ishaque, *Applied Energy* **2015**, *154*, 500–519.

[85] J. Ramos-Hernanz, J. M. Lopez-Guede, E. Zulueta, **2017**, *12*.

[86] S. A. Rahman, R. K. Varma, T. Vanderheide, *IET Renewable Power Generation* **2014**, *8*, 217–229.

[87] J. Müller, K. Bothe, S. Herlufsen, H. Hannebauer, R. Ferré, R. Brendel, *Solar Energy Materials and Solar Cells* **2012**, *106*, 76–79.

[88] M. A. Green, E. D. Dunlop, G. Siefer, M. Yoshita, N. Kopidakis, K. Bothe, X. Hao, *Progress in Photovoltaics* **2023**, *31*, 3–16.

[89] P. Singh, N. M. Ravindra, *Emerging Materials Research* **2012**, *1*, 33–38.

[90] H. Lin, G. Wang, Q. Su, C. Han, C. Xue, S. Yin, L. Fang, X. Xu, P. Gao, *Progress in Photovoltaics* **2024**, *32*, 359–371.

[91] O. Dupre, R. Vaillon, M. A. Green, *IEEE J. Photovoltaics* **2016**, *6*, 56–60.

[92] Q. Wang, B. Xu, J. Sun, H. Liu, Z. Zhao, D. Yu, C. Fan, J. He, *J. Am. Chem. Soc.* **2014**, *136*, 9826–9829.

[93] N. Rojas, M. Sánchez-Molina, G. Sevilla, E. Amores, E. Almandoz, J. Esparza, M. R. Cruz Vivas, C. Colominas, *International Journal of Hydrogen Energy* **2021**, *46*, 25929–25943.

[94] D. S. Falcão, A. M. F. R. Pinto, *Journal of Cleaner Production* **2020**, *261*, 121184.

[95] I. Dincer, A. A. AlZahrani, in *Comprehensive Energy Systems*, Elsevier, **2018**, pp. 985–1025.

[96] H. Kim, M. Park, K. S. Lee, *International Journal of Hydrogen Energy* **2013**, *38*, 2596–2609.

[97] Z. Abdin, C. J. Webb, E. MacA. Gray, *International Journal of Hydrogen Energy* **2015**, *40*, 13243–13257.

[98] R. García-Valverde, N. Espinosa, A. Urbina, *International Journal of Hydrogen Energy* **2012**, *37*, 1927–1938.

[99] A. E.-S. A. Nafeh, *Int. J. Numer. Model.* **2011**, *24*, 282–297.

[100] P. Choi, *Solid State Ionics* **2004**, *175*, 535–539.

[101] S. Touré, A. Konaté, D. Traoré, D. Fofana, *IOP Conf. Ser.: Earth Environ. Sci.* **2018**, *188*, 012041.

[102] K.-F. Chiu, Y.-R. Chen, H. C. Lin, W. H. Ho, *Surface and Coatings Technology* **2010**, *205*, 1647–1650.

[103] E. Kuhnert, V. Hacker, M. Bodner, *International Journal of Energy Research* **2023**, *2023*, 1–23.

[104] E. Van Der Roest, R. Bol, T. Fens, A. Van Wijk, *International Journal of Hydrogen Energy* **2023**, *48*, 27872–27891.

[105] "*Lithium-Ion Battery Pack Prices Hit Record Low of $139/kWh.*" BloombergNEF. (Accessed: July 2024)

[106] Hidrógeno Verde. (Accessed: July 2024)

[107] V. Ramasamy, J. Zuboy, M. Woodhouse, E. O'Shaughnessy, D. Feldman, J. Desai, A. Walker, R. Margolis, P. Basore, *Renewable Energy* **2023**.

[108] S. Krishnan, V. Koning, M. Theodorus De Groot, A. De Groot, P. G. Mendoza, M. Junginger, G. J. Kramer, *International Journal of Hydrogen Energy* **2023**, *48*, 32313–32330.

[109] "*Lithium-Ion Battery Pack Prices Hit Record Low of $139/kWh.*" BloombergNEF. (Accessed: July 2024)

[110] K. S. Awale, A. U. Kumbhar, V. A. Kole, J. B. Kamate, *J Electr Electron Syst* **2017**, *06*, DOI 10.4172/2332-0796.1000221.

[111] D. Marinič, B. Likozar, *Journal of Cleaner Production* **2023**, *408*, 137185.

[112] O. A. Yafiee, F. Mumtaz, P. Kumari, G. N. Karanikolos, A. Decarlis, L. F. Dumée, *Chemical Engineering Journal* **2024**, *497*, 154421.

[113] M. Ozkan, S. P. Nayak, A. D. Ruiz, W. Jiang, *iScience* **2022**, *25*, 103990.

[114] A. Sodiq, Y. Abdullatif, B. Aissa, A. Ostovar, N. Nassar, M. El-Naas, A. Amhamed, *Environmental Technology & Innovation* **2023**, *29*, 102991.

[115] Callen, Herbert B, *Thermodynamics and an Introduction to Thermostatistics*, John Wiley & Sons Inc, New York, **1985**.

[116] P. Atkins, J. D. Paula, J. Keeler, *Atkins' Physical Chemistry*, Oxford University Press, **2022**.

[117] V. P. Maslov, *Russ. J. Math. Phys.* **2011**, *18*, 83–101.

[118] Sara Anwar, John J. Carroll, *Carbon Dioxide Thermodynamic Properties Handbook*, Wiley, Scrivener Publishing, Beverly, MA, **2016**.

[119] C. Wang, H. Liu, X. Li, L. Zheng, *Ind. Eng. Chem. Res.* **2013**, *52*, 2470–2476.

[120] N. Sedlar, A. Irwin, D. Martin, R. Roberts, *Journal of Safety Research* **2023**, *84*, 290–305.

[121] J. Friederich, S. Lazarova-Molnar, *Journal of Manufacturing Systems* **2024**, *72*, 38–58.

[122] L. Zhou, J. Li, F. Li, Q. Meng, J. Li, X. Xu, *Journal of Cleaner Production* **2016**, *112*, 3721–3734.

[123] Elias P. Gyftopoulos, Gian Paolo Beretta, *Thermodynamics: Foundations and Applications*, Douver Publications., Mineola, New York, **1991**.

[124] J. Husebye, A. L. Brunsvold, S. Roussanaly, X. Zhang, *Energy Procedia* **2012**, *23*, 381–390.

[125] C. Azar, S. H. Schneider, *Ecological Economics* **2002**, *42*, 73–80.

[126] S.-Y. Pan, P.-C. Chiang, W. Pan, H. Kim, *Critical Reviews in Environmental Science and Technology* **2018**, *48*, 471–534.

[127] S. N. Nangle, M. Ziesack, S. Buckley, D. Trivedi, D. M. Loh, D. G. Nocera, P. A. Silver, *Metabolic Engineering* **2020**, *62*, 207–220.

[128] IRENA (International Renewable Energy Agency). **2023.**

[129] G. Calvo, J.-L. Palacios, A. Valero, *Environmental Development* **2022**, *41*, 100683.

[130] B. J. Glaister, G. M. Mudd, *Minerals Engineering* **2010**, *23*, 438–450.

[131] G. Karakatsanis, C. Makropoulos, *Entropy* **2022**, *25*, 4.

[132] K. Z. House, A. C. Baclig, M. Ranjan, E. A. van Nierop, J. Wilcox, H. J. Herzog, *Proc. Natl. Acad. Sci. U.S.A.* **2011**, *108*, 20428–20433.

[133] V. Nikulshina, D. Hirsch, M. Mazzotti, A. Steinfeld, *Energy* **2006**, *31*, 1715–1725.

[134] M. Mahmoudkhani, D. W. Keith, *International Journal of Greenhouse Gas Control* **2009**, *3*, 376–384.

[135] K. S. Lackner, *Eur. Phys. J. Spec. Top.* **2009**, *176*, 93–106.

[136] A. Martí, E. Antolín, I. Durán, S. Svatek, A. L. D. Lacey, M. Pita, M. V. Martínez-Huerta, J. C. Conesa, **2021.**

[137] K. Storrs, I. Lyhne, R. Drustrup, *International Journal of Greenhouse Gas Control* **2023**, *125*, 103878.

[138] B. Dziejarski, R. Krzyżyńska, K. Andersson, *Fuel* **2023**, *342*, 127776.

[139] E. E. Ünveren, B. Ö. Monkul, Ş. Sarıoğlan, N. Karademir, E. Alper, *Petroleum* **2017**, *3*, 37–50.

[140] R. P. Wijesiri, G. P. Knowles, H. Yeasmin, A. F. A. Hoadley, A. L. Chaffee, *Ind. Eng. Chem. Res.* **2019**, *58*, 15606–15618.

[141] I. S. Metcalfe, G. A. Mutch, E. I. Papaioannou, S. Tsochataridou, D. Neagu, D. J. L. Brett, F. Iacoviello, T. S. Miller, P. R. Shearing, P. A. Hunt, *Nat Energy* **2024**, DOI 10.1038/s41560-024-01588-6.

[142] S. J. Gerke, G. Brösigke, J.-U. Repke, *Experimental Thermal and Fluid Science* **2024**, *153*, 111131.

[143] G. R. Carmichael, O. Tarasova, Ø. Hov, L. Barrie, J. H. Butler, *Bulletin of the American Meteorological Society* **2023**, *104*, E666–E672.

[144] S. Das, *Physics Letters B* **2024**, *853*, 138653.

[145] H. B. Callen, *Thermodynamics and an Introduction to Thermostatistics*, John Wiley & Sons Inc., **1985**.

[146] K. A. Masavetas, *Mathematical and Computer Modelling* **1989**, *12*, 651–657.

[147] D. D. Wagman, *NBS Tables of Chemical Thermodynamic Properties: Selected Values for Inorganic and C1 and C2 Organic Substances in SI Units - Hardcover*, American Chemical Society, **1982**.

[148] D. N. Rihani, L. K. Doraiswamy, *Ind. Eng. Chem. Fund.* **1965**, *4*, 17–21.

[149] A. A. Zavitsas, D. W. Rogers, N. Matsunaga, *J. Org. Chem.* **2010**, *75*, 6502–6515.

[150] Z.-X. Zeng, X.-N. Li, W.-L. Xue, C.-S. Zhang, S.-C. Bian, **n.d.**, 6.

[151] N. Cohen, S. W. Benson, *Chem. Rev.* **1993**, *93*, 2419–2438.

[152] D. C. Young, *Computational Chemistry: A Practical Guide for Applying Techniques to Real World Problems*, Wiley, **2001**.

[153] A. Genoni, L. Bučinský, N. Claiser, J. Contreras-García, B. Dittrich, P. M. Dominiak, E. Espinosa, C. Gatti, P. Giannozzi, J. Gillet, D. Jayatilaka, P. Macchi, A. Ø. Madsen, L.

Massa, C. F. Matta, K. M. Merz, P. N. H. Nakashima, H. Ott, U. Ryde, K. Schwarz, M. Sierka, S. Grabowsky, *Chemistry A European J* **2018**, *24*, 10881–10905.
[154] A. Tkatchenko, *Nat Commun* **2020**, *11*, 4125.
[155] P. Hohenberg, W. Kohn, *Phys. Rev.* **1964**, *136*, B864–B871.
[156] G. Tsaparlis, G. Pantazi, E. T. Pappa, B. Byers, *Chemistry Teacher International* **2021**, *3*, 391–411.
[157] P. M. W. Gill, B. G. Johnson, J. A. Pople, M. J. Frisch, *Int. J. Quantum Chem.* **1992**, *44*, 319–331.
[158] A. D. Becke, *The Journal of Chemical Physics* **1993**, *98*, 1372–1377.
[159] J. P. Perdew, M. Ernzerhof, K. Burke, *The Journal of Chemical Physics* **1996**, *105*, 9982–9985.
[160] E. Torres, G. A. DiLabio, *J. Phys. Chem. Lett.* **2012**, *3*, 1738–1744.
[161] D. Coskun, S. V. Jerome, R. A. Friesner, *J. Chem. Theory Comput.* **2016**, *12*, 1121–1128.
[162] Y. Zhao, D. G. Truhlar, *J. Chem. Theory Comput.* **2007**, *3*, 289–300.
[163] Y. Zhao, D. G. Truhlar, *Theor Chem Account* **2008**, *120*, 215–241.
[164] C. Halsey-Moore, P. Jena, J. T. McLeskey, *Computational and Theoretical Chemistry* **2019**, *1162*, 112506.
[165] D. G. A. Smith, A. T. Lolinco, Z. L. Glick, J. Lee, A. Alenaizan, T. A. Barnes, C. H. Borca, R. Di Remigio, D. L. Dotson, S. Ehlert, A. G. Heide, M. F. Herbst, J. Hermann, C. B. Hicks, J. T. Horton, A. G. Hurtado, P. Kraus, H. Kruse, S. J. R. Lee, J. P. Misiewicz, L. N. Naden, F. Ramezanghorbani, M. Scheurer, J. B. Schriber, A. C. Simmonett, J. Steinmetzer, J. R. Wagner, L. Ward, M. Welborn, D. Altarawy, J. Anwar, J. D. Chodera, A. Dreuw, H. J. Kulik, F. Liu, T. J. Martínez, D. A. Matthews, H. F. Schaefer, J. Šponer, J. M. Turney, L.-P. Wang, N. De Silva, R. A. King, J. F. Stanton, M. S. Gordon, T. L. Windus, C. D. Sherrill, L. A. Burns, *The Journal of Chemical Physics* **2021**, *155*, 204801.
[166] Libro del Web de Química del NIST, SRD 69 n.d. https://webbook.nist.gov/cgi/cbook.cgi?ID=C124389&Mask=1 (accessed February 21, 2024)
[167] G. J. Kluitenberg, in *SSSA Book Series* (Eds.: J.H. Dane, G. Clarke Topp), Soil Science Society Of America, Madison, WI, USA, **2018**, pp. 1201–1208.
[168] P. Westh, *J. Phys. Chem.* **1994**, *98*, 3222–3225.
[169] A. Lucia, H. Henley, *Chemical Engineering Research and Design* **2013**, *91*, 1748–1759.
[170] P. M. Mathias, J. P. O'Connell, *Ind. Eng. Chem. Res.* **2012**, *51*, 5090–5097.
[171] P. M. Mathias, *Ind. Eng. Chem. Res.* **2016**, *55*, 1076–1087.
[172] K. Storrs, I. Lyhne, R. Drustrup, *International Journal of Greenhouse Gas Control* **2023**, *125*, 103878.
[173] S. Jin, Z. Hao, K. Zhang, Z. Yan, J. Chen, *Angewandte Chemie* **2021**, *133*, 20795–20816.
[174] P. Duarah, D. Haldar, V. Yadav, M. K. Purkait, *Journal of Environmental Chemical Engineering* **2021**, *9*, 106394.
[175] Y. Liu, F. Li, X. Zhang, X. Ji, *Current Opinion in Green and Sustainable Chemistry* **2020**, *23*, 10–17.
[176] C. A. R. Pappijn, M. Ruitenbeek, M.-F. Reyniers, K. M. Van Geem, *Front. Energy Res.* **2020**, *8*, 557466.
[177] D. M. Weekes, D. A. Salvatore, A. Reyes, A. Huang, C. P. Berlinguette, *Acc. Chem. Res.* **2018**, *51*, 910–918.
[178] G. Wang, J. Chen, Y. Ding, P. Cai, L. Yi, Y. Li, C. Tu, Y. Hou, Z. Wen, L. Dai, *Chem. Soc. Rev.* **2021**, *50*, 4993–5061.
[179] D. Ray, **2021**.
[180] G. A. O. Tiago, I. A. S. Matias, A. P. C. Ribeiro, L. M. D. R. S. Martins, *Molecules* **2020**, *25*, 5812.
[181] D. D. Wagman, W. H. Evans, V. B. Parker, R. H. Schumm, I. Halow, *The NBS Tables of Chemical Thermodynamic Properties. Selected Values for Inorganic and C1 and C2 Organic Substances in SI Units,* NATIONAL STANDARD REFERENCE DATA SYSTEM, **1982**.

[182] “United States Natural Gas Industrial Price (Dollars per Thousand Cubic Feet).” https://www.eia.gov/dnav/ng/hist/n3035us3m.htm (accessed May. 03, 2024).

[183] "Formic Acid Price Trend and Forecast." https://www.chemanalyst.com/Pricing-data/formic-acid-1242 (accessed Feb.27,2025).

[184] "Coke of Coal Price Index"https://businessanalytiq.com/procurementanalytics/index/coke-of-coal-price-index/ (accessed Feb.27,2025).

[185] “Pricing | Methanex Corporation.” https://www.methanex.com/our-business/pricing (accessed May. 03, 2024).

[186] “Ethylene prices globally 2022,”*Statista*. https://www.statista.com/statistics/1170573/price-ethylene-forecast-globally/ (accessed May. 03, 2024).

[187] "Propanol Prices | Historical and Current"https://www.intratec.us/chemical-markets/propanol-price (accessed Feb.27,2025).

[188] H. C. Erythropel, J. B. Zimmerman, T. M. De Winter, L. Petitjean, F. Melnikov, C. H. Lam, A. W. Lounsbury, K. E. Mellor, N. Z. Janković, Q. Tu, L. N. Pincus, M. M. Falinski, W. Shi, P. Coish, D. L. Plata, P. T. Anastas, *Green Chem.* **2018**, *20*, 1929–1961.

[189] J. J. Kaczur, H. Yang, Z. Liu, S. D. Sajjad, R. I. Masel, *C* **2020**, *6*, 33.

[190] K. W. Kimura, K. E. Fritz, J. Kim, J. Suntivich, H. D. Abruña, T. Hanrath, *ChemSusChem* **2018**, *11*, 1781–1786.

[191] K. Rossi, R. Buonsanti, *Acc. Chem. Res.* **2022**, *55*, 629–637.

[192] H. Yang, J. J. Kaczur, S. D. Sajjad, R. I. Masel, *Journal of CO2 Utilization* **2017**, *20*, 208–217.

[193] P. G. Russell, N. Kovac, S. Srinivasan, M. Steinberg, *J. Electrochem. Soc.* **1977**, *124*, 1329–1338.

[194] C. W. Li, M. W. Kanan, *J. Am. Chem. Soc.* **2012**, *134*, 7231–7234.

[195] A. H. Abdol Rahim, A. S. Tijani, S. K. Kamarudin, S. Hanapi, *Journal of Power Sources* **2016**, *309*, 56–65.

[196] S. K. Murthy, A. K. Sharma, C. Choo, E. Birgersson, *J. Electrochem. Soc.* **2018**, *165*, A1746–A1752.

[197] A. Pohjoranta, A. Mendelson, R. Tenno, *Electrochimica Acta* **2010**, *55*, 1001–1012.

[198] A. Hauch, M. L. Traulsen, R. Küngas, T. L. Skafte, *Journal of Power Sources* **2021**, *506*, 230108.

[199] S. Hernandez-Aldave, E. Andreoli, *Catalysts* **2020**, *10*, 713.

[200] A. Lim, J. Kim, H. J. Lee, H.-J. Kim, S. J. Yoo, J. H. Jang, H. Young Park, Y.-E. Sung, H. S. Park, *Applied Catalysis B: Environmental* **2020**, *272*, 118955.

[201] S. Choe, B.-S. Lee, M. K. Cho, H.-J. Kim, D. Henkensmeier, S. J. Yoo, J. Y. Kim, S. Y. Lee, H. S. Park, J. H. Jang, *Applied Catalysis B: Environmental* **2018**, *226*, 289–294.

[202] J. Bai, W. Zhou, J. Xu, P. Zhou, Y. Deng, M. Xiang, D. Xiang, Y. Su, *Molecules* **2024**, *29*, 537.

[203] G. Ma, L. Qin, Y. Liu, H. Fan, L. Qiao, C. Yu, Z. Tang, *Surfaces and Interfaces* **2023**, *36*, 102555.

[204] H. Ito, T. Maeda, A. Nakano, H. Takenaka, *International Journal of Hydrogen Energy* **2011**, *36*, 10527–10540.

[205] W. Eccles, I. Sherrington, R. D. Arnell, *Proceedings of the Institution of Mechanical Engineers, Part C: Journal of Mechanical Engineering Science* **2010**, *224*, 483–495.

[206] T. S. Light, S. Licht, A. C. Bevilacqua, K. R. Morash, *Electrochem. Solid-State Lett.* **2005**, *8*, E16.

[207] H.-L. Zuo, F.-Q. Yang, W.-H. Huang, Z.-N. Xia, *Journal of Chromatographic Science* **2013**, *51*, 704–715.

[208] K. Dettmer-Wilde, W. Engewald, Eds. , *Practical Gas Chromatography: A Comprehensive Reference*, Springer Berlin Heidelberg, Berlin, Heidelberg, **2014**.

[209] M. Swartz, *Journal of Liquid Chromatography & Related Technologies* **2010**, *33*, 1130–1150.

[210] P. Izadi, A. Kas, P. Haus, F. Harnisch, *Electrochimica Acta* **2023**, *462*, 142733.